Centro de Investigación en Matemáticas, A.C.

Analysis and visualization of phase synchronization in EEG signals during cognitive tasks

TESIS

Que para obtener el Grado de

Doctorado en Ciencias de la Computación

P R E S E N T A :

Francisco Alfonso Alba Cadena

Directores de Tesis:

Dr. José Luis Marroquín Zaleta
Dra. Thalía Harmony Baillet

Guanajuato, Gto. Marzo de 2007.

Centro de Investigación en Matemáticas, A.C.

Analysis and visualization of phase synchronization in EEG signals during cognitive tasks

TESIS

Que para obtener el Grado de

Doctorado en Ciencias de la Computación

P R E S E N T A :

Francisco Alfonso Alba Cadena

Comité de Evaluación:

Dr. Johan Jozef Lode Van Horebeek
(Presidente)

Dr. Mariano José Juan Rivera Meraz
(Secretario)

Dr. Rogelio Hasimoto Beltrán
(Vocal)

Dr. Rogelio Ramos Quiroga
(Vocal)

Dra. Thalía Harmony Baillet
(Vocal y co-directora de Tesis)

Director de Tesis:

Dr. José Luis Marroquín Zaleta

Guanajuato, Gto. Marzo de 2007.

Para Dalia.
Esto y todo lo demás.

Agradecimientos

Quiero expresar mi mas profundo agradecimiento a las siguientes personas:

- A mi asesor, el Dr. José Luis Marroquín, quien me guió pacientemente durante todo el doctorado, y de quien espero haber aprendido algo.
- A la Dra. Thalía Harmony, co-asesora de mi tesis, por su imprescindible colaboración en este trabajo, y por ayudarme a entender su significado.
- Al Dr. Johan Van Horebeek, por sus cursos de probabilidad y estadística, que fueron de gran utilidad para el desarrollo de este trabajo, y también por sus opiniones y sugerencias sobre la tesis.
- A la Dra. Thalía Fernández por la adquisición de los datos de EEG utilizados en este trabajo.
- A los doctores Mariano Rivera, Rogelio Hasimoto, Rogelio Ramos, Johan Van Horebeek, y Thalía Harmony, por aceptar ser parte de mi comité de evaluación, y por el tiempo dedicado a revisar este trabajo.
- A José Castro y su familia, por su amistad, y por aceptarnos como inquilinos.
- A todo el personal del CIMAT por su atención y apoyo.
- A Joaquín Peña y Berta González Frankenberger por su colaboración.
- A mis compañeros de doctorado: Tere Alarcón, Arturo González, Edmar Mota, Fernando Gómez, Joaquín Peña, Alonso Ramírez, y Oscar Dalmau por su amistad y apoyo.
- A Dalia, por hacer de Guanajuato un mejor lugar.
- A mis padres, Guadalupe Cadena y Alfonso Alba, por darme la oportunidad y orientarme para llegar hasta aquí.
- A mis suegros, Dalia Wong y Jorge Fernández, por su valiosa ayuda.
- Al Físico Benito Pineda, Director de la Facultad de Ciencias, por su constante apoyo.
- Al Programa de Mejoramiento del Profesorado (PROMEP) por el apoyo económico otorgado durante tres años.
- Al Consejo Nacional de Ciencia y Tecnología (CONACYT) por el apoyo económico otorgado durante mi último semestre de doctorado.

Abstract

In this thesis we propose a new methodology for the study of phase synchronization in electroencephalographic signals. This methodology attempts to overcome some of the drawbacks found in the procedures typically used in the literature by using (1) sinusoidal quadrature filters, which give a more reliable response when tuned at low frequencies, (2) instantaneous in-phase synchrony measures, (3) a Bayesian classification approach to determine the significance of the synchrony changes with respect to a neutral condition, and (4) a time-frequency-topography (TFT) visualization system which can display the results with high spatial, temporal, and frequency resolutions. All these techniques are implemented in a software program which has already been used by neuroscientists to analyze various psychophysiological experiments. We have also tested our methodology with various of the synchrony measures proposed in the literature, and performed a comparative study which highlights the advantages and disadvantages of each one. Finally, we propose a simple mathematical model for the narrow-band EEG signal observed at each electrode, which allows one to explain and simulate different synchronization patterns that can be observed with real EEG data.

Contents

List of Figures

List of Tables

Chapter 1

Introduction

1.1 Introduction to EEG

Electroencephalography (EEG) is a neuroimaging technique that consists of voltage measurements recorded by one or more electrodes placed on the scalp (non-invasive EEG), or within the cortex (intracranial EEG). The first person to obtain an EEG recording from a human brain was Hans Berger, in the 1920's. He was also the first to observe the cyclic nature of the EEG and the relation between different states of consciousness (e.g. sleep, attention processes, wakefulness, etc.) and specific EEG wave patterns, especially in the frequency range from 8 to 12 Hz (alpha range) [Berger, 1929]. Figure 1.1 shows one of the EEG recordings obtained by Berger.

Although there are some recent intracranial studies (e.g. [Lachaux et al., 2000a]), most human EEG recordings are non-invasive: the electrodes are mounted in a cap, which is put in the subject's head. The electrodes are usually systematically distributed across the scalp surface; the most widely used distribution corresponds to the 10-20 international electrode placement system (shown in Figure 1.2). This system standardizes the electrode positions and nomenclature, and also allows researchers to compare their analysis and visualization

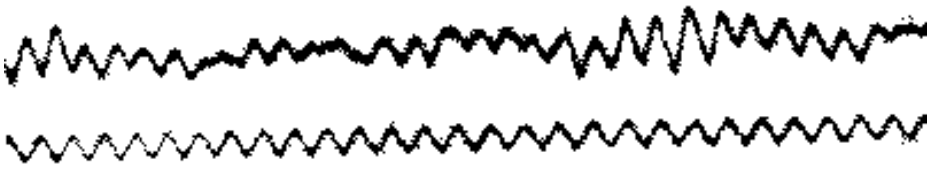

Figure 1.1: One of the first human electroencephalograms (Berger, circa 1929): the top trace is the EEG recording and the bottom trace is a 10 Hz reference signal.

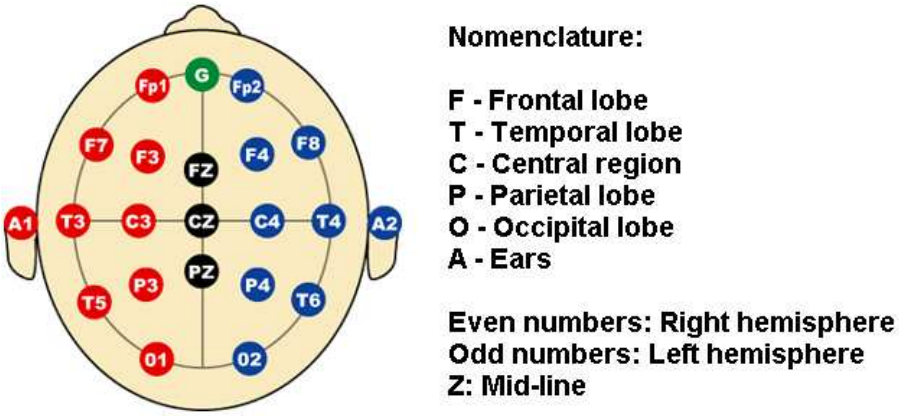

Figure 1.2: The International 10-20 electrode placement system. This diagram is copyrighted by the Immrama Institute (www.immrama.org) and used with permission.

techniques.

1.2 EEG applications

There are numerous applications of EEG in modern medicine. Some examples are:

- **Study of the properties of neural networks** - By properly designing an experiment and adequate analysis of the EEG recordings, scientists may obtain insights about neural activity and/or prove certain hypotheses which are specifically related to the task performed by the subjects.
- **Diagnostic** - EEG is used in brain-mapping for localizing the areas of epileptic activity prior to operation.
- **Therapy** - Neurofeedback consists of the self-modification of electrophysiological brain patterns. It may be used to treat psychological and neurological disorders, and also to learn mental relaxation.

We will focus on the first application, in which a psychophysiological experiment is designed, performed, and analyzed, in order to study the brain activity during the experiment. Most EEG experiments involve multiple subjects, and each subject performs the experiment multiple times. Each repetition of the experiment is called a *trial*, and the recorded data can be seen as a set of voltage time series $V_{j,e}(t)$ where j is the trial number, e is the index of the recording channel or electrode (representing the spatial position of the sensors), and t is the time index.

A wide range of psychophysiological experiments follow this scheme: each subject is presented with an stimulus (e.g. a certain image in a screen, a sound or a word, etc.) and is instructed to respond in some way (e.g. press a button) or perform a certain task (e.g. add two numbers, memorize a set, etc). EEG is recorded during the experiment, one segment per trial. Each segment starts before the stimulus presentation and finishes after the subject has responded. Thus each segment is commonly split in two parts: the *pre-stimulus segment* corresponding to the recording before the stimulus onset, and the *post-stimulus segment*, which contains all activity after the stimulus. In these experiments, one usually performs a statistical comparison between both pre and post-stimulus segments, in order to detect significant changes in the neural activity which may be related to the task performed by the subjects.

1.3 Analysis of EEG signals

In order to obtain information about the neural events taking place during the experiment, different types of analysis may be performed with the EEG data. These usually involve time-frequency decomposition techniques and statistical tools. Here we describe the most common types of analysis found in the literature.

1.3.1 Evoked potentials

Evoked activity corresponds to EEG changes which are time-locked and phase-locked to the stimulus [Pfurtscheller and Lopes da Silva, 1999]. This activity is usually obtained, for each recording channel, by averaging the recorded potentials across all trials:

$$EP_e(t) = \frac{1}{N_r} \sum_{j=1}^{N_r} V_{j,e}(t). \tag{1.1}$$

Here N_r is the number of trials, and EP_e represents the evoked activity at electrode e. These averaged signals may show significative peaks (called event-related potentials or ERP's) which may be related to the task. ERP's are named according to their latency with respect to the stimulus onset (in milliseconds), and the letter N or P indicating its sign. For example, P300 denotes a positive evoked potential taking place around 300 ms after the stimulus.

1.3.2 Power analysis

One of the most common tools used for EEG analysis consists on a spectral power decomposition at the frequency bands of interest. It is known that certain frequency bands are related to different states of attention and consciousness (see [Niedermeyer, 2004], Chapter 3); for example, the power ratio between certain pairs of bands may be used for neurofeedback therapy. Time-frequency

power analysis is also useful to detect event-related induced activity, which is time-locked but not phase-locked to the stimulus. The increases or decreases of power in specific frequency bands may be considered to be due to an increase or decrease, respectively, in the synchrony of the underlying neuronal populations [Pfurtscheller and Lopes da Silva, 1999], and thus are accordingly called "event-related synchronization" (ERS) and "event-related desynchronization" (ERD). Other works have also shown that changes in power may be related to cognitive and attentional processes (see [Harmony et al., 2004; Marroquin et al., 2004]).

1.3.3 EEG inverse problem

The inverse problem in EEG consists on localizing the current sources which are located in the brain, and which give origin to the potentials recorded by the sensors. This is an ill-posed problem and the solution is not unique; thus one must impose restraints to find a particular solution that suits a specific problem (a good review on some inverse problem methods can be found in [Pascual-Marqui, 1999]).

1.3.4 Synchrony analysis

EEG synchrony studies the dynamical connectivity patterns across neural networks, and their function as integration mechanisms. Synchrony can be studied at two levels: first, from a local point of view, where synchronization and desynchronization events between networks within a small area (separated by less than ~ 1 cm) may be reflected as power changes or bursts in the corresponding EEG channel [Varela et al., 2001]; and second, there is evidence for long-range synchronization between distant networks (not necessarily contiguous), which is reflected as some form of correlation or phase-locking between the signals from different sensors [Bressler et al., 1993; Rodriguez et al., 1999; Hoechstetter et al., 2004; Mizuhara et al., 2005].

1.4 EEG rhythms

Since the introduction of the EEG by Berger in the 1920's, researchers have recognized, categorized, and described the cyclic waveforms of EEG recordings (called *EEG rhythms*). These rhythms have been classified according to their frequency as: delta (1-4 Hz), theta (4-7 Hz), alpha (7-14 Hz), beta (14-30 Hz) and gamma (30 Hz and upwards). A thorough discussion of the neurophysiological origin of each of these rhythms can be found in [Niedermeyer, 2004] (Chapter 3).

Although it is very common to focus a particular analysis in one or more of these rhythms, it is recommended to perform the time-frequency decomposition in narrow frequency bands in order to obtain meaningful values of instantaneous amplitude and phase.

1.5 Reference electrode

The EEG measurements in a specific channel actually represent the difference of electric potentials at two electrode sites: the electrode corresponding to that channel (target electrode), and a reference electrode [Hagemann et al., 2001]. Electrical activity at either of these electrodes will be reflected in the EEG. Because of this, different placements of the reference electrode may result in very different derivations for each target electrode. Ideally, one would place the reference on a site with very low or null electrical activity. In practice, most recordings use a reference site placed on or near the head (cephalic reference), such as the neck, chin, or linked earlobes. It is also possible to use a non-cephalic reference; however, this may result in recordings largely contaminated by electrocardiogram (EKG) artifacts [Stephenson and Gibbs, 1951].

The reference problem is important in synchrony analysis because it may introduce spurious correlations between different EEG channels. However, in a cognitive task experiment, one may assume that any activity at the reference electrode is not related to the task, and thus the reference signals for different trials may be assumed to be uncorrelated, and its effect may be reduced after averaging across trials.

There are a few methods to transform the raw EEG signals into a new data set which further reduces the reference effects. Two of them are (1) current source density (CSD) estimation, which will be discussed in the following section, and (2) transformation to the average reference (AR). The AR data set is obtained by estimating the "average electrode" signal (which is the average signal of all lead signals) and subtracting it from each electrode signal to obtain a new derivation. This has the effect of re-referencing all the signals to a new virtual reference site whose activity is precisely the average of the theoretical reference-free lead signals. The problem is that, in practice, this activity is not only far from null but it is also biased towards the center the covered region, and it may also reflect changes related to the stimulus presentation in a cognitive experiment (e.g. evoked potentials may induce high activity at the virtual reference site), thus the effect of this virtual reference may not be canceled out by averaging across trials [Junghöfer et al., 1999].

An interesting discussion of different derivation methods (including linked ears, average reference, and CSD estimation) can be found in [Hagemann et al., 2001]. Hagemann's findings suggest that each method has its own limitations and some of them may be more appropriate for a specific type of analysis than the others.

1.6 Volume conduction

Another known problem is caused by the conductive properties of the cortex, skull, and scalp, which smear the potentials across the surface and reduces the

spatial resolution of the EEG [Nunez, 1995]. In 1975, Hjorth proposed a mathematical procedure to estimate the "source activity at the surface level of the scalp" [Hjorth, 1975], which is known as *scalp current density* (SCD) or *current source density* (CSD). This procedure effectively reduces volume conductor effects and yields a new set of signals which are more localized (i.e. have better spatial resolution) than the raw potentials. Moreover, CSD is not sensitive to the reference potential.

The idea behind CSD relies on estimating the current density field $\bar{J}$ from Ohm's law:

$$\bar{J} = \sigma \bar{E}, \tag{1.2}$$

where σ is the conductivity and E is the electric field. Given a surface distribution of potentials Φ we may calculate the electric field as $\bar{E} = -\nabla\Phi$, thus

$$\bar{J} = -\sigma \nabla \Phi. \tag{1.3}$$

Finally, the divergence of a vector field represents the source intensity of the field. We apply this to the current density field $\bar{J}$ to obtain the *current source density* J:

$$J = \nabla \cdot \bar{J} = -\sigma \nabla^2 \Phi. \tag{1.4}$$

According to Equation 1.4, CSD is negatively proportional to the surface Laplacian (SL) of the potentials. In practice, one is usually interested in relative changes of some measure with respect to the pre-stimulus, and the factor $-\sigma$ is canceled; thus one may work only with the SL.

During the following decade, Hjorth's procedure was refined to obtain faster and more accurate results (see [Pascual-Marqui et al., 1988], [Perrin et al., 1988, 1989]; [Law et al., 1993]). Basically, the SL is estimated by interpolating the potentials analytically for each time t, and then taking the second spatial derivatives of the interpolating function. Presently, the most used method is the one introduced by Perrin et al. in 1988, which approximates the SL by using spherical splines. More recently, Mizuhara et al. used CSD estimates to study long-range phase synchronization in a cognitive task [Mizuhara et al., 2005] and combined it with fMRI to determine which networks were being integrated during phase synchronization stages. (Functional MRI or fMRI is 3D imaging technique which is used to locate which parts of the brain are activated by showing regions with increased blood flow).

Nunez et al. [1995; 1997; 2000] have developed an extensive work on the effect of volume conduction in EEG coherence. Using simulated data from a 3 concentric spheres model, they estimated correlation coefficients for pairs of uncorrelated cortical sources using different EEG references (Cz, neck, linked ears, and average reference), cortical imaging, and Spline Laplacians ([Perrin et al., 1989, 1990; Law and Nunez, 1993]). In all cases, except Spline Laplacians, spurious high correlations were observed for short inter-electrode distances (4-8 cm) [Nunez et al., 1997]. However, since the Surface Laplacian acts as a

bandpass filter on the raw potentials, true coherence with low spatial frequency (i.e., relatively smooth across the surface) may be underestimated. Because of this, Nunez suggests to use the SL to complement, rather than replace, the raw EEG potentials: correlations may be observed at different spatial scales [Nunez et al., 1997, 2000] (just as correlations between customs of people from two different cities may differ from correlations between two families, one from each city). Therefore, raw potential, Surface Laplacian, and cortical image coherency may, in general, represent correlations at different spatial scales of cortical dynamics.

Unfortunately, there is a problem when measuring phase synchronization from SL signals: since the potentials are a smooth function of the position in the surface (partly because volume conductor effects), the Surface Laplacian, which is the second spatial derivative of the potentials, will have a very small magnitude. This means that the phase of the SL signals will be very sensitive to noise, and also to the interpolation method used to estimate the SL. Hagemann et al. [2001] also note this problem in his comparison of different reference derivations. According to [Junghöfer et al., 1999], current density measures with 32 or less channels will be unstable and inaccurate, and even for high spatial sampling density, the second derivative is much more vulnerable to noise than the scalp potentials.

An alternate solution to the volume conductor problem consists on estimating the current sources that give origin to the surface potentials. This usually involves placing various dipoles in the areas of interest and solving the inverse problem (with some necessary constraints) to find the source signals. This approach has been used by David et al. [2001], and Hoechstetter et al. [2004]. In David's method, the inverse problem is restrained by penalizing solutions which have sources with large amplitude that do not contribute to the frequency band of interest; the amount of penalization is locally determined (i.e. differs from source to source) and depends on the amount of power outside the frequency band of interest: if the signal in a given source has most of its power outside the frequency band of interest, that source will be highly penalized. Synchronization measures are usually calculated for each pair of sources, thus it is desirable to have as few sources as possible while maintaining an adequate spatial resolution. In order to minimize the number of reconstructed dipoles, David et al. use the following iterative approach: first, start with a large number of dipoles distributed uniformly across the whole cortex (with radial orientations) and solve the inverse problem for these sources. Then, the best dipoles are selected (according to a fitness measure, which is also based in the signal power outside the frequency band of interest) and the process is repeated for the selected dipoles until their fitness is higher than some threshold. Once the sources have been determined, the Single-Trial Phase-Locking Statistic (STPLS - [Lachaux et al., 2000b]), which we will describe in the next chapter, is estimated for each source pair.

One problem with the method described above is that it heavily relies on the spectral properties of the signals estimated for the full post-stimulus segment,

but does not account for possible changes of power during the course of an experiment (EEG signals are hardly static). Moreover, to analyze different frequency bands, one must solve the inverse problem and obtain a different set of sources for each band, which may provide a difficult interpretation of the results across bands.

The approach used by Hoechstetter is much simpler: the sources are placed in sites of interest which can be either pre-specified, or obtained from evoked data. Also, additional dipoles may be placed to model background activity (e.g. eye movement activity). These dipoles function as virtual sources within the brain. Later, a coherence measure (see [Gardner, 1992]) is estimated for each pair of source signals.

The problem, however, is that this method assumes that the modeled sources account for all activity recorded in the sensors and, unlike the adaptive selection approach used by David et al., this method does not attempt to find the sources whose activity may be related to the synchronous processes. Therefore, if the sources are not adequately distributed, the signals obtained for some of the dipoles may in fact represent the activity in large, overlapped cortical regions, which would defeat the purpose of source localization. Hoechstetter suggests fitting the sources to evoked activity; however, the relation between long-range synchrony and evoked activity is not yet clear.

1.7 Goals

The main goal of this work is to present a robust methodology to detect, analyze, and visualize significant changes in patterns of dynamic connectivity in both a wide spatial level (long range synchrony), and a local level (power analysis and evoked potentials). These changes may happen within a narrow frequency band and last only few dozens of milliseconds; thus it is important to preserve the time and frequency resolutions. It is also desirable that the techniques described here may be used with different synchrony measures (e.g. coherence, mutual information, etc - see Chapter 2 for more details).

While we focus in electroencephalographic signals in this work, it is intended that the most important contributions of this methodology hold for several types of neurophysiological signals, including: intracranial EEG, current sources, current density, and MEG.

The final procedure will be implemented as a Windows program with a straightforward interface and various navigating tools in order to easily identify and focus on the regions of interest. The program will

1. Allow the user to input raw EEG data in a standard file format
2. Preprocess and analyze the data to estimate and classify synchrony changes

3. Display the results in various types of graphs
4. Allow the user to save the results in a file (for further analysis with other programs)

As an example of application, the program described above will be used by neuroscientists to study the connectivity patterns in real EEG experiments from a neurophysiological point of view. We expect at least one paper to be published from these studies. Another paper describing the methodology (from a technical point of view) is already in print.

1.8 Thesis organization

The contents of this thesis are organized as follows:

- **Chapter 2** presents a summary of the most common methods and techniques used for EEG synchrony analysis. It also describes the most popular long-range synchrony measures found in the literature.
- **Chapter 3** presents a detailed description of the proposed methodology and synchrony measures.
- In **Chapter 4** we discuss different aspects of the synchrony measures presented in Chapter 2 and the ones proposed in Chapter 3, from a comparative point of view.
- **Chapter 5** focuses on a mathematical model with which one can simulate (and explain to some extent) different phenomena observed during the analysis of various real experiments.
- **Chapter 6** summarizes the main contributions of this work, and also presents the results of the neurophysiological analysis of real experiments. Ideas for future work are also presented here.
- **Appendix A** presents the resulting graphs and results for additional experiments.
- **Appendix B** describes the publications and presentations originated from this thesis.
- **Appendix C** contains the user manual for our EEG analysis software.

1.9 Experimental data

During the course of our work, we have tested the procedures using data from various EEG experiments. Here we describe each of them.

1.9.1 Figures and Words experiments

This experiments are designed for the study of categorization tasks [Harmony et al., 2001]. For the Figures experiment, white-line figures on a black background were presented to each subject. The subjects were instructed to press a button if the figure corresponded to an animal whose name started with a consonant, and another button if the figure did not correspond to an animal and the name of the figure started with a consonant. If the name started with a vowel, the subject was instructed not to respond.

The Words experiment follows a similar paradigm, with the exception that words instead of figures are presented on the screen. The subjects were instructed to press one button if the word corresponded to an animal and starts with a consonant, and another button if the word did not correspond to an animal and started with a consonant. Otherwise, the subject was instructed not to respond.

In both experiments, the subjects were 18 normal children (8 to 10 years old, 9 females), all right handed with normal neurological examination. EEG was recorded with reference to linked ears from Fp1, Fp2, F3, F4, C3, C4, P3, P4, O1, O2, F7, F8, T3, T4, T5, T6, Fz, Cz, Pz, and Oz of the 10/20 system. EOG was recorded from a supraorbital electrode and from an electrode on the external canthus of the right eye. The amplifier bandwidth was set between 0.5 and 30 Hz. EEG was sampled every 5ms using a MEDICID 3E system and stored on a hard disk for further analysis. Sampling was done every 5 ms during a time segment from 1280 ms before the stimulus to 1500 ms after its onset. Each trial was visually edited and only those corresponding to correct responses and with no artifacts were analyzed. Subjects were seated in a comfortable chair in front of the videomonitor. Stimuli were delivered by a MINDTRACER system synchronized to the MEDICID 3E acquisition system.

1.9.2 3-digit and 5-digit Sternberg experiments

In this experiment [Harmony et al., 2004], a visual warning stimulus (lasting 300 ms) is presented at the start of each trial. After two seconds, a set of three or five digits (memory set) is presented for 1500 ms. Two seconds later, a single digit (probe stimulus) is displayed for 300 ms. The subject must respond with one button if the probe was in the memory set, and with another button if it was not. In 50% of the trials, the number belonged to the memory set. The EEG was sampled each 5 ms with reference to linked ears from Fp1, Fp2, F3, F4, C3, C4, P3, P4, O1, O2, F7, F8, T3, T4, T5, T6, Fz, Cz, Pz, and Oz. Segments of 1280 ms were selected immediately before the memory set was presented (pre-segment) and immediately before the presentation of the probe stimulus (post-segment). Only correct responses and artifact-free segments were analyzed.

1.9.3 Letters experiment

This experiment corresponds to a Go/NoGo task designed to study the inhibition of the motor response. A series of uppercase letters are shown, one at a time, on the screen. The interval between the presentation of one letter and the next one is two seconds. The subject is instructed to respond with a button only if a 'X' that has been preceded by an 'O' appears. This is the Go condition. Any letter different than 'X' which has been preceded by an 'O' accounts for the NoGo condition, as it may originate the inhibition of the motor response. EEG was recorded each 5 ms from Fp1, Fp2, F3, F4, C3, C4, P3, P4, O1, O2, F7, F8, T3, T4, T5, T6, Fz, Cz, and Pz. Each segment was selected from 1 s immediately before the presentation of each letter (pre-segment) to 1560 ms immediately after (post-segment). The analysis of this experiment using the techniques described below has been submitted for publication [Harmony et al., 2006].

Chapter 2

Methods and measures for the study of EEG synchrony

2.1 Introduction

It is thought that during the execution of a relatively complex task, specialized (and possibly distant) areas of the brain interact together by means of strong reciprocal connections, forming what is called a *neural assembly* [David et al., 2003a]. The mechanisms involved in this large-scale integration are still largely unknown; however, one of the most plausible candidates is the formation of dynamical links that are reflected as some form of synchronization over different frequency bands [Varela et al., 2001] (in particular, Varela favors phase-synchronization as the most plausible mechanism).

According to Varela et al., synchronization of neural assemblies is a process that spans multiple spatial and temporal scales. In this sense, the most adequate level of synchrony analysis would be at single neuron level: in the timescale of cognitive events (typically hundreds of ms), a single neuron may fire only a few spikes, which may not be enough to activate a target neuron. However, if these spikes coincide in time with those fired by additional neurons, the target neuron may be activated. Unfortunately, it is impossible to study neural interactions at this level with the present EEG scalp sensors. On a coarser level, it is possible to record the activity of a local neural group (within a few millimeters) using intracranial EEG sensors: the recorded Local Field Potentials (LFP's) blur the contributions of the participating neurons, but at the same time highlight their common actions. In this case, a time-frequency power analysis may yield information about integration within the local network.

Finally, there are also studies of long-range synchronization, where the integrated networks are separated by $\sim$ 1 cm or more. This involves reciprocal, poly-synaptic communication paths across the networks, which result in transmission delays of at least 8 ms. It is known that the brain areas are massively

and reciprocally connected, and that such a connectivity engenders the emergence of correlations in the brain activity of the different areas [David et al., 2003a]. Numerous methods have been used to study these correlations. Most of these follow a particular scheme: (1) (optionally) pre-process the EEG signals to reduce reference and volume conduction effects, (2) perform a time-frequency decomposition of the signals, (3) estimate a synchronization measure between pairs of lead signals of interest, and (4) perform a statistical test to determine the significance of the measured synchrony with respect to the baseline. Certain aspects of (1) have already been discussed in Sections 1.5 and 1.6. We will also propose a projection method to reduce volume conduction in Section 3.7. The rest of this chapter will deal with steps (2) through (4).

2.2 Time-frequency decomposition

Electroencephalographic recordings have a cyclic nature; therefore, it is very common to analyze them in the frequency domain rather than in the time domain. On the other hand, EEG is also very dynamic, and, in many cases such as in event-related analysis, the interest is precisely in detecting changes in the spectral properties of the signals, and in determining if those changes may be related to the task which is being studied. In these cases, it becomes necessary to perform a time-frequency (TF) decomposition of the signals from which one can extract instantaneous amplitude and phase information for each frequency band (the latter being particularly important for long-range synchrony analysis). In this section we present the most common tools used to achieve this.

2.2.1 Local windowed Fourier transform

The discrete version of the Fourier theorem states that a periodic discrete function $f(t)$ can be expressed as a sum of pure complex tones as follows:

$$f(t) = \frac{1}{N} \sum_{k=0}^{N-1} F(k) \exp\left[\frac{2\pi i}{N} kt\right], \qquad n = 0, \ldots, N-1, \tag{2.1}$$

where N is the period of $f(t)$ and $F(k)$ are the *Fourier coefficients* given by

$$F(k) = \sum_{t=0}^{N-1} f(t) \exp\left[-\frac{2\pi i}{N} kt\right]. \tag{2.2}$$

F is called the *Fourier transform* (FT) of f, and it provides us with a description of the frequency content of the original signal. For example, the magnitude of $F(k)$ indicates how much of the frequency $2\pi k/N$ is present in f. In terms of EEG signals, this represents how strong is each rhythm in a given recording. One problem with the FT, however, is that it assumes the signals to be stationary (i.e. their frequency content does not change over time),

which may not be true for some signals such as EEG. The solution consists on estimating the Fourier transform "locally" within a narrow time window around t_0, and then just slide t_0 to obtain the Fourier coefficients $F(k, t_0)$ at each time. This is represented as

$$F(k, t_0) = \sum_{t=0}^{N-1} f(t)w(t - t0) \exp\left[-\frac{2\pi i}{N} kt\right], \tag{2.3}$$

where $w(t)$ is a real finite *window function* symmetric around zero. Generally, $w(t)$ decays smoothly as $|t|$ increases, so that only values relatively near t_0 have a significant weight when estimating $F(k, t_0)$. The width Δt of the window has a direct effect in the time and frequency resolution of the local Fourier transform. Narrow windows will result in a higher time resolution, since the Fourier coefficients for t_0 will be less contaminated by values distant from t_0. However, the Heisenberg Uncertainty principle states that it is not possible to determine, with arbitrary precision, both the time and frequency localization of the components of a signal. Mathematically, the product of Δt and the frequency width $\Delta\omega$ of the window function (that is, the width of the Fourier transform W of w) has a lower bound. More specifically,

$$\Delta t \Delta\omega \geq \frac{1}{4\pi}, \tag{2.4}$$

with Δt in seconds and $\Delta\omega$ in Hz. The lower bound in Equation 2.4 is reached when the window function is Gaussian, thereby providing the best compromise between time and frequency localization.

The local windowed Fourier transform is widely used in EEG research (for example, [Gross et al., 2001] and [Harmony et al., 2004]), however, it has the disadvantage of focusing only on a discrete set of frequencies given by $2\pi kS/M, k = 0, \ldots, M-1$, where M is the length of the Fourier transform, and S is the sampling rate (in Hz) of the analyzed signal. Even though the basic EEG rhythms lie on relatively wide bands, it is sometimes desirable to perform a time-frequency decomposition in narrow bands centered at arbitrary frequencies. This is especially important in phase-synchrony analysis, since the instantaneous phase of a signal, which can be obtained from the argument of the Fourier coefficients, only has a physical meaning for narrow-band signals. To overcome this, one can use a relatively large M (length) for the Fourier transform, or resort to quadrature or wavelet filters.

2.2.2 Gabor filters

Gabor filters are quadrature band-pass filters which consist of a Gaussian kernel shifted in frequency to the tuning frequency ω. The Gabor kernels are given by:

$$G_{\omega,\sigma_t}(t) = \frac{1}{Z} \exp\left[-\frac{t^2}{2\sigma_t^2}\right] \exp\left[i\omega t\right], \tag{2.5}$$

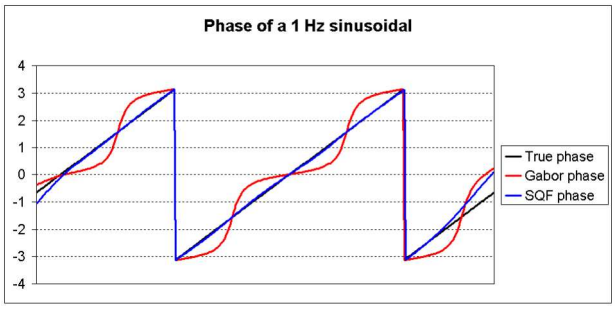

Figure 2.1: True phase and estimated phase (using Gabor and sinusoidal quadrature filters) for a 1 Hz sinusoidal signal.

where σ_t is the filter width (in time units), and Z is a normalizing constant. The frequency response of a Gabor filter is a Gaussian centered at ω with a frequency width σ_ω given by:

$$\sigma_\omega = \frac{1}{4\pi\sigma_t};$$

in other words, Gaussian filters also reach the lower bound in the Heisenberg Uncertainty principle (Equation 2.4); because of this, they are also a common choice for EEG time-frequency decomposition (see [Marroquin et al., 2004; Schack et al., 2005]).

The complex filtered signal $F_\omega(t)$ is simply obtained as the convolution of the original signal f and the filter kernel. The instantaneous amplitude and phase of the filter output can then be calculated from the magnitude and argument of $F_\omega(t)$.

A quadrature filter has the property of its frequency response being zero for all negative frequencies. For a Gabor filter, however, when the tuning frequency is relatively low, there is a chance of the filter having a strong response to negative frequencies. In this case, the quadrature property of the filter is destroyed, and the instantaneous magnitude and argument are no longer well-defined, which may lead to distorted phase estimates (see Figure 2.1).

This distortion can be easily characterized for sinusoidal signals. Given an input signal $x(t) = 2\cos 2\pi ft$, the output $y(t)$ of a unit-gain bandpass filter tuned at f Hz (obtained by convolving x with the filter kernel) will have the form

$$y(t) = e^{i2\pi ft} + \alpha e^{-i2\pi ft}, \tag{2.6}$$

where $\alpha \in [0, 1)$ is the attenuation factor of the component with negative frequency. The argument $\Phi_y(t)$ of y is given by

$$\tan \Phi_y(t) = \epsilon \tan 2\pi ft, \qquad \text{with } \epsilon = \frac{1-\alpha}{1+\alpha}. \tag{2.7}$$

On the other hand, the (unwrapped) argument of the original signal is $\Phi_x(t) = 2\pi ft$; thus one can compute the argument distortion d as

$$\begin{aligned} d(t) &= \text{wrap}(2\pi ft) - \Phi_y(t) \\ &= \text{wrap}(2\pi ft) - \arctan\left(\epsilon \tan 2\pi ft\right), \end{aligned}$$

from which one can see that $d(t) = 0$ when $t = k/4f$, $k = 0, 1, \ldots$; between these points, d will change its sign, which means it will oscillate at twice the tuning frequency f.

If $x(t)$ has a more complex structure (i.e., if it is a sum of sinusoids with different frequencies, amplitudes, and phases), the distortion cannot be characterized in an easy way, but it will also have a significant effect on the measured phase.

2.2.3 Sinusoidal quadrature filters

One alternative to Gabor filters are the sinusoidal quadrature filters (SQF's - [Guerrero et al., 2005]) whose asymmetrical frequency response has a finite support which never intersects the negative frequencies. The frequency response of an SQF is given by:

$$G_{\omega_k,h}(\omega) = \begin{cases} \frac{1}{2}\left[1 + \sin\left(\frac{(h_k + 2(\omega - \omega_k))\pi}{2h_k}\right)\right] & \text{if } \omega \in [\omega_k - h_k, \omega_k], \\ \frac{1}{2}\left[1 + \sin\left(\frac{(h + 2(\omega - \omega_k))\pi}{2h}\right)\right] & \text{if } \omega \in [\omega_k, \omega_k + h_k], \\ 0 & \text{otherwise,} \end{cases} \tag{2.8}$$

where ω_k is the tuning frequency, h is the bandwidth, and $h_k = \min\{h, \omega_k\}$. Figure 2.2 shows the frequency response curves for Gabor filters and SQF's tuned at 1 Hz and 10 Hz.

The filter kernels for SQF's can be obtained as the inverse Fourier transform (Equation 2.1) of their frequency response function. The filtered signal is then obtained by convolution with these kernels. As one can see in Figure 2.1, SQF's do not distort the phase even for low tuning frequencies. Later, we will compare the results of the actual synchrony analysis procedure using both Gabor filters and SQF's to determine how seriously the phase distortion (introduced by Gabor filters) affects our results.

2.2.4 Wavelet analysis

Wavelet analysis is equivalent to using a bank of band-pass filters, with the exception that the kernel width of the wavelet-based filters depends inversely on the tuning frequency. Lachaux et al. [1999, 2000b] use the Gabor wavelet extensively in their work. The bandwidth of the Gabor wavelets is proportional to the tuning frequency (for instance, according to [David et al., 2003a] they

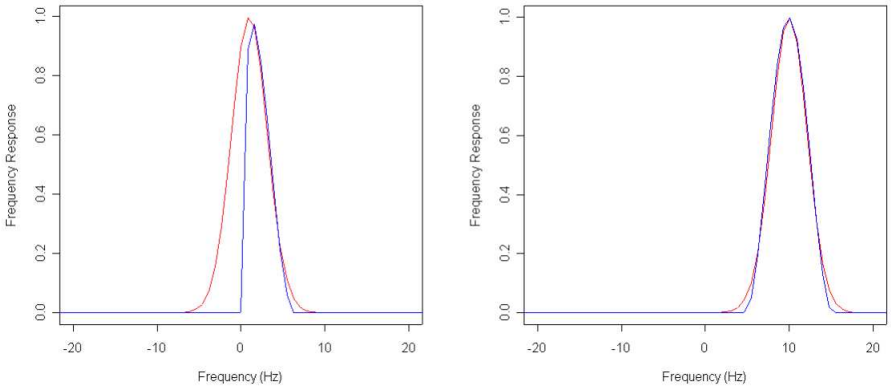

Figure 2.2: Frequency response of Gabor filters (red curve) and sinusoidal quadrature filters (blue curve) tuned at 1 Hz (left graph) and 10 Hz (right graph). At relatively high tuning frequencies, both filters have a very similar response; however, at low tuning frequencies, Gabor filters show a strong response at negative frequencies, which may result in distorted phase estimates.

chose the wavelet parameters such that at a tuning frequency of 40 Hz, the bandwidth of the filter covers from 20 Hz to 60 Hz). However, since the phase obtained from the output of a filter only has a physical meaning if the signal has narrow bandwidth, it becomes necessary to pre-filter the EEG signals before using wavelets for TF decomposition.

2.3 Long-range synchrony measures

Although it is common that several areas of the brain interact together at a given time in the course of a cognitive task, synchronization measures are usually estimated only between pairs of leads. This simplifies the problem enormously, and also makes the comparison of different measures relatively simple.

In a very general sense, two simultaneous signals are synchronized in a given time window when they show a certain correlation. This correlation can be defined in different ways, depending on the physiological motivation, for example:

1. If both signals show a spike within the time window (e.g. synchrony at neuron level).
2. If their difference in phase is relatively constant (for narrow band signals).
3. If the signals are statistically inter-dependent (e.g. if their statistical correlation is high)

Thus, a synchronization measure is one that estimates the degree of correlation (according to some criterion) between the two signals. Here we describe the most common measures found in the literature.

2.3.1 Coherence

According to [Gardner, 1992], the coherence of two zero-mean random variables X and Y can be defined simply as the squared magnitude of their correlation coefficient ρ_{XY}, given by:

$$\rho_{XY} = \frac{E\{XY^*\}}{[E\{|X|^2\}E\{|Y|^2\}]^{1/2}}, \tag{2.9}$$

where $E\{\cdot\}$ denotes the expected value. In practice, X and Y are usually series of N sample values and the empirical degree of coherence can be estimated as follows:

$$|\rho_{XY}| = \frac{|\hat{R}_{XY}|}{\left[\hat{R}_{XX}\hat{R}_{YY}\right]^{1/2}}, \tag{2.10}$$

with

$$\hat{R}_{XY} = \frac{1}{N}\sum_{i=1}^{N} X(i)Y^*(i). \tag{2.11}$$

The coherence coefficient measures the linearity of the relation between X and Y, regardless of their difference in magnitude. It is normalized between 0 and 1, where $|\rho| = 1$ means that Y can be obtained as a linear transformation of X.

If X and Y represent two time series (such as two EEG signals), it is possible to spectrally decompose the coherence by passing both X and Y through a tunable narrow-band bandpass filter, and then measuring the coherence of the filtered signals.

Coherence is widely used as a measure of EEG synchrony (see below), however, it is originally defined for stationary time-series. Since EEG signals are very dynamic, it is common to estimate the coherence $C_{XY}(t)$ across a short time window centered around a time of interest t as follows:

$$C_{XY}(t) = \frac{|\hat{R}_{XY}(t)|}{\left[\hat{R}_{XX}(t)\hat{R}_{YY}(t)\right]^{1/2}}, \tag{2.12}$$

with

$$\hat{R}_{XY}(t) = \frac{1}{2w+1}\sum_{i=t-w}^{t+w} X(i)Y^*(i). \tag{2.13}$$

The size of the time window $(2w+1)$ is typically a few hundreds of milliseconds, which corresponds to the duration of most cognitive events. By inspecting

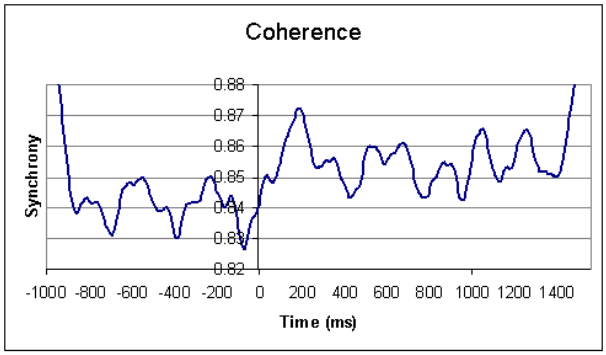

Figure 2.3: Average coherence (taken across trials) between electrodes T5 and O2 of the Figures experiment at 8 Hz. Note the border effects caused by the large window size (which is required for reliable coherence measures); these effects must be taken into account when performing a statistical significance analysis in order to avoid biasing. Disregarding these border effects (around 150 ms on each side), one can clearly see an increase on the average level of synchronization between the electrodes under study.

or analyzing $C_{XY}(t)$, it is possible to find episodes of high coherence in an experiment. As an example, Figure 2.3 shows the average 8 Hz coherence (taken across all trials) between electrodes T5 and O2 of the Figures experiment, using a window size of 105 ms ($w = 10$ samples).

In [Bressler et al., 1993], coherence is used to study the brain integration in monkeys during a visual pattern discrimination task within a GO/NO-GO scheme: depending on the stimulus, the subjects must respond (GO condition) or withhold the response (NO-GO condition). The EEG data consisted of intracranial local field potential (LFP) recordings from 15 cortical sites. In the GO condition, Bressler et al. found episodes of significantly high coherence over a broad frequency range (from 12.5 Hz to 87.5 Hz) between distant sites. According to Bressler, "elevated coherence, rather than simply appearing because of common activation of multiple cortical areas by an imposed stimulus, manifested spatially and temporally complex patterns in the period after stimulus presentation, when the monkeys had to discriminate successfully between two visual forms and then perform correctly."

Friston et al. [1997] suggests that dynamical correlations between two narrow band EEG signals may be related to changes in the phase-locking between the signals: using experimental magnetoencephalographic (MEG) data (only a component in the gamma band), they found that in episodes with high cross-correlation between two sites, the phase difference between both signals had a larger tendency towards zero, whereas in the low-correlation episodes, the histogram of the phase differences was much flatter. This is supported by a

theoretical analysis showing the relationship of the coherence measure and the distribution of the phase differences.

Gross et al. [2001] describe a method to study the neural interactions from the analysis of coherent sources. This method estimates the coherence between pairs of cortical sources (an inverse-problem approach is used to estimate the activity at these sources). Gross et al. studied the cortical interactions in a patient with Parkinson's disease and found significant coherence values in the alpha band (particularly 9 to 12 Hz) between sources separated by more than 6 cm.

Another method based on the coherence of cortical sources is proposed by Hoechstetter et al. [2004]. We have already described (in Section 1.6) the inverse approach used by Hoechstetter to obtain the source signals. These signals are then passed through a bank of bandpass filters (from 4 to 50 Hz in 2 Hz steps) and coherence was estimated between pairs of sources. As an example, the method was used to analyze a task in which four different letter strings (HHHHH, SSHSS, SSSSS, and HHSHH) were presented to the subject, who was told to indicate the central letter by pressing a key with the left or right hand, respectively. Large coherence was found in the low frequency range between the left and right visual cortex regions, and also in the gamma band between the midline-visual cortex, and the left and right motor cortex areas. A widely distributed decrease in coherence was also found around the 10 Hz range.

2.3.2 Phase Locking Statistic

According to Varela et al. [2001], the most plausible mechanism of neural integration is the formation of dynamical links, which result in an increase of phase-locking between signals. In general, two (narrow band) signals with instantaneous phases $\phi_1(t)$ and $\phi_2(t)$, respectively, are phase-locked in a time window T if

$$n\phi_1(t) - m\phi_2(t) = \text{constant}, \qquad t \in T, \tag{2.14}$$

where n and m are integers indicating the ratios of possible frequency locking (called $m : n$ synchrony). For simplicity, most studies concentrate on signals within the same frequency band (i.e. $m = n = 1$, or $1 : 1$ synchrony).

Lachaux et al. [1999] introduced a method to estimate the degree of phase-locking and detect significant synchrony values between two recording sites, in a specific frequency range. The phase-locking statistic (PLS) is defined as

$$PLS_{e_1,e_2}(t) = \frac{1}{N_r}\left|\sum_{n=1}^{N_r} \exp\left[i\left(\phi_{n,e_1}(t) - \phi_{n,e_2}(t)\right)\right]\right|, \tag{2.15}$$

where e_1 and e_2 represent the two recording sites, N_r is the number of trials, and $\phi_{n,e}$ is the instantaneous phase of the bandpass filtered signal at site e for trial n. This analysis is performed for all frequency bands of interest.

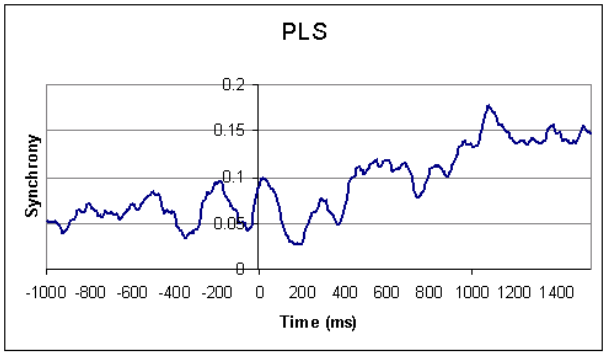

Figure 2.4: PLS estimated between electrodes T5 and O2 of the Figures experiment at 8 Hz, where an increase of synchrony can be observed in the post-stimulus segment.

The PLS equals one minus the inter-trial variance of the phase differences between the two signals (see [Fisher, 1995] for a definition of circular variance). If the phase difference varies little across trials, the PLS is close to 1; otherwise, it is close to zero. Figure 2.4 shows the estimated PLS at 8 Hz for electrodes T5 and O2 from the Figures experiment. As in the previous case (with coherence), an increment of synchronization can also be observed after the stimulus onset.

In order to determine the significance of the phase-lock values, a randomized (surrogate) set of data is constructed by shuffling trials for one of the electrodes under study. This and other methods of significance estimation will be discussed in Section 2.4.

The PLS was tested with simulated data and with real human intracortical recordings (from an epileptic patient performing a visual discrimination task - see [Lachaux et al., 1999] for details). The analysis of real data focused only on one frequency band around 45 Hz, and showed significant long-range synchronizations that emerged and disappeared over time. Short-range couplings were also found; however, in this case, the PLS decreased steadily with interelectrode separation, which suggests that those couplings were spuriously introduced by volume conductor effects.

Unlike coherence, the PLS does not assume stationarity of the signals (which can rarely be validated), and does not reduce the time resolution of the analysis. Furthermore, coherence also increases with amplitude correlation, and the relative importance of amplitude and phase correlation in the coherence measure is not clear.

PLS was used by Rodriguez et al. [1999] to study gamma synchronization during an ambiguous visual discrimination task: the subjects were shown Mooney faces, which are black and white shapes that resemble a face when

presented in upright orientation (perception condition), but are usually seen as meaningless shapes when presented upside-down (no-perception condition). Phase synchronization (within the gamma range) was studied using the PLS method, which showed differences between the perception and no-perception conditions: during perception, significant couplings between distant sites were observed that did not show in no-perception. Similarly, a global desynchronization pattern following the coupling stage was also observed only in the perception condition. Interestingly, as previously found in [Friston et al., 1997], synchronized electrodes showed a phase-lag distribution centered at zero, regardless of the interelectrode distance.

2.3.3 Single-Trial Phase Locking Statistic

One limitation of the phase-locking statistic is that it requires several trials to estimate the degree of synchrony between two signals. In some cases, it is desirable to perform a statistic with as few trials as possible, or even with single trials (for example, in experiments where a specific induced response is not necessarily time-locked to the stimulus). To overcome this limitation, the smoothed or single-trial phase-lock statistic (STPLS) was introduced [Lachaux et al., 2000b], which is given by:

$$STPLS_{e_1,e_2}(t) = \frac{1}{2w+1} \left| \sum_{t'=t-w}^{t+w} \exp\left[i\left(\phi_{e_1}(t') - \phi_{e_2}(t')\right)\right] \right|. \tag{2.16}$$

The STPLS equals one minus the variance of the phase differences across a time window centered at time t with length $2w+1$. A STPLS of 1 means that both signals are perfectly in phase across the time window. This measure appears to be more in agreement with the synchrony criterion given by Equation 2.14, at the expense of reducing the time resolution of the analysis. Figure 2.5 shows the STPLS values for electrodes T5 and O2 of the Figures experiment, at 8 Hz. The window size is 105 ms ($w = 10$). Note that the results are very similar to those obtained with coherence.

This measure has also been used by Mizuhara et al. [2005] to study neural integration during an arithmetic task. The phase-lock measure was estimated between pairs of current source density signals (see Section 1.6) and then correlated with fMRI measurements to determine which networks were involved in synchronous processes. According to the results, the fMRI showed significant responses in the parietal and temporal cortices, which were associated with phase-synchronization observed in the beta range (around 14 Hz).

Schack et al. [2005] have also used this measure to test for $1:1$ synchrony, but also provide an extended measure to study $m:n$ synchrony:

$$\Gamma_{e_1,e_2}(t) = \frac{1}{2w+1} \left| \sum_{t'=t-w}^{t+w} \exp\left[i\left(m\phi_{\omega_n,e_1}(t') - n\phi_{\omega_m,e_2}(t')\right)\right] \right|, \tag{2.17}$$

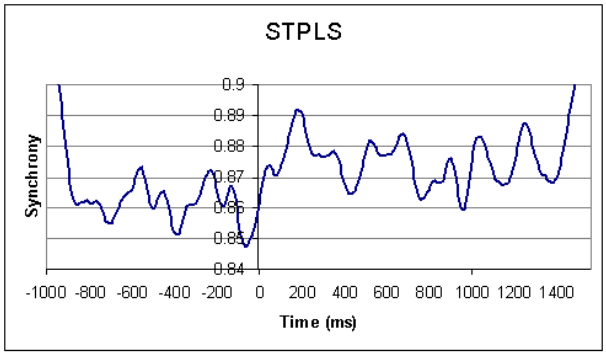

Figure 2.5: Average STPLS (estimated across all trials) between electrodes T5 and O2 of the Figures experiment at 8 Hz, where an increase of average synchrony can be observed in the post-stimulus segment (disregarding the border effects). These results are very similar to those obtained with coherence.

where $\phi_{\omega_n,e}$ is the instantaneous phase of the signal at site e, filtered around frequency ω_n. There must be a harmonic relation between the frequencies ω_n and ω_m.

This measure was used to study a working memory task where a set of 1 to 4 digits were presented to each subject, followed by an 'x' symbol indicating the beginning of the retention interval (see [Schack et al., 2005]). After the retention interval, another digit (probe) was presented and the subjects were instructed to respond with a keypress whether the probe was or was not in the set. Significant $1:1$ synchrony was found in the theta (6 Hz) and upper alpha (12 Hz) bands between distant sites (e.g. right-frontal vs. left-temporal). Inter-frequency ($m:n$) synchronization was also found between the sites F7 and O2 of the 10/20 system, corresponding to theta/upper-alpha couplings ($1:2$ ratio).

2.3.4 Generalized Synchronization

According to David et al. [2004], two dynamical systems X and Y show generalized synchronization (GS) when "the state of the response system Y is a function of the state of the driving system $X : Y = F(X)$". If F is continuous, then close points on the attractor of X should correspond to close points on the attractor of Y.

The method described in [Quian-Quiroga et al., 2002] and [David et al., 2004] to estimate the GS relies upon vectors $\vec{X}_n = [x_n, x_{n+\tau}, \ldots, x_{n+(m-1)\tau}]$ and $\vec{Y}_n = [y_n, y_{n+\tau}, \ldots, y_{n+(m-1)\tau}]$, which are embeddings of the signal x in an m-dimensional space with a delay time τ. If p_{ni} and q_{ni}, $i = 1, \ldots, k$, denote the indices of the k nearest neighbors of $\vec{X}_n$ and $\vec{Y}_n$, respectively, then one can define a measure of closeness $S_n^k(X|Y)$ between the true neighbors $\{\vec{X}_{p_{ni}}\}$ of

$\vec{X}_n$ and its mutual neighbors $\{\vec{X}_{q_{ni}}\}$. Quian-Quiroga proposes the following measure:

$$S_n^k(X|Y) = \frac{\left\langle |\vec{X}_n - \vec{X}_{p_{ni}}|^2 \right\rangle_i}{\left\langle |\vec{X}_n - \vec{X}_{q_{ni}}|^2 \right\rangle_i}, \tag{2.18}$$

where $\langle\cdot\rangle_i$ indicates the average value across $i = 1, \ldots, k$.

Equation 2.18 measures the ratio of the mean square distance between $\vec{X}_n$ and its k nearest neighbors, and the mean square distance between $\vec{X}_n$ and its mutual neighbors (with respect to $\vec{Y}_n$). By construction it is bounded between 0 and 1, where 1 means that the cloud of the k nearest neighbors of $\vec{Y}_n$ maps exactly to the cloud of k nearest neighbors of $\vec{X}_n$. Finally, synchronization measure is the average of $S_n^k(X|Y)$ over a time window $t - T \leq n \leq t + T$.

According to Quian-Quiroga, GS should be very sensitive to weak correlations (which may or may not be useful for specific applications) - this is confirmed by experiments performed by David et al. On the other hand, GS is also computationally demanding and greatly reduces the time resolution of the synchrony analysis, which may be a problem when studying the gamma band, where the synchronization periods may be relatively short. Another disadvantage of GS is that it relies on many parameters: τ, m, k, and T, which control the tradeoff between the robustness, time-resolution, and computational load of the method. Unfortunately, neither David or Quian-Quiroga provide a comparison of the behavior of GS for different parameter values.

2.3.5 Mutual Information

Mutual information (MI) is a statistical measure which estimates, for two random variables X and Y, the amount of information in X given that Y is known, and viceversa. MI is based on the entropy H of a discrete random variable $X \in \{x_1, \ldots, x_M\}$, which is given by

$$H(X) = -\sum_{i=1}^{M} p_i \ln p_i, \tag{2.19}$$

where $p_i = P(X = x_i)$. If X is continuous with a finite support, one can simply partition the support in M bins and estimate the p_i's by counting. For a bi-variate distribution, the joint entropy is defined as

$$H(X, Y) = -\sum_{i,j} p_{ij} \ln p_{ij}, \tag{2.20}$$

where $p_{ij} = P(X = X_i, Y = Y_i)$. If X and Y are independent, we have that $H(X, Y) = H(X) + H(Y)$.

The mutual information between X and Y is defined as

$$MI(X, Y) = H(X) + H(Y) - H(X, Y). \tag{2.21}$$

If X and Y are independent, then $MI(X,Y) = 0$; otherwise it will take positive values up to $H(X)$. MI basically measures the similarity between the histograms of X and Y (estimated, in our case, across a time window), thus it does not take into account any possible time lag between both signals. This makes it inadequate as a phase-locking measure. It is possible, however, to apply time-embedding techniques (for example, taking as sample data the vectors $\vec{X}_n$ used in GS) to obtain a lag-sensitive MI measure [Quian-Quiroga et al., 2002].

MI presents the same problems that GS: it is computationally expensive (compared to phase-locking measures such as coherence or PLS), and if time-embedding techniques are used, it will be at the expense of high time resolution. For these reasons, MI and GS are better suited for the analysis of stationary couplings and/or low frequency synchrony.

2.4 Statistical significance analysis

Whether one is studying evoked potentials, power changes, or synchrony between pairs of electrodes, it is likely that one will obtain a set of time series $\{X_k(t)\}$, each of which represents the computed measure for a specific combination of trial number, frequency band, electrode, or electrode pair (represented by k). For example, in the case of evoked potentials, k may represent an electrode index, and X_k would be the average signal at that electrode, whereas in the case of synchrony, k may represent a 4-tuple of the form $< j, \omega, e_1, e_2 >$ for trial j, frequency ω, and electrode pair $< e_1, e_2 >$.

Once a specific measure $X(t)$ is computed, one would like to determine, for each t, if $X(t)$ represents a significant deviation from what would be considered as a null condition (for example, if one is studying event-related activity, one can consider the pre-stimulus segment as the null condition). To do this, one can estimate the distribution of X during the null condition, and then perform a statistical test to determine if $X(t)$, for any t, comes from the null distribution.

2.4.1 Choosing the null population

The null population consists of those values of $X(t)$ which are observed during the null condition. For example, if one wants to study task-related activity, one can assume that everything that happens before the stimulus onset is part of the null condition, and significant changes in X with respect of this condition may be related with the task. In this case, one choice for the null population is simply those values of X in the pre-stimulus (i.e., $X(1), \ldots, X(T_s)$ - although in practice, possible border effects due to filtering or averaging should be taken into account). For example, this is the method used by [Marroquin et al., 2004] to estimate the significance of power changes (i.e., induced power) during a cognitive task. A similar technique was used by [Mizuhara et al., 2005].

It is also common to determine if the X values are significantly different from what can be expected by chance. In this case, one can build the null population

by taking the original data and manipulating it in order to obtain a new set of surrogate data which does not have the property of interest (i.e., the property which is being measured). In particular, when one is measuring synchrony between two signals, one would like to construct the null population so that the two surrogate signals are certainly unsynchronized. This can be achieved, for example, by shuffling the samples in each signal, which would destroy any temporal structure the signals may have. One can then compare the measured synchrony against the distribution of the surrogate data, and decide if there is significatively more synchrony than what can be expected by chance. Lachaux et al. [1999; 2000] use surrogate data to estimate the significance of their PLS and STPLS measures: the surrogate synchrony values, for two electrode sites e_1 and e_2, is obtained by shuffling the trials for e_2.

Once the null population is obtained, one can estimate its distribution in various ways, or use statistical tools, such as ANOVA, to compare the X values against the null condition. We will focus on estimating the null distribution and estimating the p-values for each $X(t)$.

2.4.2 Significance estimation: normal distribution

One of the most common methods used to determine the significance of the synchrony changes consists in assuming that the null distribution is normal with mean $\bar{X}_{\text{null}}$ and variance σ^2_{null}, and computing the Z variables given by:

$$Z(t) = \frac{X(t) - \bar{X}_{\text{null}}}{\sigma_{\text{null}}}. \tag{2.22}$$

In practice, if the size n of the null population is sufficiently large (e.g., $n > 30$), one can replace $\bar{X}_{\text{null}}$ and σ^2_{null} with the sample average and sample variance of the null population, respectively.

Under the null condition, Z is normally distributed with mean 0 and variance 1. Therefore, given the significance level α, the quantile $z_{(1-\alpha)}$ represents the threshold that the Z values must cross to be considered significantly different. For example, if $Z(t) > z_{(1-\alpha)}$, then $Z(t)$ is significatively greater than in the null condition. Common values for α are 0.05 and 0.01, corresponding to thresholds $z_{0.05} = 1.64$, and $z_{0.01} = 2.33$.

It is also possible to test the average $\bar{X}(t)$ of X across a time window against the null condition. For example, if the time window goes from $t - w$ to $t + w$, $\bar{X}(t)$ would be given by

$$\bar{X}(t) = \frac{1}{2w+1} \sum_{t'=t-w}^{t+w} X(t), \tag{2.23}$$

which is normally distributed with mean $\bar{X}_{\text{null}}$ and variance $\sigma^2_{\text{null}}/(2w+1)$. Therefore, the Z variables would be given, in this case, by

$$Z(t) = \frac{\bar{X}(t) - \bar{X}_{\text{null}}}{\sigma_{\text{null}}/\sqrt{2w+1}}. \tag{2.24}$$

2.4.3 Significance estimation: kernel density estimation

It may not be correct to assume normality for the X-values, especially if the number of trials is relatively small. In this case, the null distribution p_X can be estimated from the null population $\{x_i\}$ as the sum of superimposed kernel functions k_h centered at each x_i. In other words,

$$p_X(x) = \frac{1}{Z}\sum_{i=1}^{n} k_h(x - x_i),$$

where n is the sample size, and Z is a normalization constant chosen so that p_X integrates to 1. The parameter h specifies the width of the kernel and it determines the smoothness of p_X. Adequate choice of h depends on the sample data; however, for automated applications, a common rule of thumb for a Gaussian kernel (which we use) is provided by [Silverman, 1986]:

$$h_{opt} = 1.06\sigma n^{-1/5},$$

where σ is the standard deviation of the null population (usually estimated from the sample).

The p-value of a given x^* is then defined as $p_X(x > x^*) = 1 - p_X(x < x^*) = 1 - P_X(x^*)$ where $P_X(x)$ is the cumulative density function (cdf) corresponding to p_X, which can be defined as:

$$P_X(x^*) = \int_{-\infty}^{x^*} p(x)dx. \tag{2.25}$$

If the p-value for a given x^* is lower than the significance level α, then x^* is considered to be significative higher with respect to the null distribution. A similar test can be performed to determine if x^* is significatively lower.

In practice, one can simply obtain p_X by convolving the histogram (with equally spaced bins) of the null population with the gaussian kernel, and normalizing the resulting histogram so that it integrates to 1. One can then approximate the cdf using numerical integration methods. For example, given a histogram (h, b) where h_n represents the frequency (count) of samples which fall in the range $[b_n, b_{n+1})$ (i.e., the n-th bin), the cdf $P_X(x^*)$ can be approximated using rectangular integration (where each bin defines a rectangle whose height is h_n) as follows:

1. Compute h' as a normalized version of h; that is, $h'_n = h_n / \sum_i h_i$. h_n represents the probability of x falling into bin n.
2. Find j such that $b_j \leq x^* < b_{j+1}$.
3. Estimate the cdf as $P_X(x^*) = h'_j(x^* - b_j)/(b_{j+1} - b_j) + \sum_{i<j} h'_i$.

2.5 Visualization techniques

Synchrony values are usually estimated for various electrode pairs, at different frequencies, and for any point in the timeline. In other words, the data resulting from a synchrony analysis is 4-dimensional, which represents a visualization problem. Because of this, most works resort to averaging across time or frequency, or focus only on specific regions of the 4-dimensional synchrony space, in order to display their results.

The simplest type of display is a typical XY graph of a single-variable function. For example, one may take a fixed electrode pair and frequency, and plot the corresponding coherence time-series, or their significance values. However, this type of graph does not reveal anything about the spatial or spectral distribution of synchrony values. Other works use a matrix display of a two-variable function, in which the color assigned to each point represents the synchrony value. Typically, one fixes the electrode pair and displays a time-frequency map (an example is presented in Figure 2.6a). Many works use this type of display ([Varela et al., 2001], [Hoechstetter et al., 2004], [Schack et al., 2005]), but one may also choose a fixed time-frequency window and display the synchrony values for each electrode pair ([Lachaux et al., 1999]).

Another common type of display (shown in Figure 2.6b), for a fixed time-frequency region, consists on a head diagram where each electrode site is represented by a dot. Significant synchrony between two sites is represented by a straight line connecting the corresponding dots ([Rodriguez et al., 1999], [Varela et al., 2001], [Mizuhara et al., 2005], [Schack et al., 2005]). The problem with this display is that, when there is a considerable amount of synchronous activity, too many lines overlap and it becomes difficult to grasp the spatial distribution of the synchrony values. An alternative consists on a *multitoposcopic* display, in which at each recording site e, one shows a head diagram with the distribution of synchrony between e and every other site (Figure 2.6c).

There may be difficulties when one wants to plot a multi-toposcope for high electrode density recordings: only a certain number of toposcopes (head diagrams) can be presented within the bigger head before the graph becomes too cluttered. In Chapter 3 we will offer a few suggestions to overcome this problem.

Marroquin et al. introduced in 2004 a method for the study of EEG-based psychophysiological experiments, which analyzes power changes in EEG and presents the results in a detailed time-frequency-topography (TFT) display [Marroquin et al., 2004]. The methodology basically consists of four parts:

1. A time-frequency decomposition using Gabor filters, from which the log-power signals are obtained.

2. Estimation of a statistic $Y_{\omega,e}(t)$, which measures the mean deviation of the log-power with respect to the pre-stimulus average, for each frequency ω and electrode e.

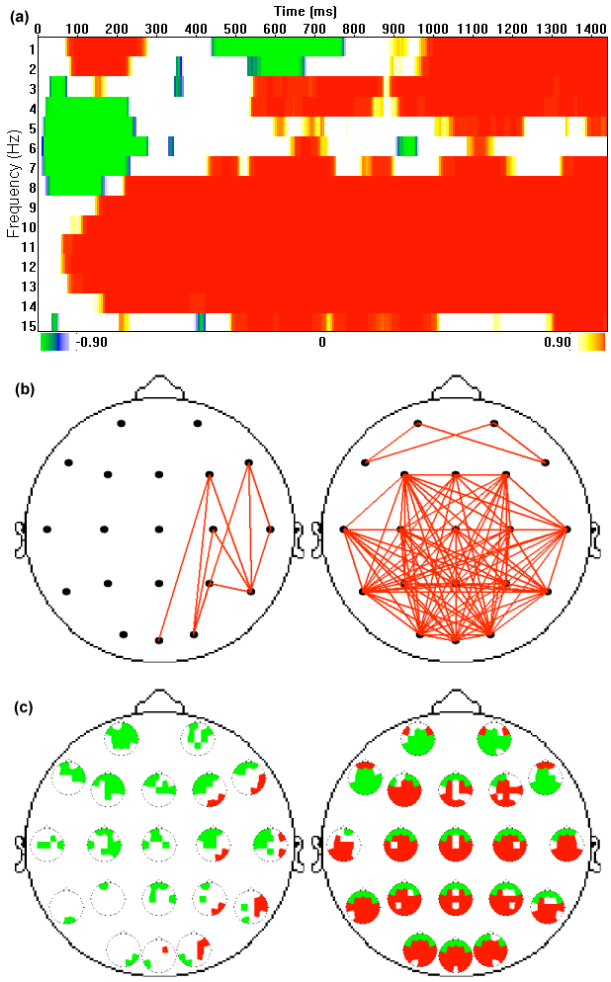

Figure 2.6: Common displays used for synchrony data: (a) Time-Frequency map of significance indexes of synchrony changes with respect to a null condition (in this case, the pre-stimulus segment) during a figure classification task ([Marroquin et al., 2004]). The data corresponds to the electrode pair Fp1-O2. Red regions correspond to significant increases in synchrony, whereas green regions indicate significant decreases. (b) Synchrony patterns observed at specific time-frequency points during the figure classification task. Only significant increases in synchrony with respect to the pre-stimulus average are shown. (c) Multitoposcopic representation of the corresponding synchrony patterns shown in (b). Both increases (red) and decreases (green) are shown.

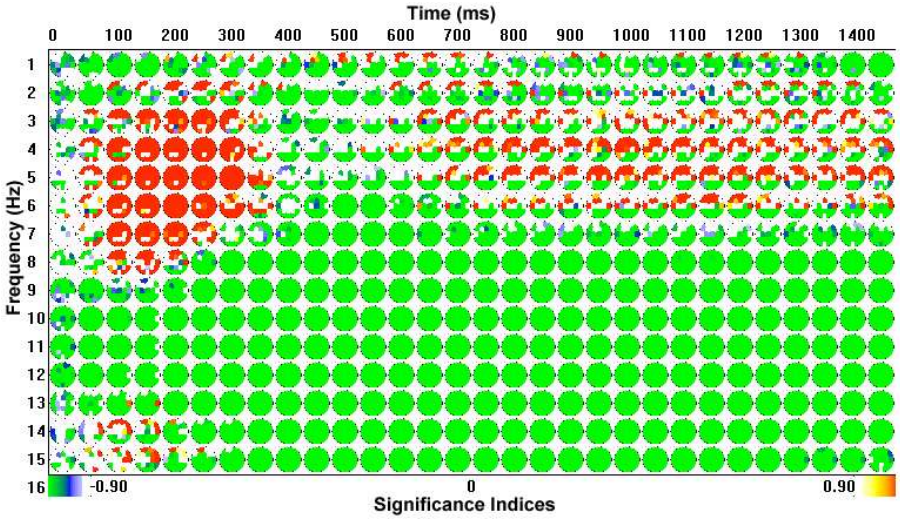

Figure 2.7: Time-frequency-topology display of significance values of power changes with respect to the pre-stimulus for a word classification task (see [Marroquin et al., 2004] for details). The significance indices range from -1 to 1, where negative values indicate a decrement of power, whereas positive values indicate power increment. Only significant values ($p < 0.1$) are plotted.

3. Estimation of a significance index $I_{\omega,e}(t)$ based on the p-value of $Y_{\omega,e}(t)$ with respect to the distribution of $Y_{\omega,e}$ in the pre-stimulus.

4. Plot the significance indices as follows: for each time t and frequency ω draw a small head diagram with the distribution of the significance values $I_{\omega,e}(t)$ for all electrodes (see Figure 2.7).

Additionally, one may perform a segmentation of the time-frequency (TF) plane in regions with homogeneous activation patterns (that is, patterns of simultaneous increases and decreases of power which are significant). For this, Marroquin et al. propose a Bayesian approach based on a Markov Random Field (MRF) model of a class field $C_{\omega,e}(t)$, which indicates if the Y-values are significantly higher (class $C = 1$), lower ($C = -1$), or equal ($C = 0$), with respect to the pre-stimulus distribution. A regularization constraint is included in the model in order to favor solutions with relative large regions with homogeneous activation patterns.

While this procedure is designed for amplitude analysis, some of the techniques it involves can also be used for synchrony analysis; particularly the display techniques, since synchrony data is highly dimensional.

Chapter 3

Phase synchrony analysis

3.1 Procedure overview

In this chapter, we describe in detail the methodology we follow for the analysis of EEG synchrony patterns. Our procedure consists of the following steps:

1. Run the EEG signals through a bank of bandpass quadrature filters and extract phase information (TF phase analysis).
2. Calculate a synchrony measure from the filtered signals.
3. Estimate the likelihoods and prior distributions for the MRF model using the synchronization values.
4. Use Bayesian estimation to find significant synchronization patterns that are persistent.
5. Display synchronization patterns as multitoposcopic graphs and time-frequency-topography (TFT) maps.

We illustrate our procedure using data from a figure classification experiment [Harmony et al., 2001] where white-line figures on a black background were presented to each subject. The subjects were instructed to press a button if the figure corresponded to an animal whose name started with a consonant, and another button if the figure did not correspond to an animal and the name of the figure started with a consonant. If the name started with a vowel, the subject was instructed not to respond. The subjects were 18 normal children (8 to 10 years old, 9 females), all right handed with normal neurological examination. EEG was recorded with reference to linked ears from Fp1, Fp2, F3, F4, C3, C4, P3, P4, O1, O2, F7, F8, T3, T4, T5, T6, Fz, Cz, Pz, and Oz of the 10/20 system. EOG was recorded from a supraorbital electrode and from an electrode on the external canthus of the right eye. The amplifier bandwidth was set between 0.5 and 30 Hz. EEG was sampled every 5ms using a MEDICID 3E system and

stored on a hard disk for further analysis. Sampling was done every 5 ms during a time segment from 1280 ms before the stimulus to 1500 ms after its onset. Each trial was visually edited and only those corresponding to correct responses and with no artifacts were analyzed. Subjects were seated in a comfortable chair in front of the videomonitor. Stimuli were delivered by a MINDTRACER system synchronized to the MEDICID 3E acquisition system.

The recorded potentials will be denoted by $V_{j,e,t} = V_{j,e}(t)$, where $j = 1, \ldots, N_r$ is the trial number, $e = 1, \ldots, N_e$ represents the electrode site, and $t = 0, \ldots, N_t - 1$ is the time index (in samples), with $t = 0$ indicating the beginning of each recording. The time of stimulus onset (pre-stimulus length) will be denoted by T_s. In particular, for the Figures experiment we have $N_r = 1290$, $N_e = 20$, $N_t = 512$, and $T_s = 200$.

The procedure has also been tested with other various experiments: a word categorization experiment ([Harmony et al., 2001]) similar to the Figures experiment (with words presented instead of figures), a working-memory task based on the Sternberg paradigm ([Harmony et al., 2004]), and a Go/NoGo experiment to study the inhibition of the motor response ([Harmony et al., 2006]). Details and results for these experiments can be found in Chapter 6.

3.2 Instantaneous phase extraction

In order to extract phase data from the EEG signals, one can perform a time-frequency decomposition using a bank of quadrature filters. We have already studied two possible choices: Gabor filters and Sinusoidal Quadrature filters (SQF's). We have chosen the Sinusoidal filters to avoid any distortion that may be introduced by Gabor filters tuned at low frequencies. Later, in Section 3.6, we will compare the results of the analysis described below, using both types of filters, and determine if there is an actual advantage of SQF's over Gabor filters.

In general, one can obtain a time-frequency decomposition of the EEG signals by convolving each $V_{j,e}$ with a bank of bandpass filters whose kernels are K_ω, where ω is the tuning frequency of the filter. In other words, the filtered signal $F_{\omega,j,e}(t)$ is given by:

$$F_{\omega,j,e} = V_{j,e} * K_\omega, \tag{3.1}$$

We have chosen a bank of filters tuned at each Hertz, from 1 Hz to $N_f = 40$ Hz, with a fixed bandwidth for all the filters, equivalent to a standard deviation $\sigma_\omega \approx 1$ Hz ($\sigma_t = 15$ samples) for the Gaussian response of Gabor kernels. This results in a bandwidth of 1.76 Hz within 3 db of attenuation. The width of Sinusoidal filters was chosen to have a similar bandwidth than Gabor filters ($h = 5\sigma_\omega$, approximately).

Finally, one can extract, from the filtered signals, the instantaneous amplitude $\hat{A}$ and argument $\hat{\Phi}$, which are given by

$$\hat{A}_{j,\omega,e}(t) = \sqrt{\Re^2(F_{j,\omega,e}(t)) + \Im^2(F_{j,\omega,e}(t))}, \tag{3.2}$$

$$\hat{\Phi}_{j,\omega,e}(t) = \text{atan2}[\Im(F_{j,\omega,e}(t)),\ \Re(F_{j,\omega,e}(t))], \tag{3.3}$$

$$\tag{3.4}$$

with $\hat{\Phi}_{j,\omega,e}(t) \in [-\pi, \pi)$.

The output of a sufficiently narrow bandpass filter can be approximated by a sinusoidal whose frequency is the tuning frequency of the filter ω, and whose argument can be expressed as $\Phi(t) = \omega t + \phi(t)$, where $\phi(t) = \Phi(t) - \omega t$ is the phase of the signal. While it is sometimes necessary to work with the phase instead of the argument of the signals, most phase-synchrony measures are based on the phase difference $\phi_1 - \phi_2$ between two signals, thus one can simply use $\Phi_1 - \Phi_2$ since the ωt terms cancel each other.

3.3 Instantaneous phase-lock measures

Here we propose two measures for in-phase synchrony (i.e., synchrony with a phase difference of zero). As a convention, we will normalize all synchrony measures between 0 and 1, so that 1 means perfect synchrony. All measures presented in Section 2.3, with the exception of Mutual Information, follow this convention.

3.3.1 Motivation

In 2003, David and Friston introduced a neural mass EEG model which simulates the activity of populations of neurons, under the assumption that the state of the population can be approximated with very few state variables [David and Friston, 2003b]. According to this model, the EEG/MEG signals from two distant cortical areas will show a phase difference of 0 (in-phase) or π (anti-phase) when there is a bidirectional coupling between the two areas. According to David and Friston [2003a], and Varela et al. [2001], the proportion of reciprocal connections in the brain is very high, suggesting that EEG synchrony may be predominantly in-phase and anti-phase synchrony. Moreover, there is experimental evidence supporting the idea that the distribution of the phase differences concentrates around zero during episodes of high synchrony (see, for example, [Friston et al., 1997; Rodriguez et al., 1999]). Therefore, it makes sense to consider as synchrony criterion the following: two signals with instantaneous phases $\phi_1(t)$ and $\phi_2(t)$ are in synchrony when $\phi_1(t) \approx \phi_2(t)$ for all t in a given time interval.

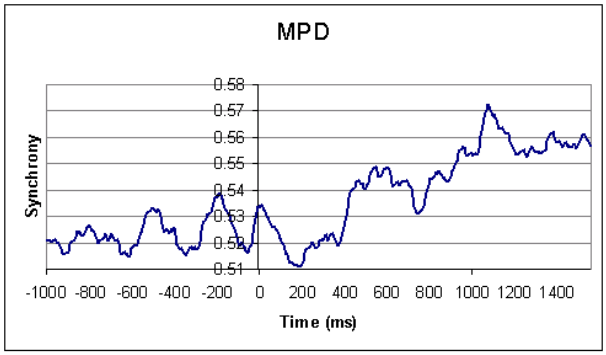

Figure 3.1: Average MPD (estimated across all trials) between electrodes T5 and O2 of the Figures experiment at 8 Hz, where an increase of synchronization can be observed after stimulus onset. Note that these results are very similar to those obtained with PLS.

In Chapter 4 we will show that synchrony measures which are estimated across a large time window, such as coherence and STPLS, may be contaminated by the dispersion of the phase at each electrode, which is not necessarily related to the degree of synchrony between the pair of signals under study. For this reason, we favor synchrony measures which are "instantaneous", in the sense that they are estimated from instantaneous values of the filtered signals (disregarding that the filtering process itself reduces the time resolution). The rest of this section deals with two synchrony measures specifically designed for instantaneous in-phase couplings.

3.3.2 Mean Phase Difference

A straightforward instantaneous in-phase synchrony measure is simply the magnitude of the phase difference $|\phi_1(t) - \phi_2(t)|$, which can be wrapped between $-\pi$ and π. This makes it easy to obtain a normalized measure based on the phase difference:

$$\mu_{j,\omega,e_1,e_2}(t) = 1 - \frac{1}{\pi}|\text{wrap}(\phi_{j,\omega,e_1}(t) - \phi_{j,\omega,e_2}(t))|, \tag{3.5}$$

where $\text{wrap}(\phi)$ returns the angle ϕ wrapped to the interval $[-\pi, \pi)$.

Figure 3.1 shows the synchronization values between sites T5 and O2, obtained with MPD at 8 Hz. As in the previous examples (for coherence, PLS, and STPLS), an increase of synchronization between these two electrodes is shown in the post-stimulus segment. Moreover, these results are very similar to those obtained with the PLS measure, even though PLS measures synchrony with a consistent phase-lag (across trials) which is not necessarily zero. This will be further discussed in Chapter 4.

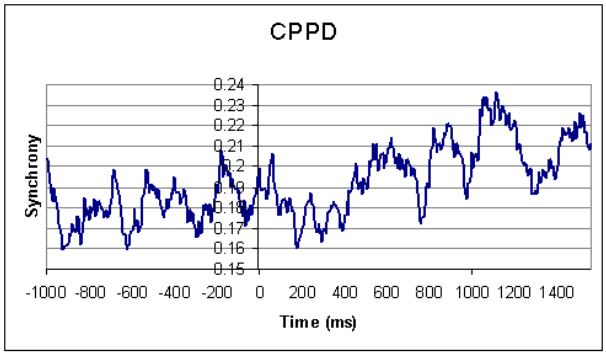

Figure 3.2: CPPD between electrodes T5 and O2 of the Figures experiment at 8 Hz. As with the other measures, an increase of synchronization can be observed in the post-stimulus segment.

3.3.3 Cumulative Probability of Phase Difference

An alternative to the MPD measure consists on estimating the probability of the phase difference being smaller (in absolute value) than some $\epsilon > 0$. This probability can be estimated across all trials for each t, ω, e_1, and e_2 as follows:

$$\mu_{\omega,e_1,e_2}(t) = \frac{1}{N_r}\sum_{j=1}^{N_r} I(|\text{wrap}(\phi_{j,\omega,e_1}(t) - \phi_{j,\omega,e_2}(t))| < \epsilon). \tag{3.6}$$

where $I(P)$ equals 1 if P is true, and zero otherwise.

This measure allows a quantification of the degree of synchrony (by means of ϵ), regardless of any further transformation applied to the measure (such as the significance analysis we perform). We have used $\epsilon = \pi/5$ rad for our tests (equivalent to 10 ms at 10 Hz), although one can also use a frequency-dependent value of ϵ given in time units.

CPPD synchronization between electrodes T5 and O2 from the Figures experiment is shown in Figure 3.2 (for $\omega = 8$ Hz).

One can modify this measure to detect anti-phase synchrony (couplings which show a phase difference of π). A simple example is given by:

$$\mu_{\omega,e_1,e_2}(t) = \frac{1}{N_r}\sum_{j=1}^{N_r} I(|\text{wrap}(\phi_{j,\omega,e_1}(t) - \phi_{j,\omega,e_2}(t) - \pi)| < \epsilon). \tag{3.7}$$

However, one must be careful not to confuse a decrease in synchrony with anti-phase couplings. This may be done, for example, by using small values for ϵ. Some preliminary results with anti-phase measures will be presented in Section 6.4.2.

3.4 Significance estimation

Since we are interested in event-related activity, we must determine how significant are the changes of synchrony with respect to the pre-stimulus segment. Following the procedure introduced by Marroquin to estimate the relative changes of EEG amplitudes [Marroquin et al., 2004], we subtract the average synchrony in the pre-stimulus segment in order to obtain the relative synchrony X_{j,ω,e_1,e_2}:

$$X_{j,\omega,e_1,e_2}(t) = \mu_{j,\omega,e_1,e_2}(t) - \frac{1}{T_s}\sum_{t'=1}^{T_s}\mu_{j,\omega,e_1,e_2}(t'), \tag{3.8}$$

where T_s is the length of the pre-stimulus segment. Finally, we take the mean relative synchrony across all trials:

$$Y_{\omega,e_1,e_2}(t) = \frac{1}{N_r}\sum_{j=1}^{N_r} X_{j,\omega,e_1,e_2}(t). \tag{3.9}$$

In the case of the CPPD measure (and also for Lachaux's PLS), $\mu_{\omega,e_1,e_2}(t)$ itself represents an average across trials, thus Y may be defined simply as

$$Y_{\omega,e_1,e_2}(t) = X_{\omega,e_1,e_2}(t) = \mu_{\omega,e_1,e_2}(t) - \frac{1}{T_s}\sum_{t'=1}^{T_s}\mu_{\omega,e_1,e_2}(t'). \tag{3.10}$$

Note that the mean of Y_{ω,e_1,e_2} in the pre-stimulus is zero, for every ω, e_1, and e_2. Positive values of Y represent synchrony increases with respect to the baseline (pre-stimulus), and viceversa.

To facilitate interpretation, we would like to classify each value of the mean relative synchrony in one of three classes:

- Significantly higher than the baseline(class $c = 1$). This corresponds to values of Y which are significantly greater than zero.
- Significantly lower than the baseline (class $c = -1$), corresponding to Y-values significantly lower than zero.
- No significant change ($c = 0$).

Here we will discuss two different ways to perform this classification.

3.4.1 Thresholded p-values from estimated distributions

A typical approach to determine the significance of the Y-values is the thresholded p-value technique described in Section 2.4.3. In this case, the null population consists of the Y values in the pre-stimulus segment (disregarding samples

for $t < 2\sigma_t$, which may be influenced by border effects). With these samples one can use kernel density estimation to construct the distribution p_0 of Y in the pre-stimulus, which can also be considered the distribution of Y given that $c = 0$ (i.e., $P(Y \mid c = 0)$). Then one can estimate a significance index S for each Y, based on the p-value, as follows:

$$S_{\omega,e_1,e_2}(t) = \begin{cases} 1 - p_0(Y > Y_{\omega,e_1,e_2}(t) \mid Y > 0) & \text{for } Y_{\omega,e_1,e_2}(t) > 0, \\ -(1 - p_0(Y < Y_{\omega,e_1,e_2}(t) \mid Y < 0)) & \text{for } Y_{\omega,e_1,e_2}(t) < 0. \end{cases} \tag{3.11}$$

The conditional probabilities in Equation 3.11 can be computed from the cumulative density function $P_0(Y^*) = p_0(Y < Y^*)$ (see Section 2.4.3) as follows:

$$p_0(Y > Y_{\omega,e_1,e_2}(t) \mid Y > 0) = \frac{1 - P_0(Y_{\omega,e_1,e_2})}{1 - P_0(0)}, \tag{3.12}$$

$$p_0(Y < Y_{\omega,e_1,e_2}(t) \mid Y < 0) = \frac{P_0(Y_{\omega,e_1,e_2})}{P_0(0)}. \tag{3.13}$$

The significance indices represent the direction of the change of synchrony with respect to the baseline (positive means increment, whereas negative means decrement), and the degree of significance of these changes. They can be used directly to obtain the class label field c by simply comparing them with a significance threshold $(1 - \alpha)$:

$$c_{\omega,e_1,e_2}(t) = \begin{cases} 1 & \text{if } S_{\omega,e_1,e_2}(t) > (1 - \alpha), \\ -1 & \text{if } S_{\omega,e_1,e_2}(t) < -(1 - \alpha), \\ 0 & \text{otherwise.} \end{cases} \tag{3.14}$$

3.4.2 Bayesian classification of significant changes in synchrony

A powerful technique for classification problems consists of Bayesian estimation with a prior Markov Random Field (MRF) model [Marroquin, 1987]. With this method, one can model the class field $c_{\omega,e_1,e_2,t}$ as a random field with a prior Gibbs distribution of the form

$$P_{MRF}(c) = \frac{1}{Z} \exp\left[-\lambda \sum_C V_C(c)\right], \tag{3.15}$$

where Z is a normalizing constant and V_C is a potential function that depends only on the values of the sites belonging to the clique C (see [Marroquin, 1987, 2001] for more details). For a classification problem, where c is discrete, a

popular model is the Ising model, which enforces c to be piece-wise constant. If we consider a first-order neighborhood system, whose cliques are single sites and nearest-neighbor pairs of sites, the Ising potentials are given by:

$$V_{r,s}(c) = \begin{cases} -1, & \text{if } c_r = c_s \\ 1, & \text{if } c_r \neq c_s \end{cases}, \tag{3.16}$$

where r and s are nearest neighbors. In our case, r and s are generally 4-tuples of the form $r = (\omega, e_1, e_2, t)$; however, at this point we are only interested in modeling persistence in time, although persistence across frequencies and spatial regularization could be taken into account to attempt an automated segmentation process.

The label field c is assumed to be Markovian (with a first-order Ising model) with distribution

$$P_c(c) = \frac{1}{Z} \exp\left[-\lambda \sum_{<r,s>} V_{r,s}(c) + \sum_r \log \alpha_{c_r}\right],$$

where α_k represents the global prior probability $\alpha_k = P(c_r = k)$. Besides the prior distribution for c, we also need the likelihood $P(Y \mid c)$, which can be written as

$$P(Y \mid c) = \prod_r P(Y_r \mid c_r) = \exp\left[\sum_r \log P(Y_r \mid c_r)\right]. \tag{3.17}$$

Using Bayes rule, the posterior distribution of c given Y can be calculated as

$$P(c \mid Y) = \frac{1}{Z'} \exp\left[\sum_r \log h_r(c_r) - \lambda \sum_{<r,s>} V_{r,s}(c)\right], \tag{3.18}$$

where Z' is a normalization constant and $h_r(k) = P(Y_r \mid c_r = k)\alpha_k$.

Given the estimator $\hat{c}$ and the true (unknown) field c, one can define a cost function $C(c, \hat{c})$ and find the optimal $\hat{c}$ by minimizing the expected value of $C(c, \hat{c})$. Since c is discrete, a suitable cost function given by Marroquin is

$$C(c, \hat{c}) = \sum_r \left[1 - \delta(c_r - \hat{c_r})\right], \tag{3.19}$$

and its expected value would be given by

$$\begin{aligned} E\left[C(c, \hat{c})\right] &= \sum_c C(c, \hat{c}) P(c \mid Y) \\ &= \sum_c \sum_r \left[1 - \delta(c_r - \hat{c_r})\right] P(c \mid Y) \\ &= K - \sum_r \sum_{c: c_r = \hat{c_r}} P(c \mid Y). \end{aligned} \tag{3.20}$$

The posterior marginal distribution for site r is defined as:

$$\pi_r(k) = \sum_{c:c_r=k} P(c \mid Y). \tag{3.21}$$

Thus the optimal estimator $\hat{c}$ (which minimizes $E[C(c,\hat{c})]$) can be found by maximizing $\pi_r(\hat{c_r})$ for each r. This estimator is known as the Maximizer of Posterior Marginals (MPM) estimator and is usually approximated using stochastic Markov-chain methods such as Metropolis or the Gibbs sampler. These algorithms, however, are computationally expensive and require an unknown number of iterations, which makes them less than adequate for our multidimensional data set. A better solution consists on approximating the posterior marginal distributions with the *empirical marginals* $p_r(k)$ [Marroquin et al., 2001]. It can be shown that the p_r vectors form a MRF with the same neighborhood system as c, thus the distribution of p is given by

$$P_p(p) = \frac{1}{Z_p} e^{-U(p)}, \tag{3.22}$$

where, for a first-order neighborhood system, $U(p)$ can be written as

$$U(p) = \sum_r |p_r - \hat{p_r}|^2 + \lambda' \sum_{<r,s>} |p_r - p_s|^2, \tag{3.23}$$

with $\hat{p_r}(k) = h_r(k) / \sum_{k'} h_r(k')$.

If c follows the Ising model, it can be shown that the field p can be modeled as a set of decoupled membrane models $p(k) = \{p_r(k), \forall r\}$ for $k = -1, 0, 1$. Therefore, the optimal p is obtained by minimizing, for each layer k, the energy function $U_k(p)$ given by

$$U_k(p) = \sum_r (p_r(k) - \hat{p_r(k)})^2 + \lambda' \sum_{<r,s>} (p_r(k) - p_s(k))^2. \tag{3.24}$$

Since each $p(k)$ is continuous, $U_k(p)$ can be minimized by solving the linear system obtained from equating the partial derivatives of U_k with respect to $p_r(k)$ to zero. However, the optimal $p(k)$ is a smoothed version of $\hat{p}(k)$, thus one can achieve a similar result by simply low-pass filtering each $\hat{p}(k)$ with a Gaussian kernel (for more details see [Marroquin et al., 1997]). Once we have p we can obtain the approximated MPM estimator as

$$c_r = \text{argmax}_k\{p_r(k)\}. \tag{3.25}$$

3.4.3 Estimation of prior distributions and likelihoods

For now, we are only interested in modeling persistence in time, thus we may estimate the time series $c_{\omega,e_1,e_2}(t) = c_{\omega,e_1,e_2,t}$ in a decoupled manner for each

ω, e_1, and e_2. To simplify things in this section, we will consider a fixed frequency ω and electrode pair (e_1, e_2) and only keep the time subindex.

In order to calculate $h_t(k)$ (and thus $p_t(k)$) we need the prior probabilities $\alpha_k = P(c = k)$ and likelihoods $P(Y_t \mid c = k)$. These can be estimated from the data if we consider that the complete distribution $P_Y(Y_t)$ can be expressed as:

$$P_Y(Y_t) = \sum_{k=-1}^{1} \alpha_k P(Y_t \mid c = k), \tag{3.26}$$

and also consider the following assumptions:

- $P(Y_t \mid c = 0)$ may be estimated empirically from the pre-stimulus data.
- $P(Y_t \mid c = 1) = 0$ for $Y \leq 0$.
- $P(Y_t \mid c = -1) = 0$ for $Y \geq 0$.

With these assumptions, we can obtain $P(c = 0)$ from Equation (3.26) as follows:

$$\alpha_0 = \frac{P_Y(0)}{P(0 \mid c = 0)} \tag{3.27}$$

and also

$$h_t(0) = \alpha_0 P(Y_t \mid c = 0) \tag{3.28}$$

$$h_t(1) = \begin{cases} P_Y(Y_t) - h_t(0), & Y_t > 0 \\ 0, & Y_t \leq 0 \end{cases} \tag{3.29}$$

$$h_t(-1) = \begin{cases} P_Y(Y_t) - h_t(0), & Y_t < 0 \\ 0, & Y_t \geq 0 \end{cases} \tag{3.30}$$

$P_Y(Y_t)$ and $P(Y_t \mid c = 0)$ can be estimated from the data Y using non-parametric kernel estimation. $P_Y(Y_t)$ is estimated using the full time segment, whereas $P(Y_t \mid c = 0)$ considers only the pre-stimulus segment.

The actual classification procedure for significative synchrony changes is performed (for each frequency ω and electrode pair (e_1, e_2)) as follows:

1. Estimate the pre-stimulus distribution $P_0(Y)$ and the full distribution $P_Y(Y)$ using kernel density estimation with bandwidth given by Silverman's rule of thumb [Silverman, 1986].
2. Estimate $\alpha_0 = P(c = 0) = P_0(0)/P_Y(0)$.
3. For each t, calculate $h_t(k)$ for $k = -1, 0, 1$ as given by Equations (3.28, 3.29, and 3.30).
4. Normalize h_t to obtain $\hat{p_t}$.

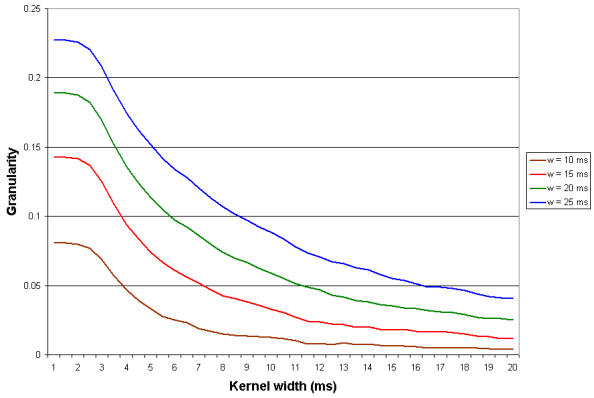

Figure 3.3: Granularity functions $G_w(\sigma_g)$ for $w = 10, 15, 20, 25$ ms. We are interested in the lowest value of σ_g for which $G_w(\sigma_g) < 0.05$.

5. Obtain $p(k)$ by convolving $\hat{p}(k)$ with a Gaussian kernel g. The width σ_g of the kernel controls the granularity of the c field (see below).

6. Approximate the MPM estimator by $c_t = \text{argmax}_k p_t(k)$ for all t.

3.4.4 Granularity and choice of σ_g

When approximating $p(k)$, we need to use an adequate width σ_g for the Gaussian kernel to filter out shorter homogeneous segments, which may not be significant in terms of persistence, and would instead break a longer segment. In particular, one would like that only those synchronous episodes with a duration greater than a minimum (physiologically motivated) value should be considered significant. According to studies related, for example, with the formation of short term memory [Jensen et al., 1996; Burle et al., 2000], this minimum value is in the order of one gamma oscillation, that is, around 20-50 ms.

To achieve this, one can define a granularity function $G(\sigma_g)$ for a given EEG dataset and see how it behaves with respect to σ_g. Our choice for G is defined as follows: for a class time series $c_{\omega,e_1,e_2} = \{c_{\omega,e_1,e_2}(t)\}$ we define the number of homogeneous segments n_{ω,e_1,e_2} as

$$n_{\omega,e_1,e_2} = \sum_{t=T_s+1}^{T} 1 + \left[1 - \delta\left(c_{\omega,e_1,e_2}(t) = c_{\omega,e_1,e_2}(t-1)\right)\right], \tag{3.31}$$

where $\delta(x)$ is the Kronecker delta function. Note that the sum is taken only on the post-stimulus segment. This is because we consider the pre-stimulus to be a single segment with class $c = 0$.

w (ms)	σ_g (ms)
10	4
15	7.5
20	11.5
25	16.5
50	76

Table 3.1: Values of σ_g (within a resolution of 0.5 ms) required to obtain $G_w(\sigma_g) < 0.05$, for various values of the granularity length w.

We also define $m_{\omega,e_1,e_2}(w)$ as the number of homogeneous segments whose length is less than w (the desired granularity length). The granularity function is then given by

$$G_w(\sigma_g) = E\left[\frac{m_{\omega,e_1,e_2}(w)}{n_{\omega,e_1,e_2}}\right], \tag{3.32}$$

where the expected value is estimated across all frequencies and electrode pairs. $G_w(\sigma_g)$ estimates the probability of having segments with length shorter than w for a given value of σ_g. One can then specify a value for w and find σ_g such that, for example, less than 5% of the segments have length less than w (i.e., $G_w(\sigma_g) < 0.05$). Figure 3.3 shows the granularity function graphs for $w = 10, 15, 20, 25$ ms for the Figures experiment using the MPD measure.

Table 3.1 shows the value of σ_g required for having less than 5% segments with length less than $w = 10, 15, 20, 25, 50$ ms. One can see that for values of w greater than 25-30 ms, the required σ_g grows considerably; however, the resulting label field c does not seem to be seriously affected, even if relatively large values of σ_g are used. In other words, the Bayesian method shown above seems to be very robust with respect to the kernel width σ_g. As an example, Table 3.2 shows the correlations, for the Figures experiment, between pairs of class fields estimated with different values of σ_g (using the MPD measure). All correlations corresponding to values of σ_g between 4 and 16.5 ms (which correspond to values of w between 10 and 25 ms) are greater than 0.97, and correlations involving $\sigma_g = 76$ ms ($w = 50$ ms) are greater than 0.91.

These results suggests that one can loosely choose σ_g from a relatively wide range of values (roughly between 10 and 50 ms). In particular, we have used $\sigma_g = 25$ ms for all our tests, and all the experiments.

3.4.5 Comparison between Bayesian estimation and thresholded p-values

We have estimated, for the MPD and CPPD measures and for each experiment, the threshold which maximizes the correlation between the class label field obtained from the Bayesian method and the one obtained from thresholded

	4 ms	7.5 ms	11.5 ms	16.5 ms	76 ms
4 ms	1.000	0.991	0.983	0.974	0.912
7.5 ms	0.991	1.000	0.991	0.982	0.916
11.5 ms	0.983	0.991	1.000	0.990	0.921
16.5 ms	0.974	0.982	0.990	1.000	0.928
76 ms	0.912	0.916	0.921	0.928	1.000

Table 3.2: Correlations between pairs of class fields with different values of σ_g (shown in bold typeface).

	Figures	Words	Go	NoGo	Stern-3	Stern-5
MPD Threshold	0.11	0.09	0.04	0.03	0.04	0.04
CPPD Threshold	0.06	0.06	0.01	0.01	0.02	0.02

Table 3.3: Threshold required to maximize the correlation between the thresholded p-values classification, and the Bayesian classification (with $\sigma_g = 16.5$ ms). The correlation is shown for each test experiment, and for the MPD and CPPD measures.

p-values (from the estimated distribution). The results are shown in the Table 3.3.

This means that the Bayesian approach yields results roughly equivalent to thresholded p-values with a threshold between 0.01 and 0.1, but this value has to be adjusted for each experiment and it is not clear how this should be done, whereas the Bayesian method permits one to specify the granularity independently of the particular experiment.

The correlations shown above change very little with respect to the granularity value, which is expected, since the Bayesian method is barely sensitive to the granularity parameter. For example, for the Figures experiment with the MPD measure, granularity values of 10, 15, 20, and 25 ms yield roughly equivalent results to a p-value threshold of 0.11, while a granularity of about 50ms corresponds to a threshold of 0.10. This robustness with respect to the granularity parameter is one of the reasons we chose the Bayesian approach.

3.5 Visualization

Synchrony data is in a four-dimensional space. Because of this, the visualization problem is not a trivial one, especially since one would like to keep as much detail as possible while displaying the data. It is very common to either focus on specific points in the time-frequency plane or condense the data by averaging in one or more dimensions.

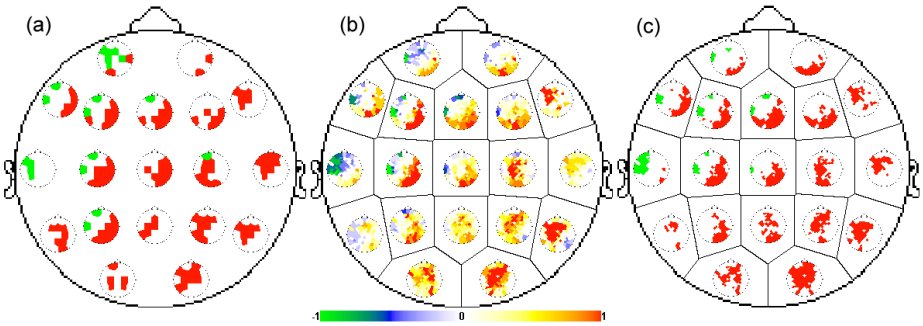

Figure 3.4: Multitoposcopic displays for a 120-channel dataset using the MPD measure: (a) uses only channels Fp1, Fp2, F3, F4, C3, C4, P3, P4, O1, O2, F7, F8, T3, T4, T5, T6, Fz, Cz, and Pz from the 10/20 system: red regions represent electrode pairs that show a significant increase in synchrony ($c = 1$), while green regions correspond to significant synchrony decreases ($c = -1$). Graphs (b) and (c) use the 120 channels grouped in 19 cortical areas corresponding to the Voronoi partition whose centers are the electrodes used in (a). For each area, one can plot a toposcope representing a statistic of the synchrony classes between each of the 120 electrodes and the electrodes within the area: (b) uses the average class $\bar{c}$ (which may be between -1 and 1), whereas (c) uses the class mode $\hat{c}$ (see text for details). The 3 multitoposcopes represent the SP obtained at t=515 ms and f=11 Hz during a Go/NoGo experiment (see [Harmony et al., 2006] for details); the rest of the examples presented in this paper correspond to the Figures experiment described in the text.

For a fixed time t and frequency ω it is possible to show the distribution of the synchrony pattern (SP) given by the class values $c_{\omega,e_1,e_2,t}$ in a multitoposcopic display, in which for each electrode e_1 one displays a head diagram (also called "toposcope") - within a bigger head - that shows the distribution of c across all sites e_2 (an example of this display can be seen in Figure 3.4a).

A problem arises when one deals with high electrode density recordings since only so many toposcopes can be displayed within the bigger head. One can use interpolation techniques to display high-density data in a single toposcope (in particular, we use a Voronoi partition [Aurenhammer, 1991] obtained by assigning each pixel in the toposcope the class corresponding to the nearest electrode), but the number of toposcopes may have to be reduced. One possibility consists in grouping the electrodes in N_g cortical areas $\{G_1, \ldots, G_{N_g}\}$, using again a Voronoi partition whose centers are, for example, the sites Fp1, Fp2, F3, F4, C3, C4, P3, P4, O1, O2, F7, F8, T3, T4, T5, T6, Fz, Cz, and Pz of the 10/20 system. One can then plot a toposcope for each group G_k computing, for each high-resolution electrode, the "most representative" synchrony class between this electrode and the electrodes in G_k. This most representative class may be computed in several ways; for example, the average class $\bar{c}$ of electrode e to

group G_k, which is computed as:

$$\bar{c}_{\omega,k,e,t} = \frac{1}{|G_k|} \sum_{e' \in G_k} c_{\omega,e',e,t} \tag{3.33}$$

or the class mode $\hat{c}$, which is computed as:

$$\hat{c}_{\omega,k,e,t} = \arg\max_{q \in \{-1,0,1\}} \left\{ \sum_{e' \in G_k} \delta(c_{\omega,e,e',t} - q) \right\}, \tag{3.34}$$

where δ is the Kronecker delta function. An example of multitoposcopes corresponding to $\bar{c}$ and $\hat{c}$ are shown in Figures 3.4b and 3.4c. More sophisticated methods could involve electrode clustering or TFT regularization; however, they are beyond the scope of this work.

Multitoposcopic displays are useful to show a detailed connectivity pattern for a fixed time and frequency; however, it is important to visualize larger regions of the time-frequency plane in order to localize zones of interest where the synchrony pattern remains almost constant and might be related to specific cognitive processes. Following the procedure given by [Marroquin et al., 2004] to analyze relative amplitude changes, we can use a Time-Frequency-Topography (TFT) display to present the data by reducing only one spatial dimension. We do this not by averaging but counting, for each electrode e, the number of electrodes that have significantly increased or decreased their synchrony with e. In other words, we can build a *synchrony increase histogram* (SIH) given by

$$H^{+}_{\omega,e}(t) \quad = \quad \sum_{e'=1}^{N_e} \delta(c_{\omega,e,e',t} - 1), \tag{3.35}$$

where $\delta(x)$ is the Kronecker delta function. $H^{+}_{\omega,e}(t)$ is the number of significantly stronger couplings (with respect to the pre-stimulus segment) for electrode e at time t and frequency ω. This can be thought as a degree of connectivity involving electrode e relative to the pre-stimulus.

Similarly, we can define a *synchrony decrease histogram* (SDH) as

$$H^{-}_{\omega,e}(t) \quad = \quad \sum_{e'=1}^{N_e} \delta(c_{\omega,e,e',t} - (-1)), \tag{3.36}$$

These histograms can be presented in a TFT display as shown in Figure 3.5.

3.5.1 Partitioned TF synchrony maps

The TFT visualization system provides at the same time a detailed view that shows which regions of the cortex are involved in synchronous processes at

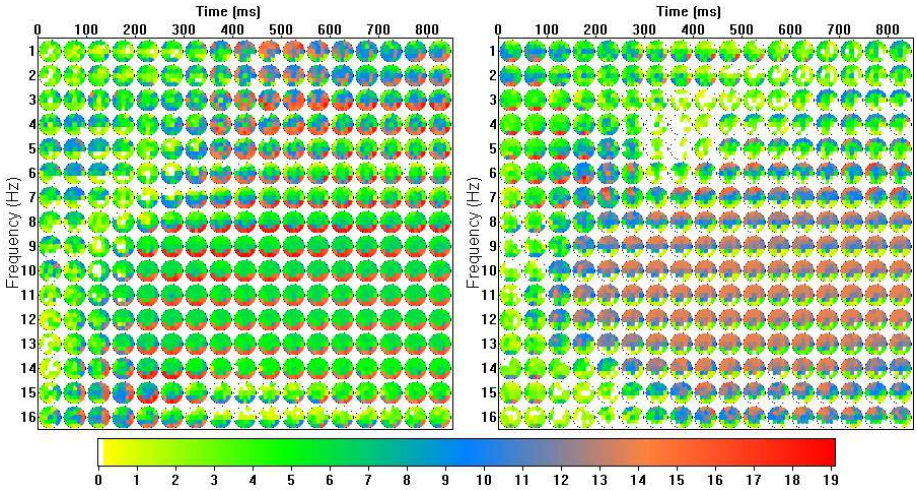

Figure 3.5: Synchrony histograms for the Figures experiment displayed as Time-Frequency-Topography (TFT) maps. The left and right maps show the synchrony increase and decrease histograms, respectively, for the MPD measure. The color scale represents the number of electrodes whose synchronization with a given electrode e increases (left) or decreases (right) significatively.

any time and frequency, and also a condensed view where one can see larger Time-Frequency regions which share the same synchronization pattern. This allows one to easily perform a manual partition of the TF plane where each region is assigned a representative multitoposcopic pattern; for example, the representative SP can be obtained by computing, for each electrode pair, the average class or the class mode of that pair across the TF region. Another option is to choose a fixed point within the TF region (e.g., the region center) and use the SP corresponding to that point to represent the region.

An example of manually partitioned MPD maps is shown in Figure 3.6 for the Figures experiment.

It is also possible to produce an automated partition by frequency bands (delta, theta, alpha, etc.), and at regular time intervals. An example of this is shown in Figure 3.7. The frequency bands are delta (1 to 3 Hz), theta (4 to 7 Hz), alpha (8 to 12 Hz) and low beta (13 to 18 Hz) with a segment interval of 300 ms. In the lower-left corner of each segment we show the estimated variance of $c_{\omega,e,e',t}$. For regions with high variance , the representative SP may not be consistent across region; however, one can subdivide the region for a more detailed analysis.

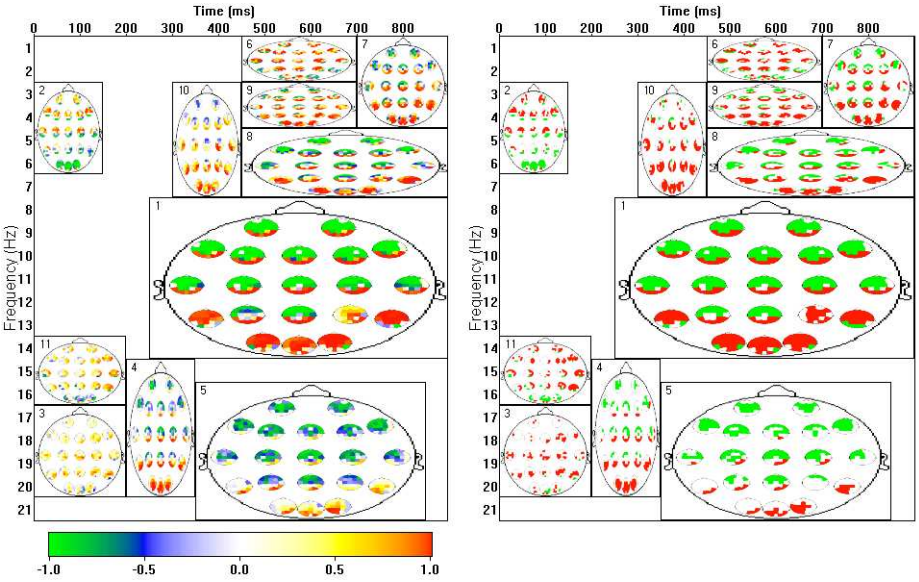

Figure 3.6: Manually-segmented MPD synchrony map for the Figures experiment. The left map uses the average class (represented by the color scale) for each electrode pair to construct the representative SP's, whereas the right map uses the class mode.

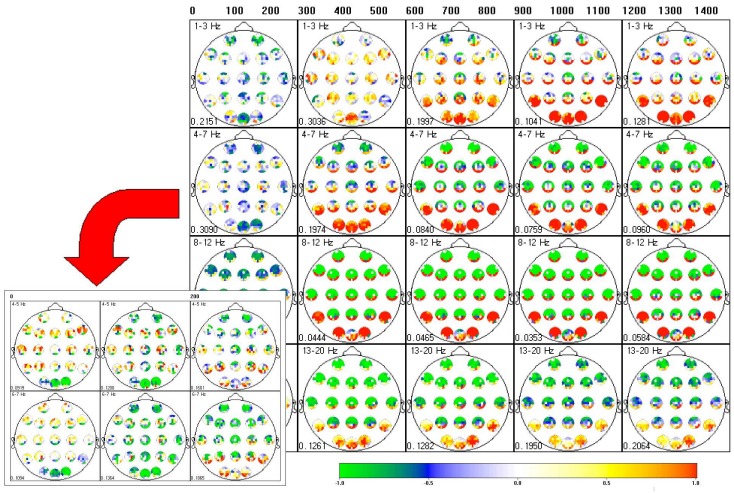

Figure 3.7: Automatically partitioned MPD maps for the Figures experiment (using the average class of each TF region as representative). Regions with high-variance can be subdivided into smaller, more consistent regions.

3.6 Gabor filters vs Sinusoidal filters

We have performed a series of tests in order to demonstrate the improvement of SQF's over Gabor filters for synchrony estimation. From Figure 2.1 one can see that the distortion produced by the Gabor filter (at tuning frequencies less than 6 Hz) consists of an oscillation at twice the tuning frequency. For these tests we applied the synchrony measure (based on $\Delta\Phi$) and statistical analysis described below. Using Gabor filters, the sensitivity of the synchrony measure shows a cyclic dependence on the time t, which corresponds to the distortions in the phase observed in Figure 2.1.

The simulated data used for the tests is obtained from a very simple model which consists of a 2 Hz sinusoidal plus noise. The signals are given by:

$$V_{j,e} = \cos(2\pi f_0 t + \phi_{j,e}) + R_{j,e}(r,t), \qquad \phi_{j,e} \sim \mathcal{N}(0,\sigma), \tag{3.37}$$

where j is the trial number, e the electrode index, $f_0 = 2Hz$ is the frequency of the sinusoidal, and σ is the standard deviation of the distribution of the phases, which controls the degree of synchrony between the signals. The noise function $R_{j,e}(r,t)$ depends on the "noise level" r. For our tests we used two electrodes ($e = 1, 2$), $\sigma_{\text{pre}} = \pi/10$ (pre-stimulus σ), and $\sigma_{\text{post}} = \pi/20$ (post-stimulus σ). Since $\sigma_{\text{pre}} > \sigma_{\text{post}}$, we are thus modeling an increase of synchrony in the full post-stimulus segment. We have generated 20 datasets with 50 trials each. For each dataset we perform the procedure described below in order to obtain a label field $c_{\omega,e_1,e_2}(t)$, which indicates if synchrony between e_1 and e_2 at a frequency ω is significantly higher ($c = 1$), lower ($c = -1$), or equal ($c = 0$) with respect to the pre-stimulus average. Focusing only on frequency $\omega = 2\pi f_0$ and electrode pair $< 1, 2 >$, we expect to obtain $c(t) = 1$ for all t in the post-stimulus.

For the first test we used Gaussian noise given by

$$R_{j,e}(r,t) \sim \mathcal{N}(0,r). \tag{3.38}$$

With a noise level $r = 0.5$, the average class $\bar{c}(t)$ across all datasets is shown in Figure 3.8 (a). The blue line represents the results obtained using Gabor filters, whereas the red line corresponds to sinusoidal quadrature filters. The oscillating distortion is clearly present with the Gabor filters, and it corresponds to a frequency of 4 Hz (twice the tuning frequency). Figure 3.8 (b) shows the proportion of detected couplings ($c(t) = 1$) in the post-stimulus segment with respect to the noise level r - these results are also averaged across the 20 datasets. The proportion should remain close to 1, however, Gabor filters clearly start to fail with $r > 0.3$.

The second test uses a sum of interfering sine waves as noise function:

$$R_{j,e}(r,t) = \sum_{f!=f_0} \frac{a_f}{f} \cos(2\pi f t + \phi_f), \qquad a_f \sim \mathcal{U}(0,r),\ \phi_f \sim \mathcal{U}(0,2\pi). \tag{3.39}$$

The sum is taken across frequencies from 1 to 50 Hz, except the frequency of interest f_0, and the components are attenuated according to their frequency.

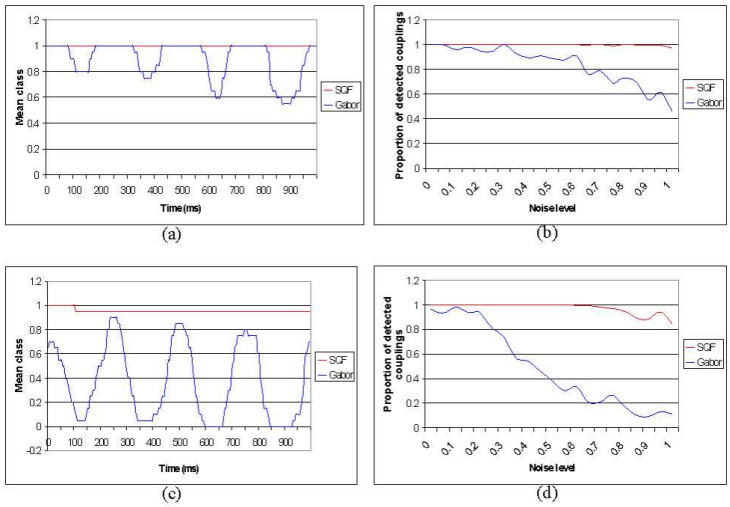

Figure 3.8: Comparison between sinusoidal and Gabor filters using simulated data with Gaussian noise for (a) and (b), and with interference of sinusoidals for (c) and (d). Graphs (a) and (c) show the average class $\bar{c}(t)$ computed across 20 datasets, whereas (b) and (d) show the proportion of detected couplings with respect to the noise level.

As in the previous test, we calculated the average class $\bar{c}$ and the proportion of detected couplings with respect to the noise level. The results, presented in Figure 3.8 (c) and (d), show the same differences as in the previous example.

It is worth mentioning that using real EEG datasets (such as the Figure experiment signals), there are clear differences between the results obtained with SQF's and those obtained from Gabor filters in the first 6 Hz. The tests with simulated data indicate that the results with Gabor filters may not be reliable in the delta and theta bands.

3.7 Reducing volume conduction effects

In Section 1.6 we discussed the problem of volume conduction in EEG, which may introduce spurious correlations in the EEG signals. One of the best solutions so far, as reported by Nunez et al. [1995; 1997; 2000], consists in estimating the Surface Laplacian (SL) of the raw potentials; however, a high spatial sampling rate (e.g, more than 64 electrodes distributed across the whole surface) is required to obtain an accurate SL, and even in that case, the phase of the SL signals may be very sensitive to noise [Junghöfer et al., 1999; Hagemann et al.,

2001]. On the other hand, most of our datasets contain only 19 or 20 channels, which is not enough for a reliable SL estimation.

Another solution, developed in collaboration with Joaquín Peña, is to use instead the phase of a new set of signals which are projections of the scalp potentials to cortical sites located directly below the actual electrodes. These signals may be obtained by placing dipoles (sources) in the cortical sites and solving the corresponding inverse problem.

The relation between the potentials and the current density at each source is given by:

$$\mathbf{\Phi} = \mathbf{K}\mathbf{J}, \tag{3.40}$$

where $\mathbf{\Phi}$ is a vector (of length N_e) of potentials measured at each electrode, $\mathbf{J} = (\mathbf{j_1}, \ldots, \mathbf{j_{N_s}})$ is comprised of the current densities $\mathbf{j}_k = (j_{kx}, j_{ky}, j_{kz})^T$ at each source $k = 1, \ldots, N_s$, and $\mathbf{K}$ is an $N_e \times 3N_s$ matrix (the *lead field*), which transforms current densities into surface potentials [Malmivuo and Plonsey, 1995; Pascual-Marqui, 1999]. $\mathbf{K}$ depends on the electrode positions, the physical and geometrical properties of the volume conductor, and the position of the source dipoles. In particular, we compute $\mathbf{K}$ using a three concentric sphere head model [Zhang, 1995].

The inverse problem consists in finding $\mathbf{J}$, given $\mathbf{\Phi}$ and $\mathbf{K}$. This is typically an ill-posed problem, since the number of unknowns ($3N_s$) is usually larger than the number of equations (N_e). In order to make this problem well posed, we place one dipole in the cortex area directly below each electrode, with radial direction (i.e., perpendicular to the surface and pointing outwards).

In general, one can write the current densities for each source as $\mathbf{j}_k = \alpha_k \mathbf{q}_k$, $|\mathbf{q}_k| = 1$, where $\mathbf{q}_k$, is the direction of the k-th dipole, and α_k its strength. One can also write the lead field $\mathbf{K}$ as:

$$\mathbf{K} = \begin{bmatrix} \mathbf{k}_{11} & \mathbf{k}_{12} & \cdots & \mathbf{k}_{1N_s} \\ \mathbf{k}_{21} & \mathbf{k}_{22} & \cdots & \mathbf{k}_{2N_s} \\ \vdots & \vdots & & \vdots \\ \mathbf{k}_{N_e1} & \mathbf{k}_{N_e2} & \cdots & \mathbf{k}_{N_eN_s} \end{bmatrix}, \tag{3.41}$$

with $\mathbf{k}_{ij} = [k_{i(3j)} \quad k_{i(3j+1)} \quad k_{i(3j+2)}]$.

The surface potentials are thus given by

$$\mathbf{\Phi} = \begin{bmatrix} \mathbf{k}_{11}\alpha_1\mathbf{q}_1 + \mathbf{k}_{12}\alpha_2\mathbf{q}_2 + \cdots + \mathbf{k}_{1N_s}\alpha_{N_s}\mathbf{q}_{N_s} \\ \mathbf{k}_{21}\alpha_1\mathbf{q}_1 + \mathbf{k}_{22}\alpha_2\mathbf{q}_2 + \cdots + \mathbf{k}_{2N_s}\alpha_{N_s}\mathbf{q}_{N_s} \\ \vdots \\ \mathbf{k}_{N_e1}\alpha_1\mathbf{q}_1 + \mathbf{k}_{N_e2}\alpha_2\mathbf{q}_2 + \cdots + \mathbf{k}_{N_eN_s}\alpha_{N_s}\mathbf{q}_{N_s} \end{bmatrix} \tag{3.42}$$

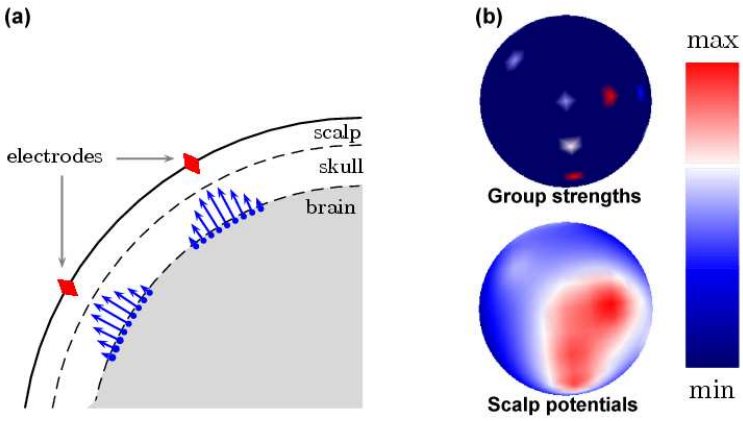

Figure 3.9: **(a)** Dipole groups under each electrode within a three concentric sphere model. **(b)** Scalp potentials obtained with the forward equation and the given group strengths.

$$= \underbrace{\begin{bmatrix} \mathbf{k}_{11}\mathbf{q}_1 & \mathbf{k}_{12}\mathbf{q}_2 & \cdots & \mathbf{k}_{1N_s}\mathbf{q}_{N_s} \\ \mathbf{k}_{21}\mathbf{q}_1 & \mathbf{k}_{22}\mathbf{q}_2 & \cdots & \mathbf{k}_{2N_s}\mathbf{q}_{N_s} \\ \vdots & \vdots & & \vdots \\ \mathbf{k}_{N_e1}\mathbf{q}_1 & \mathbf{k}_{N_e2}\mathbf{q}_2 & \cdots & \mathbf{k}_{N_eN_s}\mathbf{q}_{N_s} \end{bmatrix}}_{\mathbf{L}} \underbrace{\begin{bmatrix} \alpha_1 \\ \alpha_2 \\ \vdots \\ \alpha_{N_s} \end{bmatrix}}_{\alpha}$$

If the dipole directions $\mathbf{q}_k$, $k = 1, \ldots, N_s$ are known, then one can compute the matrix $\mathbf{L}$. Moreover, if there is only one source per electrode (i.e., $N_s = N_e$), then the problem becomes well-posed as the number of unknowns (i.e., the α_k's) equals the number of equations. In this case, $\mathbf{L}$ is square and the inverse problem has a unique solution given by:

$$\hat{\alpha} = \mathbf{L}^{\dagger}\mathbf{\Phi}. \tag{3.43}$$

Where $\mathbf{L}^{\dagger}$ is, in general, the pseudoinverse of $\mathbf{L}$ [Vogel, 2002], which can be obtained, for example, by singular value decomposition (SVD - [Press et al., 1992]).

Instead of a single dipole per electrode, one can also place a group of cortical dipoles (for each recording site) whose strengths decrease exponentially with the distance to the central dipole (the one located right below the electrode - see Figure 3.9a). In other words, the amplitude of all the dipoles in the group is determined by the strength of the central dipole (the "group strength"). The inverse problem can be solved in a similar manner: one can write the potentials $\mathbf{\Phi}$ as the product of a square matrix $\mathbf{L}$ and the vector of group strengths α, where $\mathbf{L}$ (and its pseudoinverse) can be computed. Figure 3.9b shows an example of

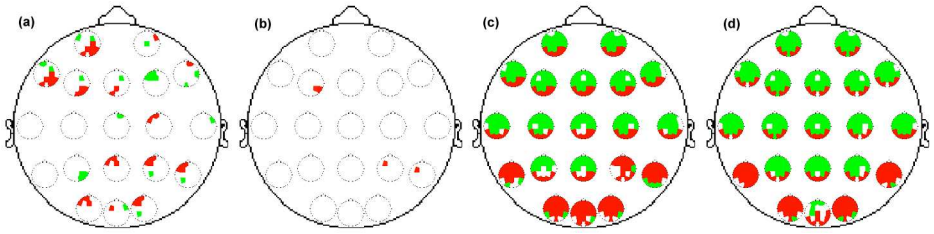

Figure 3.10: Examples of synchrony patterns obtained with scalp potentials and their corresponding projected signals (see text for details).

scalp potentials obtained from the given group strengths, using the forward model ($\mathbf{\Phi} = \mathbf{L}\alpha$).

The projection of scalp potentials to the cortical group strengths reduces the conductor effects of the scalp and skull, and provides better spatial localization than the raw scalp potentials, but with a magnitude large enough to obtain reliable phase estimations. Figures 3.10a and 3.10b show the resulting synchrony patterns obtained for synthetic signals using raw potentials (3.10a) and the projected signals (3.10b). The test signals were obtained by placing one dipole near F3 and another between P4 and T6 of the 10/20 system, whose output is a sinusoidal signal, and solving the forward problem to obtain scalp readings. Noise was added to all electrode readings. The dipoles are unsynchronized (out of phase) in the pre-stimulus segment (not shown) and in perfect synchrony in the post-stimulus. The graphs show significant increment (red) or decrement (green) in synchrony for all electrode pairs. The synchrony pattern obtained from projected signals clearly shows a better localization of the synchronized regions. Another example, with real EEG signals from the Figures experiment, is shown in Figures 3.10c (scalp potentials) and 3.10d (cortical projections). Note that, in this case, synchronous activity also appears to be smeared when using potentials: sites P4 and Oz show a significant increment in synchrony with almost every other site; however, most of these couplings do not show when using projected signals, possibly indicating that they were spurious.

Chapter 4

Comparative study between synchrony measures

4.1 Measure comparisons in the literature

A few works have focused on the evaluation of different synchronization measures, using real and simulated EEG data. In one of these papers ([Quian-Quiroga et al., 2002]), interaction between the left and right hemispheres of a rat are analyzed with various synchrony measures. This includes both linear (correlation / coherence) and non-linear (generalized synchronization, mutual information, phase-locking) interdependences.

According to Quian-Quiroga, all the measures (with the exception of MI) ranked the synchronization levels in the same way; that is, the periods of low and high synchrony, respectively, were similarly distinguished by every measure. However, the separation between low and high synchrony periods was more noticeable with non-linear measures (GS and STPLS) than with coherence. This may indicate that most couplings have a non-linear nature (e.g. phase-locking, as Varela suggests). In the case of mutual information, Quian-Quiroga et al. used a time-embedding technique to transform the data to a m-dimensional space, which made it difficult to obtain a good estimation of the joint entropy as the joint probability matrix was very sparse. Because of this, it was not possible to obtain robust estimations of the MI, which dramatically depended on m.

In 2003, David and Friston introduced a neural mass EEG model, which simulates the activity of populations of neurons, under the assumption that the state of the population can be approximated with very few state variables [David and Friston, 2003b]. This model is based on a simpler model ([Jansen and Rit, 1995]) that is able to produce any of the common EEG rhythms (alpha, beta, etc.).

In the simulations performed by David et al., it was observed that when both

areas were bidirectionally coupled, the phase-shift between the two signals was equal to zero, and it was shown that for bidirectional couplings, the phase-shift is equal to either 0 or π, depending on the propagation delay. According to David and Friston [2003b] and Varela et al. [2001], the proportion of reciprocal connections in the brain is very high. This supports the findings in [Friston et al., 1997; Rodriguez et al., 1999], where a tendency of the phase-differences towards zero were associated with synchronous episodes (see Sections 2.3.1 and 2.3.2).

In their following article ([David et al., 2004]), David and Friston tested various synchronization measures using simulated data. The measures were: cross-correlation (with zero time-lag), mutual information, generalized synchronization, and the single-trial phase-locking value. The simulations were obtained with their neural mass model, using a symmetric configuration for a bidirectional coupling, and a parameter $k \in [0, 1]$, which specifies the coupling strength. A series of surrogate (uncoupled) signals were generated with $k = 0$ in order to obtain the null distributions of the synchrony measures.

In a first analysis, the coupling sensitivity of the various measures was tested using broadband signals, as a function of the coupling strength k. While all measures increased accordingly with k, GS showed a better response to weak couplings ($k < 0.125$), while MI was better for strong couplings. The next analysis evaluates the response to the time-window size used to estimate the measures. The window was varied from 0.2 to 2 s, and the z-scores (with respect to the null distribution from an uncoupled model) were estimated for each measure. In this case, GS resulted to be the most reliable estimator.

For narrow-band analysis, the coupled and uncoupled signals were band-pass filtered from 2 to 50 Hz, each 2 Hz, and the synchrony measures were estimated for each frequency. The resulting z-scores were plotted as a function of frequency. The graphs for all measures had a similar shape; however, the z-scores for mutual information were much higher, suggesting that MI may be more sensitive to frequency-specific synchrony.

The next analysis focused on the sensitivity of the measures to non-linear couplings. In this case, the surrogate population is designed to preserve the linear properties of the original data, while destroying the non-linear dependencies (see [David et al., 2004] for details). This method was applied to the simulated broadband signals, and the synchrony measures were estimated as a function of the coupling strength. Cross-correlation and mutual information were insensitive to non-linear couplings, while with GS and phase synchronization, the non-linearities accounted for a small fraction of the synchrony value.

David et al. concluded that although the results of the four measures tested were very similar, one should be careful when studying functional connectivity using electrophysiological signals. One should not make too many assumptions about the type of interactions; therefore, instead of relying on a single measure, it is more advisable to apply various measures, each of which is sensitive to different aspects of synchronization.

4.2 Comparison of synchrony measures

The procedure described in Chapter 3 can be used with any of the synchrony measures presented in Section 2.3. In particular, we have tested the PLS, STPLS, and coherence measures. GS and MI have not been implemented for the reasons explained in Sections 2.3.4 and 2.3.5.

For the rest of this chapter, we will present various interesting results which may help in determining the advantages and disadvantages of each measure.

4.2.1 TFT Synchrony maps

We have computed the following measures for the Figures experiment:

- Mean Phase Difference (MPD)
- Cumulative Probability of Phase Difference (CPPD), with $\epsilon = \pi/5$ rad.
- Lachaux's Phase Locking Statistic (PLS)
- Single-Trial PLS (STPLS), with a window size of 105 ms ($w = 10$ samples).
- Coherence, with a window size of 105 ms.

Figure 4.1 show the SIH's for all the measures (full SIH, SDH, and partitioned maps will be presented in Appendix A).

From these maps, one can observe that CPPD and PLS produce similar results to the MPD measure. On the other hand, STPLS and coherence yield similar results themselves but different from MPD. This suggests that the synchrony measures may be divided in two groups.

4.2.2 Correlation between measures

Given two synchrony measures, μ^1 and μ^2, one can estimate the class label fields c^1 and c^2, and compute a correlation measure between the two class fields. Typically, the correlation between two random variables X and Y is given by

$$\mathrm{cor}(X, Y) = \frac{E\left[(X - EX)(Y - EY)\right]}{\sigma_X \sigma_Y}, \tag{4.1}$$

where $E[\cdot]$ denotes the expected value, and σ_X is the standard deviation of X. Using this correlation measure, we have computed the degree of interdependence between each pair of measures for the Figures experiment. The results are presented in Table 4.1, where two groups are clearly defined by high correlation values: one group consisting of MPD, CPPD, and PLS, and the other consisting of STPLS and coherence. Similar results have been obtained with

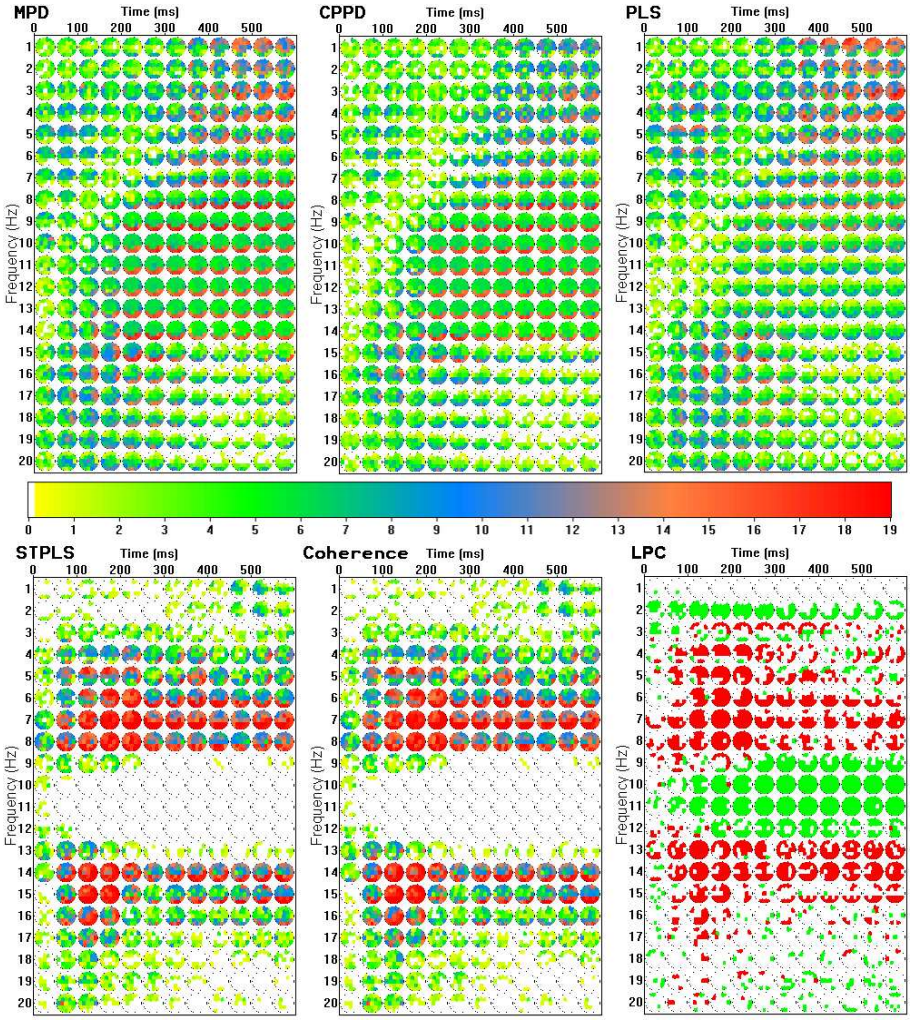

Figure 4.1: Synchrony increase histograms for the Figures experiment using the five synchrony measures: MPD, CPPD, PLS, STPLS, and coherence. The bottom-right graph corresponds to the TFT map of significant changes in the LPC measure (red represents significant increases, whereas green corresponds to significant decreases) - see text for details.

	MPD	CPPD	PLS	STPLS	Coherence
MPD	1.000	0.835	0.853	0.477	0.508
CPPD	0.835	1.000	0.755	0.500	0.525
PLS	0.853	0.755	1.000	0.503	0.536
STPLS	0.477	0.500	0.503	1.000	0.872
Coherence	0.508	0.525	0.536	0.872	1.000

Table 4.1: Correlation (as defined by Equation 4.1) between pairs of synchrony measures.

	MPD	CPPD	PLS	STPLS	Coherence
MPD	1.000	0.816	0.885	0.544	0.568
CPPD	0.816	1.000	0.767	0.583	0.600
PLS	0.885	0.767	1.000	0.557	0.583
STPLS	0.544	0.583	0.577	1.000	0.870
Coherence	0.568	0.600	0.583	0.870	1.000

Table 4.2: Probability of equal class (as defined by Equation 4.2) between pairs of synchrony measures.

other experiments (besides the Figures experiment) and will be presented in Appendix A.

Another dependence measure, which may be more adequate for class data, can be defined as the probability of $c^1_{\omega,e_1,e_2,t} = c^2_{\omega,e_1,e_2,t}$ (probability of equal class - PEC), which can be estimated as

$$\mathrm{pec}(\mu_1, \mu_2) = \frac{1}{N_f N_e^2 N_t} \sum_{\omega,e_1,e_2,t} \delta(c^1_{\omega,e_1,e_2,t} - c^2_{\omega,e_1,e_2,t}), \tag{4.2}$$

where δ is the Kronecker delta function. Table 4.2 shows the dependence values for all pairs of measures using Equation 4.2; the two groups of measures can also be distinguished here.

It is worth noting that STPLS and coherence are computed across a time window, whereas the other measures are "instantaneous", in the sense that they only use the phase difference at a single time point. This may be a determining factor in the behavior of a given measure.

One interesting fact is the high correlation between MPD and PLS. By looking at Equation (2.15) one can see that PLS actually measures the consistency of the phase difference across all trials. A high correlation between MPD and PLS suggests that the processes that result in high in-phase synchronization are fairly consistent across trials and subjects, and thus may be related to the task.

Furthermore, the CPPD measure is also highly correlated to the MPD, suggesting that synchronization effectively happens with near-zero phase difference.

This is in accordance with the neural mass model proposed by David and Friston [2003a] and other works ([Friston et al., 1997; Rodriguez et al., 1999]) which have also found zero-centered phase difference distributions during synchronous episodes between two electrodes.

4.2.3 Response to induced activity

One could argue that instantaneous synchrony measures (such as MPD) may be more sensitive to variations in the latency of event-related responses across trials (latency jitter); in other words, these measures may not respond adequately to induced activity.

Typically, induced activity is revealed by performing a time-frequency decomposition of each trial, and averaging a positive definite function of the filters' output (e.g., the power) across all trials, whereas evoked activity is obtained by first averaging the raw signals across trials, and then applying a positive definite function (power analysis) to the average signals [David et al., 2006]. The difference is that in the former case (induced responses) there will be no cancelations during averaging, whereas in the latter (evoked) case, there may be cancelations due to differences in sign across trials. It is clear then, that the methodology presented in Chapter 3 is basically an induced response analysis, where the positive definite function is the synchrony measure (we may call it "induced synchrony"), instead of the power; this function is averaged across trials and then the baseline is subtracted. This suggests that the analysis procedure, with any of the synchrony measures previously presented, should be at least as sensitive to induced responses as the typical average-power analysis. Of course, because of additional averaging across time, STPLS and coherence may be more robust to larger amounts of latency jitter.

In Section 6.4.1 we will briefly discuss some preliminary results about the relationship between evoked potentials and induced synchrony, and the mechanisms which generate both types of activity.

4.2.4 Local phase dispersion

Let us recall the equation for Lachaux's single-trial phase-locking statistic:

$$\mathrm{STPLS}_{e_1,e_2}(t) = \frac{1}{2w+1}\left|\sum_{t'=t-w}^{t+w} \exp\left[i\left(\phi_{e_1}(t') - \phi_{e_2}(t')\right)\right]\right|. \qquad (4.3)$$

The STPLS is equal to one minus the dispersion of the phase difference between the two electrodes under study, estimated across a time window centered at t. Note that if one of the phases remains relatively constant within the time window, then the STPLS will be approximately equal to one minus the dispersion of the other phase. This suggests that it may be interesting to study the correlation between the local phase dispersion and each synchrony measure. To

	MPD	CPPD	PLS	STPLS	Coherence
LPC	0.091	0.035	0.131	0.698	0.673
Power	-0.028	-0.122	0.067	0.266	0.273

Table 4.3: Correlation between significance indexes of LPC/Power changes, and the average class at each electrode, for each synchrony measure.

do this, one can define a local phase constancy (LPC) measure as the average across trials of one minus the dispersion of the phase at each electrode. The LPC is thus given by

$$\mathrm{LPC}_{\omega,e}(t) = \frac{1}{N_r}\sum_{j=1}^{N_r}\frac{1}{2w+1}\left|\sum_{t'=t-w} t + w\exp\left[i\phi_{j,\omega,e}\right]\right|. \tag{4.4}$$

One can then estimate a TFT map of significant changes of the LPC measure with respect to the pre-stimulus, as described in Section 3.4. In particular, we use the significance indexes obtained from p-values (Section 3.4.1), which we denote here as $\mathrm{LPC}^S_{\omega,e}(t)$. The TFT map of LPC changes is shown in Figure 4.1 (bottom-right). Note the similarity between this map and the SIH's for STPLS and coherence: increases in the LPC correspond to increases in STPLS and coherence; moreover, the green region in the LPC map (around 9-12 Hz) corresponds to high values in the SDH's of STPLS and coherence (see Appendix A).

In order to estimate the correlation between significant changes in the LPC and significant changes in a synchrony measure, one can compute the average class at each electrode, which is given by

$$c^{\mathrm{avg}}_{\omega,e}(t) = \frac{1}{N_e-1}\sum_{e'=1}^{N_e} c_{\omega,e,e',t}. \tag{4.5}$$

Here we divide by $N_e - 1$ instead of N_e since $c_{\omega,e,e,t} = 0$ for every electrode e. Table 4.3 shows the correlation between LPC^S and the average class (c^{avg}) corresponding to each of the tested measures. Note that the correlation values corresponding to STPLS and coherence are significatively higher than for the other measures.

These results suggest that STPLS and coherence may be seriously influenced by changes in the dispersion of the local phase measured at each electrode; in other words, they may be more sensitive to local processes which are not necessarily related to the synchronization between the two electrodes under study. For these reasons, we believe that instantaneous measures may be better suited for synchrony analysis.

As a sidenote, Table 4.3 also shows that STPLS and coherence are slightly more correlated to instantaneous power changes. This makes sense for coherence, since it uses both the magnitude and phase of the signals; however, the

correlation indexes are not large enough to suggest a strong dependence between power and long-range synchrony.

4.2.5 Influence of volume conduction

We have already discussed the importance of the volume conductor in the study of EEG synchrony. Some authors argue that a synchronization measure that favors phase differences of zero (such as the MPD) would be highly sensitive to volume conduction; however, this is not entirely clear. Lachaux et al. [1999] mention that "another common assumption is that the phase difference between electrodes should be zero in case of conduction synchrony. This is usually false: even if two electrodes record the same group of sources, the signals of these electrodes are different linear combinations of the source amplitudes, ... Therefore, the phase of the original signals recorded by the two electrodes should be different, except if all the sources have the same phase". In other words, if several sources influence two different sites via volume conduction, their net influence on the resulting electrode signals will correspond to different linear combinations of these source signals (with coefficients given by the corresponding attenuations), thus producing different phases. From this viewpoint, there is no reason to think that MPD or CPPD will be more influenced by volume conduction than the other measures. Furthermore, the MPD and CPPD measures are highly correlated to Lachaux's PLS measure, which measures synchrony with a constant phase lag (not necessarily zero), suggesting that at least these three measures are similarly affected by volume conduction.

Lachaux also suggests that one may be able to identify conduction synchrony by looking at the neighboring sites of the two electrodes. In other words, if conduction synchrony is observed between two electrodes, then one must also observe high synchrony between their neighbors. One can test this by defining a neighborhood N_i for each electrode e_i, and then counting, for each electrode pair $< e_1, e_2 >$ for which an increase in synchrony is observed, the number of pairs $< e_r, e_s >$, $e_r \in N_1$, $e_s \in N_2$ whose synchrony also increases. If this number is relatively high for all t, it may suggest a higher amount of spurious couplings due to volume conduction (although this is not necessarily true). One can then compare these values for different synchronization measures to see if any of them may be more sensitive to conduction effects. With this in mind, one can define a neighbor-synchrony measure Z^+, which is given by:

$$Z^+_{\omega,e_1,e_2,t} = \frac{\sum_{r\in N_1, s\in N_2} \delta(c_{\omega,e_r,e_s,t} - 1)}{|N_1||N_2|} \cdot \delta(c_{\omega,e_1,e_2,t} - 1), \tag{4.6}$$

where c is the class label field obtained from thresholded p-values (as shown in Section 3.4.1). Here we avoid using the Bayesian classification since the regularization may introduce spurious correlations among neighboring electrodes. Note also that we are dividing by the size of the neighborhoods; this is done in order to normalize the measure, since different electrodes may have differ-

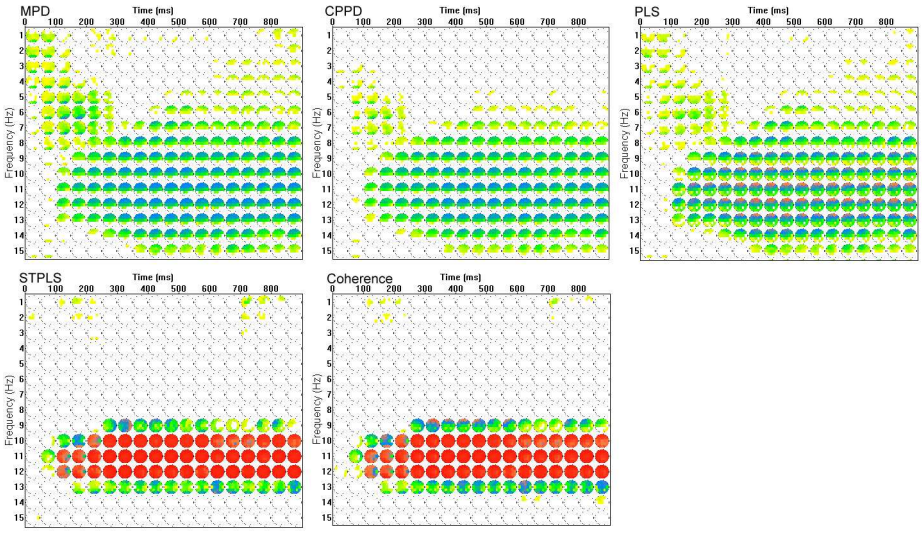

Figure 4.2: TFT maps of neighbor synchrony (Z^+) for the Figures experiment using the five synchrony measures: MPD, CPPD, PLS, STPLS, and coherence.

ent neighborhood sizes. We have chosen a neighborhood radius such that each electrode has at least one neighbor.

By inspecting the TFT maps of the average Z^+ for each electrode (Figure 4.2), one can see that, if anything, STPLS and coherence show larger Z^+ values, although in a narrower frequency band, than the other measures. In order to obtain a more conclusive result, we averaged Z^+ across all the electrode pairs which show an increase of synchrony, and across all time and frequency points. The averaged $\overline{Z^+}$ is thus given by

$$\overline{Z^+} = \frac{\sum_{\omega,e_1,e_2,t} Z^+_{\omega,e_1,e_2,t}}{\sum_{\omega,e_1,e_2,t} \delta(c_{\omega,e_1,e_2,t} - 1)}. \tag{4.7}$$

One can think of $\overline{Z^+}$ as the conditional probability of some neighbor of e_1 increasing its synchrony with some neighbor of e_2, given that the synchrony between e_1 and e_2 increases. Table 4.4 presents the resulting $\overline{Z^+}$ for each synchrony measure. Effectively (and surprisingly), STPLS and Coherence show a higher average neighbor synchrony, although the difference does not seem significant. In any case, it is clear that the in-phase synchrony measures (MPD and CPPD) do not yield $\overline{Z^+}$ values which are significantly greater than the other measures, and thus there is no evidence supporting the claim that these measures may be more sensitive to volume conduction effects.

	MPD	CPPD	PLS	STPLS	Coherence
$\overline{Z^+}$	0.1139	0.0639	0.0989	0.1606	0.1607

Table 4.4: Average neighbor synchrony $\overline{Z^+}$ for each synchrony measure applied to the Figures experiment.

4.2.6 Conclusions

The results shown in the previous sections suggest that

1. Phase synchrony effectively happens, in most cases, with near-zero phase difference between pairs of leads.
2. Phase synchrony, when happens, is relatively consistent across trials.
3. Instantaneous phase-lock measures are less sensitive to changes in the dispersion of the local phase at each electrode, and thus may be better suited for synchrony analysis than measures which are computed across a time window (disregarding filtering effects).
4. All measures should respond to induced activity; however, measures computed across a time window may be less sensitive to latency jitter.
5. All measures seem to be equally sensitive to volume conductor effects.

Chapter 5

Apparent phase and amplitude

In the previous chapters we have described our methodology for the analysis of synchronization patterns, and shown the advantages of the proposed measures (MPD and CPPD) over some of the measures in the literature. We have used these techniques to study a few real EEG datasets, and now we proceed to describe our findings.

In this chapter, we propose a simple mathematical model of the narrow-band signal captured by an electrode. With this model, one can explain and simulate most of the synchronization patterns that result from the analysis of the experiments. The following chapter will deal with the neurophysiological interpretation of such patterns.

5.1 Motivation

From the analysis of the Figures, Words, Go/No-Go, and Sternberg experiments, one can observe certain phenomena (some of which have been previously reported) that may appear counter-intuitive; for example:

1. Synchronous episodes occur with near-zero phase lag, regardless of the distance between leads. This has also been observed in [Friston et al., 1997] and [Rodriguez et al., 1999], and is in accordance with David and Friston's neural mass model.

2. It is possible that two or more electrodes increase their synchrony with another electrode, which acts as a nodal point, and at the same time observe a decrease of synchronization between the non-nodal sites. One example of this phenomenon is the synchrony pattern observed in the alpha band (8-12 Hz) in Figures 3.6 and 3.7: the occipital leads increase their synchrony with most of the other electrodes, while fronto-parietal

leads show a decrease of synchrony among them. This phenomenon can also been observed in other studies, such as [Rodriguez et al., 1999], [Varela et al., 2001], and [David et al., 2003b].

3. When an electrode e increases its synchrony with many other sites, there is a high probability of observing a significant power change at e in the same frequency band. If the non-nodal sites show a decrease of synchronization, the power at e will decrease, and viceversa.

These phenomena may be explained if one supposes that the signal recorded by a scalp electrode results in fact from the sum of macroscopic oscillations produced by functionally different neural populations. This assumption is supported by the following considerations: a scalp electrode provides estimates of synaptic action averaged over tissue masses containing between 10^7 and 10^9 neurons [Nunez, 1995]. There is evidence (obtained, for example, using retrogradely transported flourescent dyes [Morecraft et al, 1993], and single-cell recordings [Quintana and Fuster, 1999]) of extensively intermingled populations of neurons connected with different areas (e.g., frontal eye fields and posterior parietal cortex). Moreover, when performing a computational task, neurons may quickly associate into a functional group while disassociating from concurrently activated groups [Haalman and Vaadia, 1998].

5.2 Population model

The facts exposed above suggest that one may be able to model certain aspects of the EEG dynamics by expressing each electrode signal as the sum of oscillating functions (e.g., sinusoidals) corresponding to the average activity of each contributing population. It is also plausible that, in order to develop a macroscopic oscillation, the neurons of each sub-population must be synchronized. Therefore, a reasonable model for a complex narrow-band EEG signal is:

$$V(t) = \sum_k \alpha_k \cos(\omega_k t + \phi_k), \tag{5.1}$$

where the positive coefficients α_k depend on the amplitude and relative size of subpopulation k, and ϕ_k is the corresponding phase. Note that this model allows neurons to de-couple from their current sub-population and synchronize with a different sub-population, only by adjusting the corresponding α_k's.

The apparent amplitude A^*_ω and phase ϕ^*_ω (at frequency ω) of an EEG signal are those which are obtained by performing a time-frequency decomposition of the signal. For the population model (Equation 5.1), one can obtain the apparent amplitude and phase by passing V through a band-pass quadrature filter tuned at frequency ω. If the filter is sufficiently narrow, the components

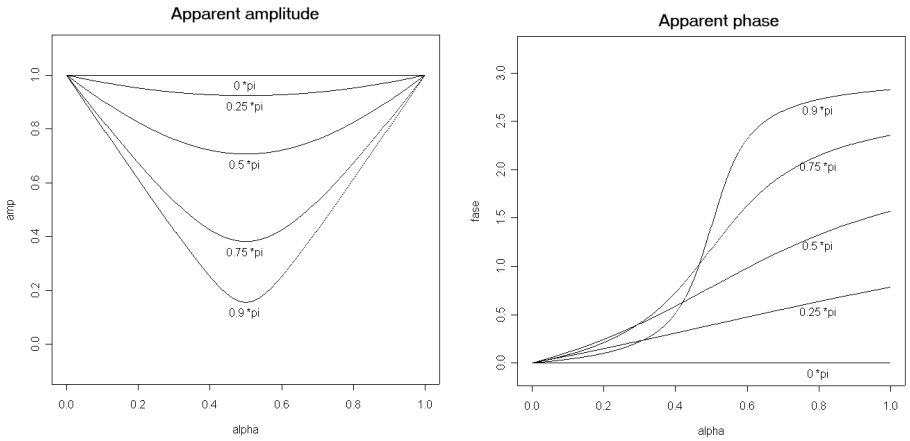

Figure 5.1: Apparent amplitude and phase versus underlying phase difference $\phi_1 - \phi_2$ and proportion α of oscillators with phase ϕ_1 for a 2-population model.

of V with $\omega_k \neq \omega$ will be attenuated; therefore, the complex filtered signal S can be approximated by:

$$S_\omega(t) = \sum_{k:\omega_k=\omega} \alpha_k e^{i(\omega t+\phi_k)}, \tag{5.2}$$

Since $S_\omega(t) = A^*_\omega(t)\exp[i\Phi^*_\omega(t)]$, where $\Phi^*_\omega(t) = \omega t + \phi^*_\omega(t)$ is the argument of the signal, it is possible to cancel the frequency component $e^{i\omega t}$ in the previous expressions to obtain:

$$A^*_\omega(t)\exp\left[i\phi^*_\omega(t)\right] = \sum_{k:\omega_k=\omega} \alpha_k \exp\left[i\phi_k\right]. \tag{5.3}$$

In other words, the apparent amplitude and phase are those of the resultant of the sum of vectors $\alpha_k \exp[i\phi_k]$, $k : \omega_k = \omega$ in the complex plane. Particularly, for two sub-populations ($k = 1, 2,\ \alpha = \alpha_1 = 1 - \alpha_2$), we have that

$$(A^*_\omega)^2 = a^2 + b^2, \tag{5.4}$$
$$\tan\phi^*_\omega = b/a, \tag{5.5}$$

with

$$a = \alpha\cos\phi_1 + (1-\alpha)\cos\phi_2, \tag{5.6}$$
$$b = \alpha\sin\phi_1 + (1-\alpha)\sin\phi_2. \tag{5.7}$$

Figure 5.1 shows (for two sub-populations) how the apparent amplitude and phase vary with respect to the phase difference $(\phi_1 - \phi_2)$ and proportion α.

Note that according to this model, a decrease of amplitude may be caused by a local resynchronization process where a group of neurons change their phase resulting in a more uniform proportion of sub-populations. Also, according to this, variations in the apparent phase may be related either to variations in the phase of some sub-populations (lack of local synchronization), or to changes in the size coefficients (which may be considered as local resynchronization processes). With this in mind, one could consider the local phase constancy (as defined by Equation 4.4) as a measure of local synchrony.

5.3 Zero-phase synchrony

With the population model one can explain why the apparent phase difference between two synchronized distant regions can be zero, in spite of the fact that there may be a significant transmission delay: with two sub-populations one can model a unidirectional coupling between two distant cortical areas, in the sense that a sub-population in one area drives a sub-population in the other area with a certain phase lag δ. For a bidirectional coupling we just add a reciprocal connection, with the same phase lag. Figure 5.2 shows a schematic of two populations in bidirectional coupling. If all sub-populations have approximately the same size (i.e. $\alpha = 0.5$), then the apparent amplitude and phase for each electrode would be given by

$$A_1^* \exp[i\phi_1^*] = 2\cos\left(\frac{\phi_1 - \phi_2}{2}\right) \exp\left[i\frac{\phi_1 + \phi_2}{2}\right], \tag{5.8}$$

$$A_2^* \exp[i\phi_2^*] = 2\cos\left(\frac{\phi_1 - \phi_2 - 2\delta}{2}\right) \exp\left[i\frac{\phi_1 + \phi_2}{2}\right]. \tag{5.9}$$

So that $\phi_1^* - \phi_2^* \approx 0$, except in the case where

$$\frac{\phi_1 - \phi_2 + 3\pi}{2} < \delta < \frac{\phi_1 - \phi_2 + \pi}{2}, \tag{5.10}$$

in which case $\phi_1^* - \phi_2^* \approx \pi$, which is in accordance with David and Friston's neural mass model [2003].

5.4 Nodal points

In all the real EEG datasets we have analyzed, one can observe sites that show, in a specific time-frequency window, a significant increment of synchrony with a large group of electrodes. These sites act as characteristic nodes of a particular network, hence we call them *nodal points*. It is common, although counter-intuitive, that the group of electrodes synchronized to a nodal point show a lack of synchrony, often observed as desynchronization, among themselves. One

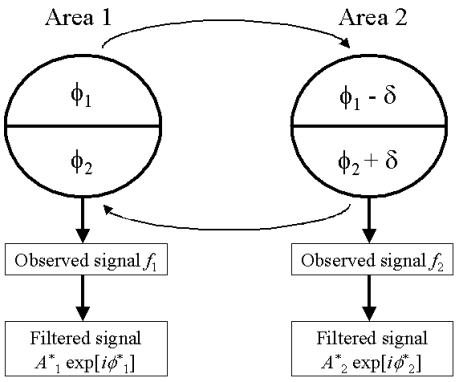

Figure 5.2: Bidirectional coupling between two areas with two sub-populations each. If the sub-populations are all the same size, the apparent phase difference $\phi_1^* - \phi_2^*$ will be either 0 or π.

illustrative example of this phenomenon can be seen in the alpha band (8-12 Hz) in Figures 3.6 and 3.7, where occipital leads (electrodes T5, T6, O1, O2, and Oz) show an increase of synchrony with most of the sites, and at the same time, frontal and central leads show a synchrony decrease among them.

Let us consider three electrodes: e_1 shows an increase in synchrony with both e_2 and e_3. One would expect e_2 and e_3 to be also coupled, but this does not always happen. In fact, sometimes e_2 and e_3 show a decrease in synchrony. The answer, in terms of the population model, is that synchronization occurs between sub-populations (as shown in the previous section) by resynchronization processes which affect the sub-population sizes (the α_k coefficients), and are reflected in changes in the apparent phase which the MPD and CPPD measures can detect. A simple example of this model (for three electrodes) is shown in Figure 5.3: an increase in synchrony between e_1 and e_2 (i.e.- an increase of $\alpha_{1,1}$ and $\alpha_{2,1}$) may result in a decrease of synchrony between e_2 and e_3 since the sum of sub-population sizes must remain constant for each electrode. Of course, with a larger number of sub-populations, more complex synchronization patterns can be simulated.

On the other hand, we have observed that the relative increase in synchrony with a nodal point is usually correlated with a significant power decrease in the nodal point itself. To study this in detail, we define a site e as k-nodal at time t and frequency ω if it shows significant increase in synchronization with at least k different sites. Figures 5.4a and 5.4b show, respectively, all 15-nodal sites for the Figures experiment, and the corresponding TFT map of significant power changes. In this example, one can clearly see that most of the nodal sites suffer a power decrease.

To confirm this, one can estimate the proportion of nodal sites in which

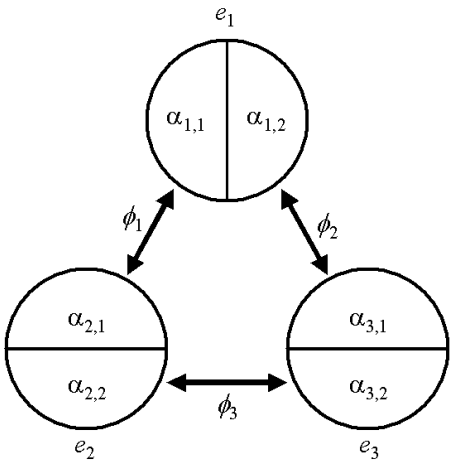

Figure 5.3: Population model for three inter-coupled electrodes. The phases ϕ_i represent the apparent phase of the sub-populations involved in each bidirectional coupling.

an amplitude decrease is observed: let N_k be the number of k-nodal points in the TFT space and A_k^- the number of k-nodal points that also show a power decrease, then the conditional probability of significant power decrease given that a site is k-nodal can be estimated by $P_k^- = A_k^-/N_k$. One may similarly estimate the probability of amplitude increment P_k^+. These probabilities are shown in Figure 5.5, where it is clear that P_k^- increases with the number of couplings k.

This behavior may also be simulated with the population model: suppose the population covered by the nodal point is divided into various sub-populations, each one of which is coupled with a different site (see Figure 5.6a). If the sites to which the nodal point is connected are not in synchrony, the underlying sub-population phases may assumed to be fairly different. In other words, the underlying phases $\{\phi^j\}$ will show high dispersion, which will be reflected as a low apparent amplitude $A^*_{\omega e}$ (Equation 5.3). Figure 5.6b shows a synthetic example which simulates a nodal point placed at O2. The particular model for each signal VS_e is given by

$$VS_e(t) = \sum_{k=1}^{N_k} \alpha_{e,k} \cos(\omega t + \phi_k) + \epsilon_e(t), \qquad \epsilon_e(t) \sim \mathcal{N}(0, \sigma_\epsilon) \tag{5.11}$$

with $N_k = N_e$, $\omega = 10$ Hz (for this example), $\sigma_\epsilon = 0.02$, and underlying phases $\phi_k \sim \mathcal{U}(-\pi, \pi), k = 1, \ldots, N_k$. In the pre-stimulus segment, neurons under site e oscillate predominantly with phase ϕ_e, thus there is little synchronous activity. This may be accomplished by assigning $\alpha_{e,e}$ a higher value than $\alpha_{e,k}, k \neq e$ for

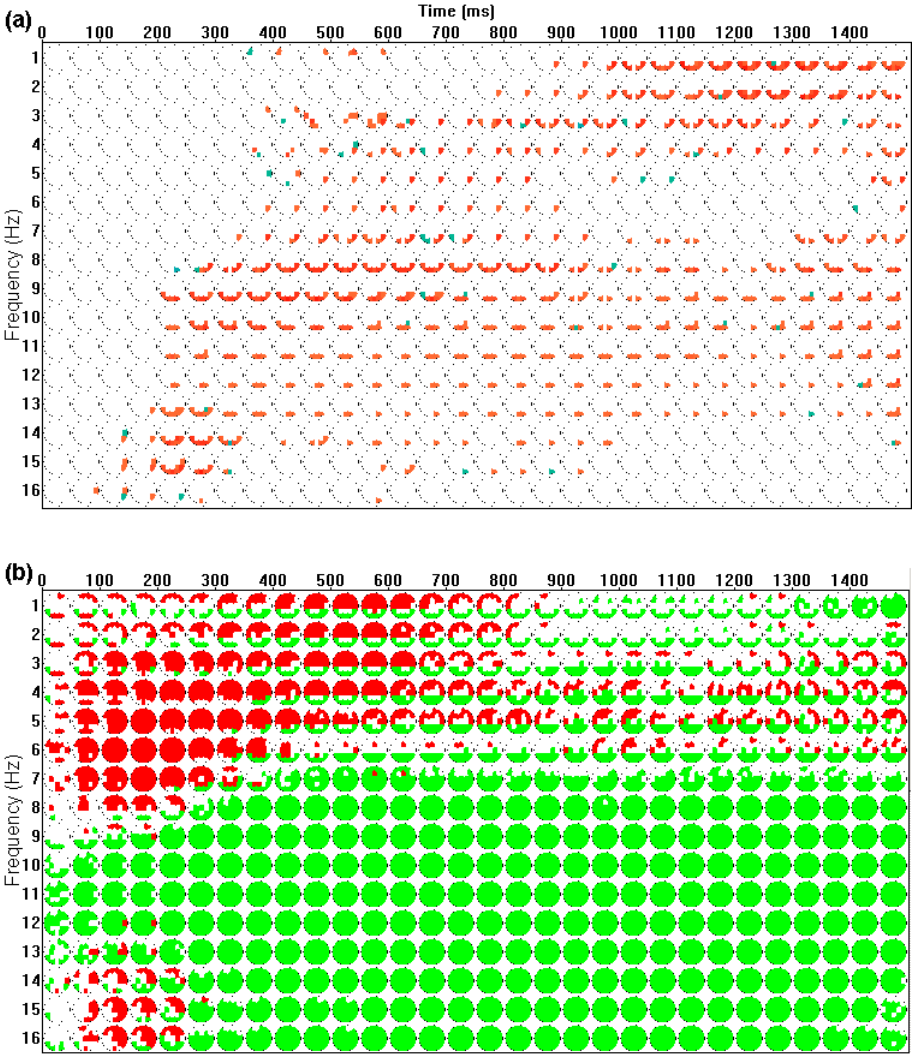

Figure 5.4: **(a)** TFT map of 15-nodal points (i.e., sites which increase their synchrony with at least 15 other sites) for the Figures experiment. **(b)** TFT map of significant amplitude changes (red = increase, green = decrease).

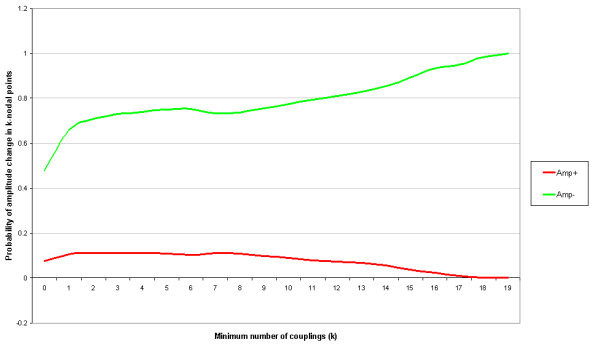

Figure 5.5: Conditional probabilities of amplitude increment (red) and decrease (green) in k-nodal points, for the Figures experiment.

each $e = 1, \ldots, N_e$. Specifically, we have that

$$\alpha_{e,k} = \begin{cases} |\eta_{e,k}|, \eta_{e,k} \sim \mathcal{N}(0, \sigma) & \text{if } k \neq e, \\ 1 - \sum_{k \neq e} \alpha_{e,k} & \text{if } k = e. \end{cases} \tag{5.12}$$

with $\sigma = 0.01$ for this particular example.

In the post-stimulus we model site e_{nod} as a nodal point by increasing the proportion of sub-populations with phases $\phi_k, k \neq e_{\text{nod}}$ (at the expense of a lower $\alpha_{e_{\text{nod}},e_{\text{nod}}}$). This will also cause a drop in the nodal site's amplitude, just as expected. The $\alpha_{e_{\text{nod}},k}$'s in our example are almost uniformly distributed:

$$\alpha_{e_{\text{nod}},k} = \begin{cases} |\frac{1}{N_e} + \eta'_{e_{\text{nod}},k}|, \eta'_{e_{\text{nod}},k} \sim \mathcal{N}(0, \sigma) & \text{if } k \neq e_{\text{nod}}, \\ 1 - \sum_{k \neq 1} \alpha_{e_{\text{nod}},k} & \text{if } k = e_{\text{nod}}. \end{cases} \tag{5.13}$$

Additionally, we have modeled a synchrony decrease among all non-nodal sites by halving the variance of the α_{ek}'s in Equation (5.12) (only for non-nodal sites in the post-stimulus segment). This can be seen as a resynchronization process where half the neurons of each sub-population k under site e change their phase from ϕ_k to ϕ_e, which results in a decrease in synchrony with site k.

Amplitude decreases in nodal points have also been observed in three other experiments (Words and Sternberg - see Appendix A). Two more experiments (Letters) show a different behavior: there is a high probability of observing a power increases in nodal points. In this case, however, the sites in synchrony with the nodal point show significant coupling between them, suggesting a low dispersion of the subjacent phases, which may account for the increase in amplitude.

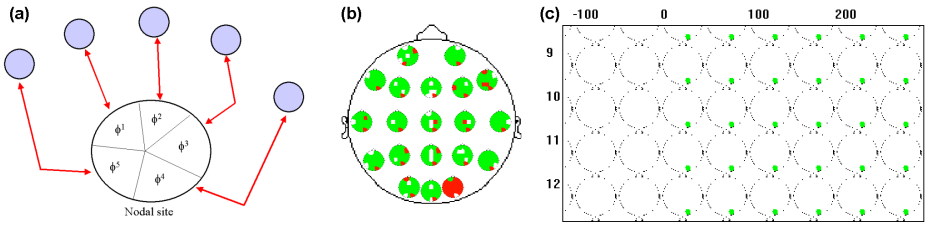

Figure 5.6: **(a)** Population model applied to a nodal point: each sub-population under the nodal site is coupled with a different site (shown in blue). The blue sites show no interaction between themselves thus the phases $\{\phi^j\}$ may be different enough to originate a drop in the nodal point's apparent amplitude. **(b)** Synchrony pattern obtained in the alpha band (post-stimulus segment) for the synthetic example of a nodal point (generated with the population model - see text for details). **(c)** TFT map of significant power changes from -100 to 300 ms (0 ms being the time of stimulus onset) for the synthetic nodal-point example: a clear power drop in the nodal site can be observed.

Chapter 6

Results and conclusions

6.1 Software application

The methodology described in the previous chapters has been implemented in a software program, which performs the time-frequency decomposition of the raw EEG signals, estimates any of the measures previously described, and then performs a significance test using either Bayesian classification or thresholded p-values. The results can be presented in various types of display: multitoposcopes, TFT maps, and partitioned synchrony maps.

The following measures are currently implemented in the program:

- Changes in log-power with respect to the pre-stimulus (typical induced-power analysis)
- MPD
- CPPD (with threshold ϵ given in radians or ms)
- PLS
- STPLS (with window size w given in ms)
- Coherence (with window size w given in ms)
- LPC (with window size w given in ms)
- Local phase constancy across trials (LPCT)

Additionally, the program can perform the same type of studies on evoked potentials (e.g., potentials averaged across trials), with the exception of those measures which require multiple trials to be estimated (CPPD and PLS).

For any of the synchrony measures, the program can display the following maps:

- TFT Histograms of significant synchrony increases (or decreases) for each electrode
- TF Histograms of significant synchrony increases (or decreases) across all the surface
- Multitoposcopic display of synchrony patterns for a given time and frequency
- Partitioned synchrony maps with a representative multitoposcope for each TF region
- TF maps of class labels for a given electrode pair (an example can be seen in Figure 6.6)

A full manual of the program can be found in Appendix C.

6.2 Analysis of real EEG data

We have used the software application in collaboration with Dr. Thalía Harmony and Ph.D. student Berta González to study the dynamic synchrony changes in the Figures and Letters experiments. In this section we summarize our findings. All synchrony histograms and TFT maps for each experiment can be found in Appendix A.

6.2.1 Results from the Figures experiment

Recall that we are measuring the changes in synchrony during a particular state in relation to a previous condition that is considered neutral. These changes can be observed, concurrently, at all frequencies. For example, there is an increase in synchrony in the delta band (1-3 Hz) in the anterior regions between 450 and 600 ms; after this time, the synchrony increased mainly in the posterior regions (Figure A.2). In the first 150 ms in the delta and theta bands there was a decrease in synchrony in occipital regions (Figure A.3); this may be due to the activation of the visual areas produced by the stimuli. In the theta range (4-7 Hz), the most generalized change in synchronization in the EEG after 300 ms is the phase-lock increase between posterior and anterior regions, which can be observed in the partitioned map (Figure A.1). This pattern may be related to activation of Working Memory (WM), which is the process of actively maintaining a representation of information for a brief period of time so that it is available for use. Attention, decoding, perception and maintenance in memory are processes that involve the activation of WM. According to [Ungerleider et al., 1998], visual working memory involves the concerted activity of a distributed neural system, including posterior areas in visual cortex and anterior areas in prefrontal cortex.

The increase in theta (4-7 Hz) power in frontal regions (Figure A.4) has been also related to activation of WM [Gevins et al., 1997; Rhom et al., 2001]. Anterior regions are also involved in encoding [Klimesch, 2004] and maintaining the information in memory [Barde and Thompson-Schill, 2002]. Sarnthein et al. [1998] report an increase in coherence in the theta range between prefrontal and posterior electrodes during retention of a string of characters.

In the alpha range (8-12 Hz), simultaneously with the increase in synchrony in the occipital regions, there was a decrease in synchrony between all regions except the occipital leads and the frontal regions on which synchrony increases. This increase may be indicating the projection loops between attentional control system in prefrontal cortex and activated meaning representations in semantic memory in posterior regions. The decrease in synchrony in the alpha band between 100 and 1500 ms coincides with the phenomena described in the 1930s by Adrian and Mathews of amplitude decrease (which can also be observed in Figure A.4) or "desynchronization" and it has been related to attention [Gevins et al., 1997; Rhom et al., 2001; Klimesch, 1999].

Another change that was observed is the increase of synchrony in occipital regions in the beta band. In humans, in intracranial recordings that limited regions of extrastriate visual areas, separated by several centimeters, EEG activity in the beta range (15-25 Hz) became synchronized in an oscillatory mode during the rehearsal of an object in visual short-term memory. According to Tallon-Baudry et al. [2001] these findings confirm experimentally the hypothesis of a functional role of synchronized oscillatory activity in the coordination of distributed neural activity in humans, and support Hebb's [1949] popular concept of short-term memory maintenance by reentrant activity within the activated network.

In the gamma band (30-40 Hz), an increase of synchrony in the interval 200-300 ms was observed. This has been related to visual search and perception [Tallon-Baudry et al., 1997]. The increase in synchronization during the interval of 600 to 800 ms around 34 Hz might be related to preparation of the motor response.

6.2.2 Results from the Letters experiment

Synchronization during the Go and NoGo conditions from the Letters experiment was studied using signals from projections to cortical sources (see Section 3.7) instead of raw potentials.

In the Go/NoGo paradigm, overall brain activity seems to involve several sub-processes, namely discrimination between the stimuli, activation of working memory, a decision whether or not to move, and initiation or inhibition of the motor actions [Shibata et al., 1999]. Anticipatory processes are also involved [Basar-Eroglu et al., 1992].

In the analysis of power changes (Figures A.35 for the Go condition, and A.47 for the NoGo condition) we observed an increase of delta activity from 100

to 450 ms in the Go condition and from 0-500 ms in the NoGo condition. This has been related to decision making and matching processes [Basar-Eroglu and Demiralp, 2001] and to inhibition of non-related task processes during attention to internal processes [Harmony et al., 1986]. In the Letters experiment, the delta power increase could be related to any of the processes mentioned.

Increases in theta (4-7 Hz) amplitude and synchronization have been mainly related to activation of Working Memory (WM) [Gevins et al., 1997, 1998; Rhom et al., 2001; Harmony et al., 2001, 2004]. The WM model of Baddeley [1999] distinguishes central executive functions from storage functions related to two slave systems, the phonological loop, maintaining verbal information, and a visuospatial sketch pad, responsible for the transient storage of visuospatial information. Frontal lobes have been considered the neural substrate of the central executive processes, but growing evidence has shown that executive functions do not only rely on prefrontal cortical activation but also on a distributed frontoparietal network [Sauseng et al., 2005; Osaka et al., 2004]. Visual WM involves the concerted activity of a distributed neural system which included posterior areas in the visual cortex and anterior areas in the prefrontal cortex [Ungerleider et al., 1998].

Theta activity in anterior regions is also involved in encoding [Klimesch, 1999] and in maintaining the information in memory [Barde and Thompson-Schill, 2002]. Sarnthein et al. [1998] found an increase in theta coherence between prefrontal and posterior electrodes during retention of a string of characters. These authors also reported that gamma (19-32 Hz) synchrony increased during both perception and retention intervals, suggesting that locally driven synchrony might take place in the gamma range, whereas inter-areal interactions, as in WM, appear at lower frequencies.

Shack et al. [2005] suggested that theta activity reflects central executive functions whereas upper alpha may be important for the reactivation of long-term memory codes in short-term memory.

Mazaheri and Picton [2005] reported that induced theta activity might be related to memory or attentional processes. An increase in theta power at around 300 ms after stimuli occurred with episodic memory [Klimesch, 1999]. Recognition memory, which is likely to be involved in target discrimination, has also been found to be related to synchronization of theta rhythm [Burgess and Gruzelier, 1997]. Frontal theta activity has been observed during focused attention and in association with response processing [Gevins et al., 1997]. Bastiaansen and Hagoort [2003] report that experimental evidence largely supports the hypothesis that theta activity plays a functional role in cell assembly formation, a process that may constitute the neural basis of memory formation and retrieval.

Simultaneously with the increase in power in the theta range (0-400 ms), there is also an increase of power in the alpha band in the first 200 ms, and later, a decrease in alpha power (200-1000 ms) in the Go condition. In the NoGo

condition there was a generalized increase in theta power from 0 to 500 ms, and at 8 and 9 Hz, a power increase from 0 to 450 ms. Power decrease in the Go condition was observed after 250 ms in frequencies from 8 to 29 Hz and in the NoGo condition from 600 to 900 ms in the theta range and from 50 to 300 ms at 18-20 Hz.

The decrease in power in the alpha band between 100 and 1000 ms coincides with the "desynchronization" phenomenon described in the 1930s by Adrian and Mathews, which has been related to attention [Gevins et al., 1997; Rhom et al, 2001; Klimesch, 1999]. Alpha suppression in response to effortful mental tasks has been interpreted as the marker of activation of functionally involved brain areas. However, this response is inconsistent and depends on the specific cognitive strategies employed by the subjects [Kolev et al., 2001]. In our experiment, in the Go condition, alpha power increased in the first 200 ms, and decreased afterwards. However in the NoGo condition, alpha power increased for a prolonged period up to 500 ms. Decreases in power in low alpha band in the NoGo condition were observed only from 600 to 850 ms. According to Kolev et al. [2001], enhanced early alpha oscillation to task stimuli within 0-250 ms may be related to task stimulus evaluation.

Alpha synchronization increased in both conditions (Figures A.33 for the Go condition, and A.45 for the NoGo condition), mainly between posterior regions and the remaining cortex. The right lateral occipital region is selectively activated during visuospatial attention [Foxe et al., 2003], which may explain our results showing this particular increase in synchronization between occipital (more in the right hemisphere) regions and the rest of the cortex.

In this experiment, one can also observe an increase of synchrony in occipital regions in the beta band. Transient long-range phase synchronization in the beta band has been related to the fronto-parietal-temporal attentional network during an attentional task [Croxson et al., 2005]. Beta synchronization across the hemispheres was reported during the perception of objects [Von Stein and Sarnthein, 1999] and during mental calculation [Mizuhara et al., 2005]. This is also supported by the report by Tallon-Baudry et al. [2001] about the role of synchronized activity in the coordination of distributed neural activity, as described in the previous section.

Oscillatory synchronization has been suggested to characterize a neuronal assembly coding for an object. Neurons distributed across different brain areas would synchronize their firing in the gamma band [Singer, 1993], supporting the idea of a role of gamma band synchrony in feature binding [Tallon Baudry et al., 1997]. In the gamma band an increase of synchrony in the first 200 ms was observed only in the Go condition. According to Karacas et al. [2001] the early high gamma response (¿75 Hz) that occurred as a phase-locked activity in the early time window of 0-150 ms is obtained regardless of stimulus type and task demands; thus, it is not a perceptual phenomenon, but instead it represents sensory processes. However, this was not confirmed with our experiments, since no gamma change was observed in the NoGo condition, although we did not

explore such high frequencies. This increase in synchrony in the gamma band has been related to visual search and perception [Tallon Baudry et al., 1997]. The increase in synchronization during the interval of 700 to 1300 ms in the gamma band might be related to preparation of the motor response, since it was observed only in the Go condition, which confirms other studies [Salenius et al., 1996].

Multitoposcopes corresponding to a partition by bands of frequency and time intervals gives a clear picture of the changes produced in synchrony (Figures A.32 and A.44, for Go and NoGo, respectively). In the Go condition, delta synchrony increases during the whole post-stimulus interval, whereas in the NoGo condition the synchrony increases only from 0-900 ms. In the theta band very similar changes were observed for both conditions, with a large increase in synchrony in the interval 300-600 ms. In the low beta band increases in synchrony were observed in all intervals in the NoGo condition. In the high beta and in the high gamma bands, very similar changes were observed in both conditions. However in the low gamma band (30-40 Hz), opposite effects were observed in the two conditions: increases in synchrony in all intervals in the Go condition but only decreases in synchrony in the NoGo condition. These great differences may be due to preparation and motor activation during the Go condition [Salenius et al., 1996].

6.3 Conclusions

During the performance of different cognitive and sensorial brain tasks, several neuronal assemblies, which are not necessarily contiguous, may become active simultaneously and generate synchronized macroscopic oscillations. This dynamic reorganization produces complex patterns of synchronization and desynchronization between different cortical areas, with respect to a previous state considered as neutral. Based on this, significative increases in synchrony measurements between leads indicate that the cortical areas corresponding to those leads may be integrating a network related to a particular psychophysiological process. Thus, EEG synchrony measures between regions may yield important information about the dynamics of cell assemblies.

In this work, we have favored instantaneous in-phase (i.e.- zero phase difference) synchrony measures, such as MPD and CPPD, for various reasons: first, there is extensive evidence showing that, in most cases, the phase difference between two areas changes towards zero when the areas are coupled; this evidence includes studies with real EEG data by Friston et al. [1997] and Rodriguez et al. [1999], theoretical results from mathematical models (David and Friston's neural mass model, and our population model) where bidirectional couplings result in synchrony with a phase-lag of zero or π, reports by David and Friston [2003b] and Varela et al. [2001] arguing that the proportion of bidirectional connections in the brain is very high, and the high correlation between MPD,

CPPD, and PLS (which is not an in-phase measure). Second, instantaneous measures do not seem to be as affected by local phase dispersion as those measures which are estimated within a time window (e.g., coherence and STPLS). And third, our tests have shown that MPD and CPPD are not affected by volume conduction more than any of the other measures discussed here. On the other hand, coherence and STPLS may be more robust to latency jitter, and thus provide better detection of induced responses, but unfortunately, in this case, local phase dispersion may seriously mask the long-range synchronous activity.

Even if MPD and CPPD have clear advantages, other steps involved in the detection of phase synchronization must be performed with care. The first problem which concerns us is the possible spurious couplings introduced by volume conduction. Although various techniques have been proposed to reduce the volume conduction effects, none of them has proven to be sufficiently reliable. Estimation of the Surface Laplacian (SL), favored by Nunez [1995, 1997, 1999], requires a high electrode density, and thus cannot be applied to most of our datasets. On the other hand, solutions based on the inverse problem depend, in great measure, on constraints which are relatively arbitrary. In any case, one should use these solutions to complement the results obtained with raw potentials, and not as the only representation of the EEG dynamics.

Another problem is related to the time-frequency decomposition techniques used to extract the phase of the signals. As we have shown, the more popular Gabor filters and wavelets may not be adequate for low frequency analysis (delta and theta bands). In general, one must design the filters such that they have no significant response to negative frequencies. Sinusoidal quadrature filters appear to be a reliable solution to this problem.

To determine which synchrony values are significantly different from the pre-stimulus state, we subtract the baseline average, and then use a Bayesian classification method with a Markov Random Field model instead of the typical thresholded p-values. The Bayesian approach permits one to impose regularity constraints that control the granularity of the results. This is particularly important for instantaneous measures, which produce results that are relatively noisier than those measures estimated across a time window (e.g., coherence), and also has the advantage that the resulting class field is relatively robust to a wide range of values for the constraint parameter, whereas the p-value threshold, in the other case, has to be adequately chosen for each particular experiment.

Once the class label field for a particular synchrony measure has been computed, it is possible to present the results in various ways. A multitoposcopic display is useful to show the synchrony pattern corresponding to a specific time and frequency point or window. One can then plot a partitioned synchrony map by drawing a series of multitoposcopes that would cover the time segments and frequency bands of interest. On the other hand, TFT synchrony histograms can be used to display the number of connections (with respect to the baseline) in which each electrode participates: regions with high inter-connectivity may

represent integrated networks which are related to specific cognitive or sensorial processes. All these visualization tools allow the neuroscientist to explore the changes of electroencephalographic states during the course of a cognitive experiment with great detail. The analysis of the Figures and Letters experiments provide an illustrative example of the usefulness of these techniques.

Finally, a population model for the apparent phase and amplitude observed at an electrode can successfully simulate the synchrony patterns observed in real EEG data, including some interesting phenomena such as the existence and behavior of nodal points.

6.4 Future work

Here we discuss a few recent ideas that we intend to develop in the future. Additionally, and in conjunction with the UNAM Neurobiology Institute (INB-UNAM), we expect to analyze various EEG experiments, which may require specific changes in the methodology.

6.4.1 Evoked potentials and synchronization

EEG activity is typically characterized as evoked (i.e., phase-locked to the stimulus), or induced (time-locked but not necessarily phase-locked). In practice, evoked activity is revealed by averaging the EEG signals across trials, and performing a spectral analysis on the averaged signals: any activity which is not phase-locked to the stimulus will show a certain amount of phase dispersion across trials, which will result in destructive interference when averaging, leaving only the evoked responses untouched. On the other hand, induced activity is obtained by performing the spectral power analysis for each trial, and then averaging the power across trials.

One of the mechanisms which are thought to generate evoked responses is the *partial phase-resetting* [Makeig et al., 2002; Penny et al., 2002], in which a particular combination of the network's current state and the network's input cause the system's phase to be reset to a certain value. Figure 6.1 shows the average potentials obtained from the GO condition of the Letters experiment. In this example, one can see that some of the peaks (e.g., around 150 ms and 300 ms) are observed in several sites, suggesting a relation between evoked activity and long-range in-phase and anti-phase synchronization. However, even if the phase-resetting mechanism may affect various networks located in different cortical areas, one could argue that due to the variations in the transmission delay of the reset signal, the affected areas will not necessarily be in perfect synchrony after their phase has been reset. In other words, if an evoked potential is observed in various areas, one may not necessarily observe in-phase synchronization between those areas. The opposite is also plausible: two cortical areas may increase their synchrony (with respect to the baseline), but if there is no

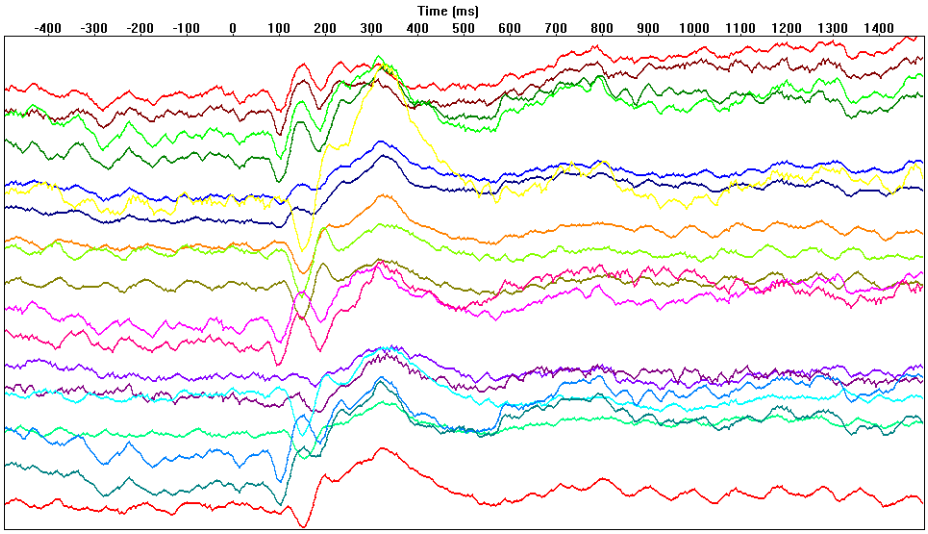

Figure 6.1: Evoked potentials for the GO condition of the Letters experiment: for each electrode, the average signal (estimated across trials) is displayed.

event-related phase-resetting mechanism affecting the subjacent phase of those areas in each trial, an evoked potential may not be generated. In any case, a measure of phase constancy across trials may yield some additional information about this type of mechanism.

Other authors (e.g., [Freeman and Schneider, 1982]) argue that evoked potentials originate, in fact, from an event-related activation of neural assemblies distinct from background dynamics [Fell et al., 2004]; in other words, the stimulus causes certain neural assemblies to generate a particular waveform, which may be reinforced by averaging across trials.

It is also possible that a mixture of both mechanisms is present in the development of evoked activity [Penny et al., 2002; Fell et al., 2004]. It would be interesting, then, to study the evoked potentials, along with other measures (e.g., induced power, synchronization, and phase constancy across trials), and try to distinguish between all possible cases. As an example of how this problem can be approached, we present in Figure 6.2 the following maps for the Letters experiment (GO condition):

(a) TFT map of changes in evoked power (EP); that is, the power of the average signals

(b) TFT map of changes in local phase constancy across trials (LPCT)

(c) SIH of evoked MPD (eMPD) synchrony (i.e., MPD between pairs of average signals)

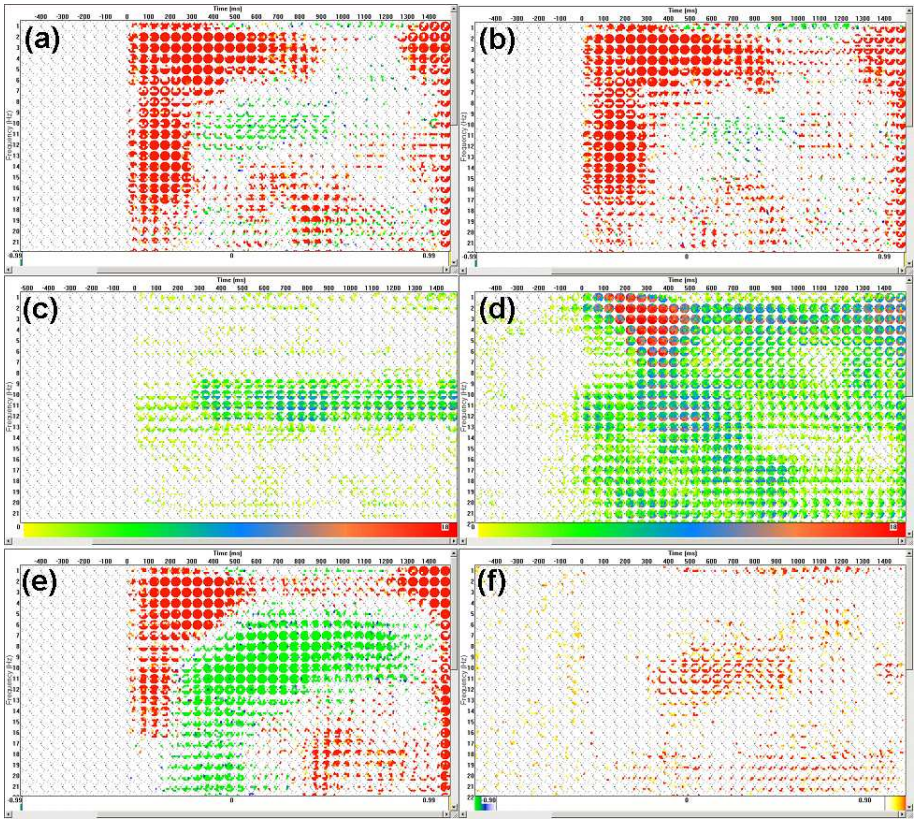

Figure 6.2: **(a)** TFT map of significant EP changes (red = increase, green = decrease). **(b)** TFT map of significant LPCT changes (red = increase, green = decrease). **(c)** TFT histogram of evoked MPD increases. **(d)** TFT histogram of induced MPD increases. **(e)** TFT map of total power changes with respect to the pre-stimulus. **(f)** TFT map of total power minus evoked power.

(d) SIH of induced MPD (iMPD) synchrony

(e) TFT map of induced power changes with respect to the pre-stimulus

(f) TFT map of induced power minus evoked power (significance values)

Note that the first two maps (evoked power and phase constancy across trials) are very similar. This supports to some extent the theory of phase-resetting. On the other hand, there is also some correlation between evoked and induced power; in fact, the difference between induced and evoked power appears to be significant in only a few places, particularly after 350 ms (Figure 6.2f). This suggest that a certain evoked waveform develops right after the stimulus and is consistent in each trial. As time goes by, it is less likely that

event-related processes (particularly, the cognitive ones) will be phase-locked to the stimulus, and thus the differences between induced and evoked activity become more significant.

In Figure 6.1, one can see that, at around 150 ms, there is evoked activity in the alpha/low-beta range at many electrodes, which appears to be in synchrony (both in-phase and anti-phase); however, the iMPD map (Figure 6.2d) does not show such synchrony. If one closely inspects the peaks of the raw evoked potentials, one can see small differences in latency between electrodes, supporting the idea that the phase-resetting mechanisms do not affect all areas at the exact same time. It is also interesting that there is very little evoked synchrony (Figure 6.2c), compared to induced synchrony (possibly also due to the peak latency variations between leads).

Between 300 and 600 ms one can also see (in the iMPD map) a certain amount of synchronous activity in the alpha range ($\sim$ 12 Hz), which does not coincide with an increase in EP.

This suggests three different cases of correlation between EP changes and induced synchrony changes between two areas, that may be of interest:

1. The two areas show an increase in evoked power and their synchronization also increases.

2. The two areas show an increase in evoked power but not in synchronization.

3. The two areas show an increase in synchronization but not in evoked power.

Each of these cases may represent a different type of process. In order to obtain a detailed view of the coincidences between EP increases and induced synchrony increases, one can plot the coincidence map C given by

$$C_{\omega,e_1,e_2,t} = \begin{cases} 1 & \text{if } c^{\text{ep}}_{\omega,e_1,t} = c^{\text{ep}}_{\omega,e_2,t} = 1 \text{ and } c^{\mu}_{\omega,e_1,e_2,t} = 1 \\ 2 & \text{if } c^{\text{ep}}_{\omega,e_1,t} = c^{\text{ep}}_{\omega,e_2,t} = 1 \text{ and } c^{\mu}_{\omega,e_1,e_2,t} \neq 1 \\ 3 & \text{if } (c^{\text{ep}}_{\omega,e_1,t} \neq 1 \text{ or } c^{\text{ep}}_{\omega,e_2,t} \neq 1) \text{ and } c^{\mu}_{\omega,e_1,e_2,t} = 1 \\ 0 & \text{otherwise,} \end{cases} \tag{6.1}$$

where c^{ep} is the class field corresponding to EP changes, and c^{μ} is the class field corresponding to synchrony measure μ. Figure 6.3 shows the coincidence map for the GO condition using MPD as synchrony measure.

Each of the three cases described above can be explained with the population model and a phase-resetting mechanism: consider the model for two bidirectionally coupled areas, and suppose that the subjacent phase of each

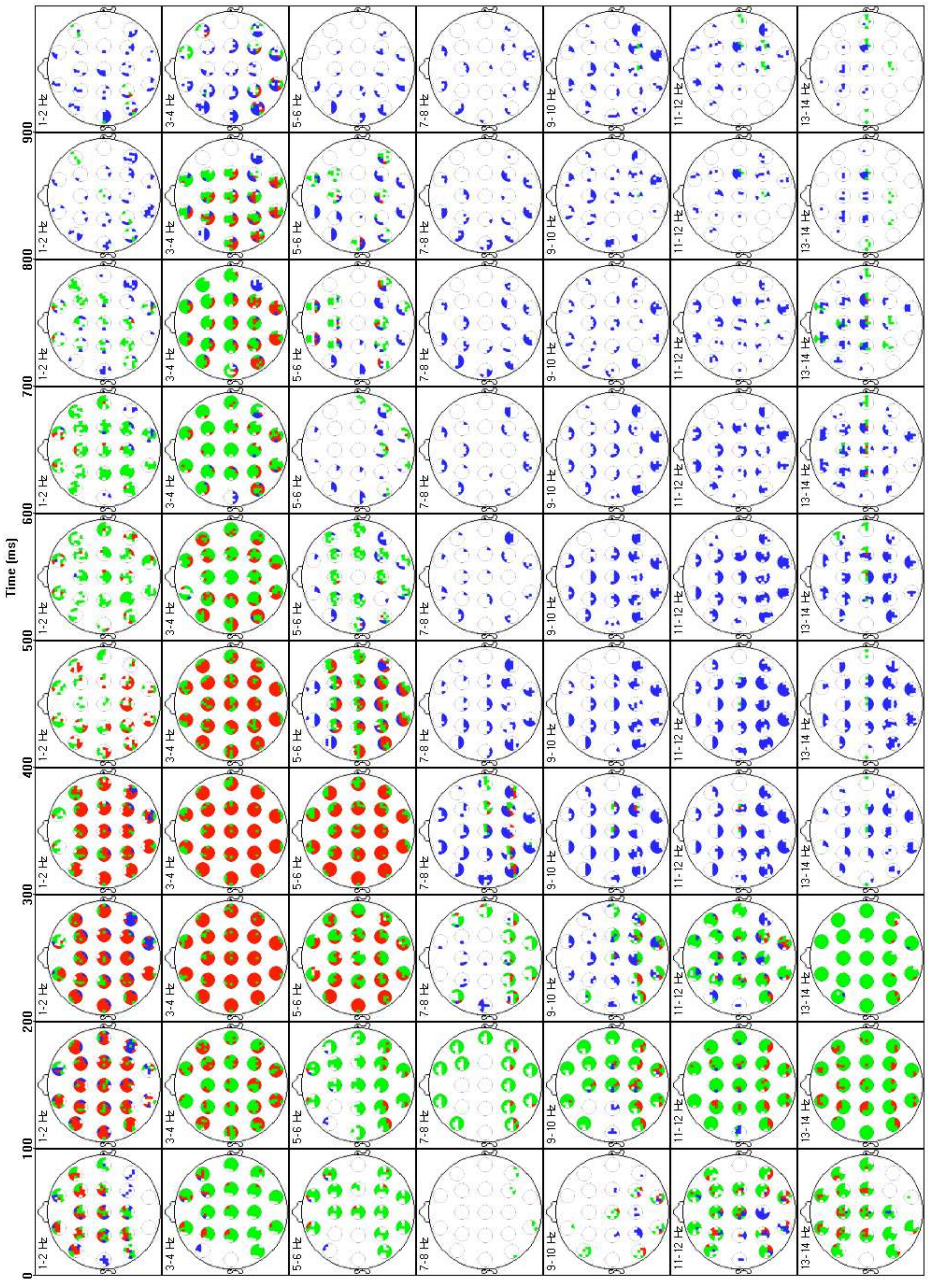

Figure 6.3: Partitioned map of coincidences between EP increases and iMPD increases: red means an increase in EP (at both electrodes) and an increase in iMPD ($C = 1$), green means increase in EP but not in iMPD ($C = 2$), and blue means increase in iMPD but not in EP ($C = 3$).

driving sub-population can be reset with an external signal r (see Figure 6.4a). Note that r is delayed at each area i by λ_i, thus the subjacent phases are not necessarily reset at the exact same time. On the other hand, the coupling parameter α is related with the sub-population sizes; for example, perfect in-phase synchrony is obtained with $\alpha = 0.5$ (i.e.- sub-populations of the same size).

If an event-related reset signal is sent to either (or both) areas, an evoked potential (i.e.- an increase in EP) will be observed, and depending on the difference $\lambda_1 - \lambda_2$, an increase in iMPD may also been observed (case $C = 1$) even if the true synchronization between the two areas has not changed. In this case, it is not possible to distinguish if an increase in iMPD (i.e., near zero apparent phase difference) is due to a true increase in synchronization, or due to a phase-resetting mechanism which acts upon both areas almost at the same time. On the other hand, if $\lambda_1 - \lambda_2$ is large enough, resetting the subjacent phases in both driving sub-populations will not result in spurious high synchrony (case $C = 2$).

If there is phase-resetting but no true coupling (Figure 6.4b), one will observe an increase in EP, and may or may not observe a (spurious) increase in iMPD (cases $C = 1$ and $C = 2$, respectively).

The last case ($C = 3$) is explained, according to the model in Figure 6.4c, where there is coupling but no phase-resetting. The change in iMPD may be caused simply by a change in the subjacent sub-population sizes (i.e.- a resynchronization process where more neurons become part of the sub-populations involved in the bidirectional coupling), such that α changes towards 0.5. The idea of neurons resynchronizing to a different sub-population is supported by studies by Haalman and Vaadia [1998], which show that when performing a computational task, neurons may quickly associate into a functional group while disassociating from concurrently activated groups.

David et al. [2006] have also studied the mechanisms which generate evoked and induced responses (in terms of power), from the viewpoint of their neural mass model [David et al., 2003]. According to them, there are two types of mechanisms: *dynamic mechanisms*, which consist of modulations of the neuronal input, and *structural mechanisms*, which correspond to changes in the system's causal structure (e.g., the model parameters). David et al. study how a mixture of these mechanisms is reflected as evoked and induced responses.

In our population model, the resetting function r is the system's input, thus one can consider the phase-resetting mechanism as a dynamic one. Furthermore, the resynchronization of neurons from one sub-population to another may be considered a structural mechanism. Our intention is to study in more depth these mechanisms, and their expression in terms of evoked power, induced power, and long-range phase synchronization.

6.4.2 Anti-phase synchrony

Earlier, we discussed the concept of anti-phase synchronization; that is, coupling with a phase difference of π radians. Both, David and Friston's neural mass

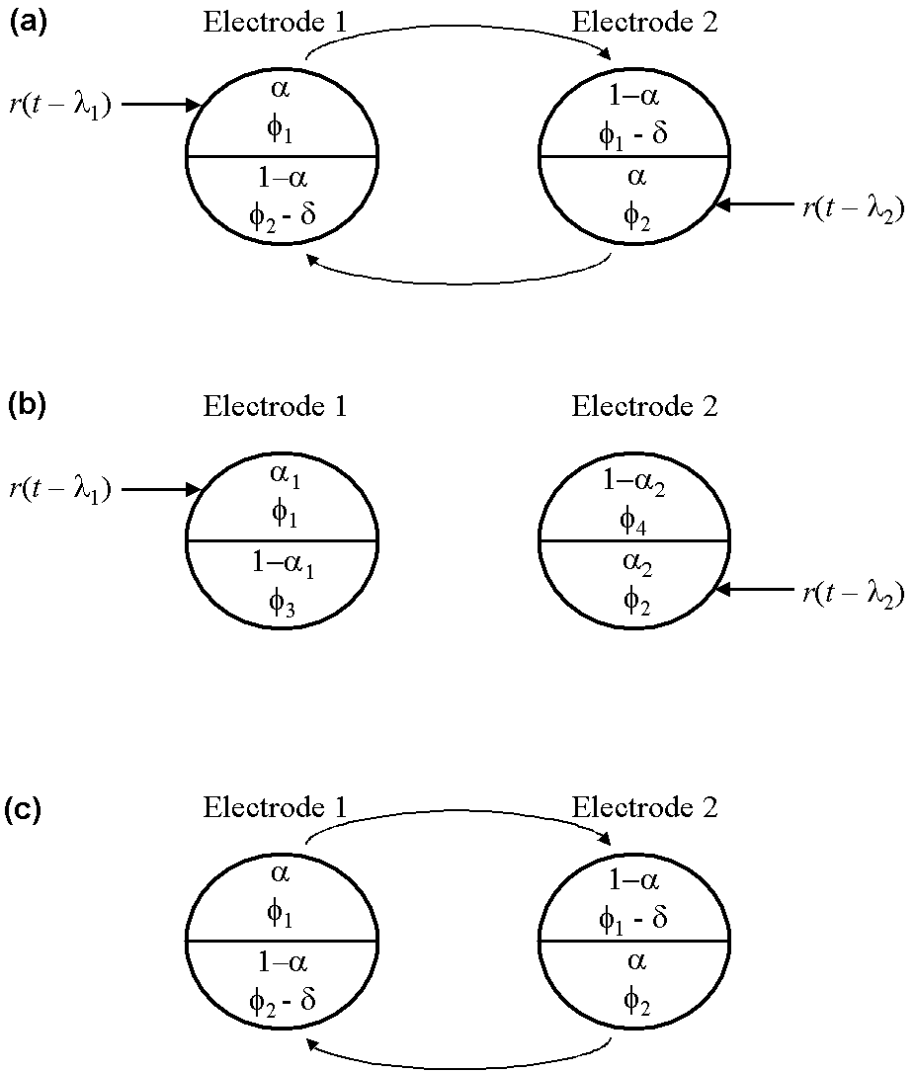

Figure 6.4: Population model for two bidirectionally coupled areas (with coupling parameter α), with a phase-resetting signal r affecting the driving subpopulations.

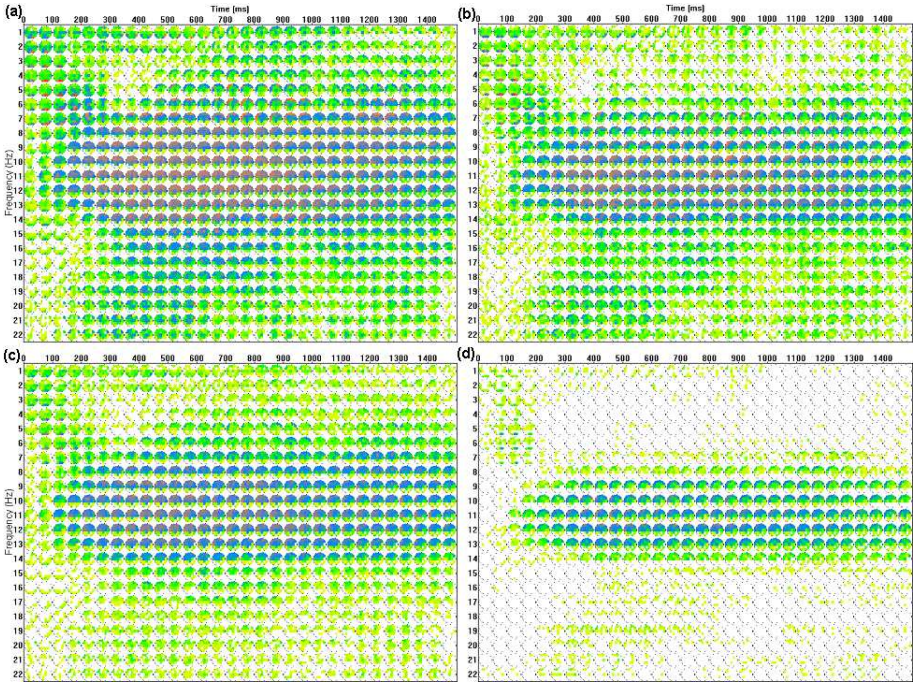

Figure 6.5: **(a)** SDH of CPPD for $\epsilon = \pi/5$ rad. **(b)** SIH of AP-CPPD for $\epsilon = \pi/5$ rad. **(c)** SDH of CPPD for $\epsilon = \pi/20$ rad. **(d)** SIH of AP-CPPD for $\epsilon = \pi/20$ rad.

model, and our population model, yield a phase difference of zero or π for two areas which are bidirectionally coupled. Moreover, as can be seen in Figure 6.1 (around 150 ms), when some electrodes show a positive evoked potential, others display a negative peak at approximately the same latency, suggesting the presence of anti-phase synchrony.

Therefore, it would be interesting to develop a method to detect true anti-phase couplings, and study its relation with in-phase synchrony and evoked potentials. As a first approach, an anti-phase CPPD (AP-CPPD) measure has already been proposed in Section 3.3.3 (Equation 3.7). The problem with this measure is that it is highly correlated (negatively) with the in-phase CPPD. This means that it is not easy to distinguish, with these measures, between increases in anti-phase synchrony and decreases in in-phase synchrony. One thing that helps is using small values for the threshold ϵ, at the expense of a more conservative criteria for synchrony (e.g., fewer significative changes with respect to the baseline).

An example of these measures is shown in Figure 6.5. Here we present the synchrony decrease histograms of the (in-phase) CPPD measure, and synchrony increase histograms of the anti-phase CPPD, for ϵ values of $\pi/5$ and $\pi/20$.

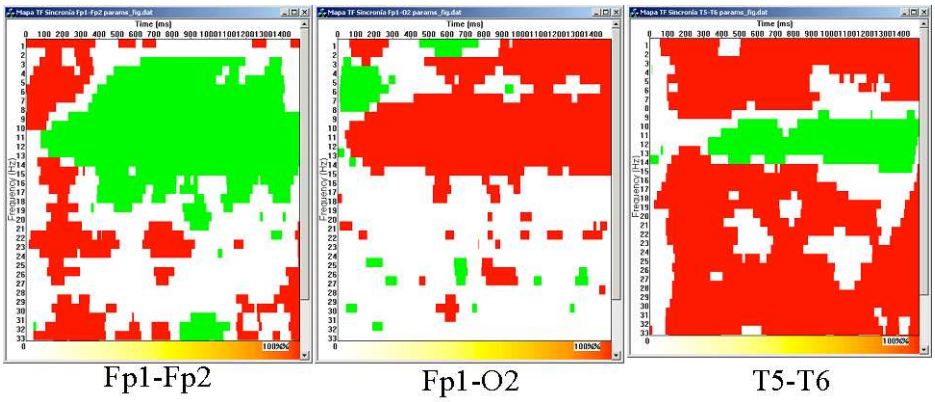

Figure 6.6: Time-Frequency maps of class label fields (red = increase, green = decrease) for the MPD measure, corresponding to electrode pairs Fp1-Fp2, Fp1-O2, and T5-T6 of the Figures experiment.

For larger ϵ values, the CPPD SDH and AP-CPPD SIH are relatively similar, whereas smaller thresholds seem to be more adequate to discern between the anti-phase synchronization and desynchronization.

6.4.3 Synchrony at multiple frequencies

Another interesting phenomenon is the ability of two electrodes to display in-phase synchronization at various frequencies, at the same time. To see this, one can plot the TF map of class labels for a particular pair of electrodes. Figure 6.6 shows a few examples of this behavior for pairs Fp1-Fp2, Fp1-O2, and T5-T6 of the Figures experiment. The case of T5-T6 is particularly interesting since there is an increase in synchronization in the delta and theta bands, a decrease in the alpha and low beta bands, and then another increase in the beta and gamma bands. This may be explained by the idea (already discussed in Section 5.1) that during certain tasks, neurons may become part of a functional group, while disassociating from other groups. If these functional groups generate macroscopic oscillations at different frequencies, then one may be able to see synchronization patterns which are multiplexed across a wide frequency range, such as those in Figure 6.6. It is possible, then, that in order to obtain a full picture of the synchronization pattern at a given time, one should integrate the information for all frequency bands in a single display.

Appendix A

Synchrony maps from additional experiments

In this appendix we present the resulting maps for each of the datasets described in Section 1.9. These maps have been computed using both raw potentials and projected signals (see Section 3.7). Here is a list of the corresponding figures.

- **Figures experiment**
  - A.1.- Partitioned synchrony map using raw potentials
  - A.2.- SIH of MPD using raw potentials
  - A.3.- SDH of MPD using raw potentials
  - A.4.- TFT map of power changes using raw potentials
  - A.5.- TFT map of LPC changes using raw potentials
  - A.6.- Correlation between measures using raw potentials
  - A.7.- Conditional probabilities of power change in nodal points using raw potentials
  - A.8.- Partitioned synchrony map using projected signals
  - A.9.- SIH of MPD using projected signals
  - A.10.- SDH of MPD using projected signals
  - A.11.- TFT map of power changes using projected signals
  - A.12.- TFT map of LPC changes using projected signals
- **Words experiment**
  - A.13.- Partitioned synchrony map using raw potentials
  - A.14.- SIH of MPD using raw potentials
  - A.15.- SDH of MPD using raw potentials

- A.16.- TFT map of power changes using raw potentials
- A.17.- TFT map of LPC changes using raw potentials
- A.18.- Correlation between measures using raw potentials
- A.19.- Conditional probabilities of power change in nodal points using raw potentials
- A.20.- Partitioned synchrony map using projected signals
- A.21.- SIH of MPD using projected signals
- A.22.- SDH of MPD using projected signals
- A.23.- TFT map of power changes using projected signals
- A.24.- TFT map of LPC changes using projected signals

- **Letters experiment (GO condition)**
  - A.25.- Partitioned synchrony map using raw potentials
  - A.26.- SIH of MPD using raw potentials
  - A.27.- SDH of MPD using raw potentials
  - A.28.- TFT map of power changes using raw potentials
  - A.29.- TFT map of LPC changes using raw potentials
  - A.30.- Correlation between measures using raw potentials
  - A.31.- Conditional probabilities of power change in nodal points using raw potentials
  - A.32.- Partitioned synchrony map using projected signals
  - A.33.- SIH of MPD using projected signals
  - A.34.- SDH of MPD using projected signals
  - A.35.- TFT map of power changes using projected signals
  - A.36.- TFT map of LPC changes using projected signals

- **Letters experiment (NO-GO condition)**
  - A.37.- Partitioned synchrony map using raw potentials
  - A.38.- SIH of MPD using raw potentials
  - A.39.- SDH of MPD using raw potentials
  - A.40.- TFT map of power changes using raw potentials
  - A.41.- TFT map of LPC changes using raw potentials
  - A.42.- Correlation between measures using raw potentials
  - A.43.- Conditional probabilities of power change in nodal points using raw potentials
  - A.44.- Partitioned synchrony map using projected signals
  - A.45.- SIH of MPD using projected signals

- A.46.- SDH of MPD using projected signals
- A.47.- TFT map of power changes using projected signals
- A.48.- TFT map of LPC changes using projected signals

- **3-digit Sternberg experiment**
  - A.49.- Partitioned synchrony map using raw potentials
  - A.50.- SIH of MPD using raw potentials
  - A.51.- SDH of MPD using raw potentials
  - A.52.- TFT map of power changes using raw potentials
  - A.53.- TFT map of LPC changes using raw potentials
  - A.54.- Correlation between measures using raw potentials
  - A.55.- Conditional probabilities of power change in nodal points using raw potentials
  - A.56.- Partitioned synchrony map using projected signals
  - A.57.- SIH of MPD using projected signals
  - A.58.- SDH of MPD using projected signals
  - A.59.- TFT map of power changes using projected signals
  - A.60.- TFT map of LPC changes using projected signals

- **5-digit Sternberg experiment**
  - A.61.- Partitioned synchrony map using raw potentials
  - A.62.- SIH of MPD using raw potentials
  - A.63.- SDH of MPD using raw potentials
  - A.64.- TFT map of power changes using raw potentials
  - A.65.- TFT map of LPC changes using raw potentials
  - A.66.- Correlation between measures using raw potentials
  - A.67.- Conditional probabilities of power change in nodal points using raw potentials
  - A.68.- Partitioned synchrony map using projected signals
  - A.69.- SIH of MPD using projected signals
  - A.70.- SDH of MPD using projected signals
  - A.71.- TFT map of power changes using projected signals
  - A.72.- TFT map of LPC changes using projected signals

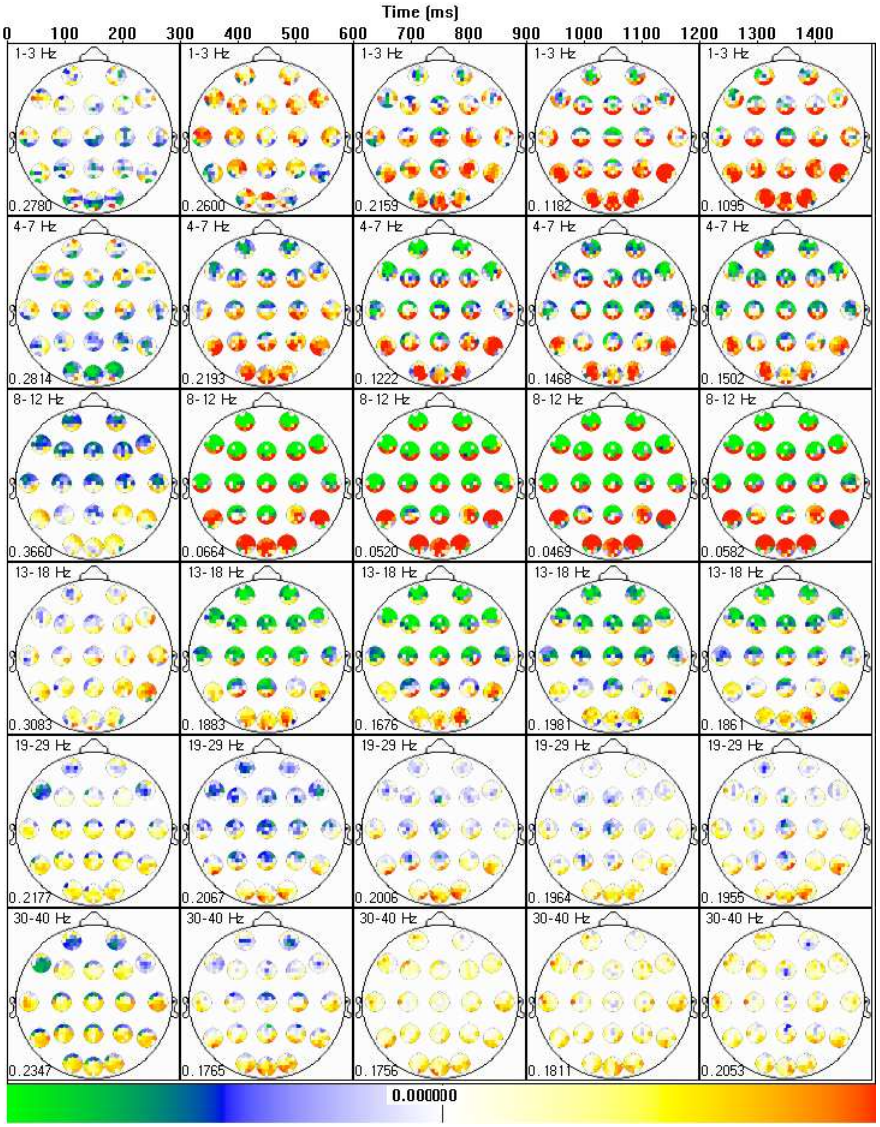

Figure A.1: Full automatic partition for the Figures experiment (raw potentials).

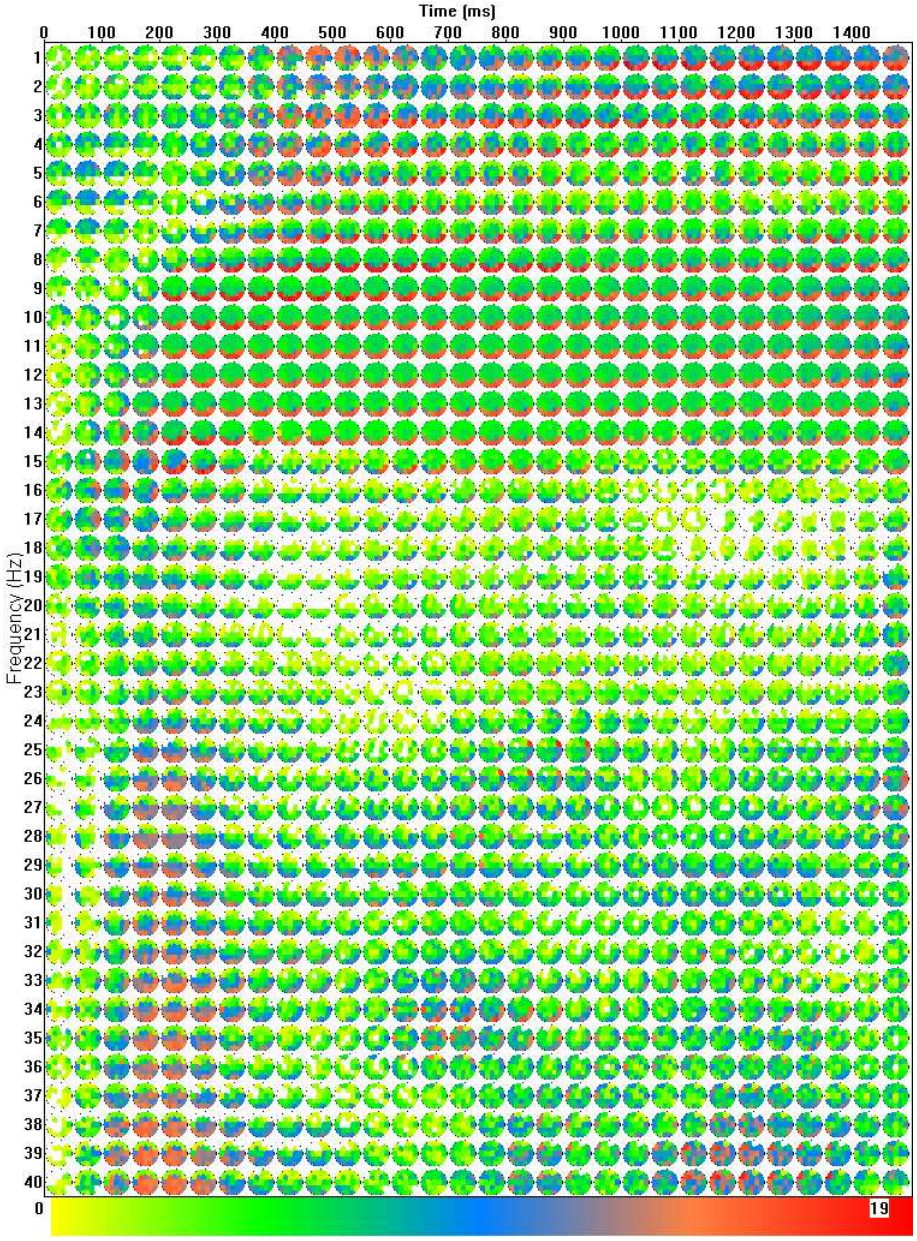

Figure A.2: Full synchrony increase histogram for the Figures experiment (raw potentials).

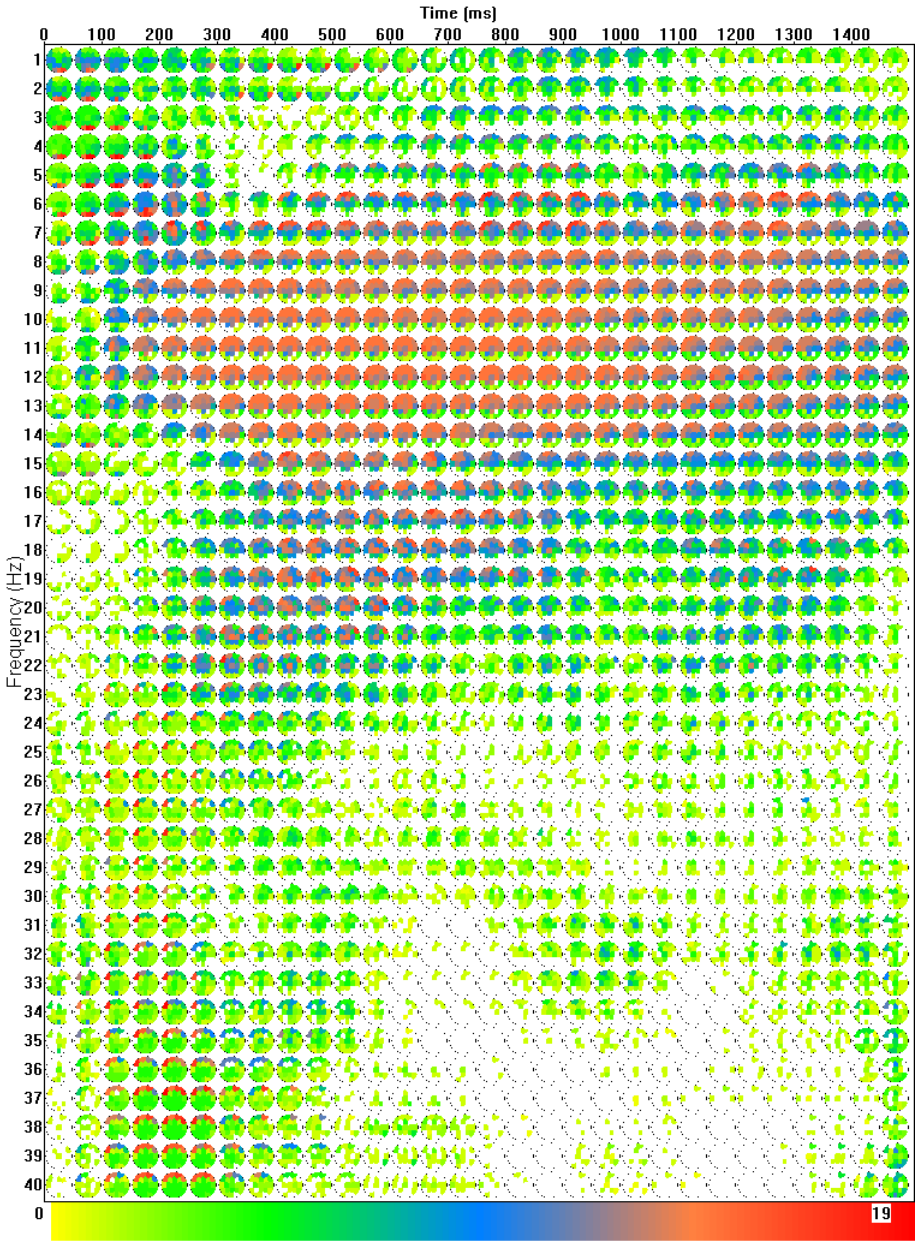

Figure A.3: Full synchrony decrease histogram for the Figures experiment (raw potentials).

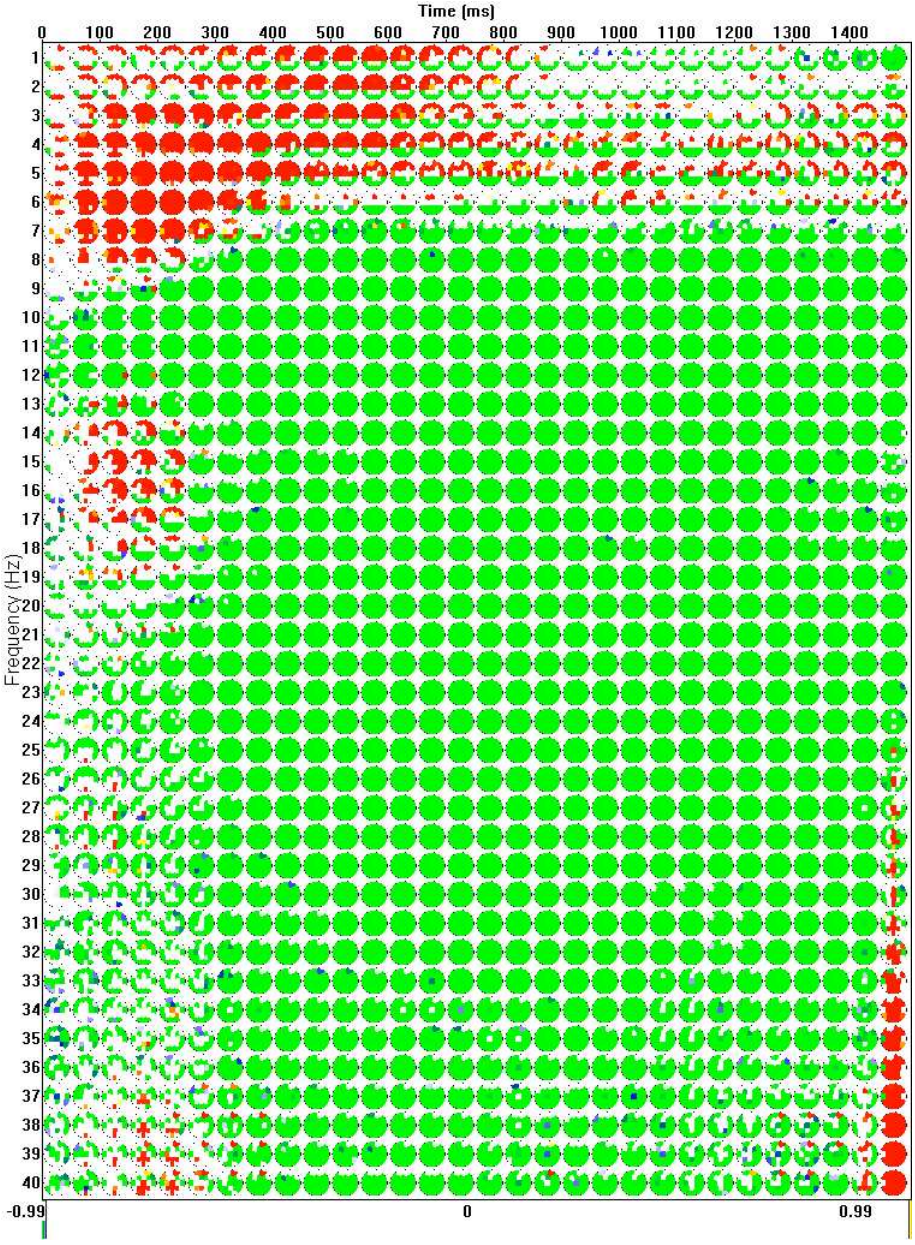

Figure A.4: Map of significant amplitude changes for the Figures experiment (raw potentials).

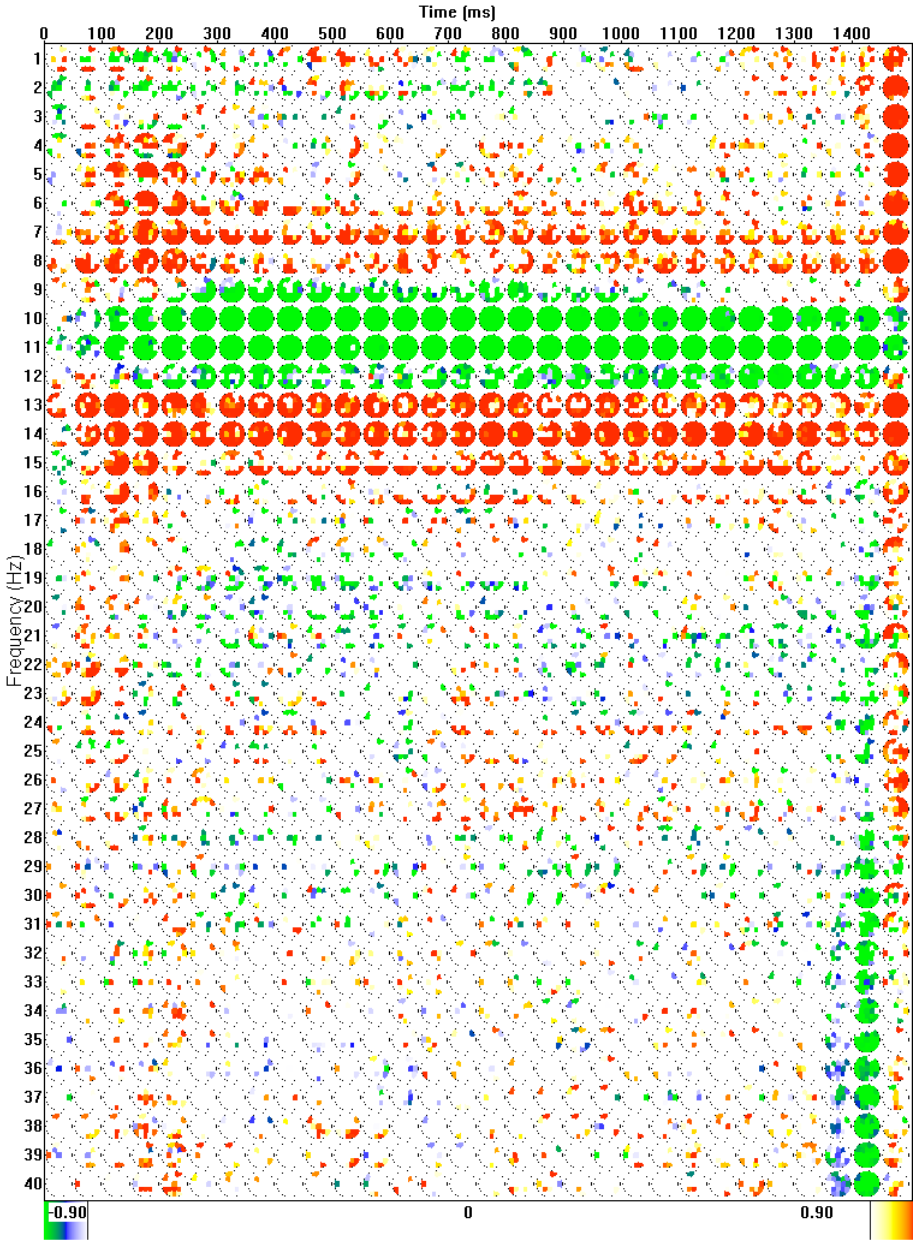

Figure A.5: Map of significant LPC changes for the Figures experiment ((raw potentials).

	MPD	CPPD	PLS	STPLS	Coherence
MPD	1	0.881	0.799	0.185	0.27
CPPD	0.881	1	0.689	0.15	0.227
PLS	0.799	0.689	1	0.278	0.363
STPLS	0.185	0.15	0.278	1	0.947
Coherence	0.27	0.227	0.363	0.947	1

	LPD
MPD	0.132
CPPD	0.094
PLS	0.168
STPLS	0.823
Coherence	0.78

Figure A.6: Correlation table of synchrony measures for the Figures experiment (raw potentials).

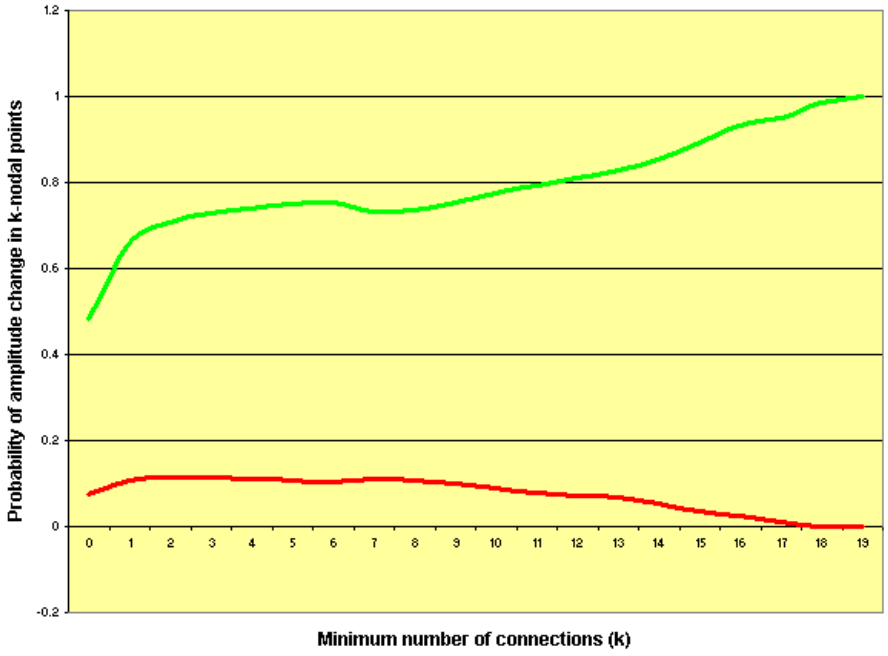

Figure A.7: Conditional probabilities of amplitude increase (red) and decrease (green) in nodal points for the Figures experiment (raw potentials).

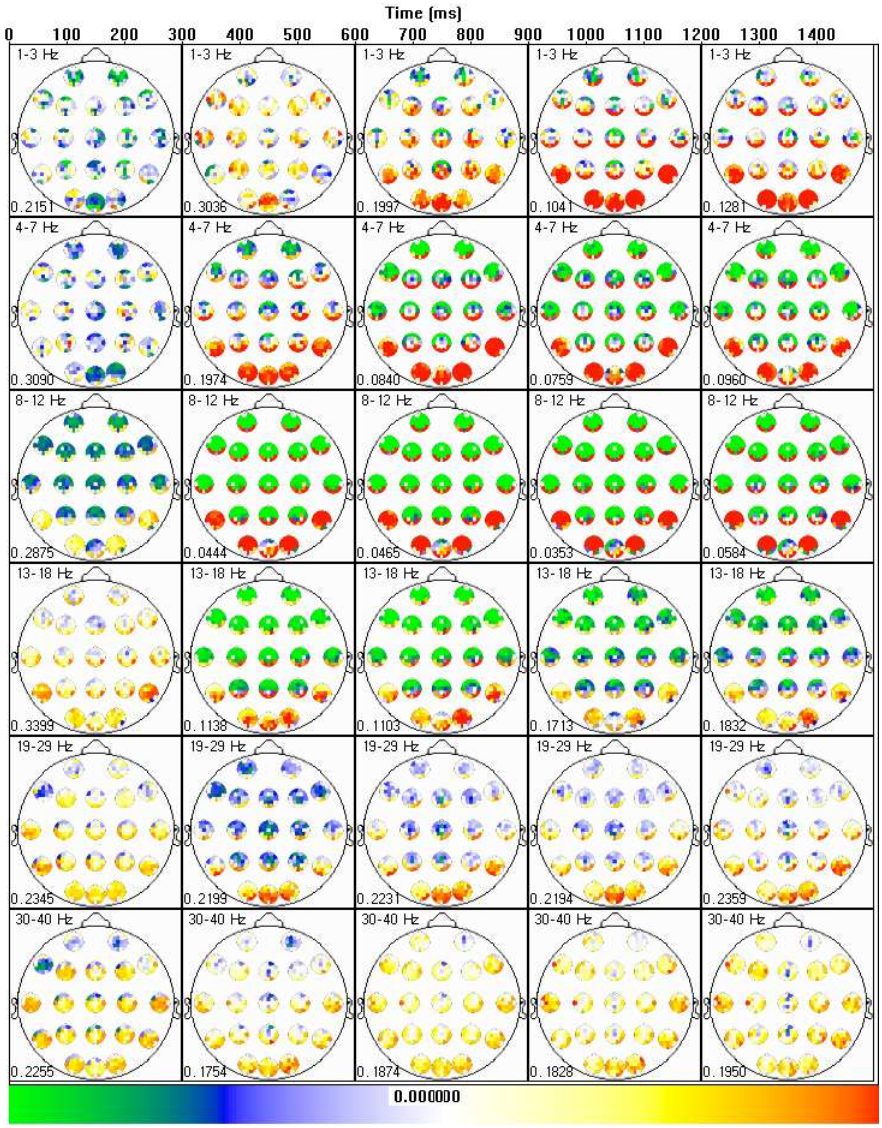

Figure A.8: Full automatic partition for the Figures experiment (projected signals).

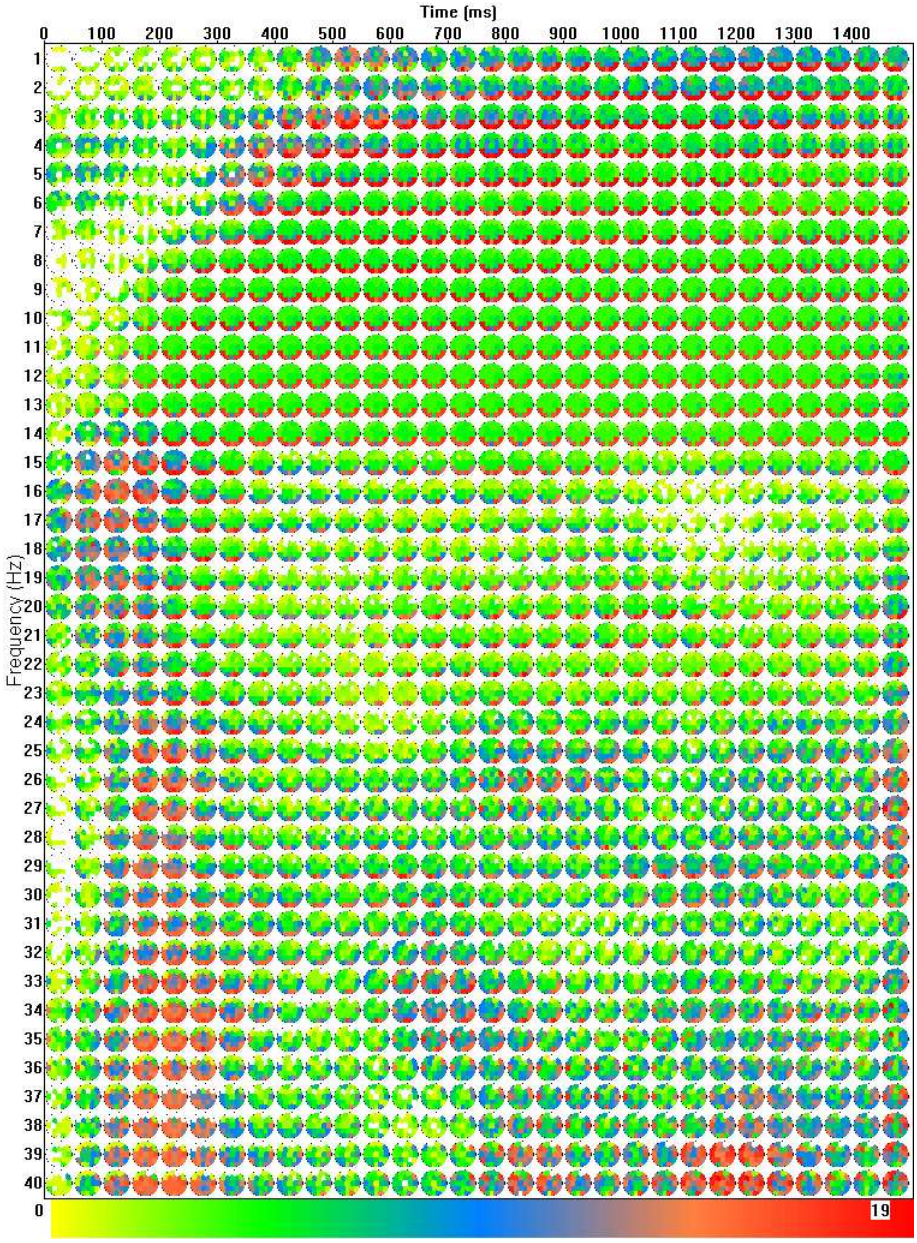

Figure A.9: Full synchrony increase histogram for the Figures experiment (projected signals).

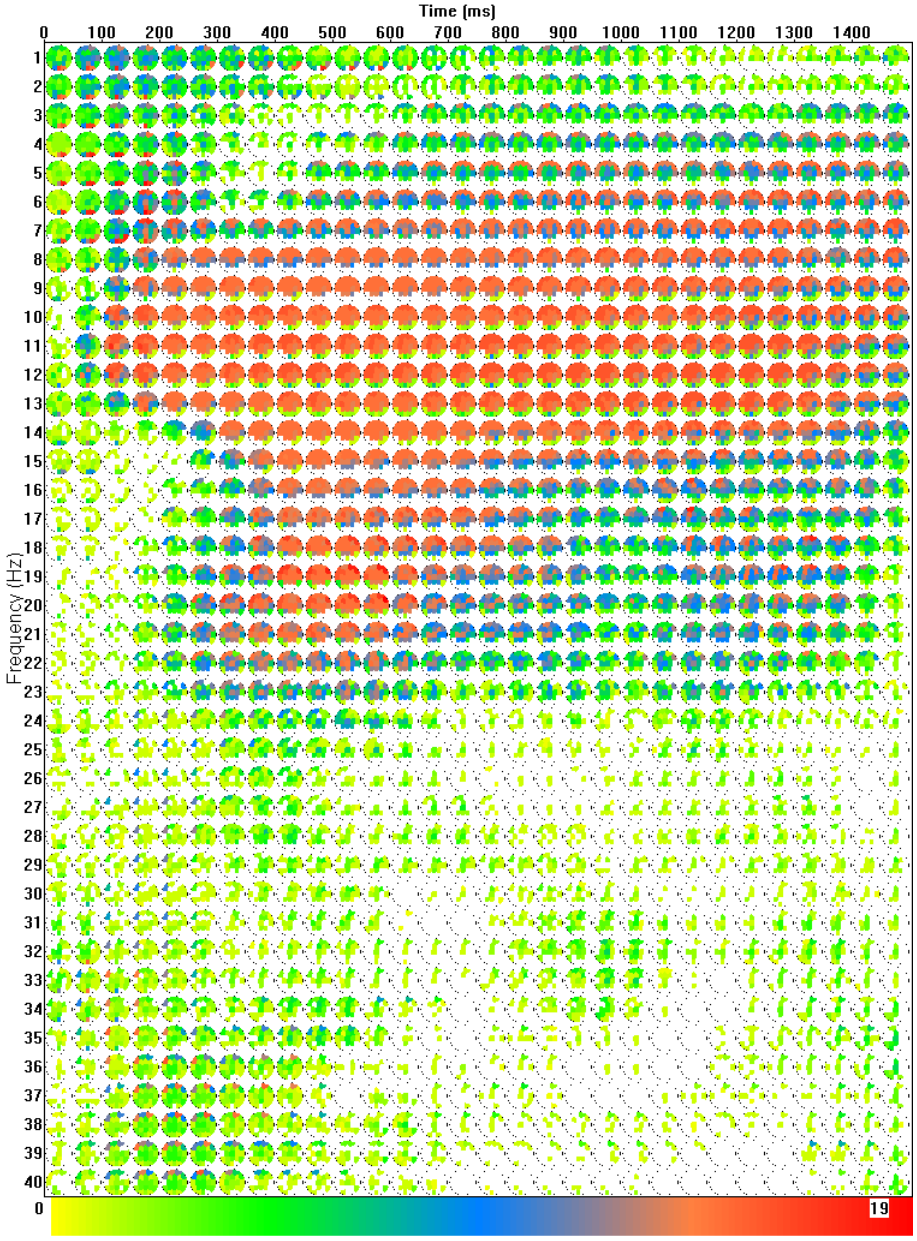

Figure A.10: Full synchrony decrease histogram for the Figures experiment (projected signals).

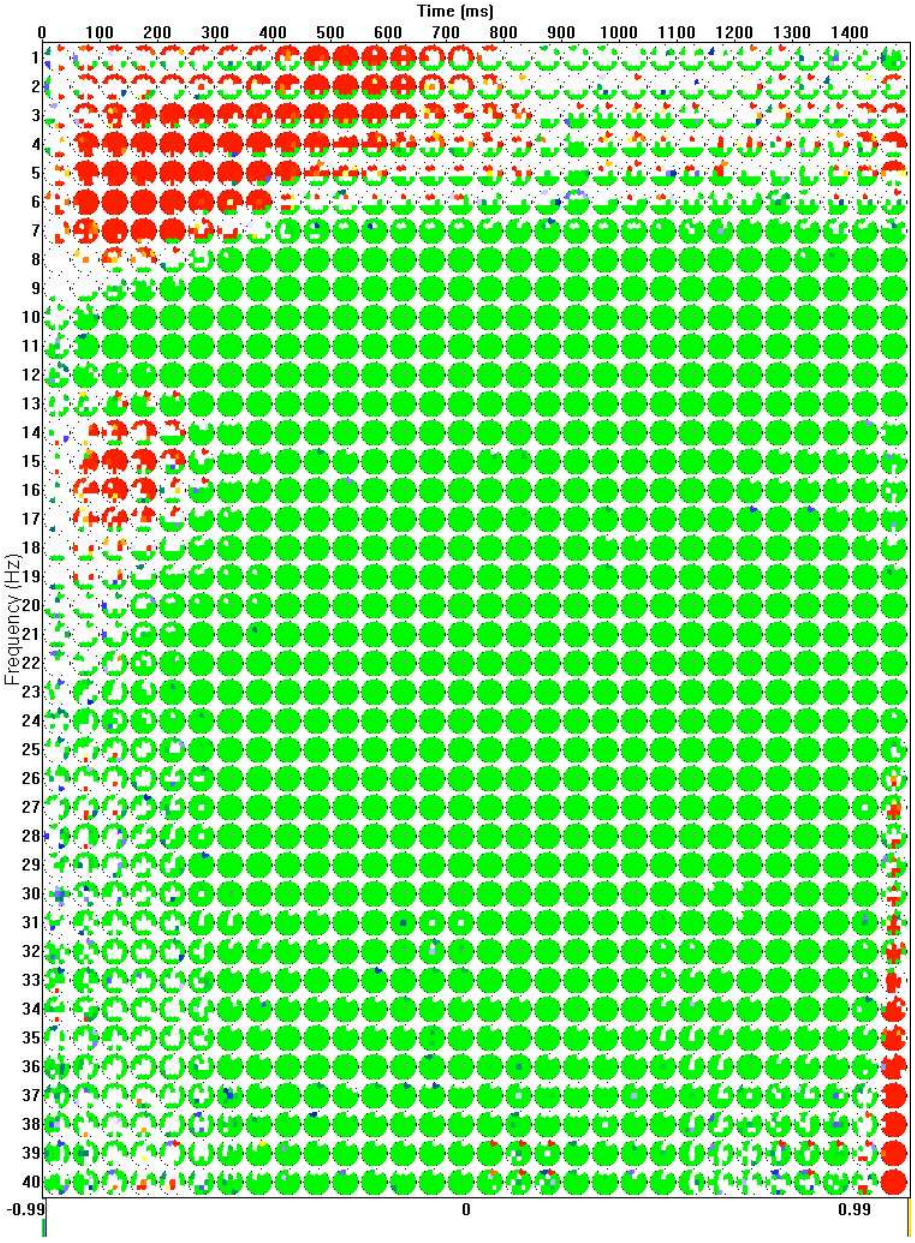

Figure A.11: Map of significant amplitude changes for the Figures experiment (projected signals).

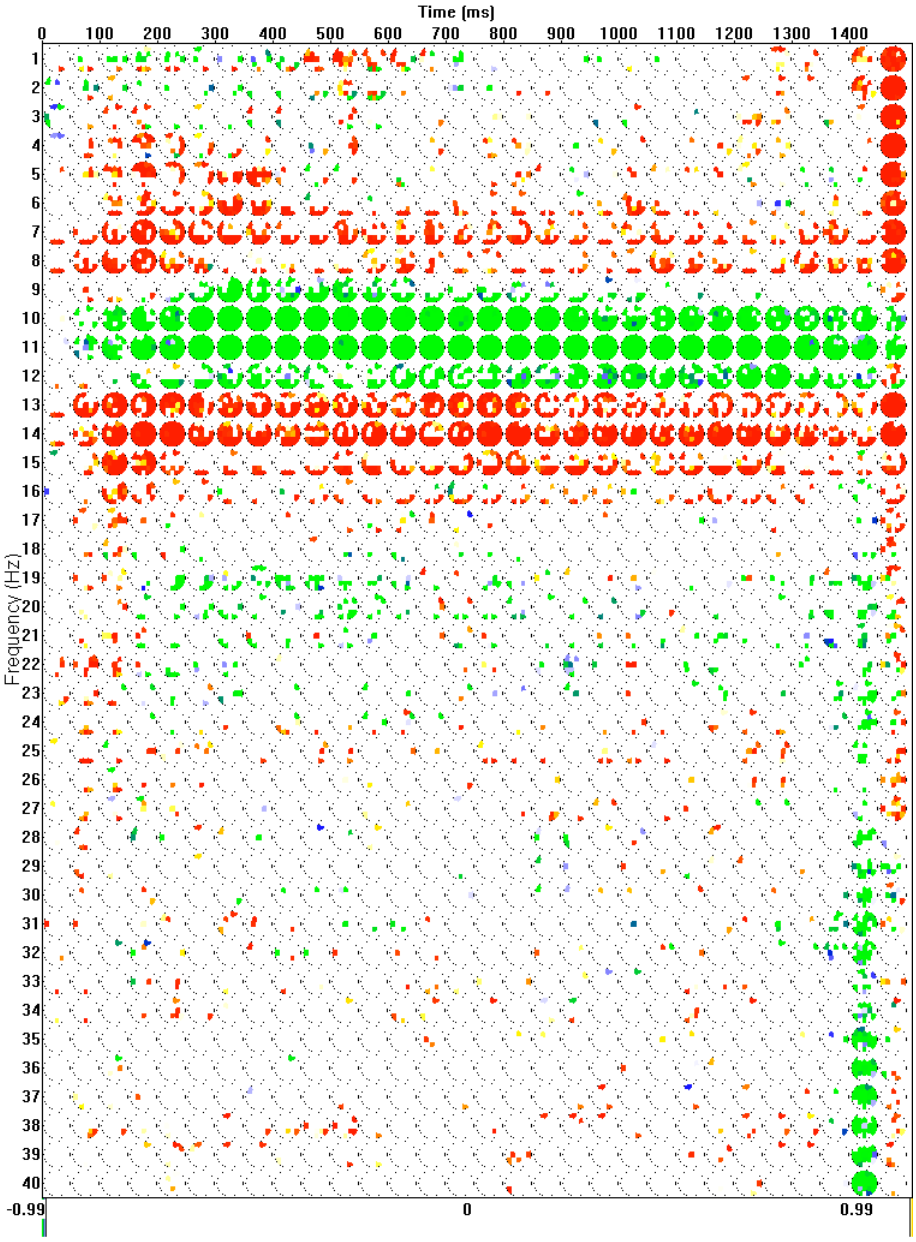

Figure A.12: Map of significant LPC changes for the Figures experiment (projected signals).

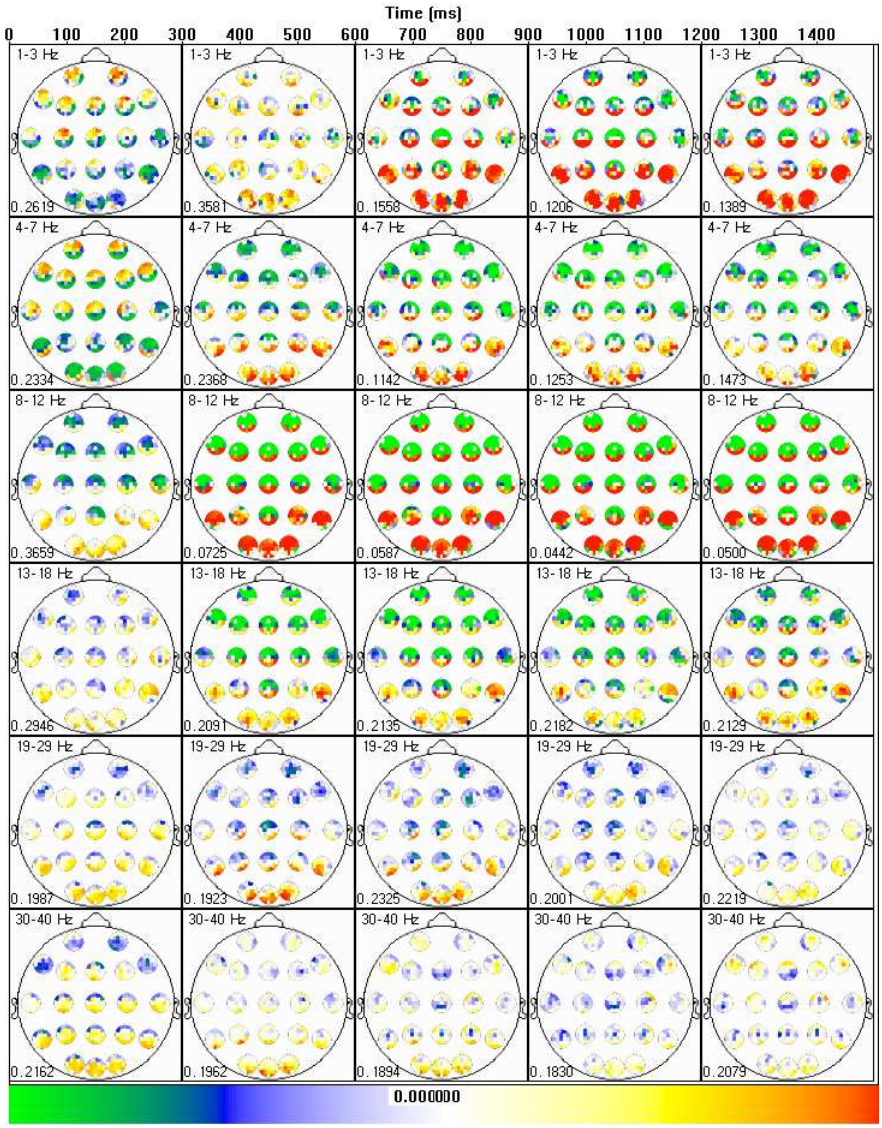

Figure A.13: Full automatic partition for the Words experiment (raw potentials).

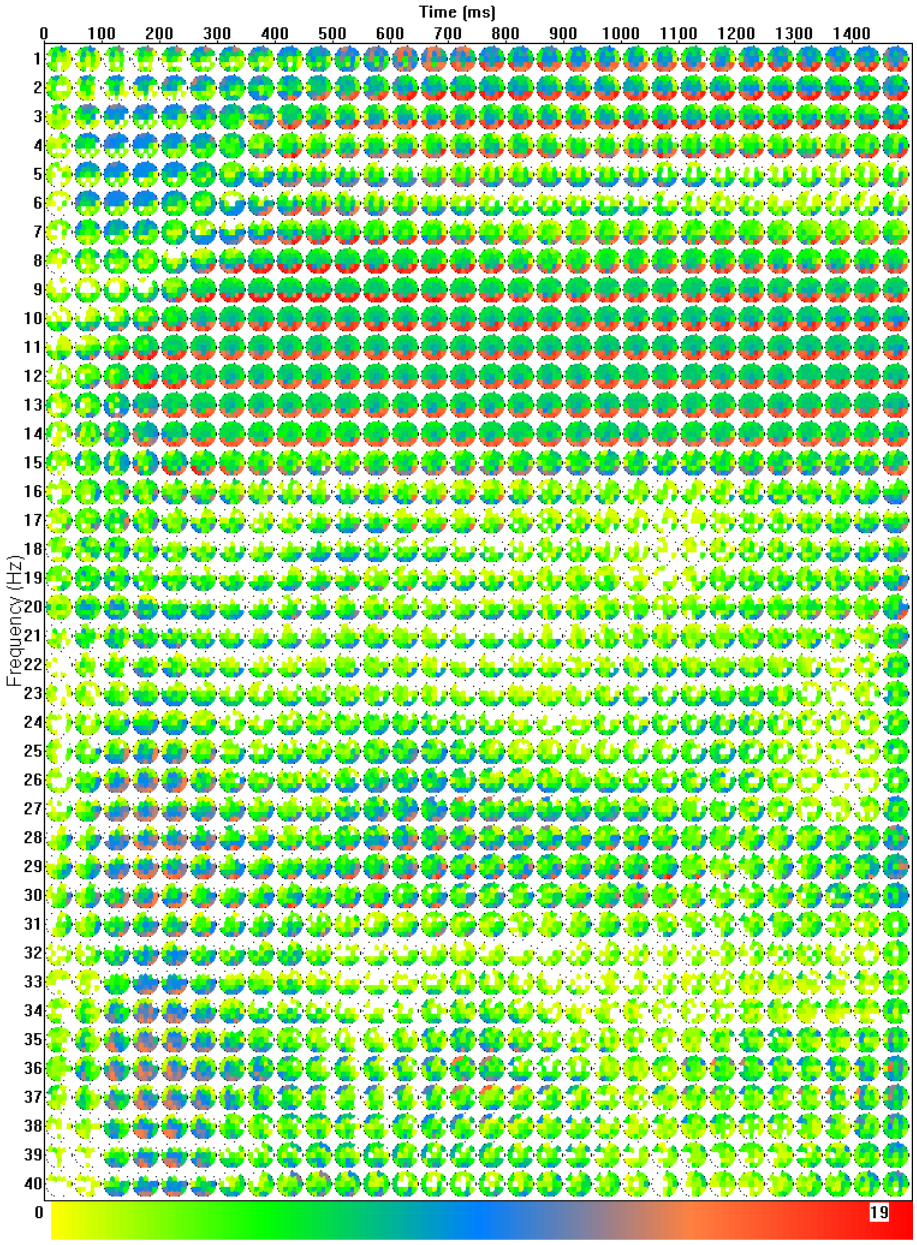

Figure A.14: Full synchrony increase histogram for the Words experiment (raw potentials).

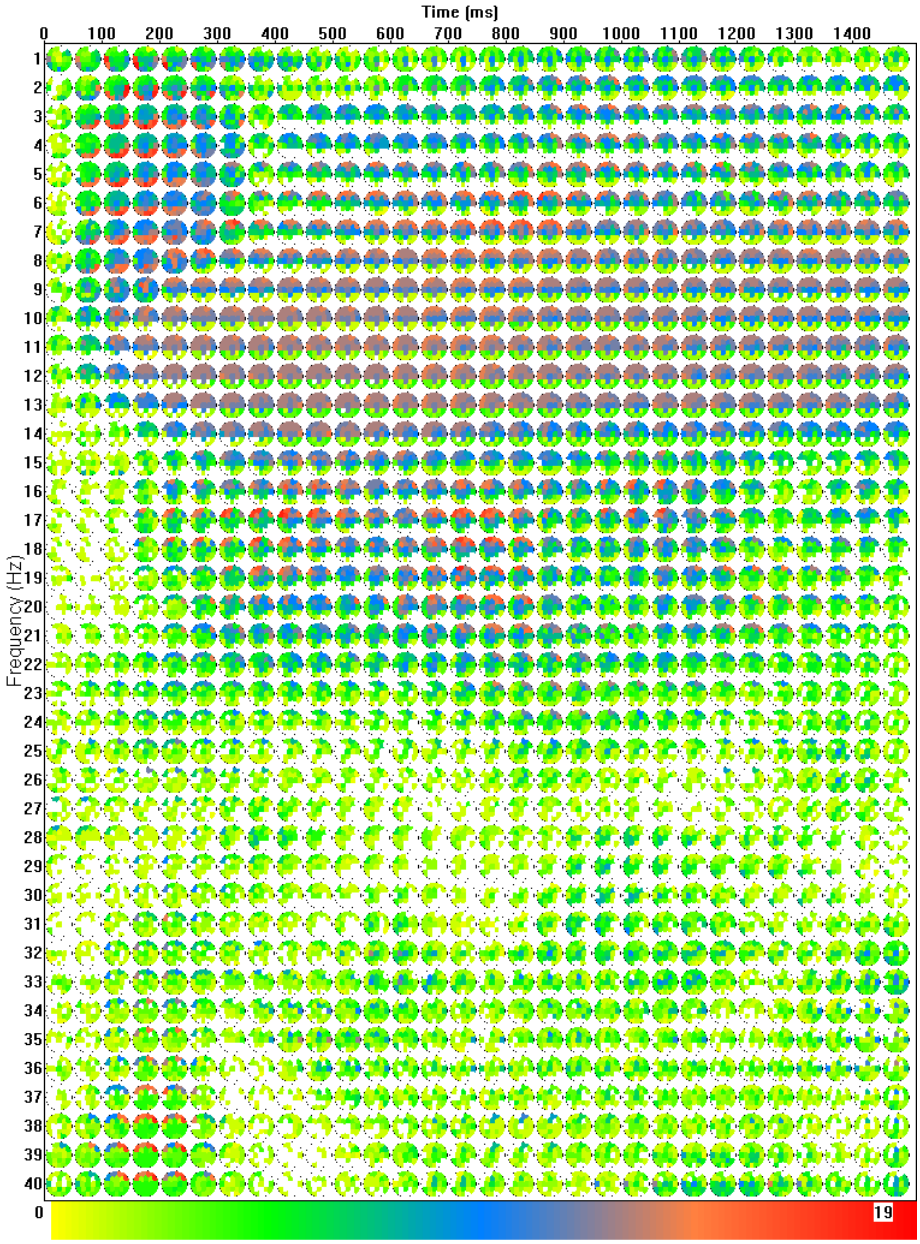

Figure A.15: Full synchrony decrease histogram for the Words experiment (raw potentials).

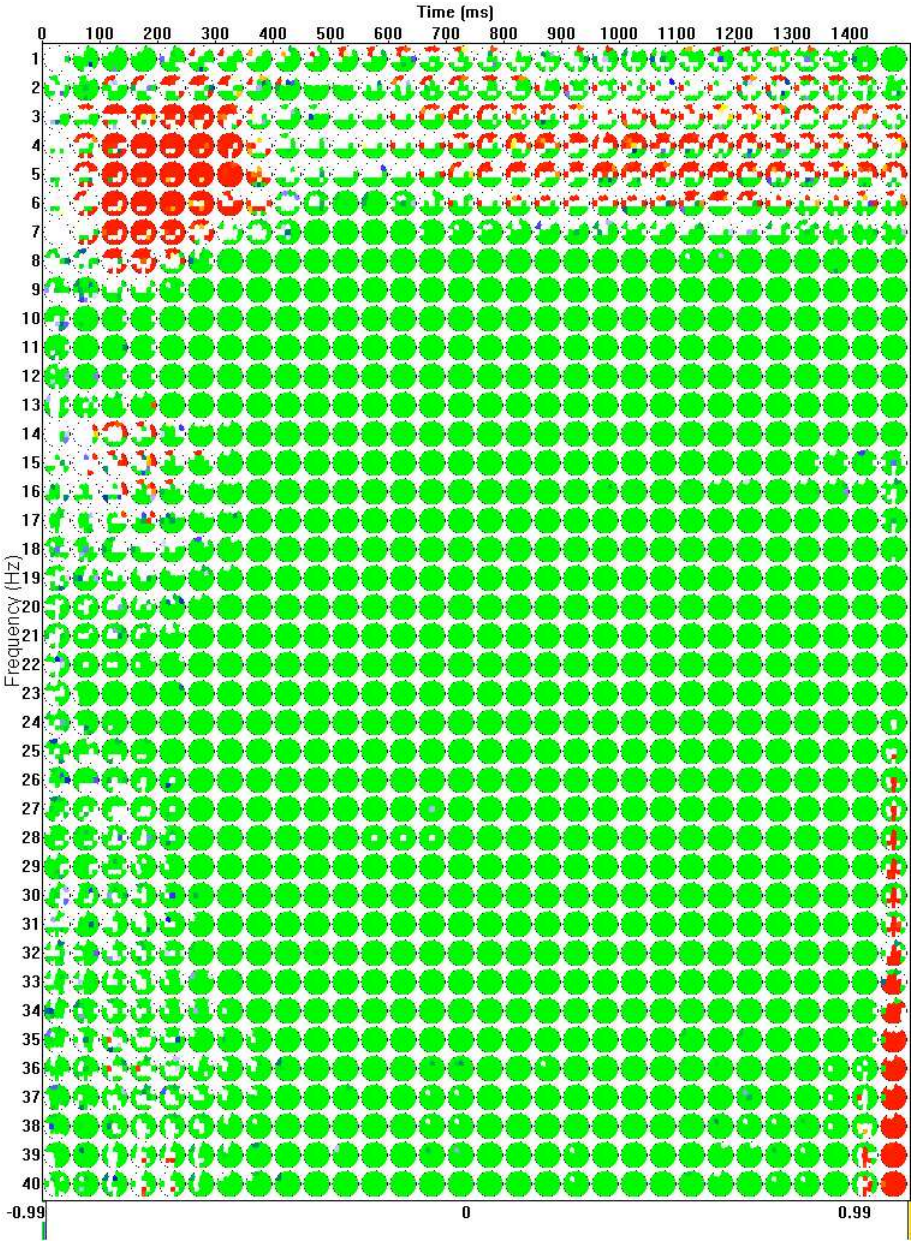

Figure A.16: Map of significant amplitude changes for the Words experiment (raw potentials).

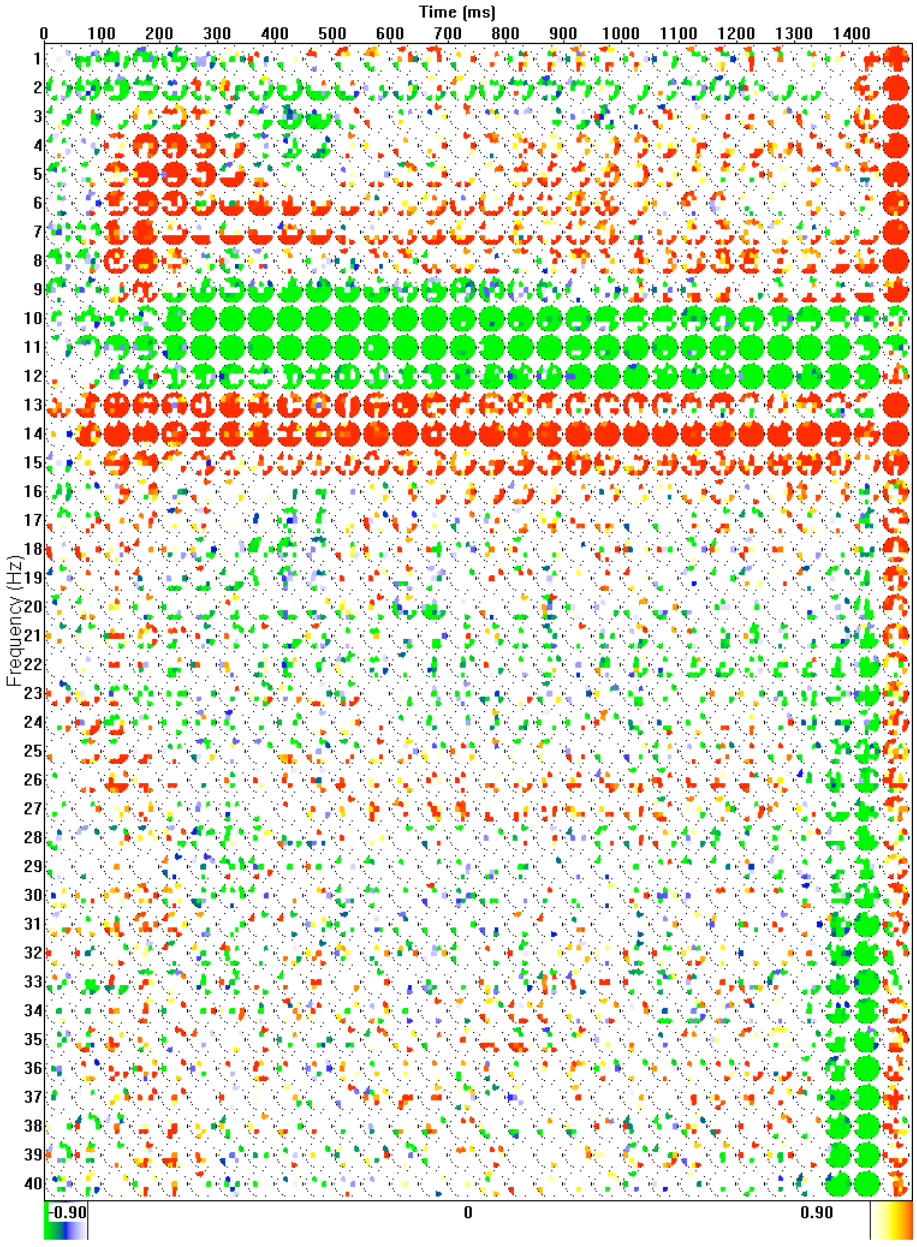

Figure A.17: Map of significant LPC changes for the Words experiment ((raw potentials).

	MPD	CPPD	PLS	STPLS	Coherence
MPD	1	0.877	0.796	0.15	0.232
CPPD	0.877	1	0.687	0.126	0.202
PLS	0.796	0.687	1	0.247	0.331
STPLS	0.15	0.126	0.247	1	0.939
Coherence	0.232	0.202	0.331	0.939	1

	LPD
MPD	0.131
CPPD	0.092
PLS	0.164
STPLS	0.831
Coherence	0.792

Figure A.18: Correlation table of synchrony measures for the Words experiment (raw potentials).

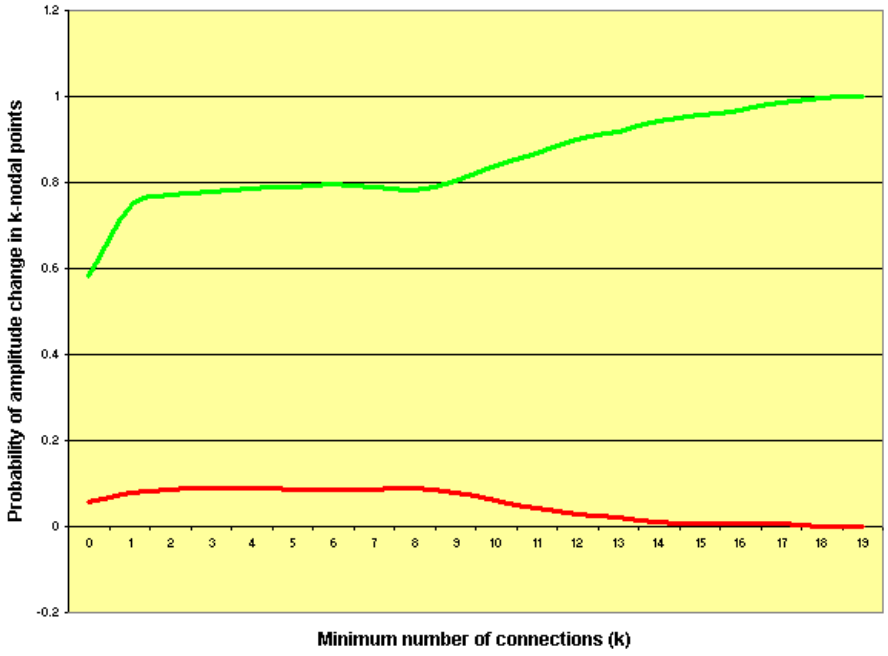

Figure A.19: Conditional probabilities of amplitude increase (red) and decrease (green) in nodal points for the Words experiment (raw potentials).

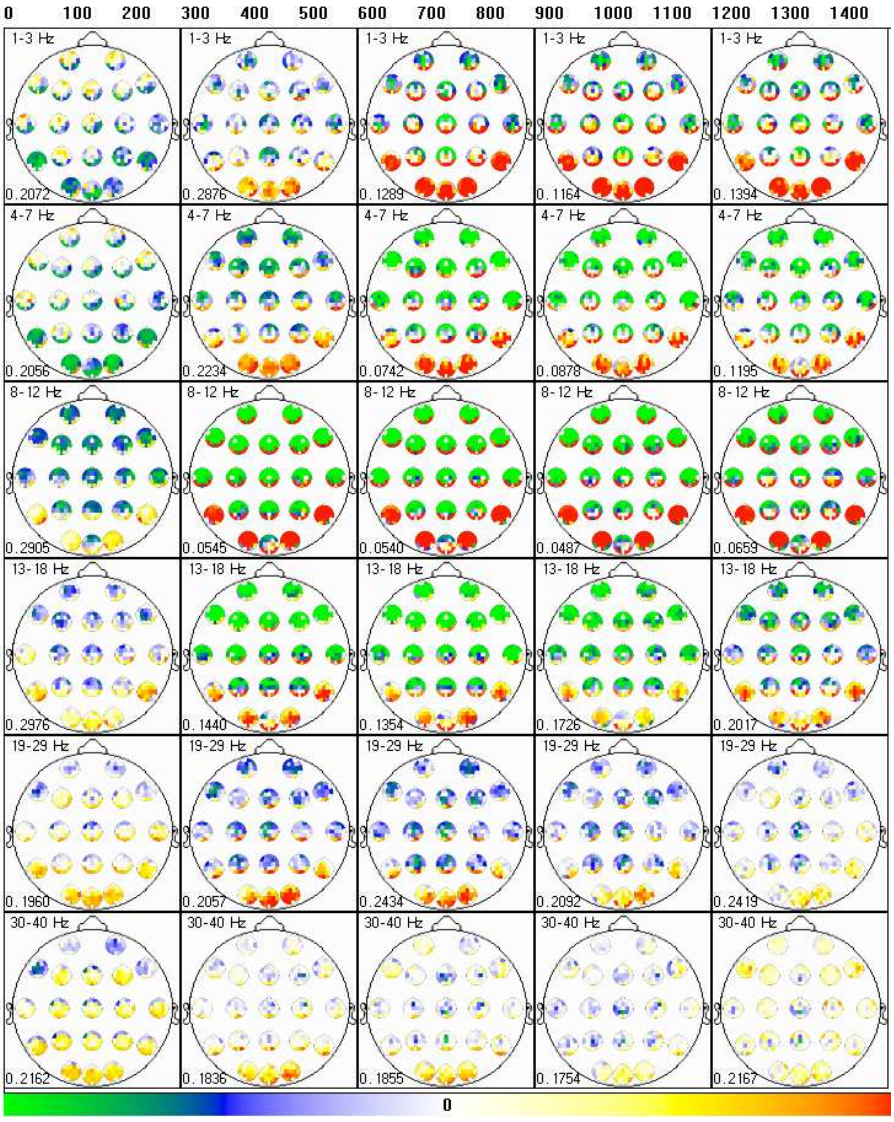

Figure A.20: Full automatic partition for the Words experiment (projected signals).

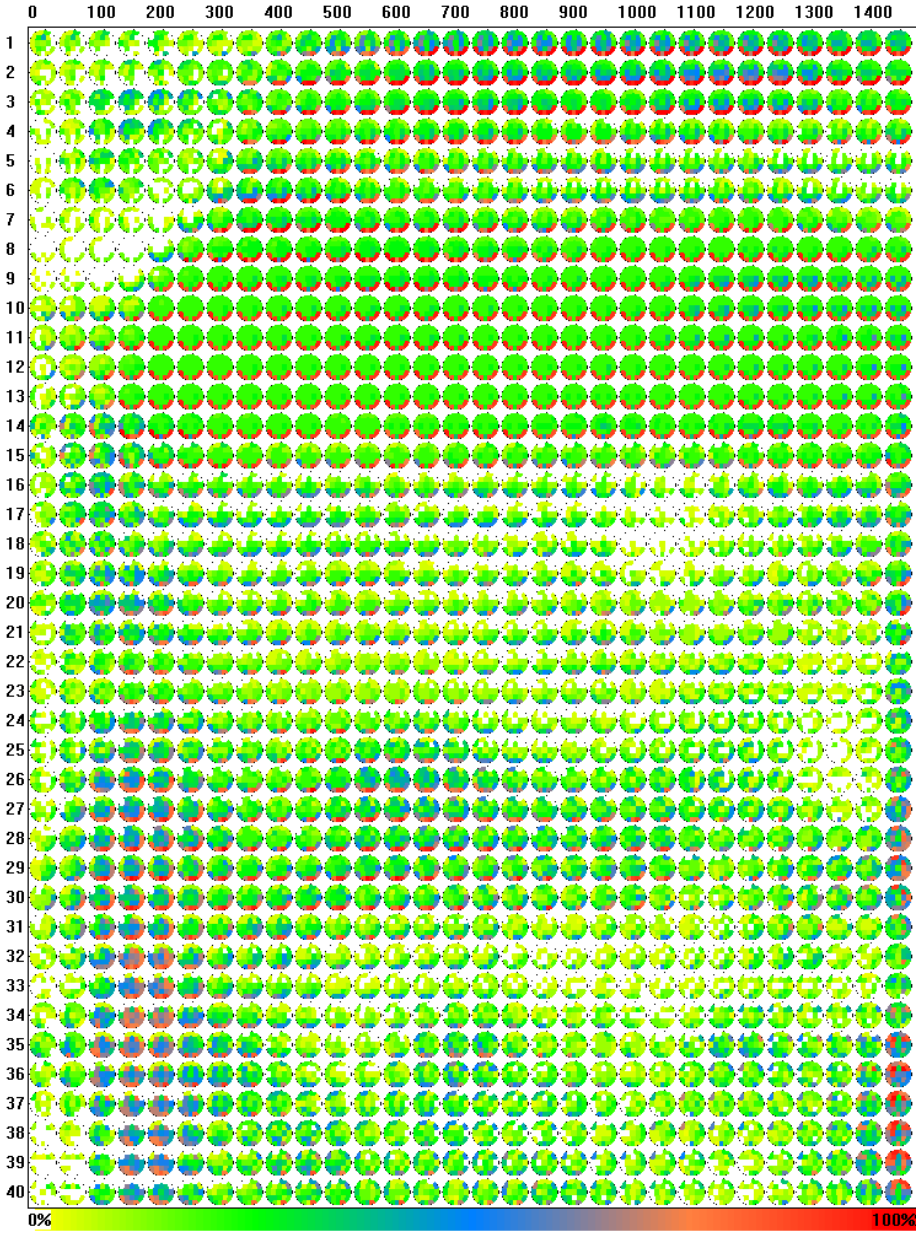

Figure A.21: Full synchrony increase histogram for the Words experiment (projected signals).

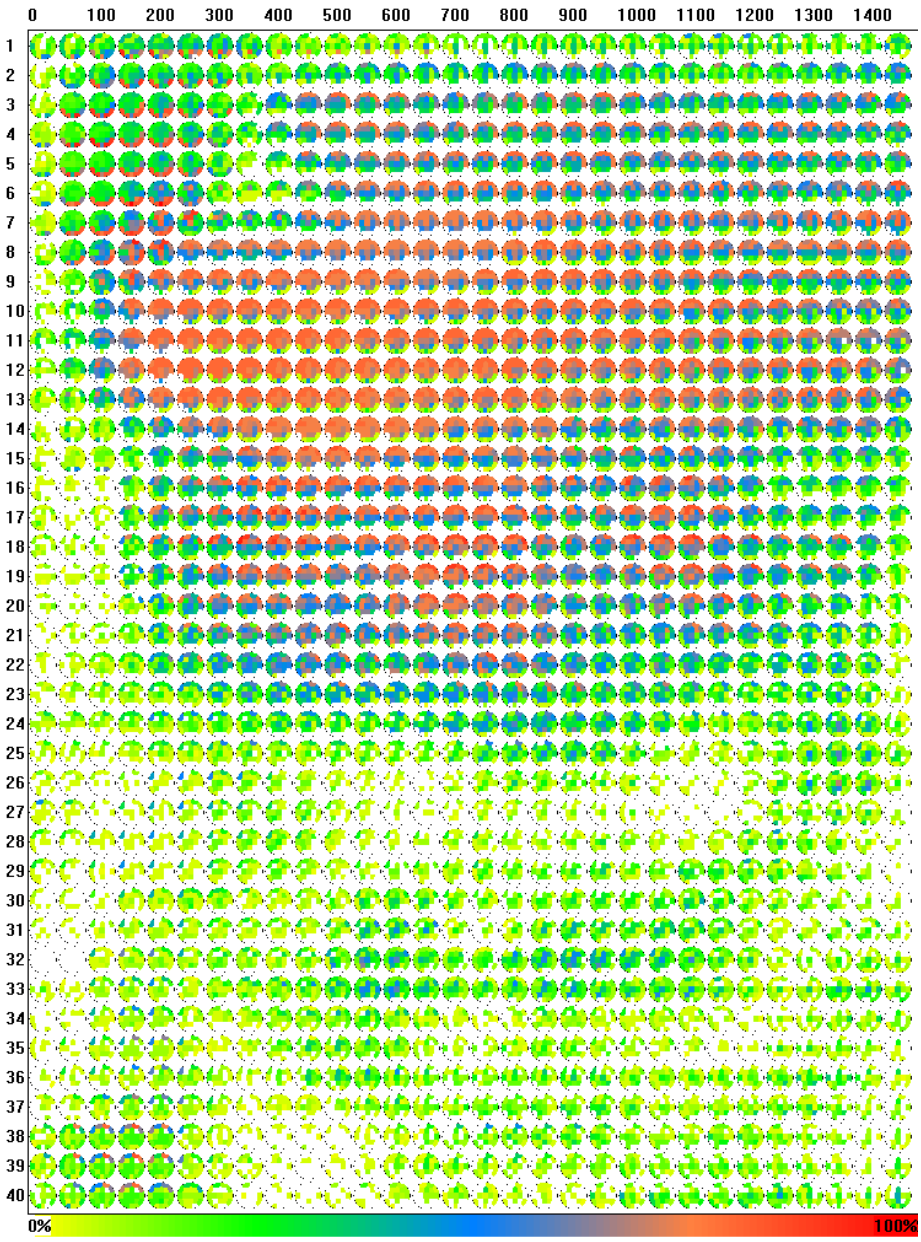

Figure A.22: Full synchrony decrease histogram for the Words experiment (projected signals).

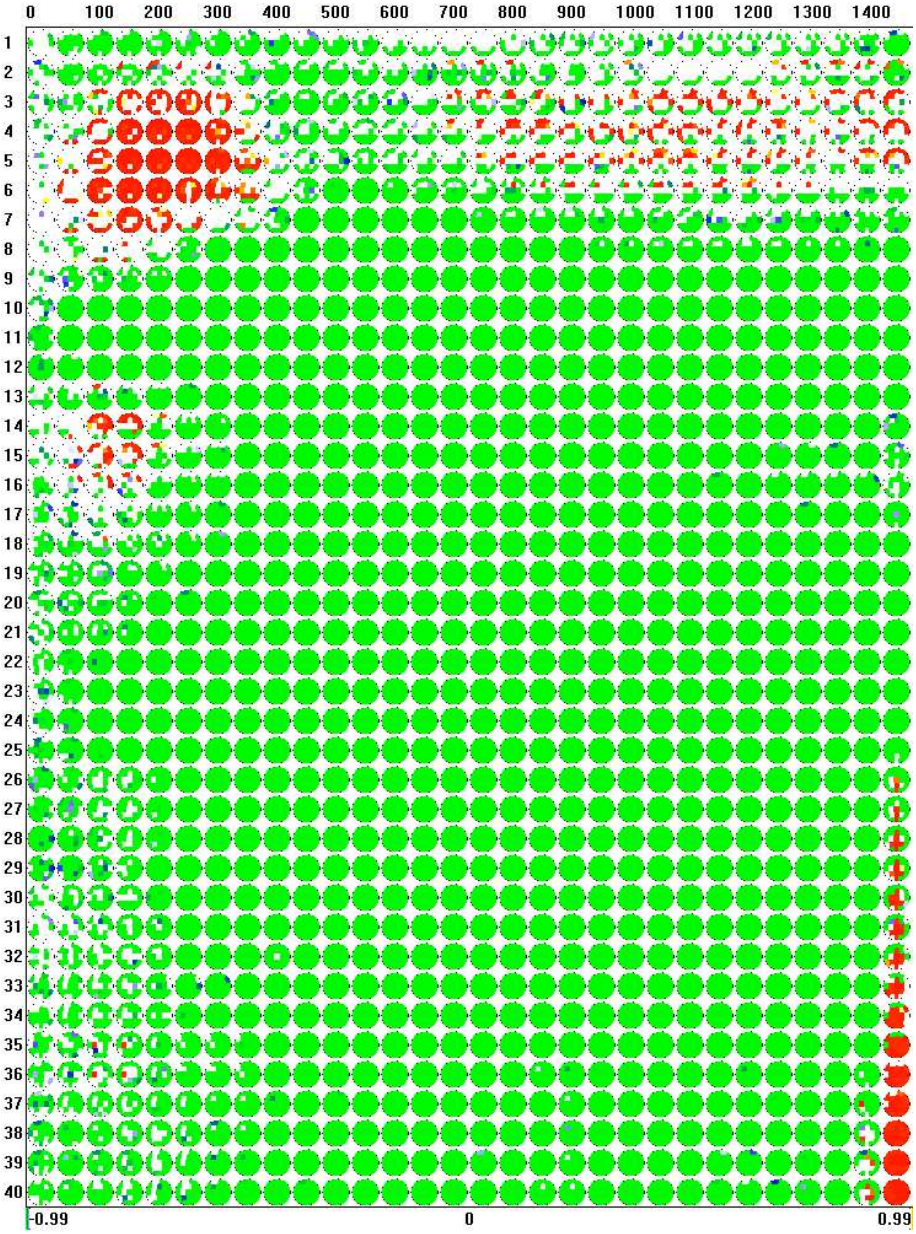

Figure A.23: Map of significant amplitude changes for the Words experiment (projected signals).

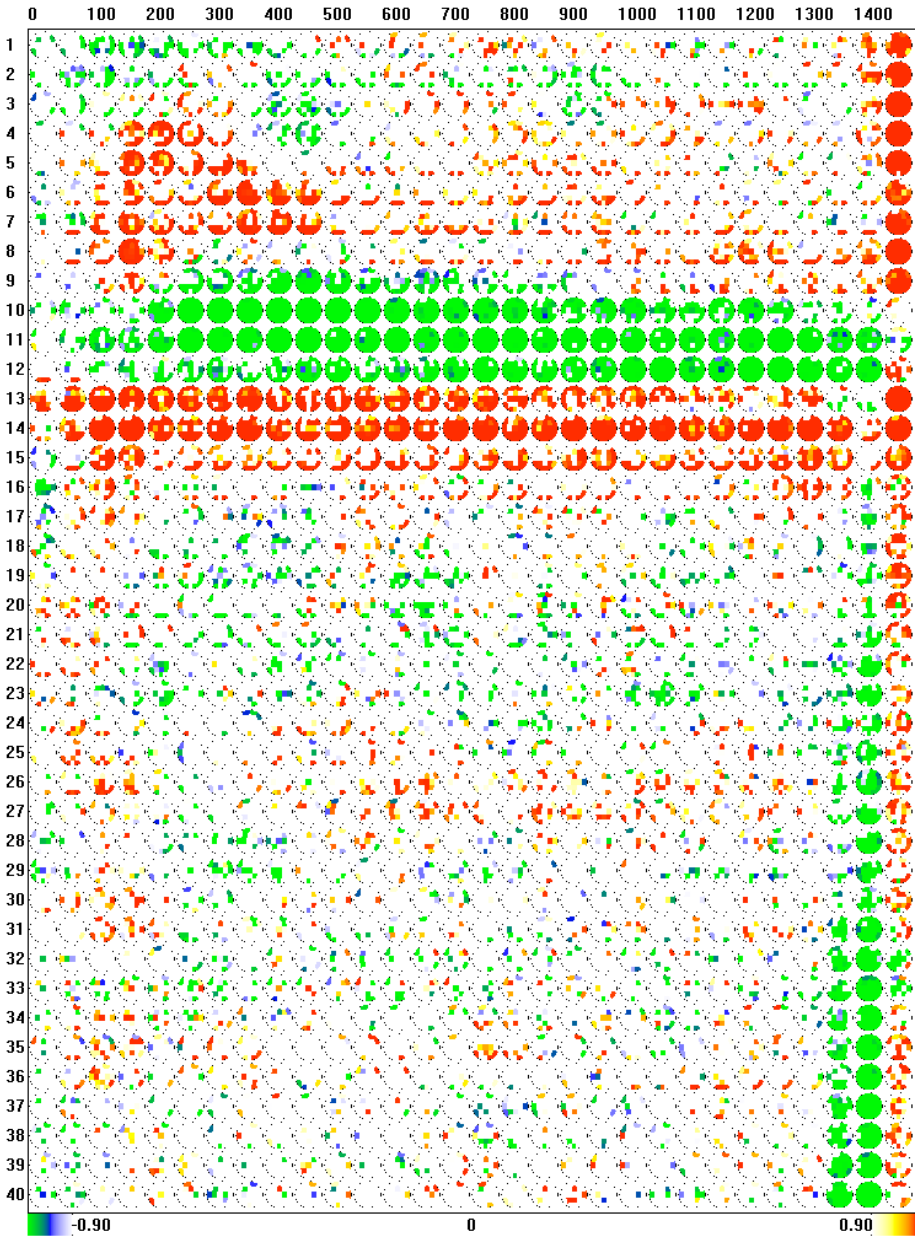

Figure A.24: Map of significant LPC changes for the Words experiment (projected signals).

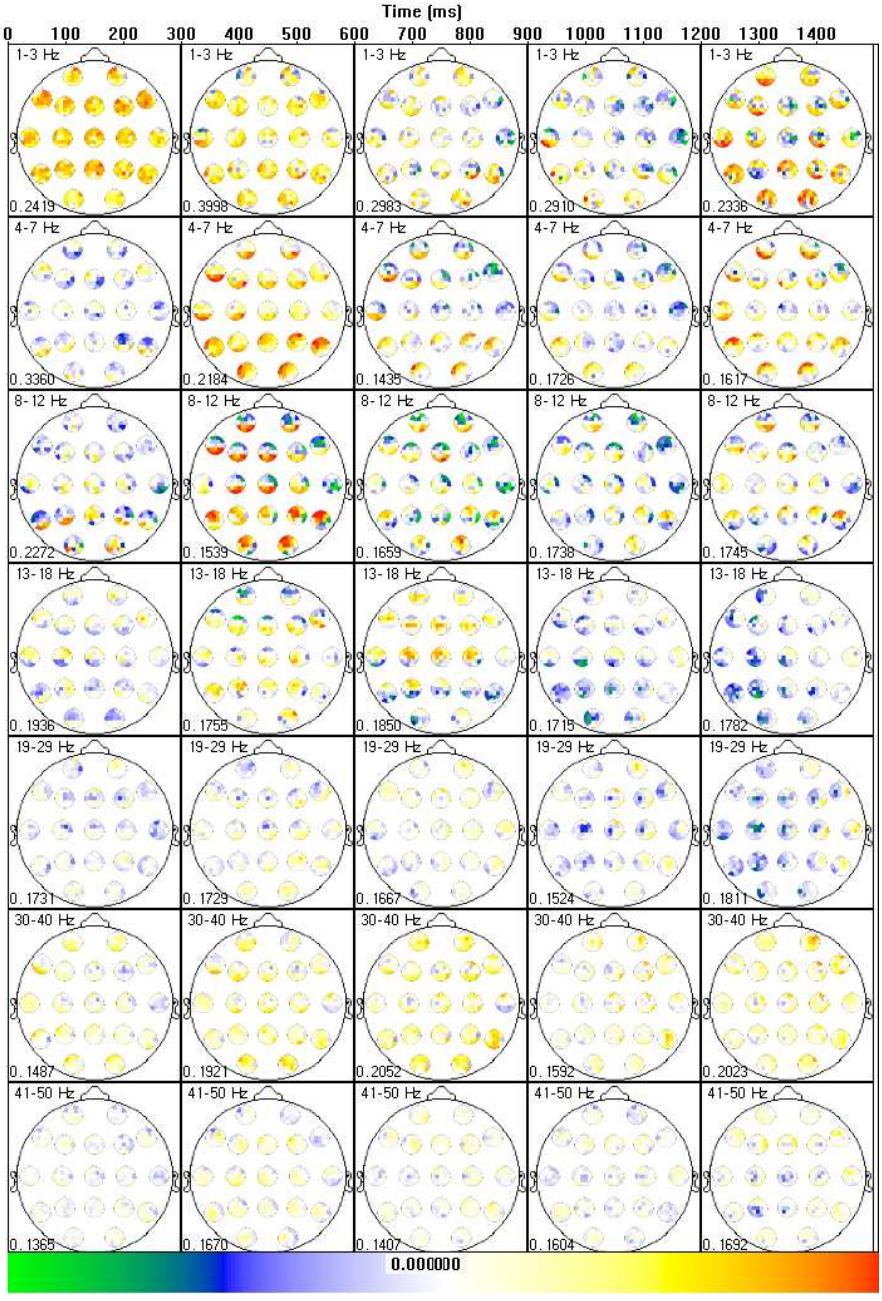

Figure A.25: Full automatic partition for the Letters (GO condition) experiment (raw potentials).

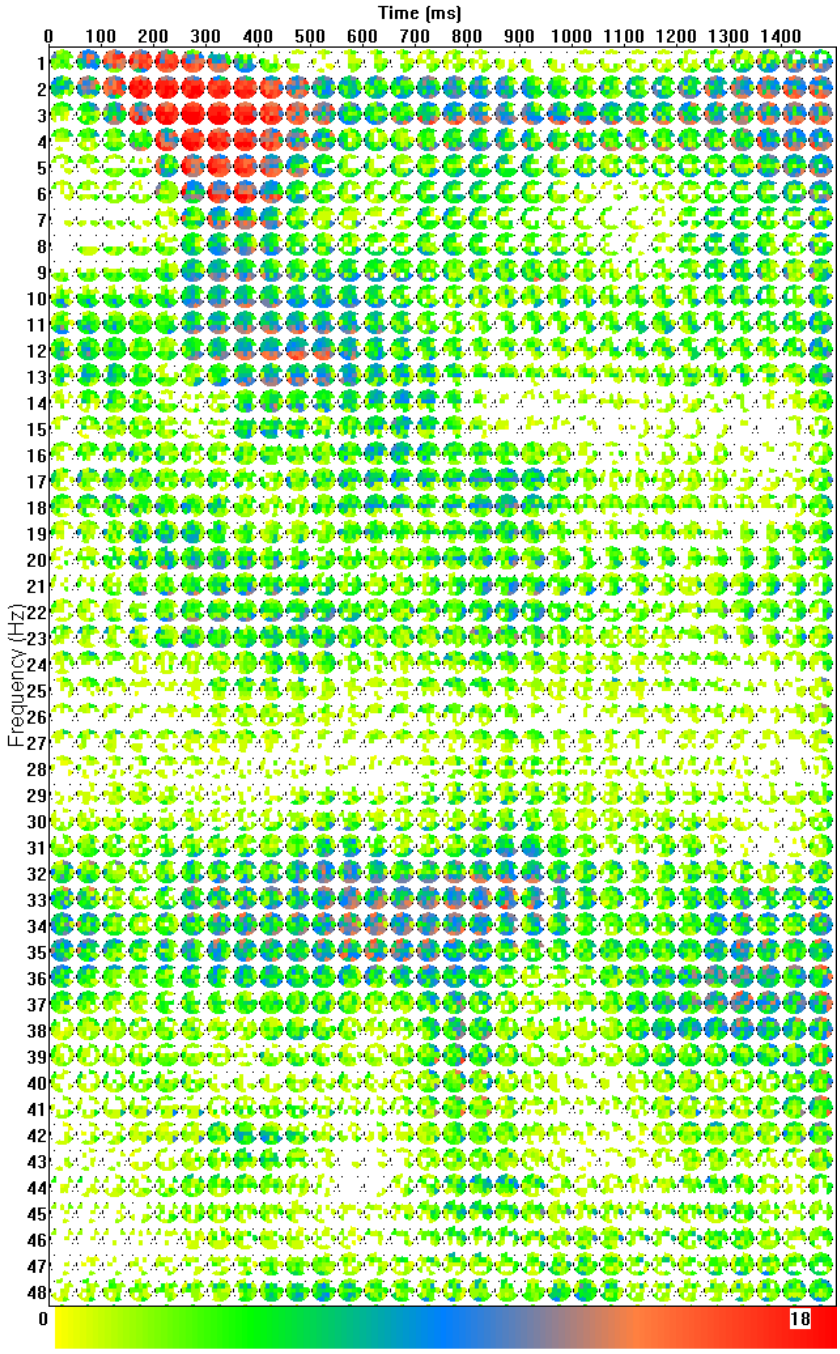

Figure A.26: Full synchrony increase histogram for the Letters (GO condition) experiment (raw potentials).

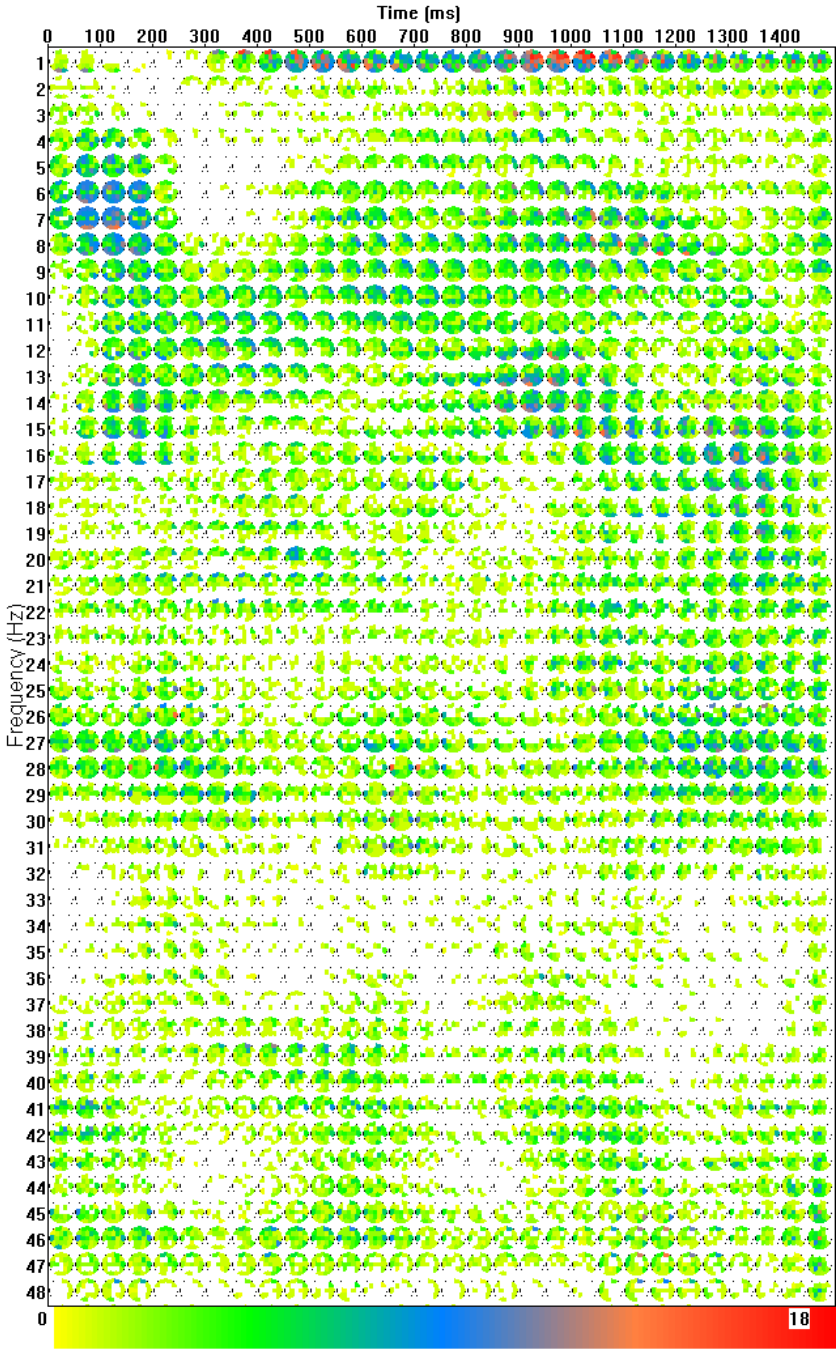

Figure A.27: Full synchrony decrease histogram for the Letters (GO condition) experiment (raw potentials).

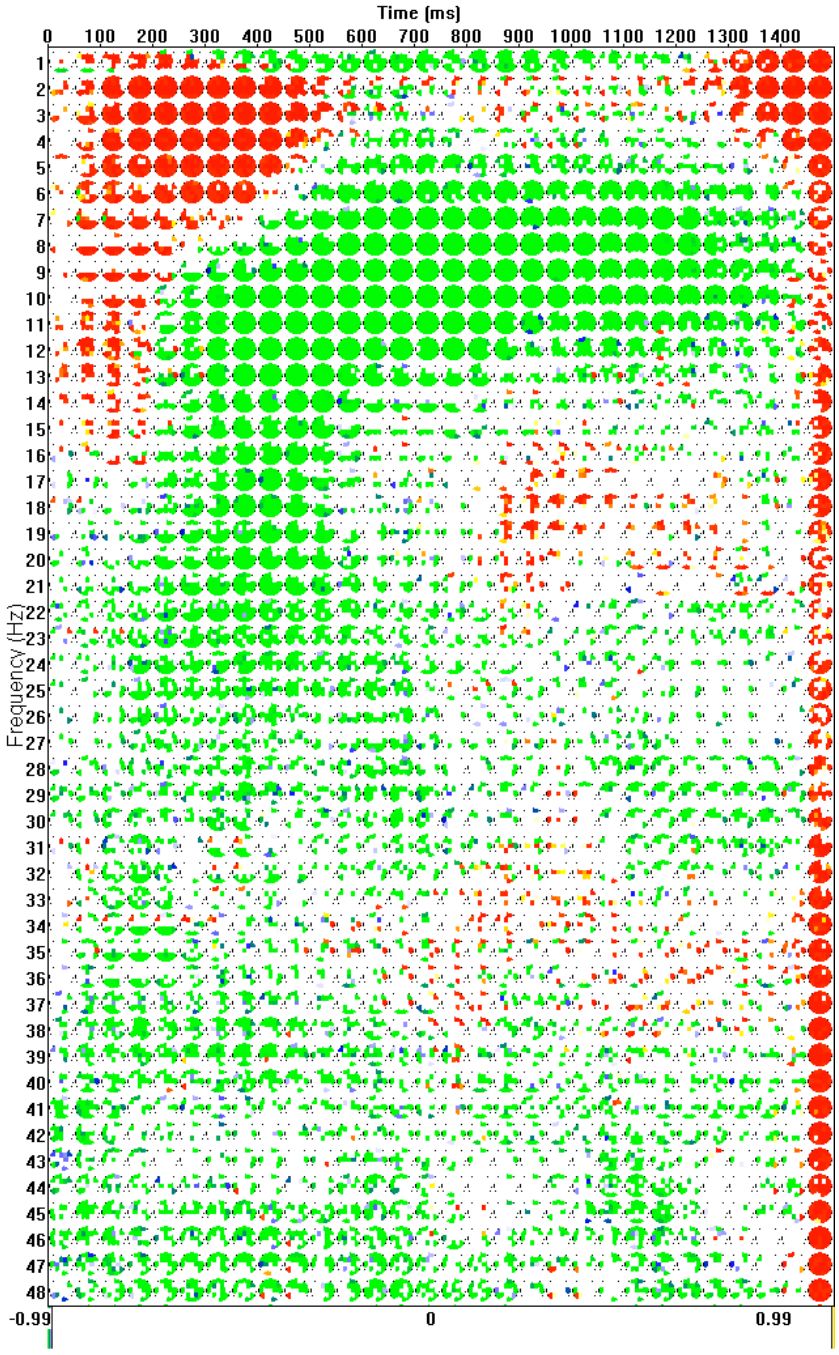

Figure A.28: Map of significant amplitude changes for the Letters (GO condition) experiment (raw potentials).

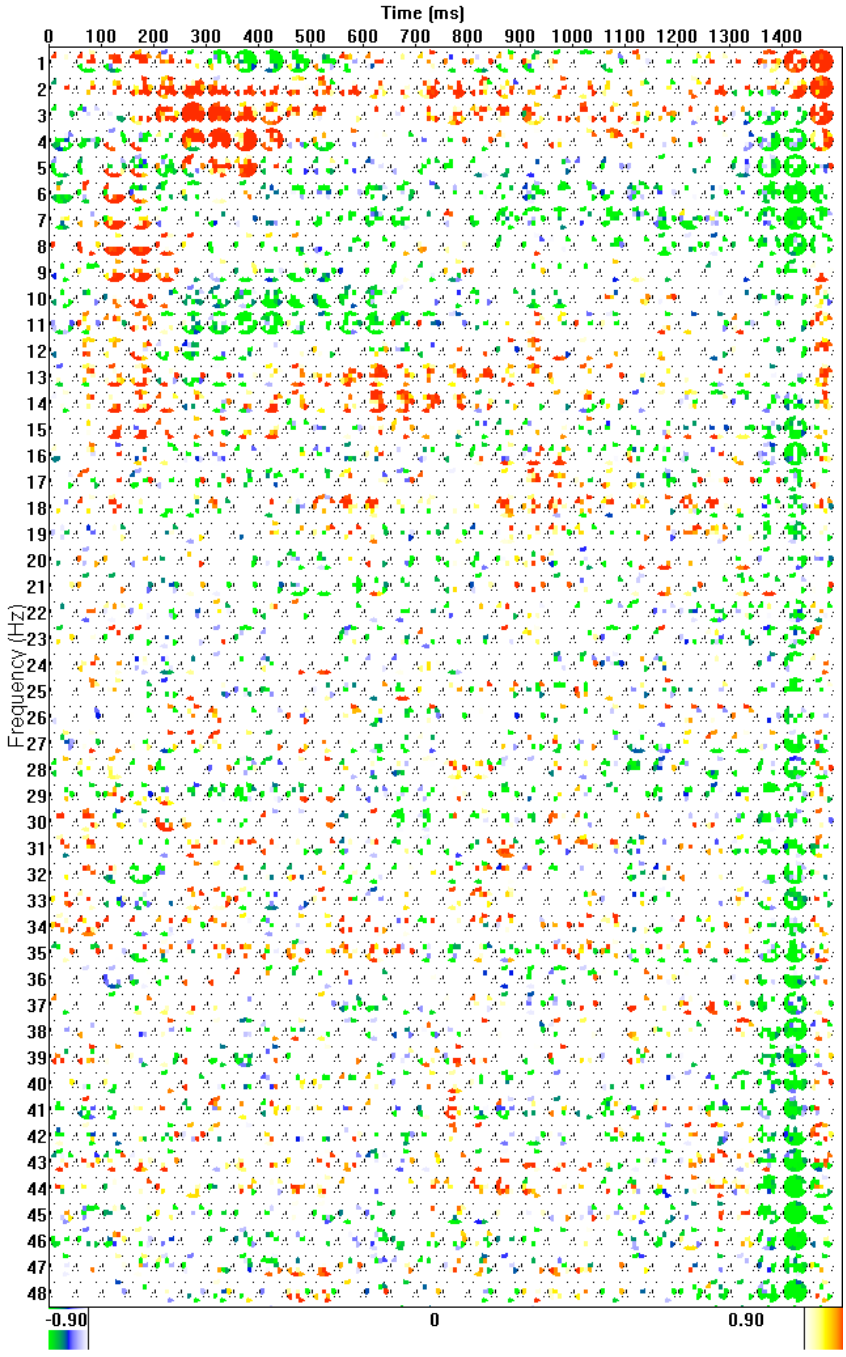

Figure A.29: Map of significant LPC changes for the Letters (GO condition) experiment ((raw potentials).

	MPD	CPPD	PLS	STPLS	Coherence
MPD	1	0.74	0.861	0.285	0.34
CPPD	0.74	1	0.635	0.204	0.247
PLS	0.861	0.635	1	0.331	0.386
STPLS	0.285	0.204	0.331	1	0.876
Coherence	0.34	0.247	0.386	0.876	1

	LPD
MPD	0.257
CPPD	0.193
PLS	0.27
STPLS	0.857
Coherence	0.798

Figure A.30: Correlation table of synchrony measures for the Letters (GO condition) experiment (raw potentials).

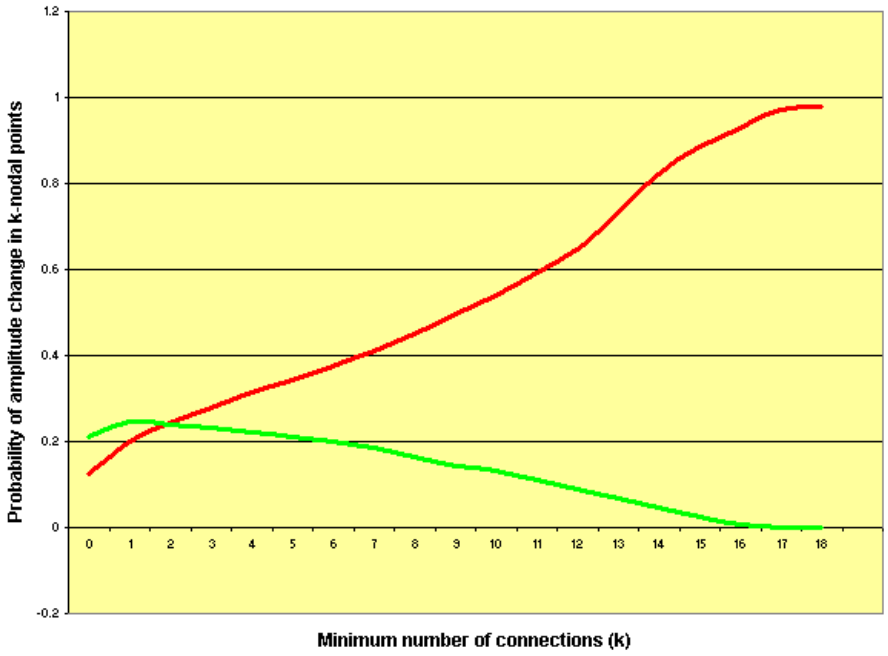

Figure A.31: Conditional probabilities of amplitude increase (red) and decrease (green) in nodal points for the Letters (GO condition) experiment (raw potentials).

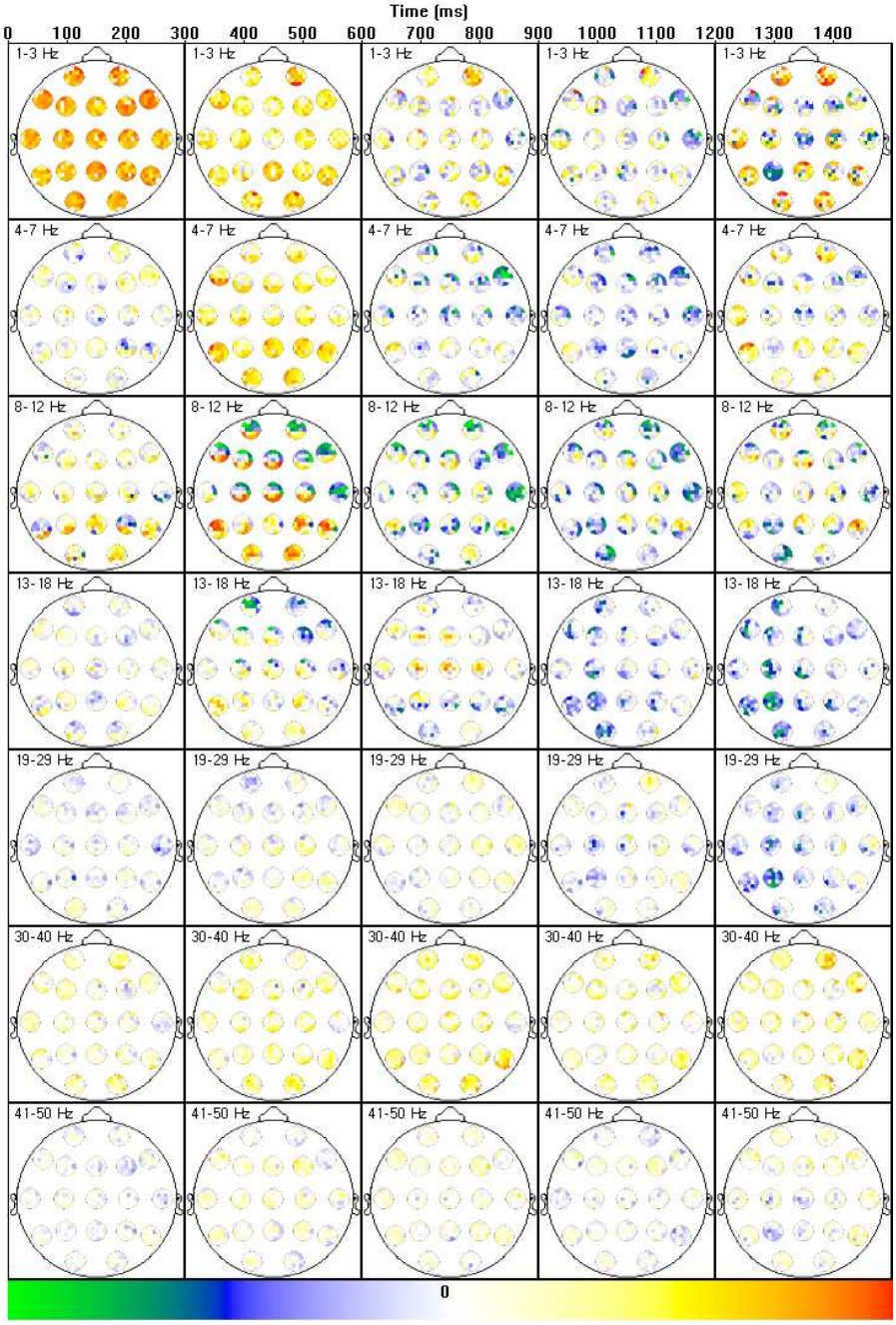

Figure A.32: Full automatic partition for the Letters (GO condition) experiment (projected signals).

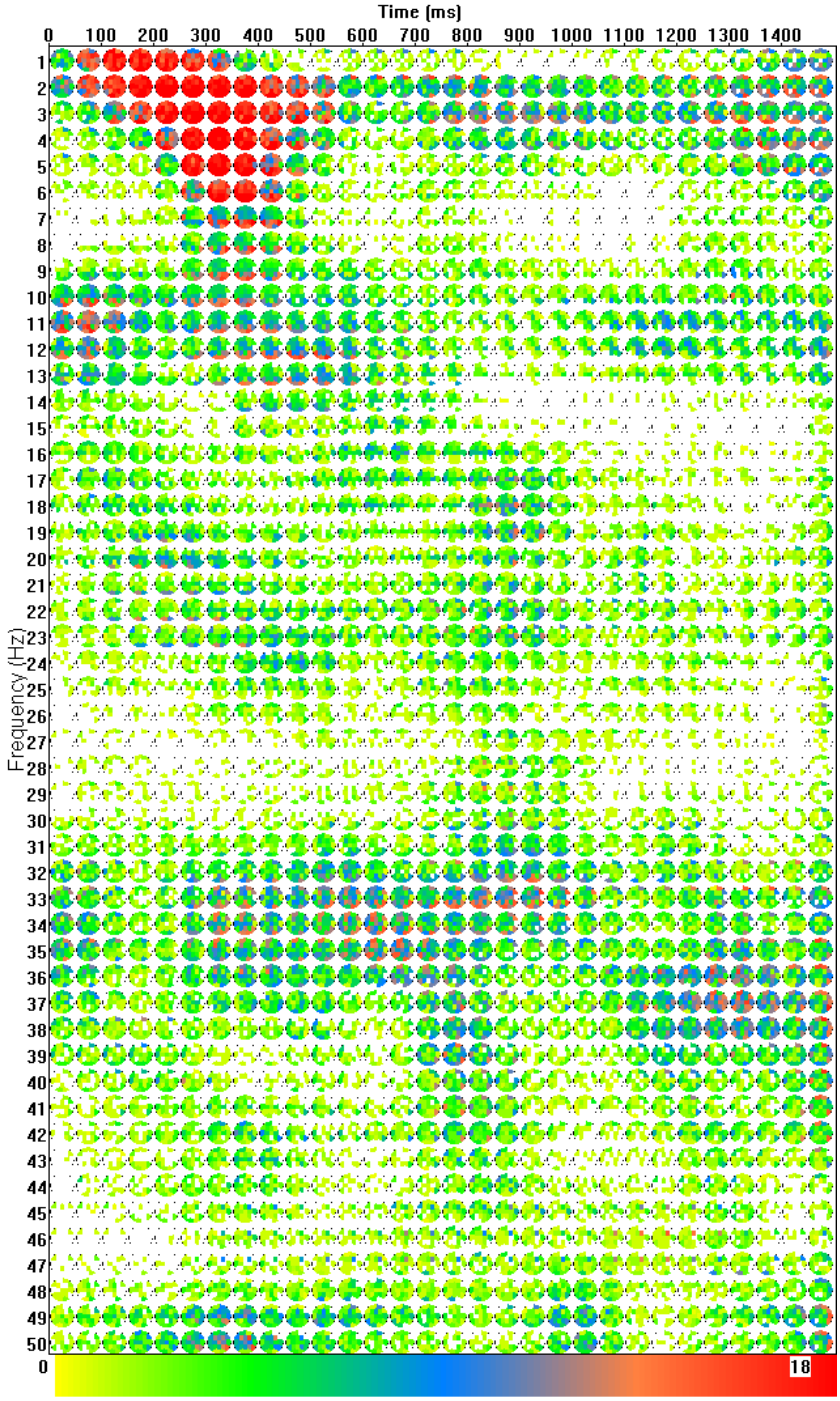

Figure A.33: Full synchrony increase histogram for the Letters (GO condition) experiment (projected signals).

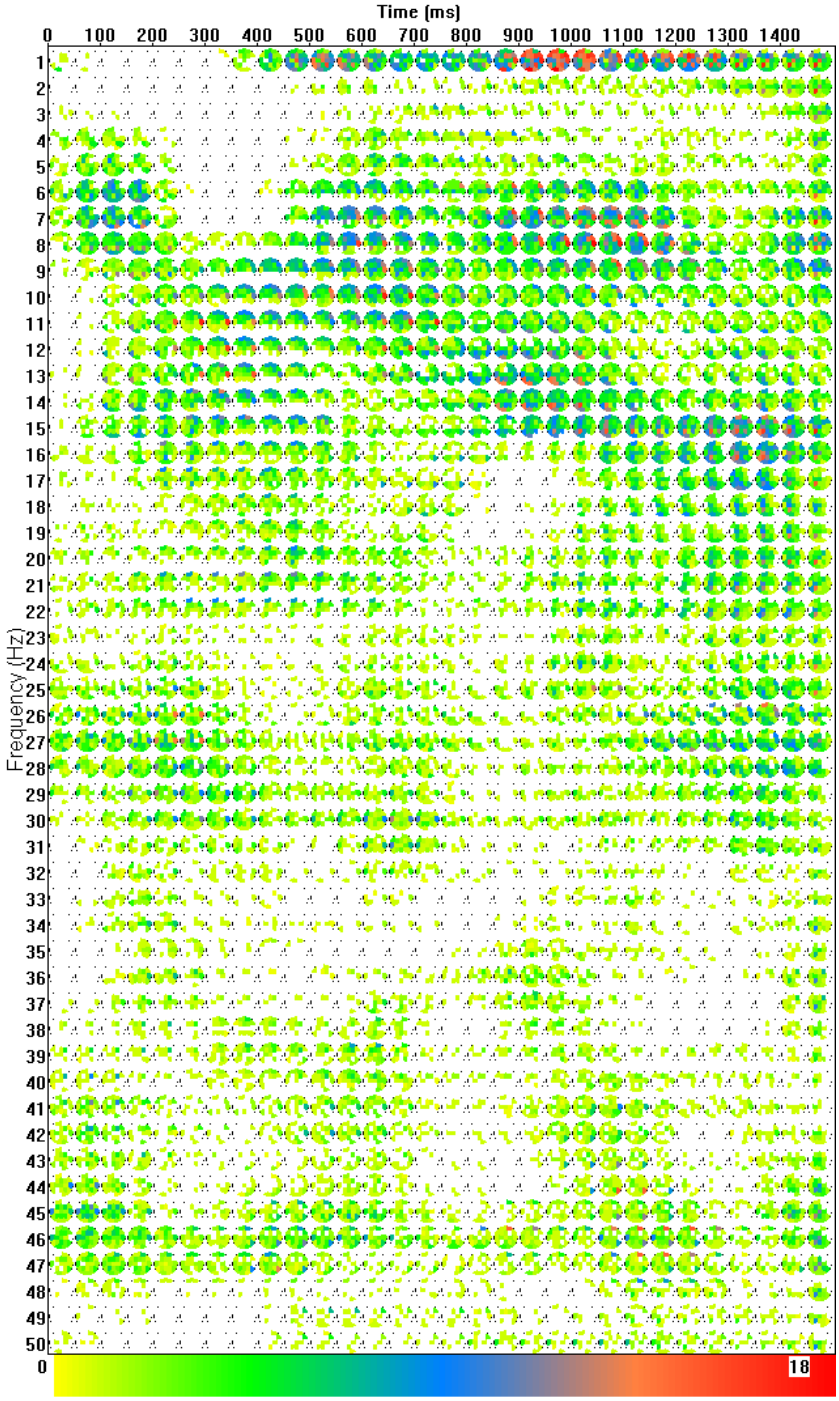

Figure A.34: Full synchrony decrease histogram for the Letters (GO condition) experiment (projected signals).

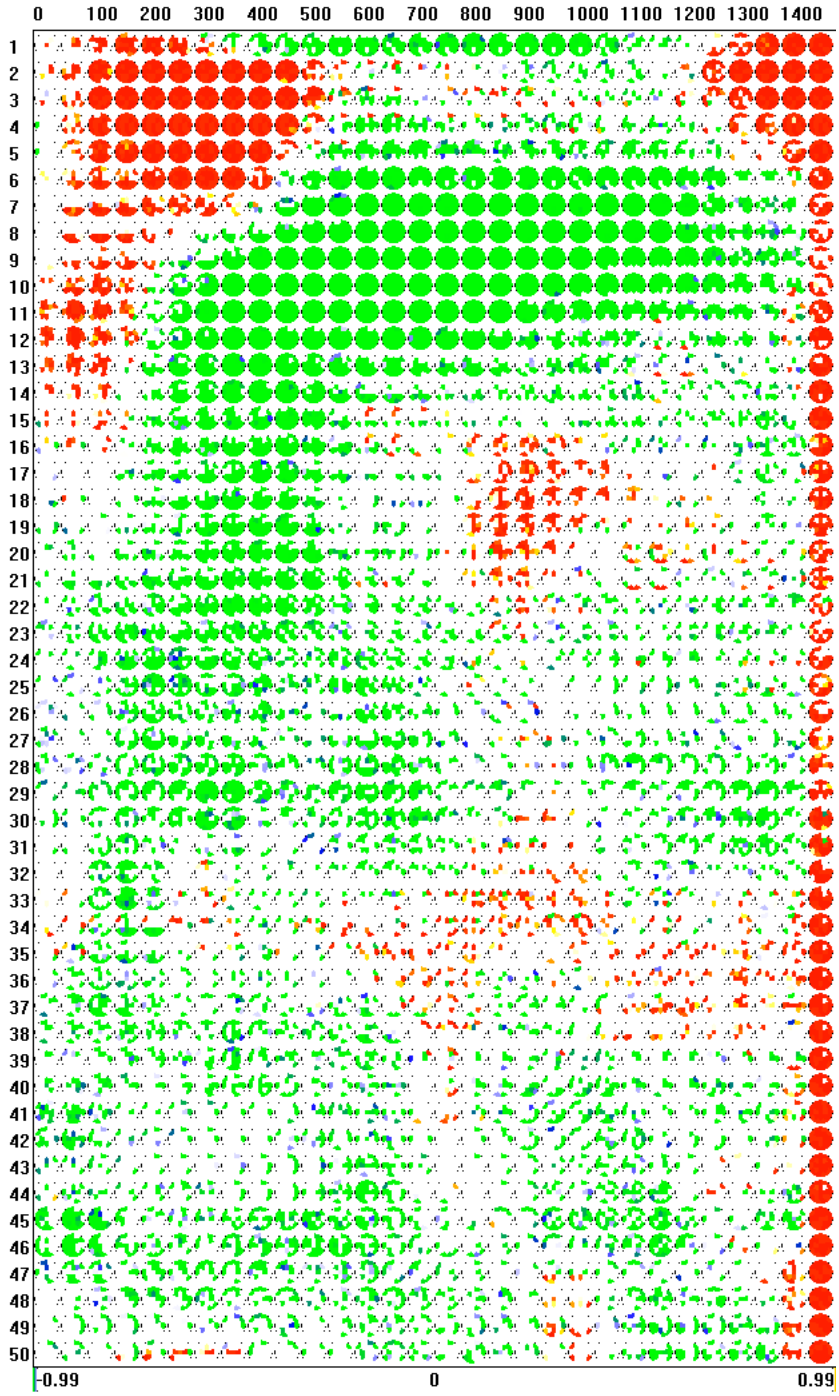

Figure A.35: Map of significant amplitude changes for the Letters (GO condition) experiment (projected signals).

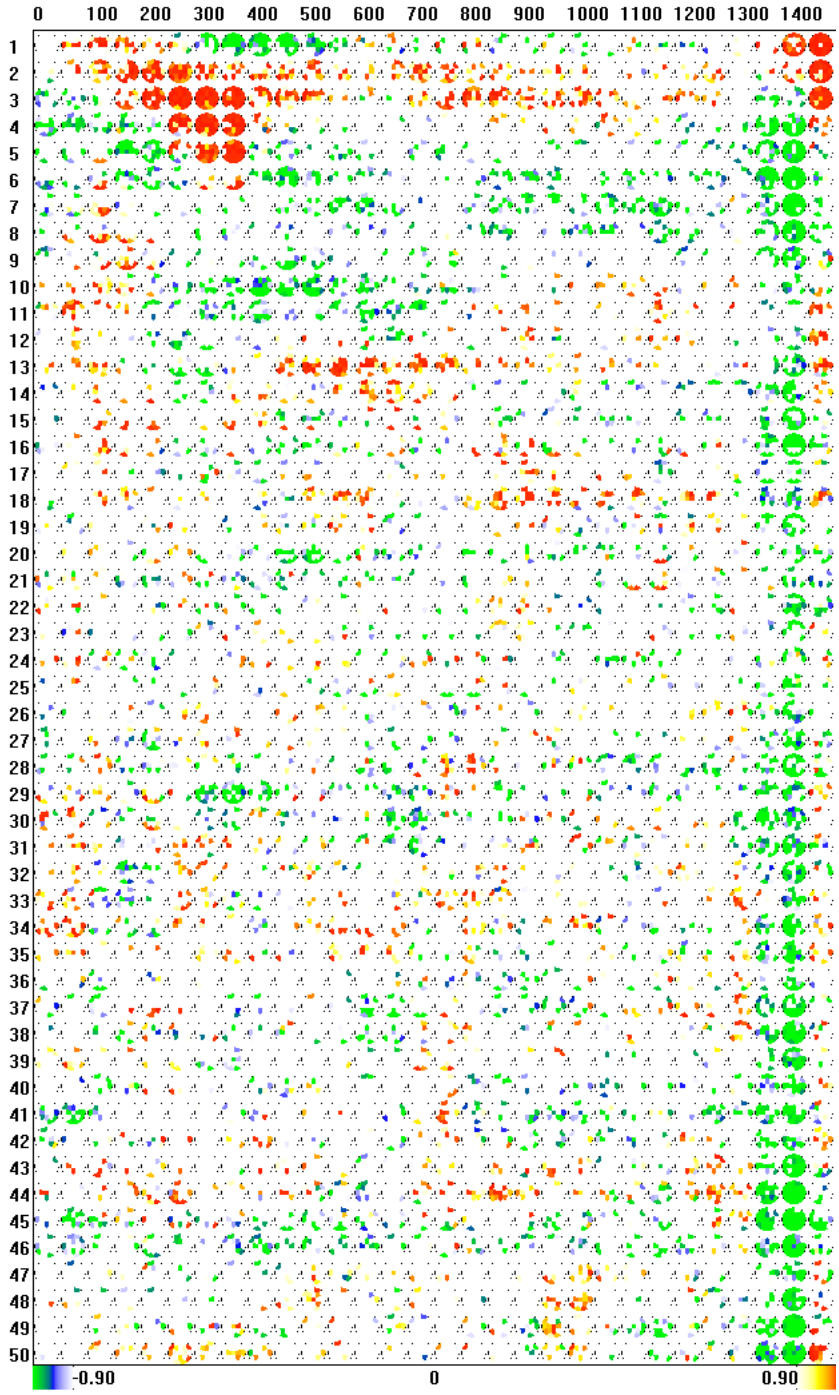

Figure A.36: Map of significant LPC changes for the Letters (GO condition) experiment (projected signals).

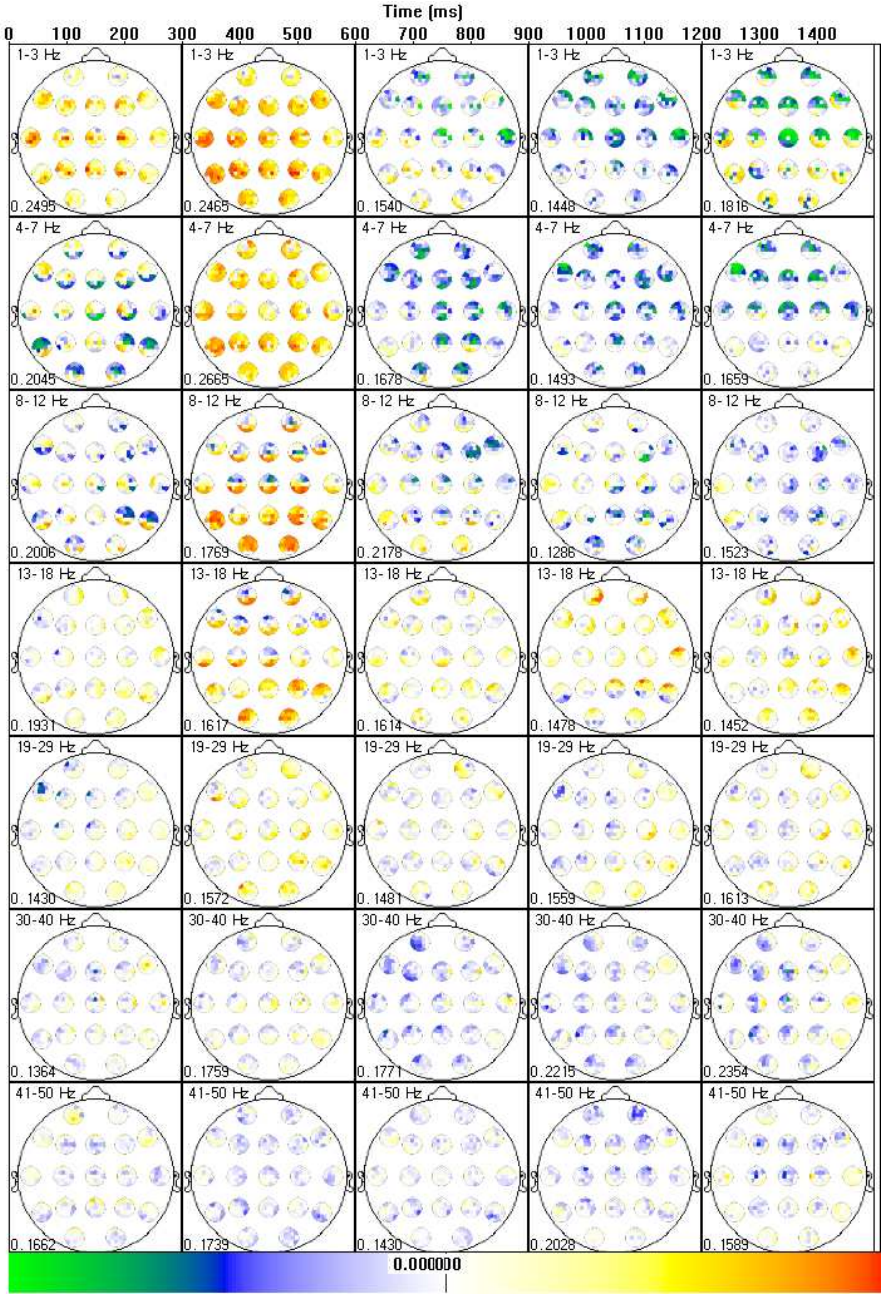

Figure A.37: Full automatic partition for the Letters (NO-GO condition) experiment (raw potentials).

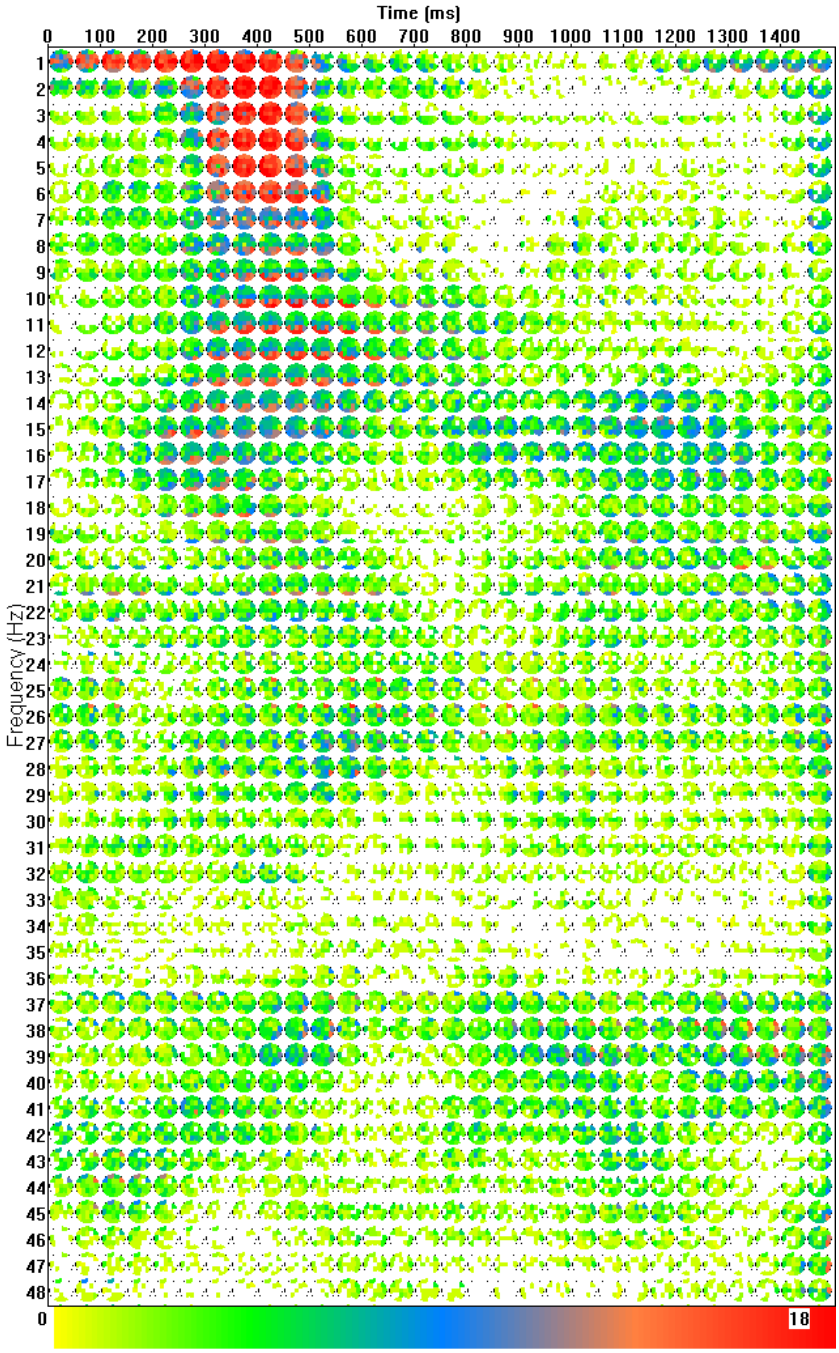

Figure A.38: Full synchrony increase histogram for the Letters (NO-GO condition) experiment (raw potentials).

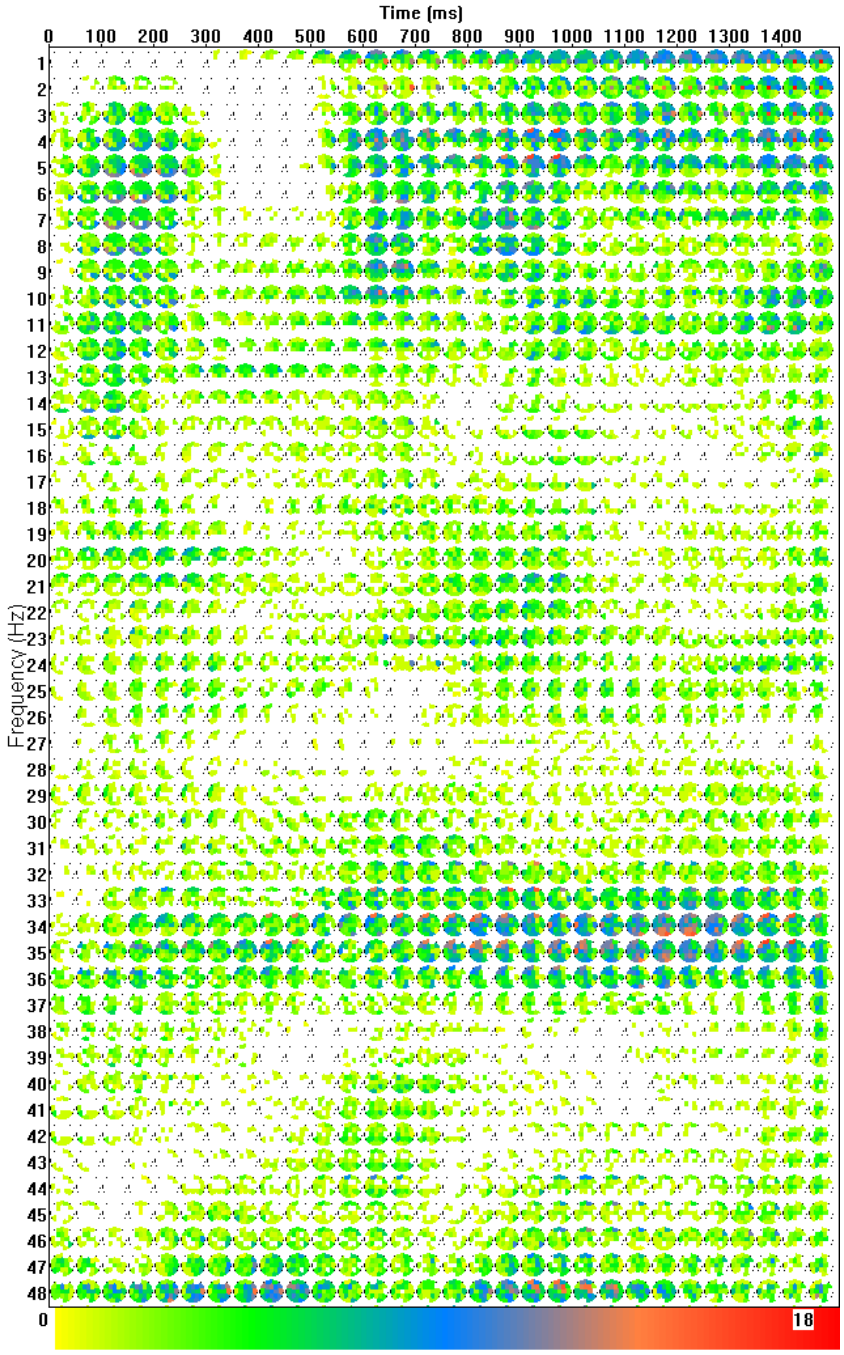

Figure A.39: Full synchrony decrease histogram for the Letters (NO-GO condition) experiment (raw potentials).

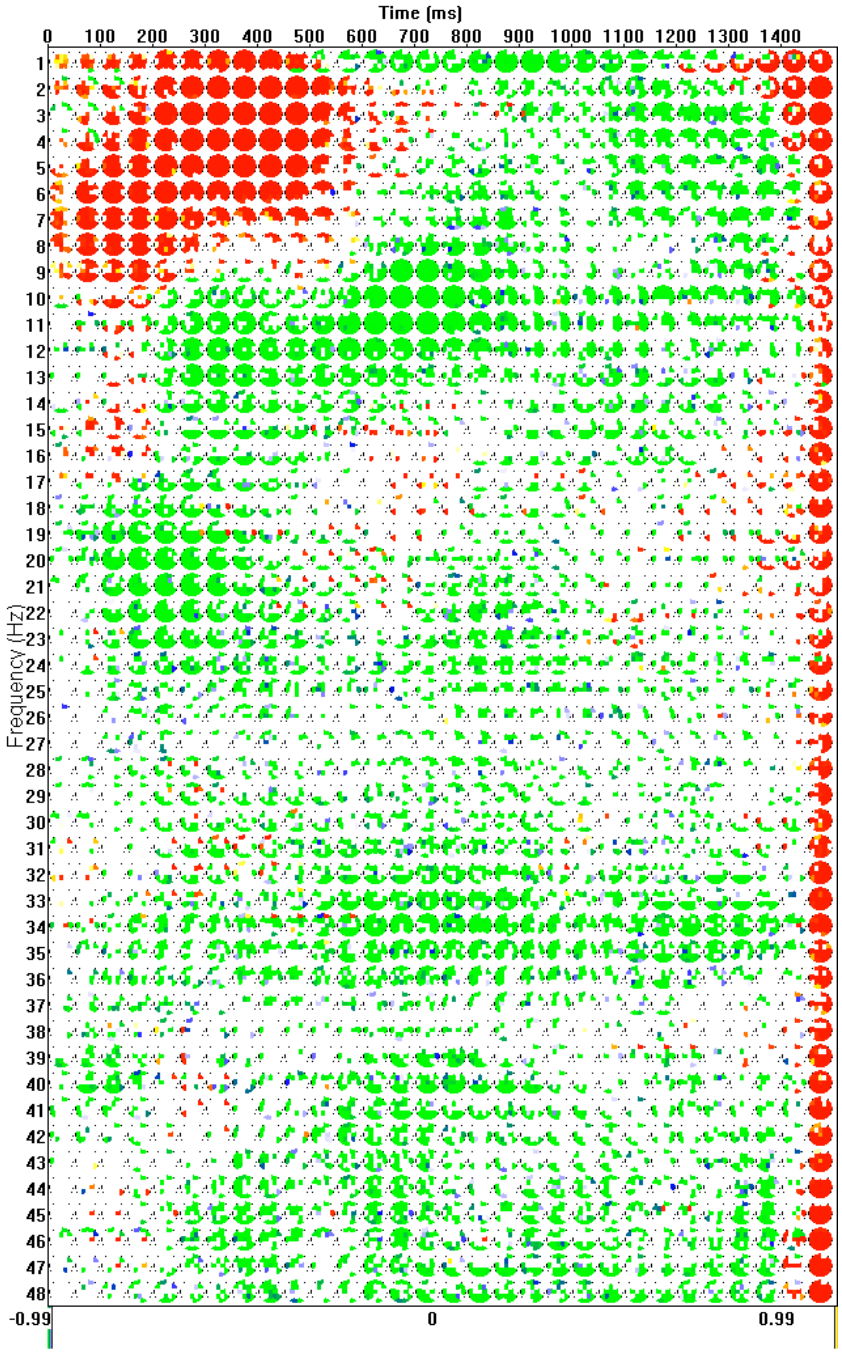

Figure A.40: Map of significant amplitude changes for the Letters (NO-GO condition) experiment (raw potentials).

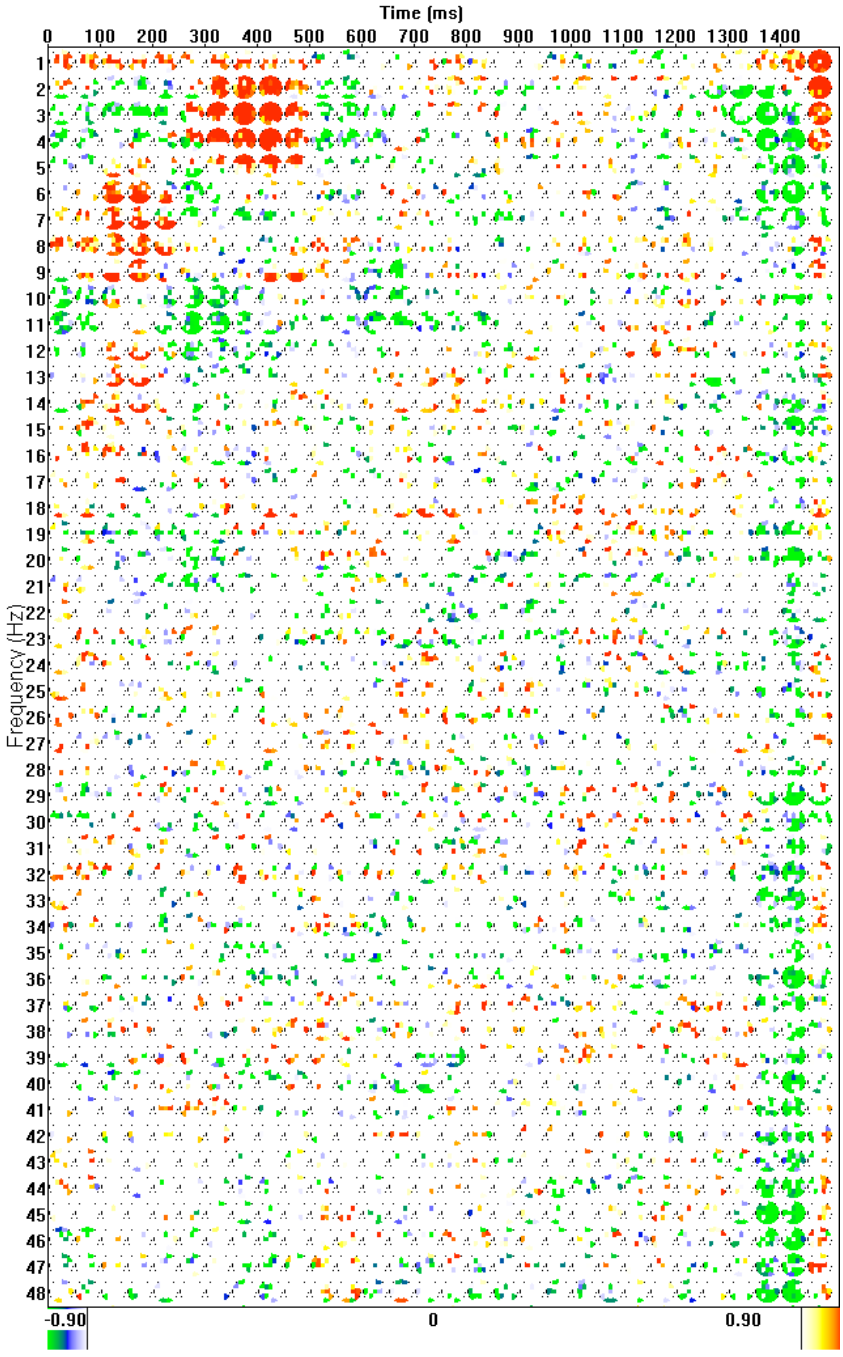

Figure A.41: Map of significant LPC changes for the Letters (NO-GO condition) experiment ((raw potentials).

	MPD	CPPD	PLS	STPLS	Coherence
MPD	1	0.747	0.854	0.294	0.355
CPPD	0.747	1	0.631	0.233	0.283
PLS	0.854	0.631	1	0.334	0.397
STPLS	0.294	0.233	0.334	1	0.869
Coherence	0.355	0.283	0.397	0.869	1

	LPD
MPD	0.255
CPPD	0.212
PLS	0.257
STPLS	0.854
Coherence	0.794

Figure A.42: Correlation table of synchrony measures for the Letters (NO-GO condition) experiment (raw potentials).

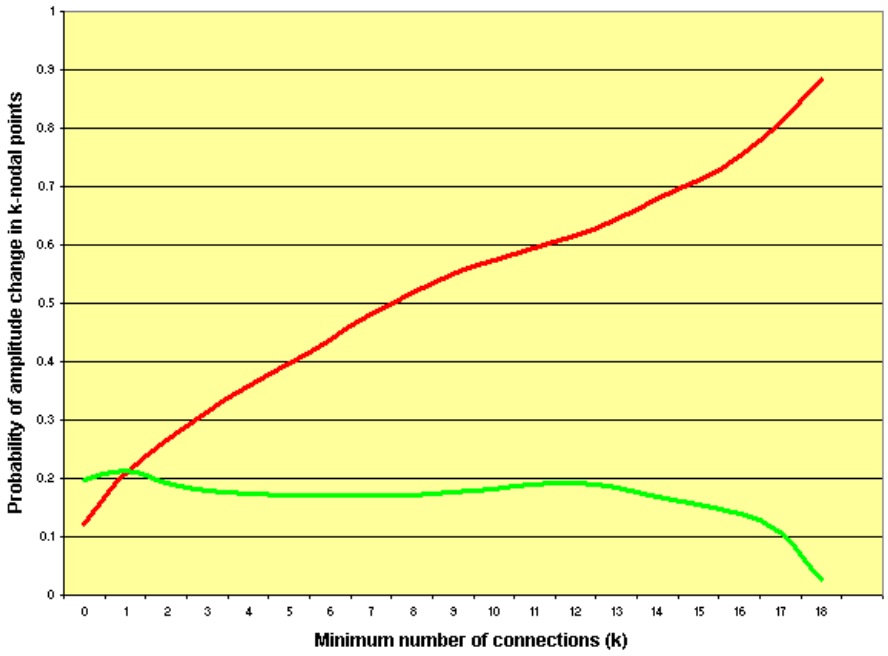

Figure A.43: Conditional probabilities of amplitude increase (red) and decrease (green) in nodal points for the Letters (NO-GO condition) experiment (raw potentials).

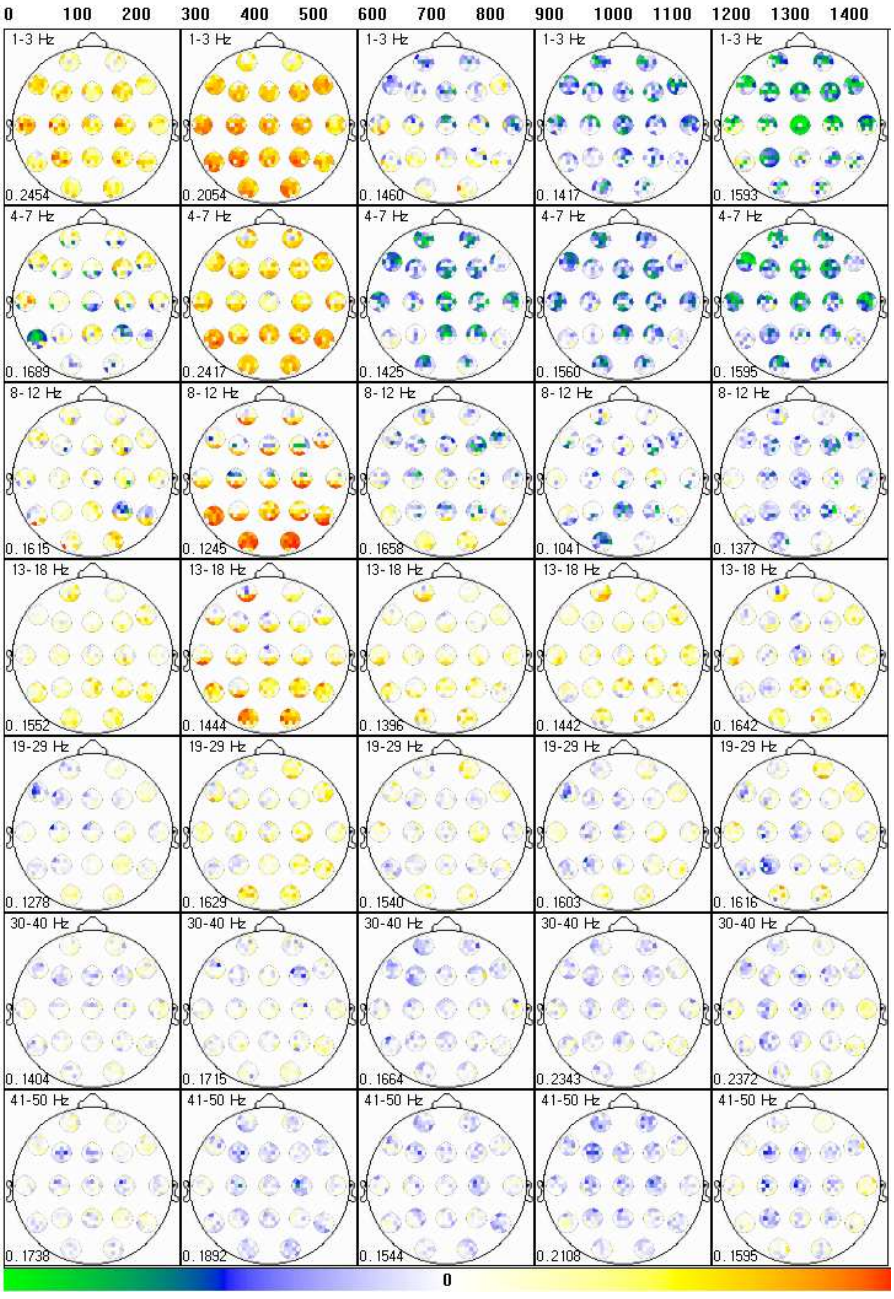

Figure A.44: Full automatic partition for the Letters (NO-GO condition) experiment (projected signals).

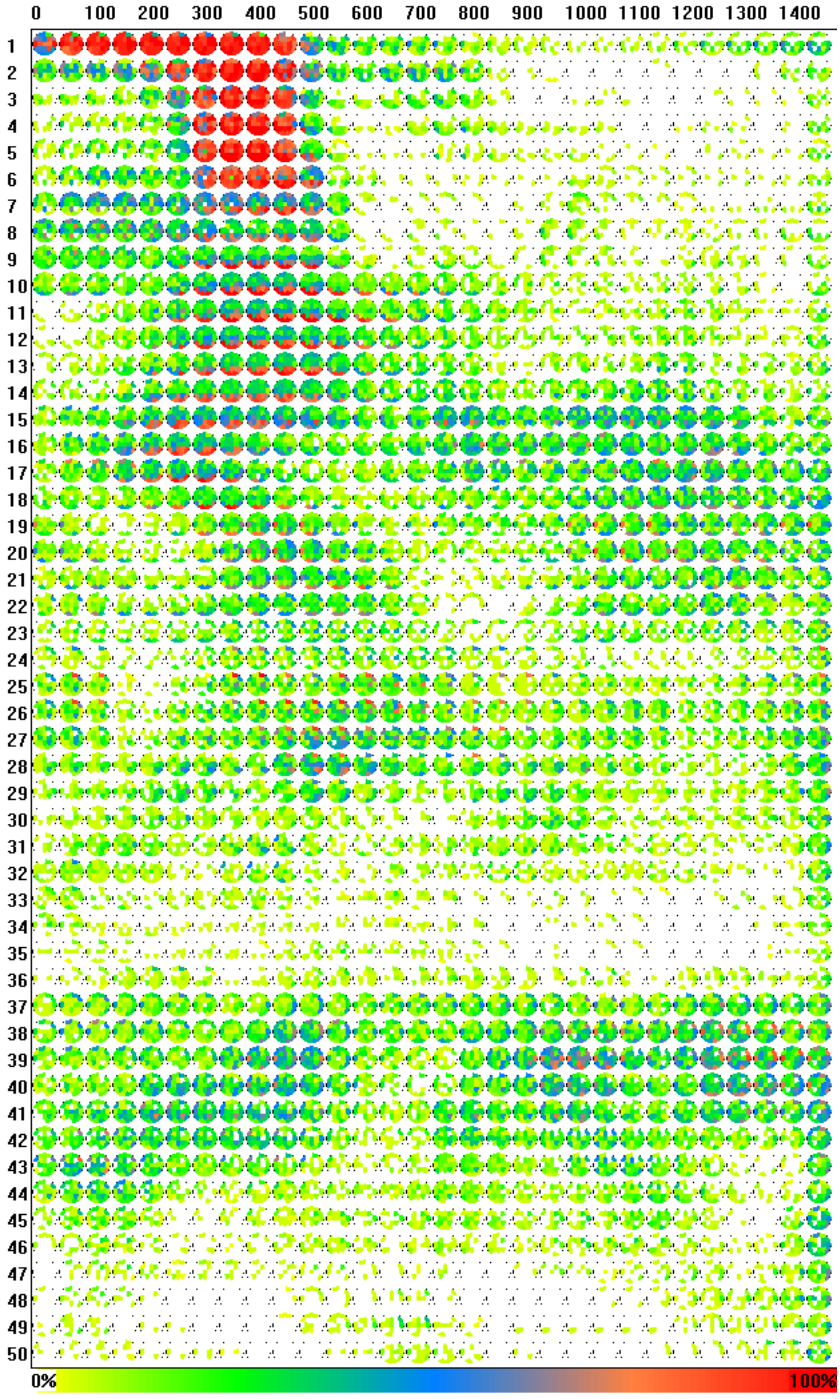

Figure A.45: Full synchrony increase histogram for the Letters (NO-GO condition) experiment (projected signals).

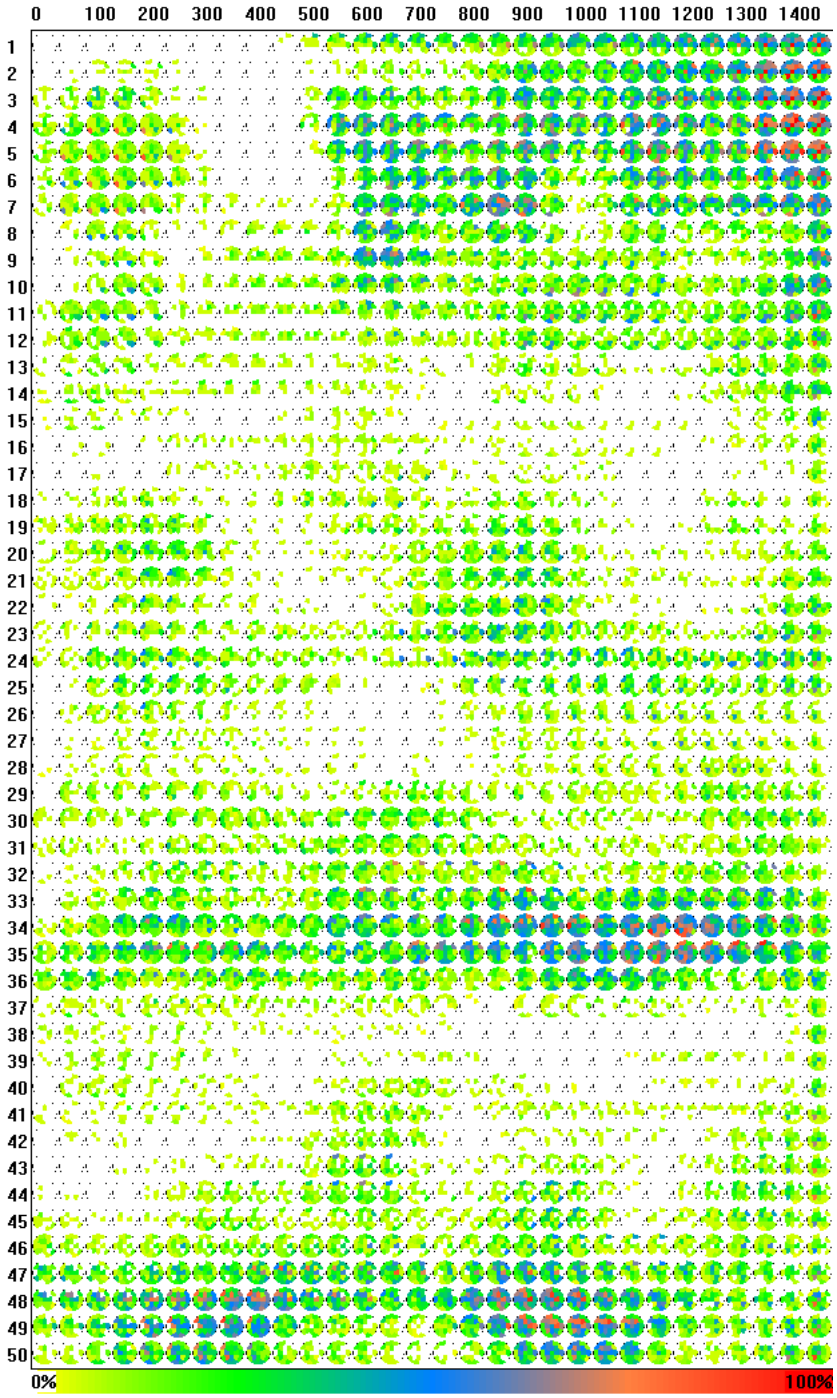

Figure A.46: Full synchrony decrease histogram for the Letters (NO-GO condition) experiment (projected signals).

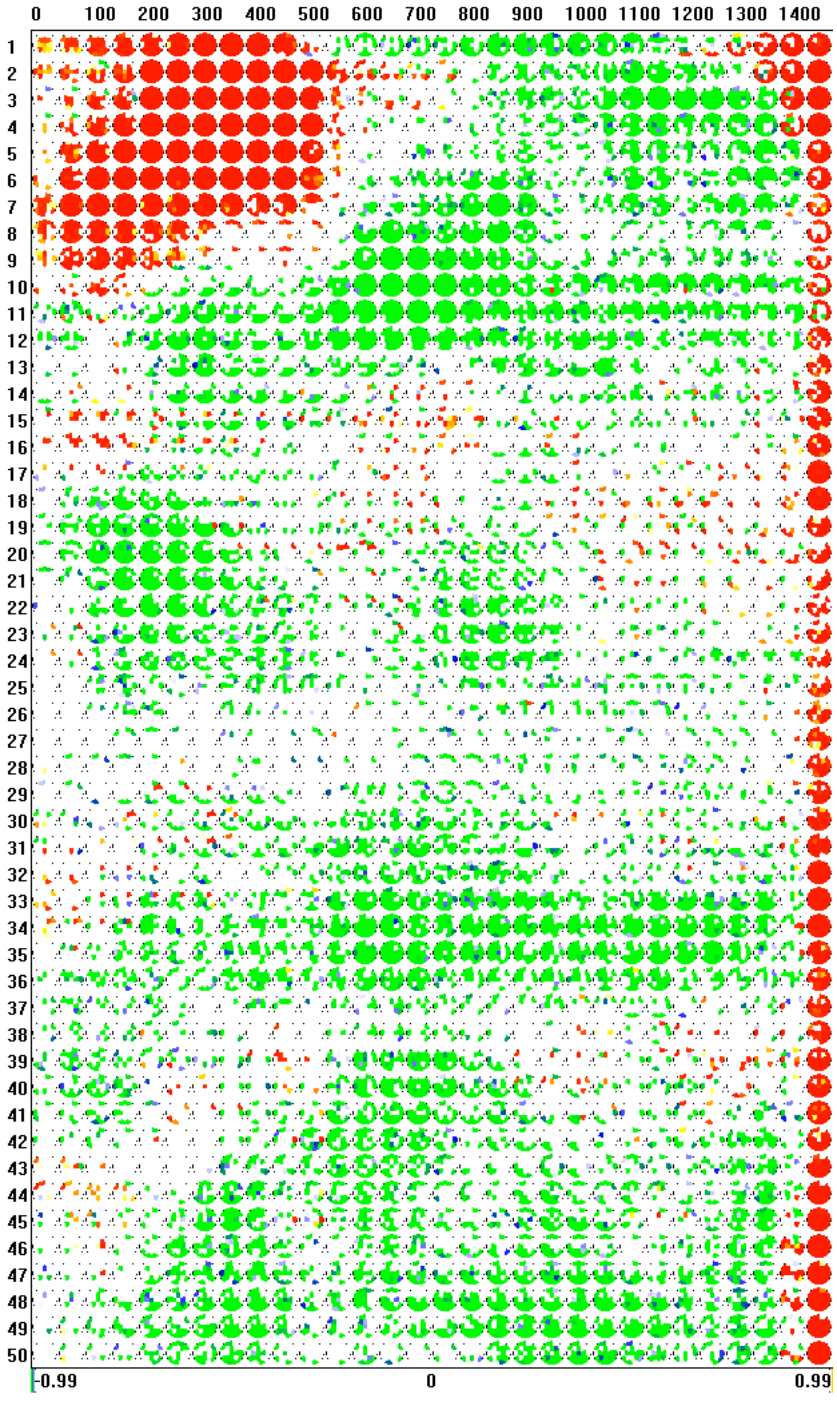

Figure A.47: Map of significant amplitude changes for the Letters (NO-GO condition) experiment (projected signals).

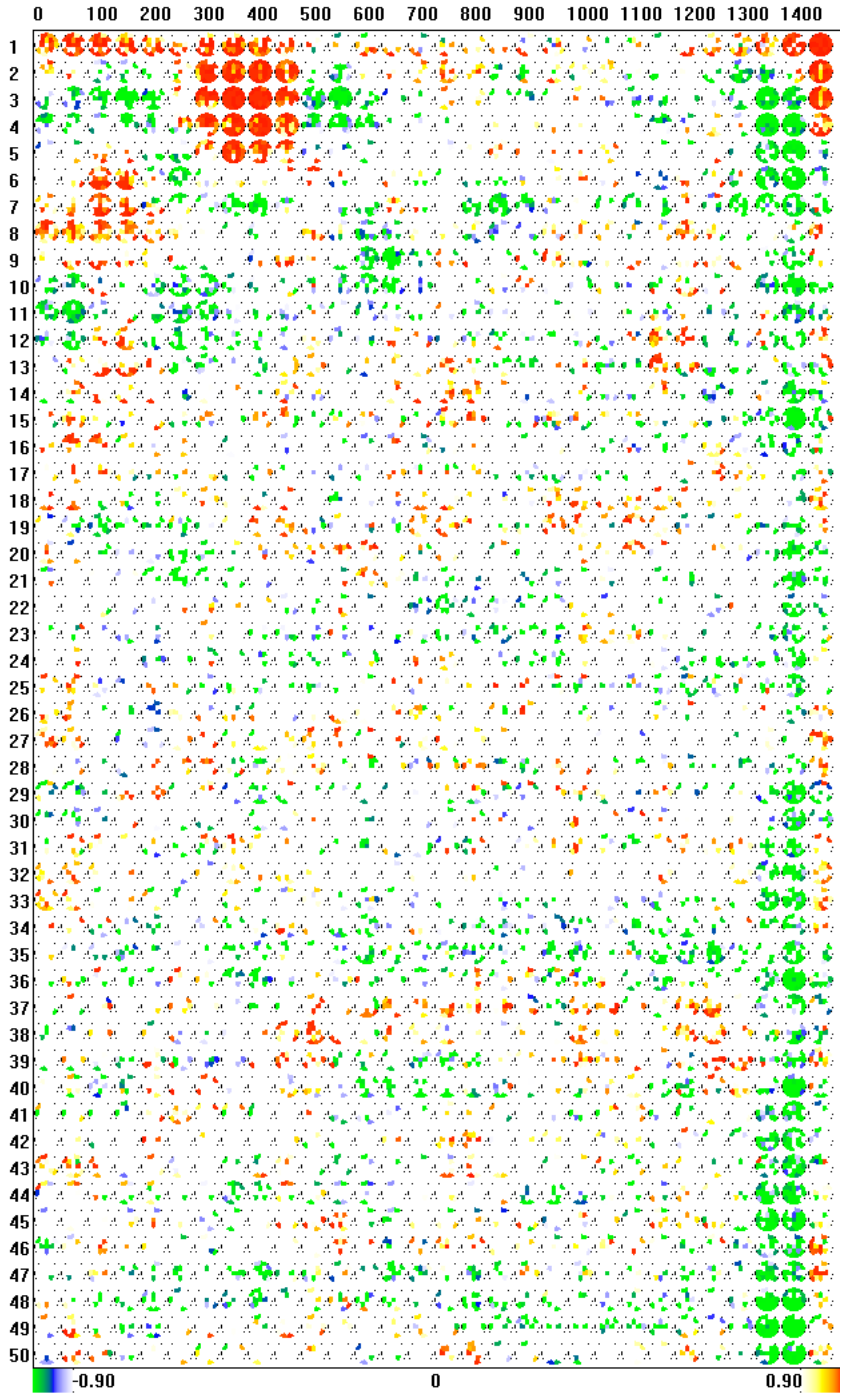

Figure A.48: Map of significant LPC changes for the Letters (NO-GO condition) experiment (projected signals).

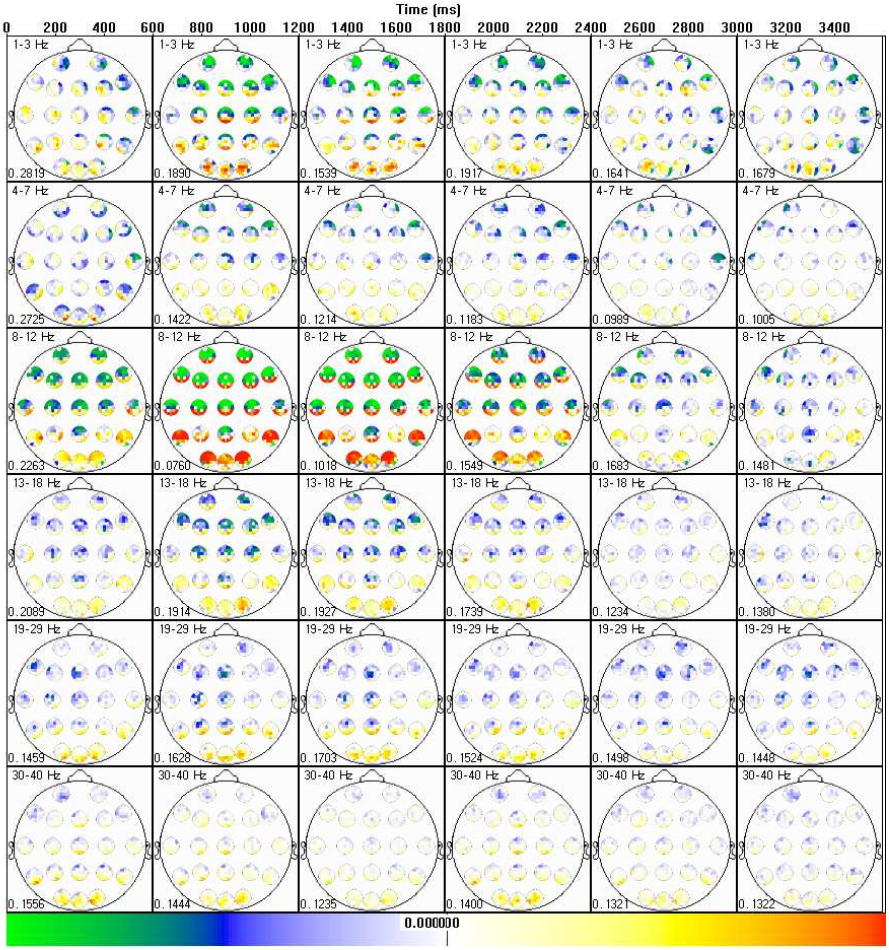

Figure A.49: Full automatic partition for the 3-digit Sternberg experiment (raw potentials).

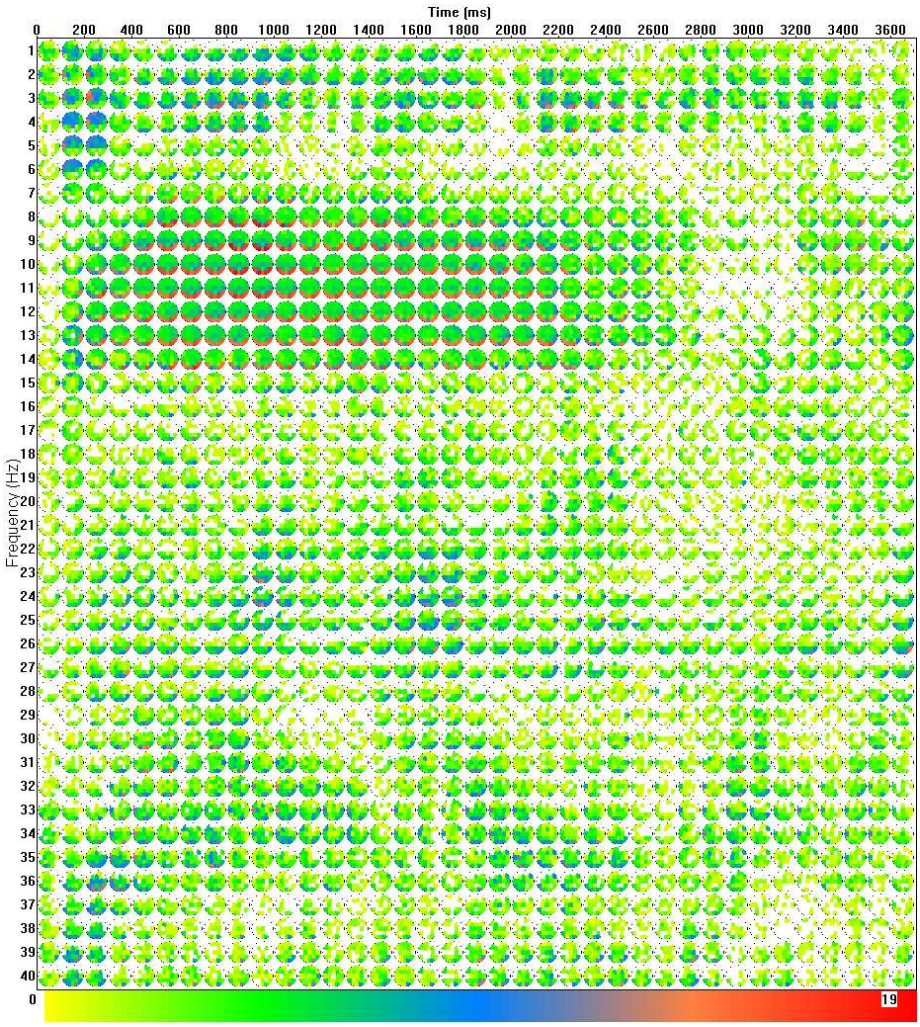

Figure A.50: Full synchrony increase histogram for the 3-digit Sternberg experiment (raw potentials).

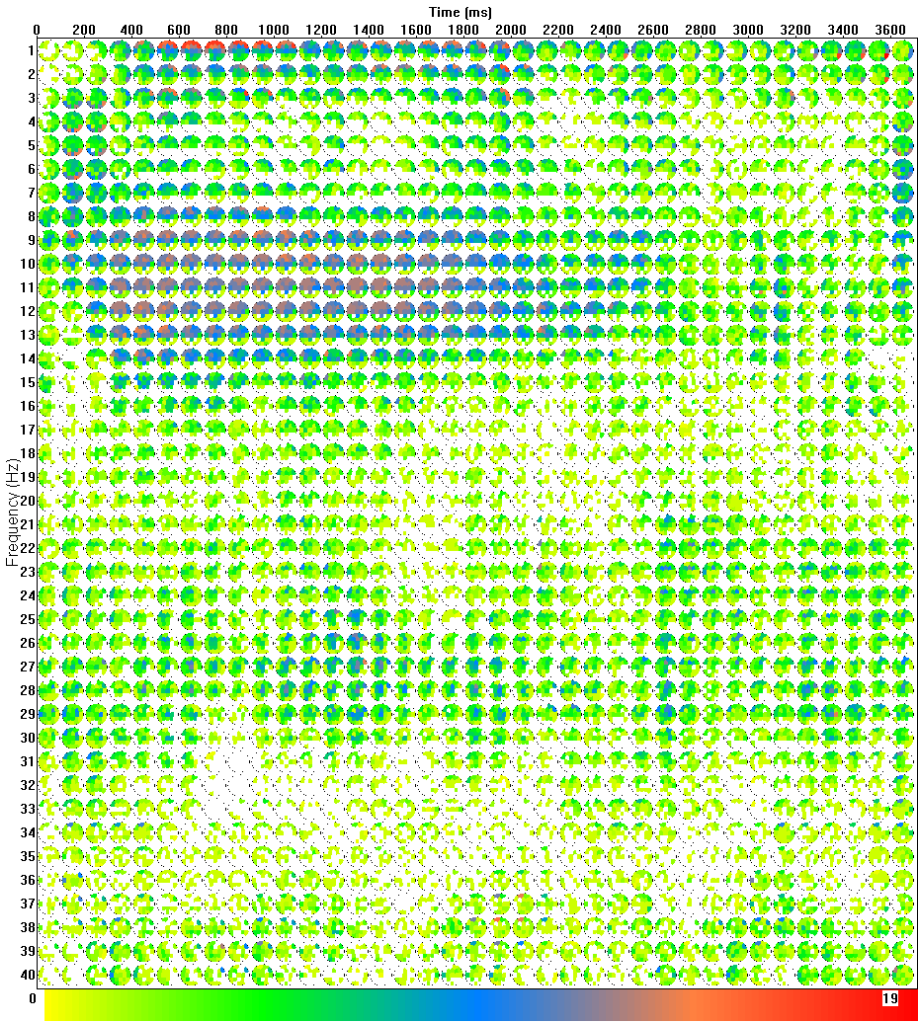

Figure A.51: Full synchrony decrease histogram for the 3-digit Sternberg experiment (raw potentials).

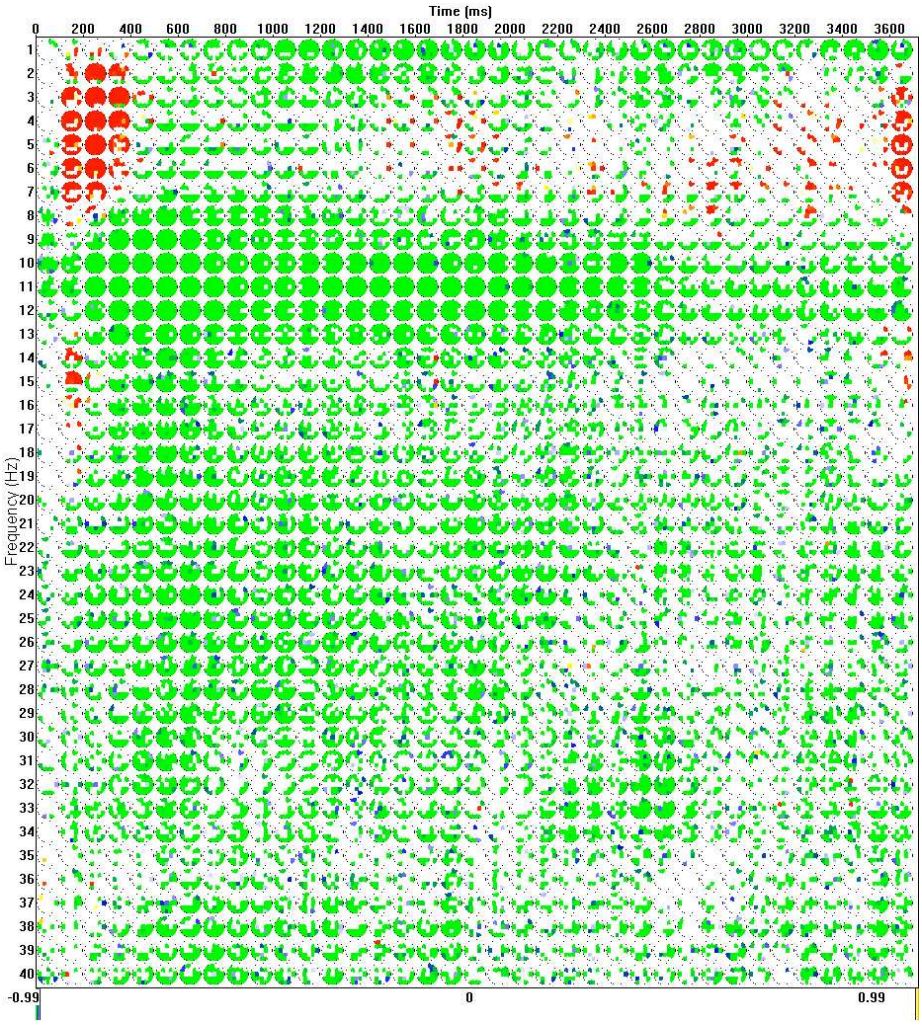

Figure A.52: Map of significant amplitude changes for the 3-digit Sternberg experiment (raw potentials).

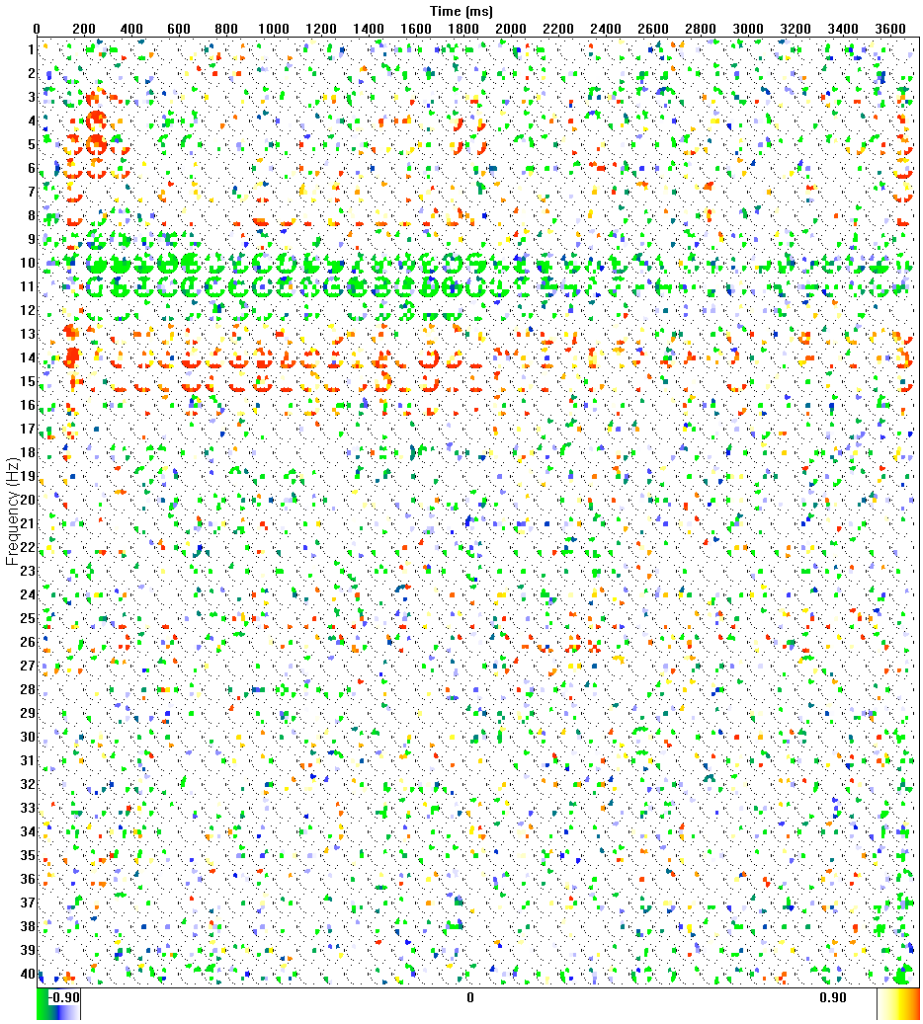

Figure A.53: Map of significant LPC changes for the 3-digit Sternberg experiment ((raw potentials).

	MPD	CPPD	PLS	STPLS	Coherence
MPD	1	0.772	0.751	0.187	0.248
CPPD	0.772	1	0.556	0.128	0.174
PLS	0.751	0.556	1	0.275	0.342
STPLS	0.187	0.128	0.275	1	0.912
Coherence	0.248	0.174	0.342	0.912	1

	LPD
MPD	0.151
CPPD	0.114
PLS	0.198
STPLS	0.848
Coherence	0.796

Figure A.54: Correlation table of synchrony measures for the 3-digit Sternberg experiment (raw potentials).

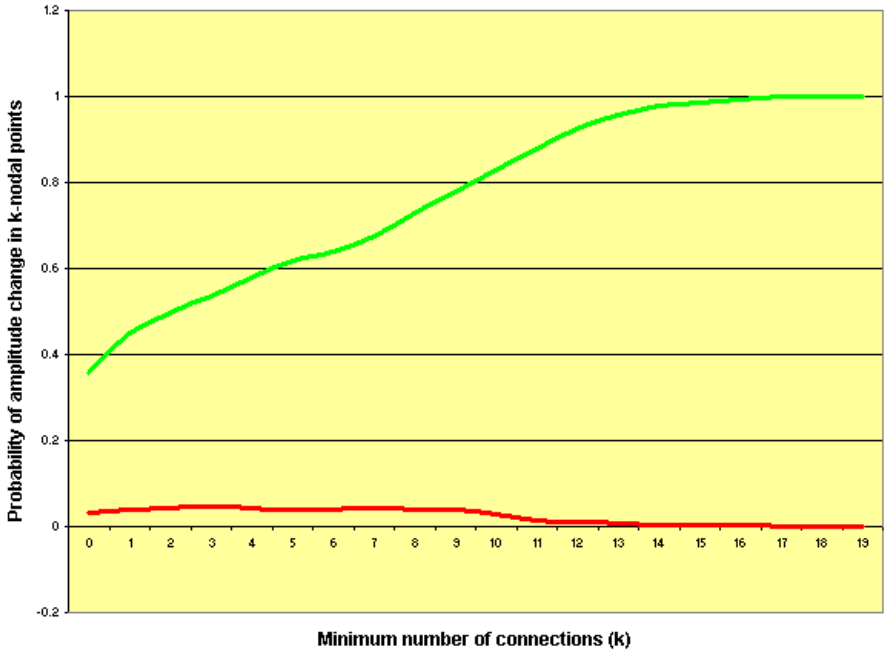

Figure A.55: Conditional probabilities of amplitude increase (red) and decrease (green) in nodal points for the 3-digit Sternberg experiment (raw potentials).

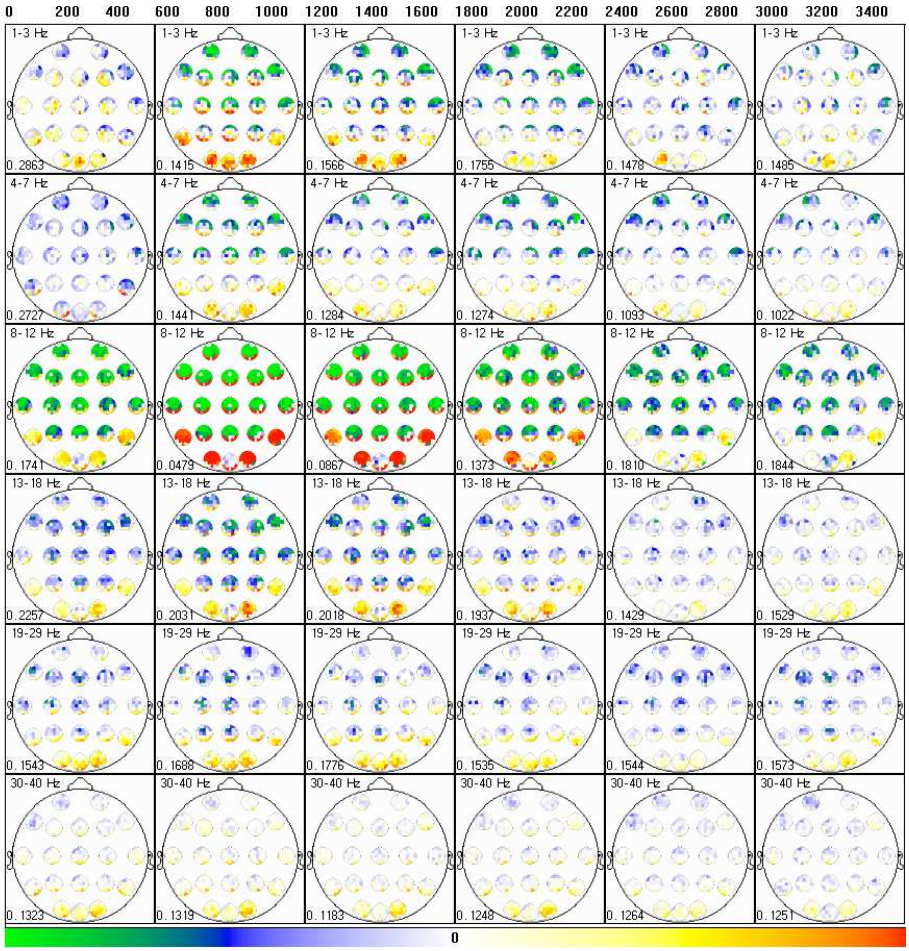

Figure A.56: Full automatic partition for the 3-digit Sternberg experiment (projected signals).

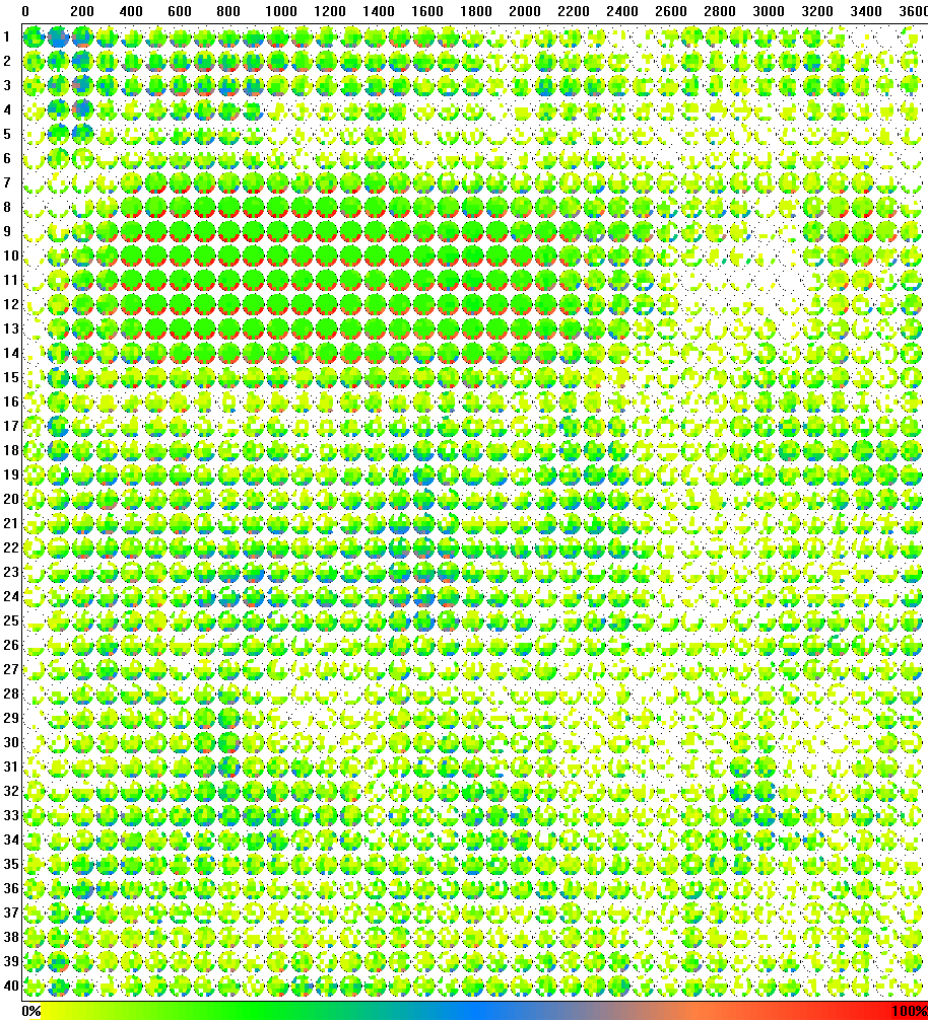

Figure A.57: Full synchrony increase histogram for the 3-digit Sternberg experiment (projected signals).

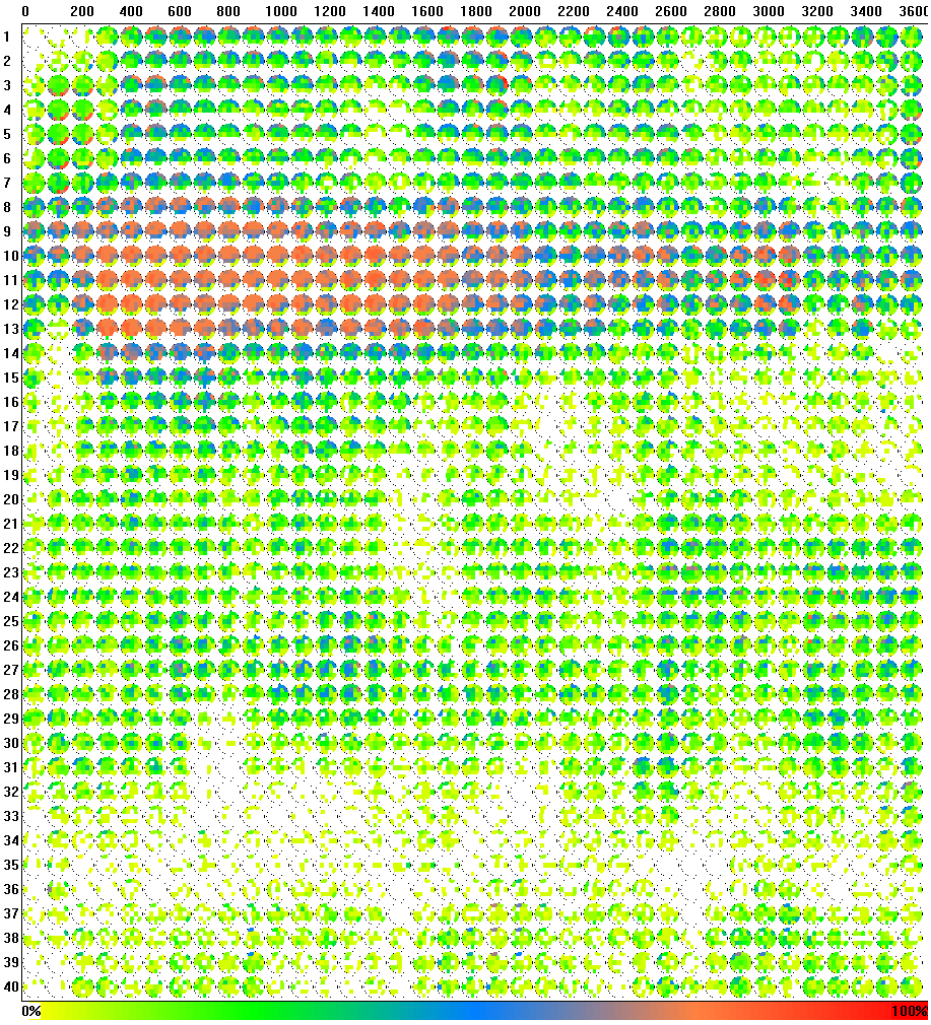

Figure A.58: Full synchrony decrease histogram for the 3-digit Sternberg experiment (projected signals).

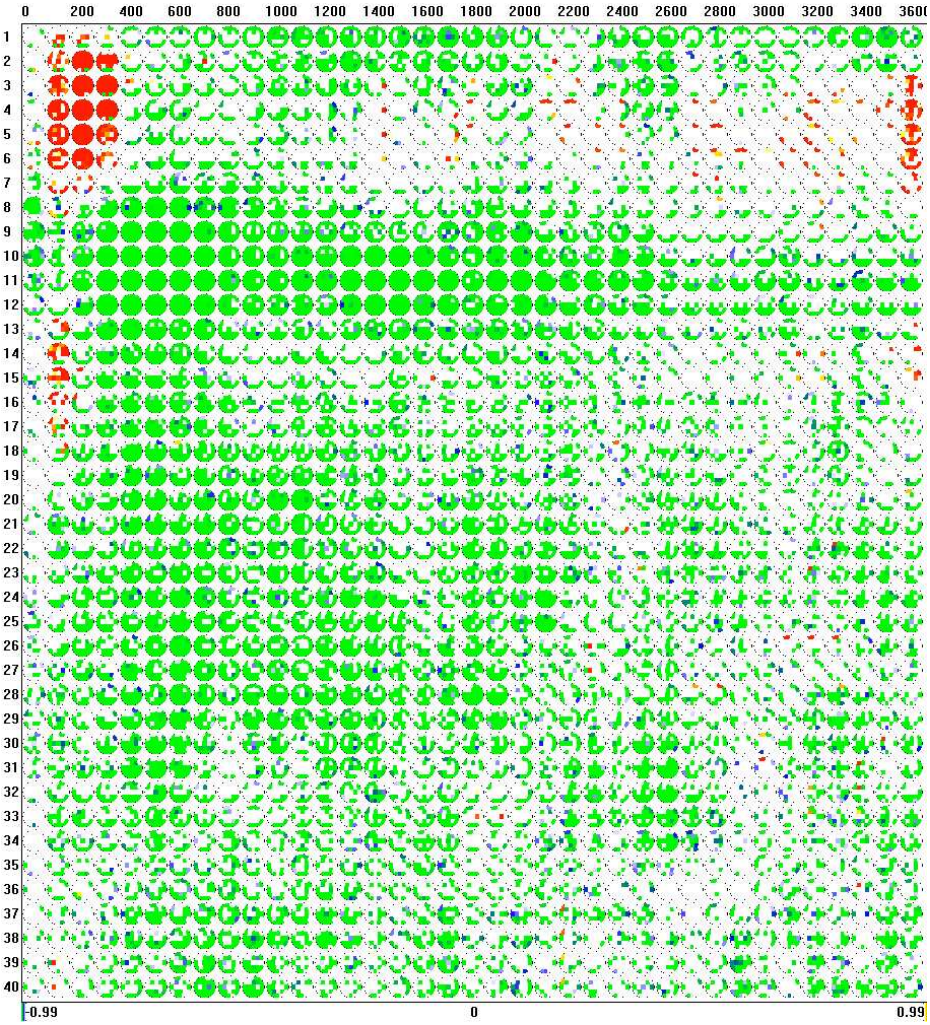

Figure A.59: Map of significant amplitude changes for the 3-digit Sternberg experiment (projected signals).

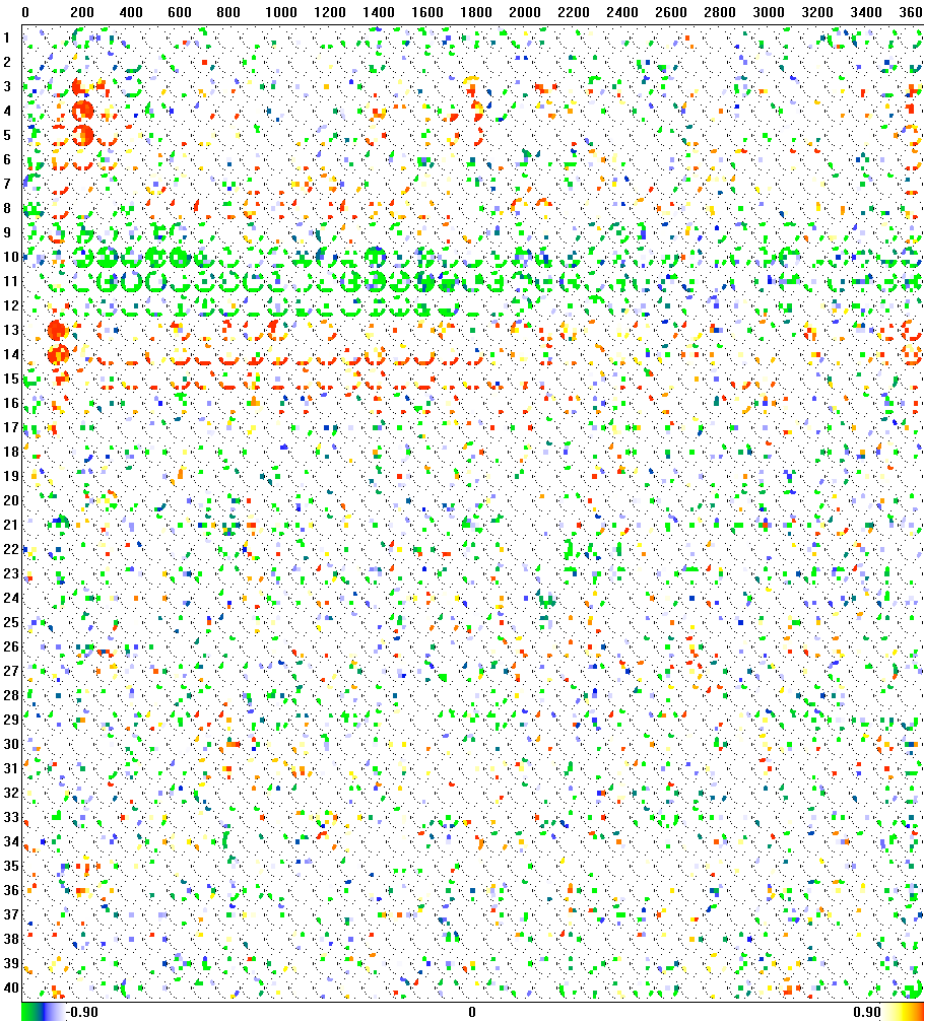

Figure A.60: Map of significant LPC changes for the 3-digit Sternberg experiment (projected signals).

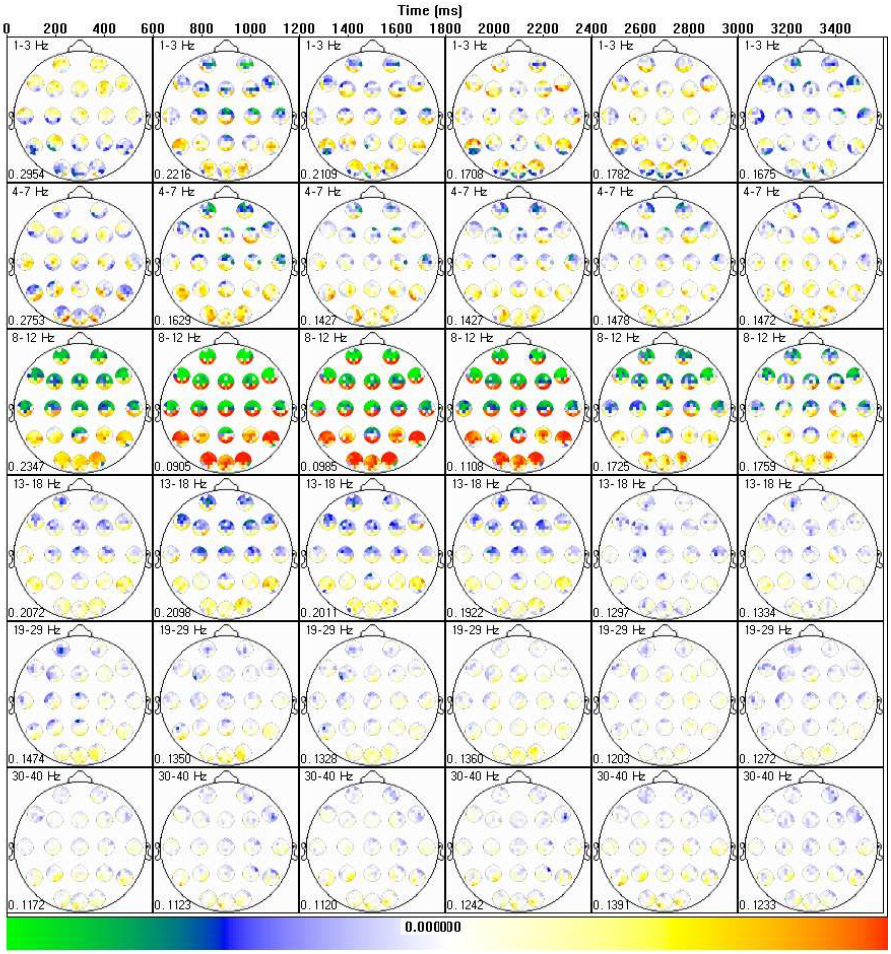

Figure A.61: Full automatic partition for the 5-digit Sternberg experiment (raw potentials).

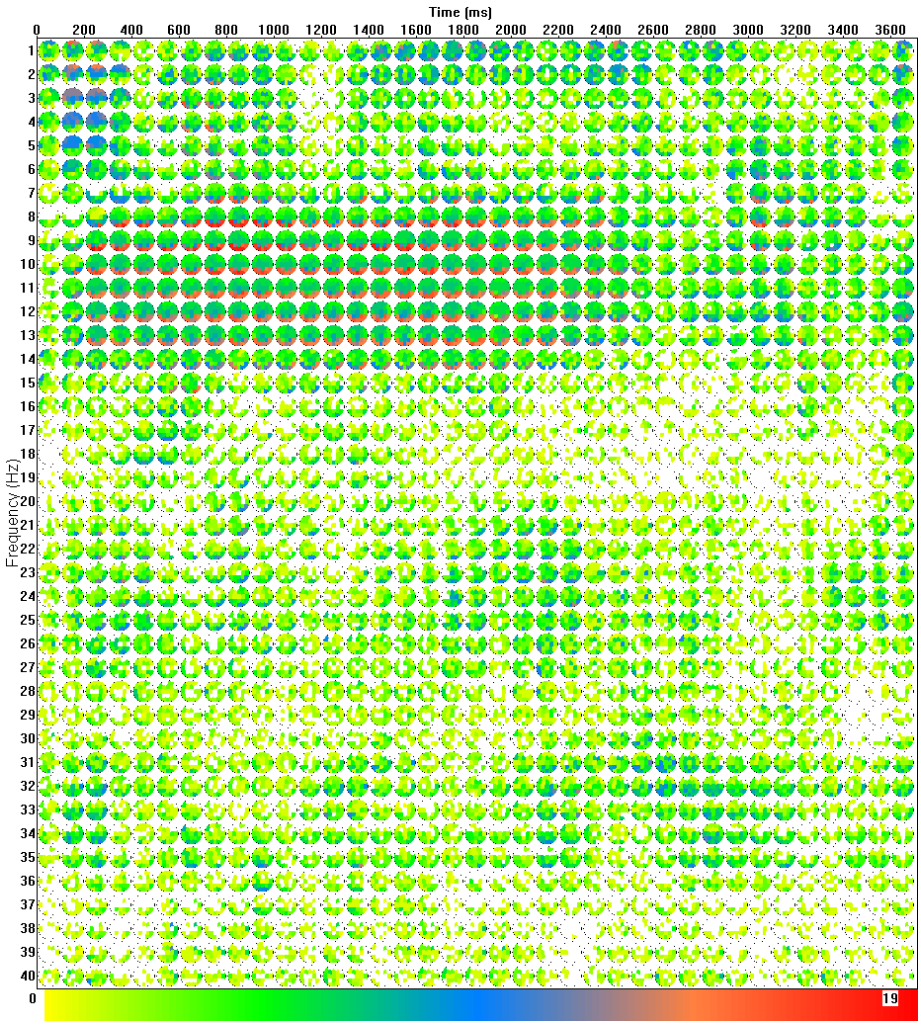

Figure A.62: Full synchrony increase histogram for the 5-digit Sternberg experiment (raw potentials).

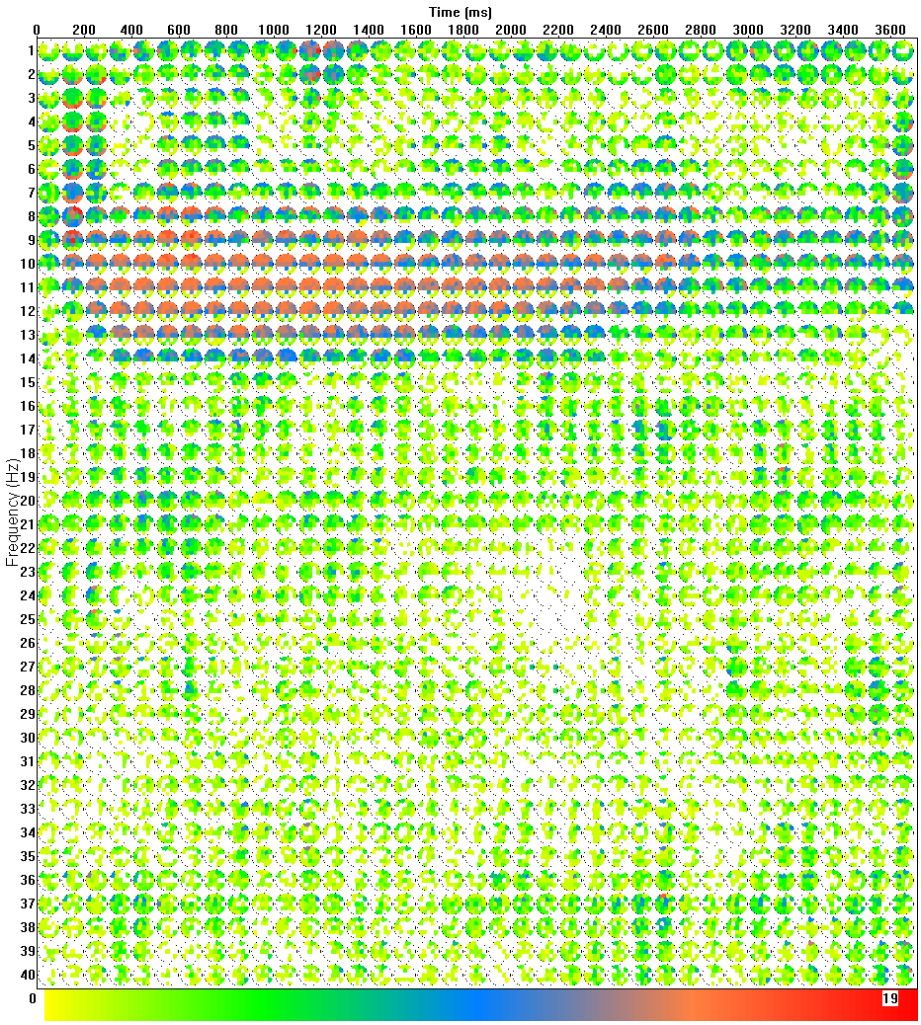

Figure A.63: Full synchrony decrease histogram for the 5-digit Sternberg experiment (raw potentials).

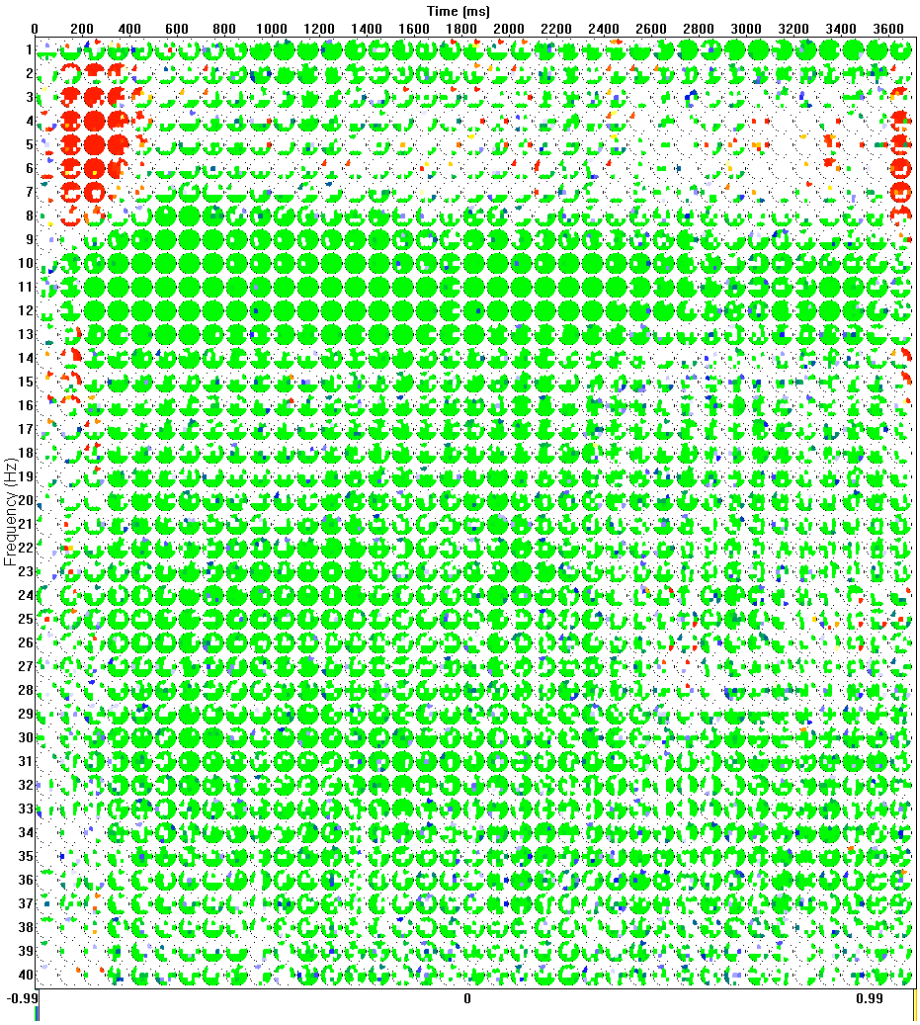

Figure A.64: Map of significant amplitude changes for the 5-digit Sternberg experiment (raw potentials).

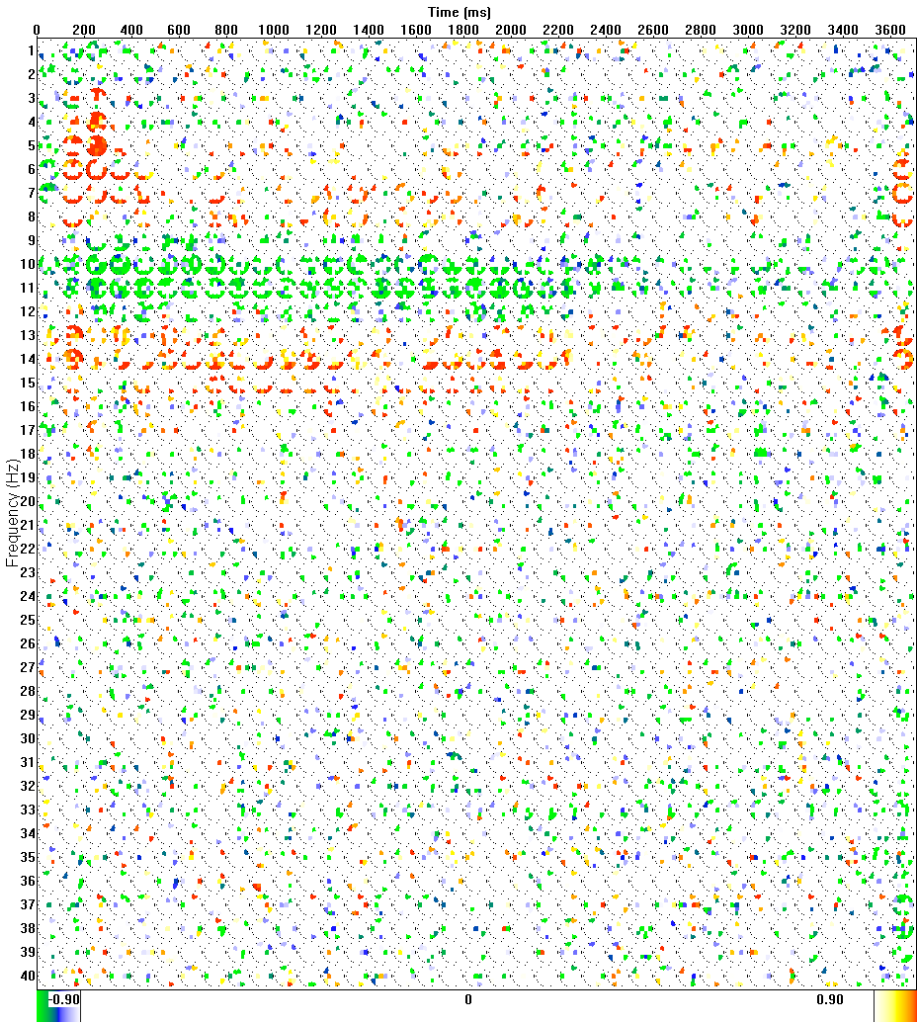

Figure A.65: Map of significant LPC changes for the 5-digit Sternberg experiment ((raw potentials).

	MPD	CPPD	PLS	STPLS	Coherence
MPD	1	0.765	0.746	0.185	0.246
CPPD	0.765	1	0.548	0.133	0.18
PLS	0.746	0.548	1	0.272	0.335
STPLS	0.185	0.133	0.272	1	0.913
Coherence	0.246	0.18	0.335	0.913	1

	LPD
MPD	0.167
CPPD	0.143
PLS	0.22
STPLS	0.843
Coherence	0.796

Figure A.66: Correlation table of synchrony measures for the 5-digit Sternberg experiment (raw potentials).

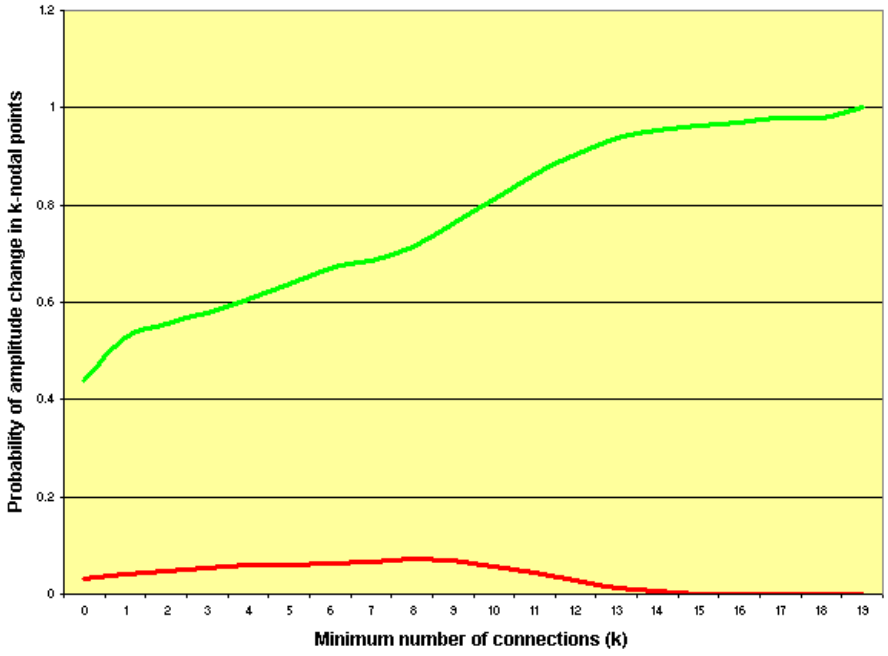

Figure A.67: Conditional probabilities of amplitude increase (red) and decrease (green) in nodal points for the 5-digit Sternberg experiment (raw potentials).

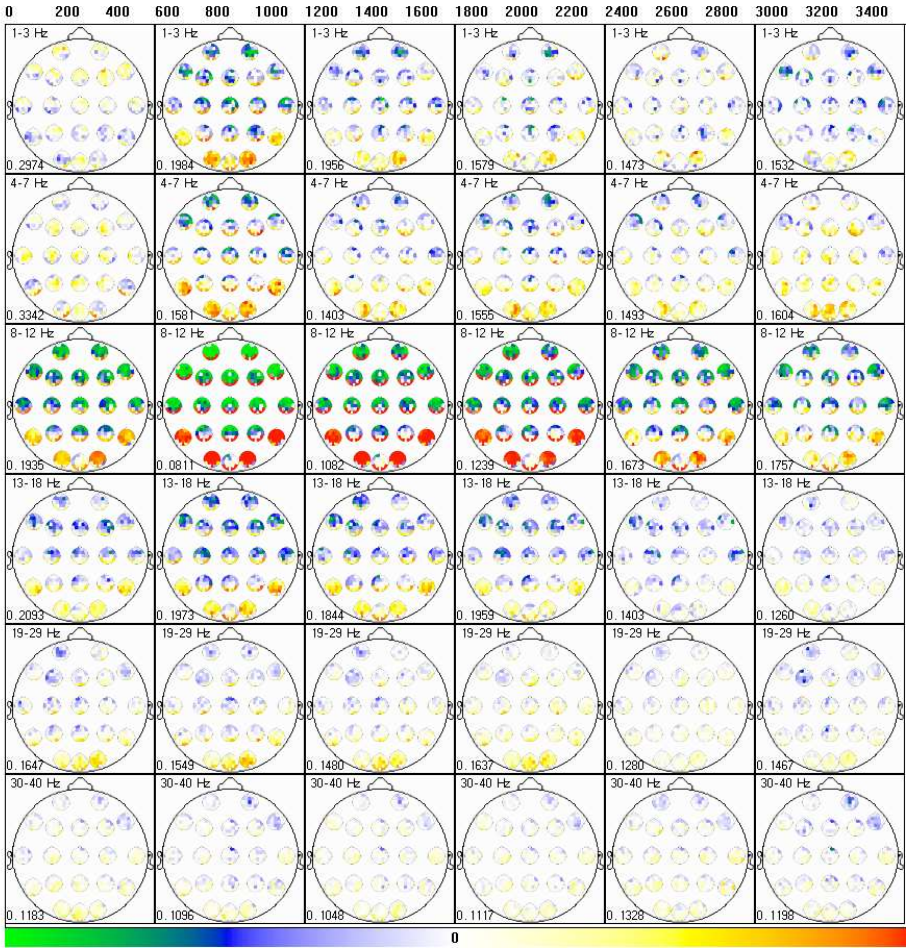

Figure A.68: Full automatic partition for the 5-digit Sternberg experiment (projected signals).

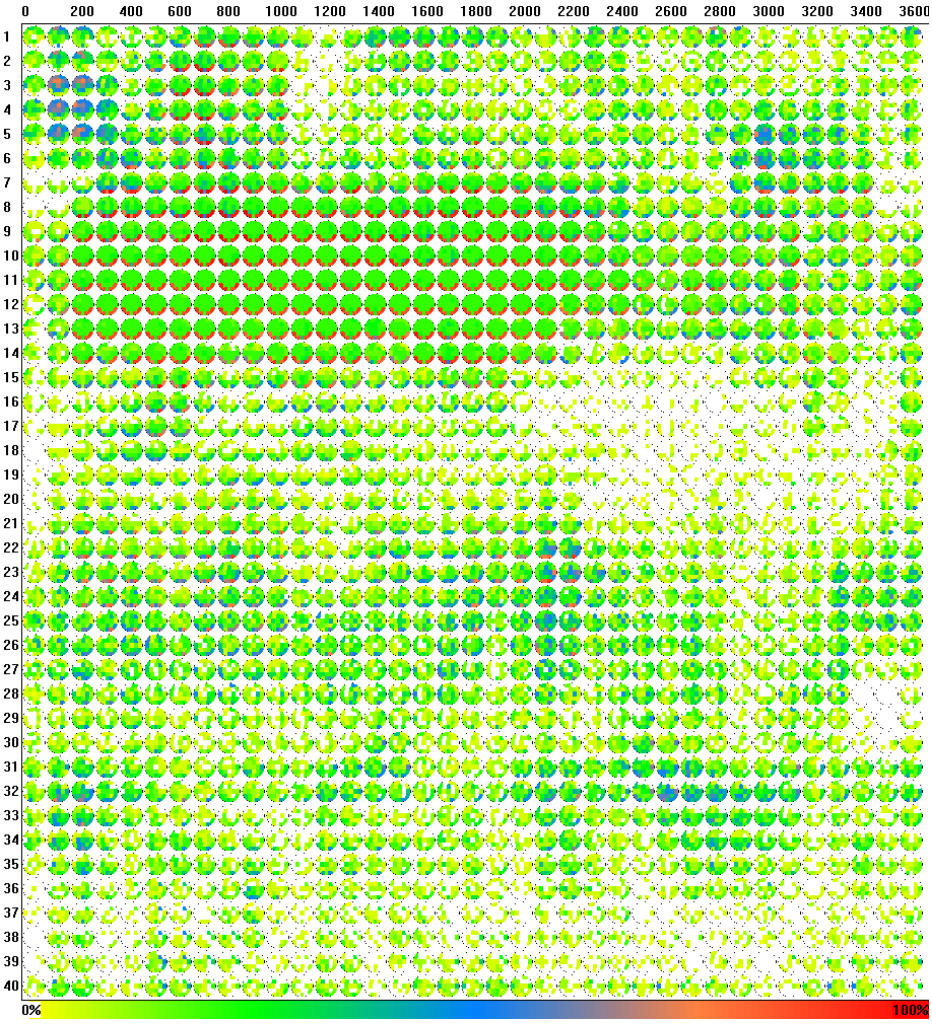

Figure A.69: Full synchrony increase histogram for the 5-digit Sternberg experiment (projected signals).

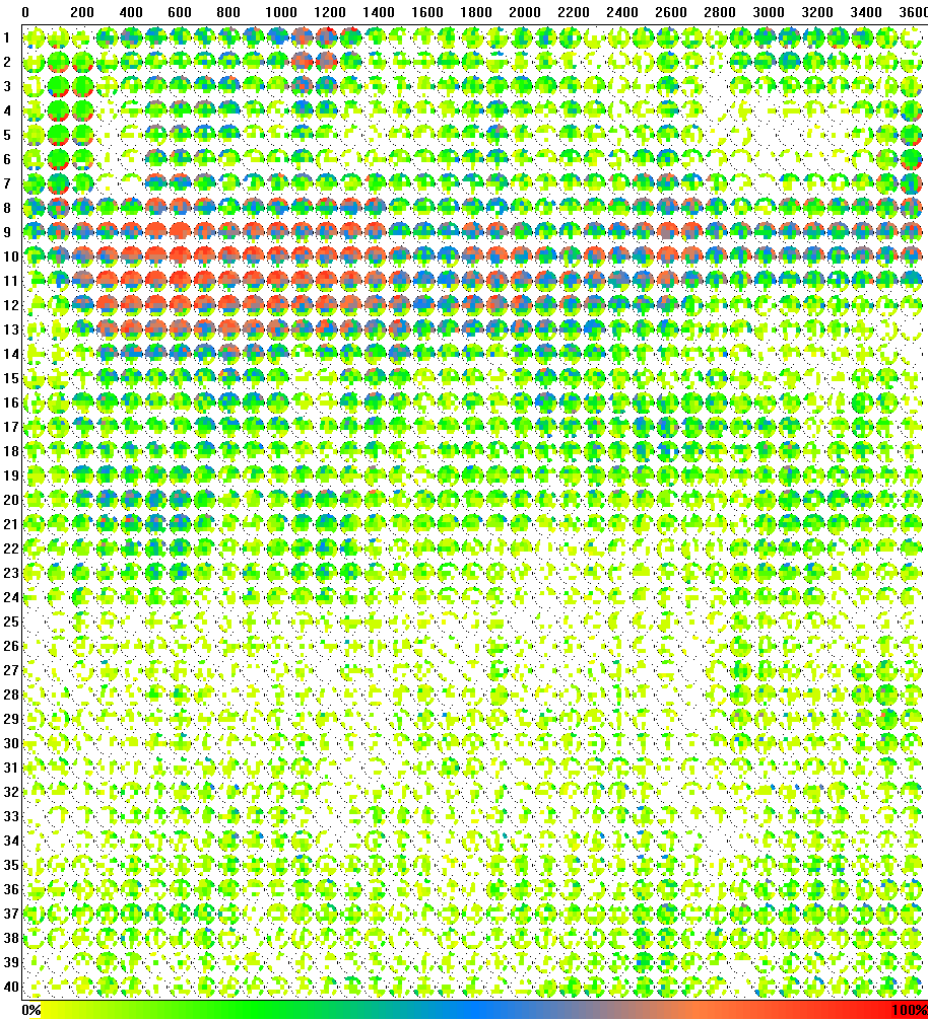

Figure A.70: Full synchrony decrease histogram for the 5-digit Sternberg experiment (projected signals).

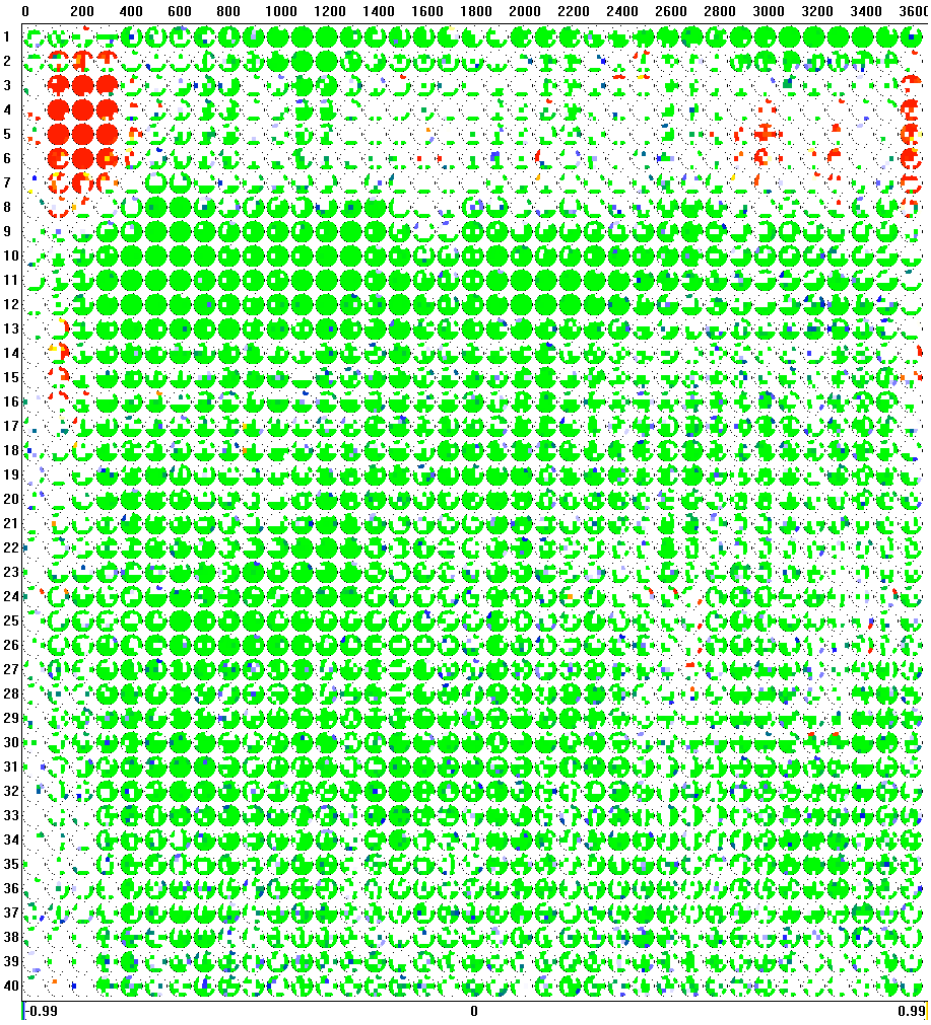

Figure A.71: Map of significant amplitude changes for the 5-digit Sternberg experiment (projected signals).

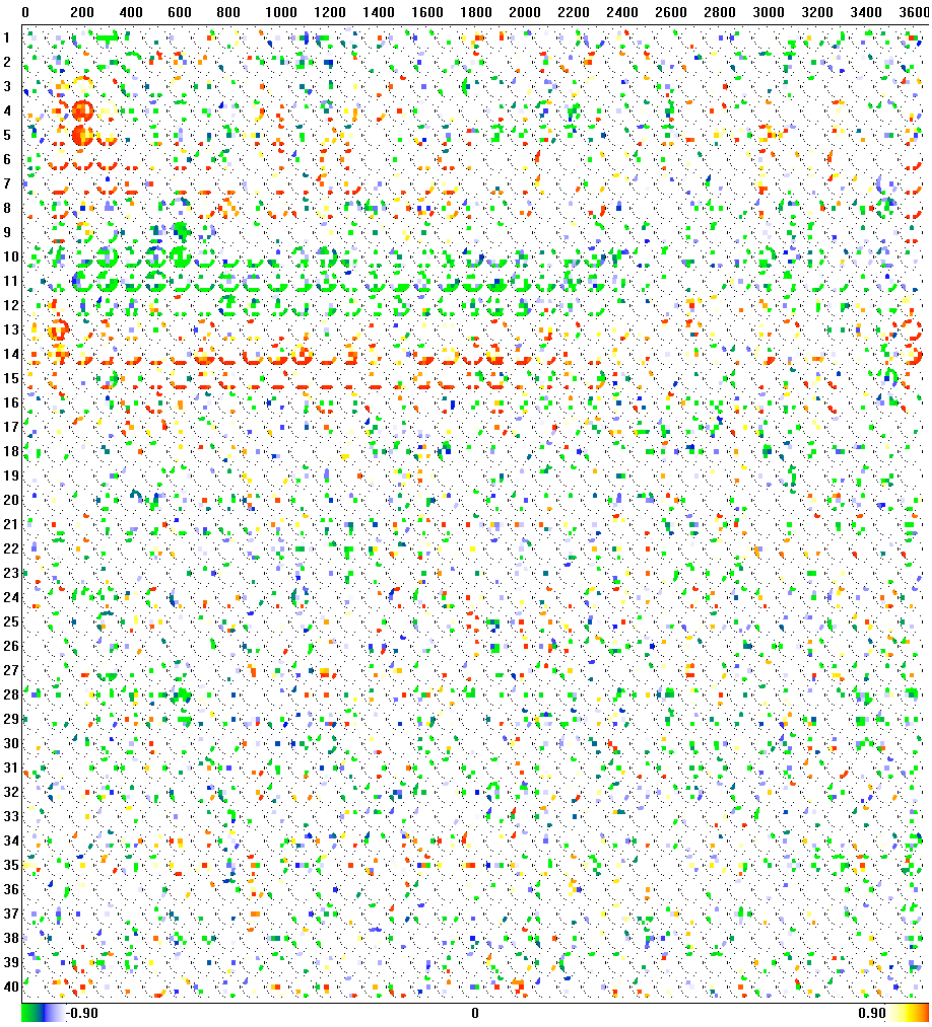

Figure A.72: Map of significant LPC changes for the 5-digit Sternberg experiment (projected signals).

Appendix B

Published works

The following publications and presentations have originated from our work:

- Poster presentation:

  Alba, F.A., Marroquin, J.L., Harmony, T., 2005. An EEG-based methodology for the study of dynamical brain connectivity during cognitive tasks. IX International Conference of Cognitive Neuroscience. Sep, 2005. Havana, Cuba.

- Technical report:

  Alba, A., Marroquin, J.L., Peña, J., Harmony, T., 2006. Analysis and Visualization of EEG Event-Induced Dynamic Synchronization Patterns in Cognitive Tasks. Technical Communication No I-06-05/08-03-2006 (CC/CIMAT).

  `http://www.cimat.mx/reportes/enlinea/I-06-05.zip` (zipped PDF)

- Research article:

  Alba, A., Marroquin, J.L., Peña, J., Harmony, T., Gonzalez-Frankenberger, B., 2006. Exploration of event-induced EEG phase synchronization patterns in cognitive tasks using a timefrequency-topography visualization system. J Neurosci Methods. Vol. 161, Issue 1: 166-182. (in press - uncorrected proof shown below)

Another paper on the analysis of the Letters experiment is being prepared for publication.

+Model
NSM4414 1–17
ARTICLE IN PRESS

ELSEVIER

Journal of Neuroscience Methods xxx (2006) xxx–xxx

JOURNAL OF NEUROSCIENCE METHODS

www.elsevier.com/locate/jneumeth

Exploration of event-induced EEG phase synchronization patterns in cognitive tasks using a time–frequency-topography visualization system

Alfonso Alba [a,c,*], Jose L. Marroquin [a], Joaquin Peña [a], Thalia Harmony [b], Berta Gonzalez-Frankenberger [b]

[a] *Centro de Investigation en Matematicas (CIMAT), Guanajuato, Mexico*
[b] *Instituto de Neurobiologia, UNAM Campus Juriquilla, Queretaro, Mexico*
[c] *Facultad de Ciencias, UASLP, San Luis Potosi, Mexico*

Received 3 August 2006; received in revised form 16 October 2006; accepted 25 October 2006

Abstract

In this paper, we present a method for the study of synchronization patterns measured from EEG scalp potentials in psychophysiological experiments. This method is based on various techniques: a time–frequency decomposition using sinusoidal filters which improve phase accuracy for low frequencies, a Bayesian approach for the estimation of significant synchrony changes, and a time–frequency-topography visualization technique which allows for easy exploration and provides detailed insights of a particular experiment. Particularly, we focus on in-phase synchrony using an instantaneous phase-lock measure. We also discuss some of the most common methods in the literature, focusing on their relevance to long-range synchrony analysis; this discussion includes a comparison among various synchrony measures. Finally, we present the analysis of a figure categorization experiment to illustrate our method.

Keywords: EEG; Phase synchronization; Time–frequency-topography; Sinusoidal filters; Markov random field; Bayesian classification

1. Introduction

In recent years, there has been an increasing interest in EEG related to patterns of synchronization and desynchronization that are observed in the electrophysiological activity of the brain. Interest in these phenomena has developed as a result of the view that they might provide a window on the dynamics of cell assembly formation, by which spatially distributed brain areas become linked together in dynamic networks involved in sensory integration, object representation, and memory encoding or retrieval (Kirschfeld, 2005; Bastiaansen and Hagoort, 2003).

Oscillations in the EEG indicate periodic activity of large populations of synchronized neurons which are usually called neuronal assemblies, a term coined by Hebb (1949). The formation of such assemblies is observed in various sensory, behavioral or cognitive states. Several kinds of events, the most notably being sensory stimuli, produce two different types of EEG changes: "evoked" activities which are exactly time-locked and phase-locked to the stimulus, and "induced" activities which are changes in the EEG that are only approximately time-locked, but not phase-locked (Pfurtscheller and Lopes da Silva, 1999), and thus cannot be extracted by a simple linear method such as averaging, but may be detected by frequency analysis. Induced activity is thought to reflect functional changes in the parameters controlling dynamic interactions within and between brain structures. This means that these induced-related phenomena represent frequency specific changes of the ongoing EEG activity, and may consist, in general terms, either on increases or decreases of power in specific regions of the time–frequency (TF) plane. This may be considered to be due to an increase or a decrease in synchrony of the underlying neuronal populations, respectively (Pfurtscheller, 1977, 1992), and thus are accordingly called "event-related synchronization" (ERS) and "event-related desynchronization" (ERD). These events may be characterized by specific activation patterns, which are located in particular regions of the TF plane, and which may be associated with specific cognitive sub-processes (Marroquin et al., 2004; Harmony et al., 2001).

There is, however, another important characteristic of these events, which cannot be measured directly by relative power changes: the formation of dynamic global assemblies, which

* Corresponding author at: CIMAT, Apartado Postal 402, Guanajuato, Gto. 36240, Mexico. Tel.: +52 473 7327155x49673; fax: +52 473 7325749.
E-mail address: falbac@cimat.mx (A. Alba).

0165-0270/$ – see front matter © 2006 Published by Elsevier B.V. All right reserved.
doi:10.1016/j.jneumeth.2006.10.018

according to the definition by Varela et al. (2001), are "distributed local networks of neurons transiently linked by reciprocal dynamic (possibly long range) connections". It is generally accepted that these connections are correlated with the synchronization of the corresponding EEG signals in particular regions of the TF plane (Varela et al., 2001; Lopes da Silva, 1991; Singer, 1993). Also, simulations performed with neural mass models show that a bidirectional coupling of two remote cortical areas is reflected as phase synchronization of MEG/EEG oscillations (David and Friston, 2003), which supports the idea that EEG synchrony is highly related to physiological connectivity in the cortex and thus can be used as a measure for long-range interaction.

For these reasons, there have been a number of studies of long range synchronization of EEG signals (Bressler, 1995; Friston et al., 1997; Lachaux et al., 1999, 2000; Rodriguez et al., 1999). Most of these studies, however, have some limitations: on one hand, the high dimensionality of the synchrony data implies a visualization problem. Most works on the field avoid this problem by averaging across a large time window (Quian Quiroga et al., 2002; David et al., 2004; Mizuhara et al., 2005) and/or by limiting the analysis to specific frequency bands (Lachaux et al., 1999; Rodriguez et al., 1999). This is far from ideal since many synchronization patterns appear only in small regions of the TF plane and one cannot obtain, from these results, a complete overall picture of the synchronization dynamics across different frequencies, which may correspond to specific cognitive sub-processes. Another problem is related to the way in which significant synchronization changes are detected. These significant changes must be characterized by a persistent relative phase-locking (or phase scattering) between the signals that correspond to each pair of electrode locations; in other words, to estimate the degree of EEG synchronization one must determine the significance of a phase-locking measure and its consistency across a given time window. The most widely used synchrony measures, such as coherence and the *single trial phase-locking statistic* (STPLS) (Lachaux et al., 2000), attempt to measure this indirectly by computing the synchrony values over a given time interval. The problem with this approach is that, as will be shown later, these measures are strongly affected by local phase dispersion changes occurring in either one of the two signals, which may interfere with the detection of true synchronization or de-synchronization events.

In 2004, Marroquin et al. introduced an exploratory method for the study of ERS and ERD events (power changes), based on time–frequency-topography (TFT) displays which provided a detailed view of the topographical distributions of EEG dynamic power changes with respect to the pre-stimulus, across the full post-stimulus time segment, and at the same time, across all frequencies. The purpose of this work is to extend the TFT exploratory analysis in order to study long-range interactions using various synchrony measures, such as coherence and measures based on the phase difference of the signals. We improve the accuracy of the analysis in terms of the time–frequency decomposition by using sinusoidal quadrature filters (Guerrero et al., 2005) instead of the more popular Gabor filters, and focus on a phase-locking measure which is instantaneous and thus is not dominated by local phase dispersion. Time-persistence is then handled via Bayesian estimation of a hidden Markov random field (MRF) that models a label field in TF space that classifies the interactions between signal pairs as significantly higher, lower or equal to the corresponding pre-stimulus average value. We also present a TFT visualization method that permits one to obtain a full detailed overview of the dynamic synchronization patterns (SP's), which may be correlated with concurrent cognitive processes whose expression is multiplexed at different frequencies. A comparison between different synchrony measures from an interpretative point of view is also presented. Finally, the effectiveness of these techniques is illustrated with the analysis of SP's associated with a figure classification task.

2. Materials and methods

Throughout this presentation we illustrate our procedure using data from a figure classification experiment (Harmony et al., 2001) where white-line figures on a black background were presented to each subject. The subjects were instructed to press a button if the figure corresponded to an animal whose name started with a consonant, and another button if the figure did not correspond to an animal and the name of the figure started with a consonant. If the name started with a vowel, the subject was instructed not to respond. The subjects were 18 normal children (8–10 years old, 9 females), all right handed with normal neurological examination. EEG was recorded with reference to linked ears from Fp1, Fp2, F3, F4, C3, C4, P3, P4, O1, O2, F7, F8, T3, T4, T5, T6, Fz, Cz, Pz, and Oz of the 10/20 system. EOG was recorded from a supraorbital electrode and from an electrode on the external canthus of the right eye. The amplifier bandwidth was set between 0.5 and 30 Hz. EEG was sampled every 5 ms using a MEDICID 3E system and stored on a hard disk for further analysis. Sampling was done every 5 ms during a time segment from 1280 ms before the stimulus to 1500 ms after its onset. Each trial was visually edited and only those corresponding to correct responses and with no artifacts were analyzed. Subjects were seated in a comfortable chair in front of the videomonitor. Stimuli were delivered by a MINDTRACER system synchronized to the MEDICID 3E acquisition system.

We have also tested our method with other various experiments: a word categorization experiment (Harmony et al., 2001) similar to the Figures experiment (with words presented instead of figures), a working-memory task based on the Sternberg paradigm (Harmony et al., 2004), and a Go/NoGo experiment to study the inhibition of the motor response (Harmony et al., submitted for publication). The analysis of these experiments essentially confirms the main results described in this paper; however, for reasons of space we do not include such studies here. Details of these results can be found in (Alba et al., 2006).

2.1. Methodology

Our procedure consists of the following steps:

1. Run the EEG signals through a bank of bandpass quadrature filters and extract phase information (TF phase analysis).

Please cite this article in press as: Alba A, et al., Exploration of event-induced EEG phase synchronization patterns in cognitive tasks using a time–frequency-topography visualization system, J Neurosci Methods (2006), doi:10.1016/j.jneumeth.2006.10.018

2. Calculate a synchrony measure from the filtered signals.
3. Estimate the likelihoods and prior distributions for the MRF model using the synchronization values.
4. Use Bayesian estimation to find significant synchronization patterns that are persistent.
5. Display synchronization patterns as multitoposcopic graphs and time–frequency-topography (TFT) maps.

2.2. Time–frequency phase analysis

To obtain the phase information of the EEG signals, one may pass each signal through a bandpass filter at the frequency of interest. As in a previous work (Marroquin et al., 2004), we have chosen to use a bank of quadrature filters centered at each Hz and with a fixed bandwidth (about 1.76 Hz within 3 db of attenuation) to facilitate interpretation. One common choice for filters are the Gabor filters (Gabor, 1946), which provide the best balance between time and frequency localization in terms of the Heisenberg product. However, because of their Gaussian frequency response, at lower tuning frequencies Gabor filters may have a significant response to negative frequencies and lose their quadrature property, which results in distorted phase estimates (see Fig. 1a). In particular, if a unit-gain Gabor filter tuned at a frequency of h Hz has gain equal to α (with $\alpha < 1$) for the corresponding negative frequency $-h$, the argument of the complex filter output at time t corresponding to an input signal $s(t) = \cos(2\pi ht + \phi)$, where ϕ is a constant phase, will be

$$\hat{\Phi}(t) = \rho(\Phi(t)) = \arctan\left(\frac{1-\alpha}{1+\alpha}\tan\ \Phi(t)\right), \quad (1)$$

where $\Phi(t) = 2\pi ht + \phi$ is the argument of the ideal output $e^{i\Phi(t)}$ (obtained with $\alpha = 0$). The distortion signal $d(t) = \Phi(t) - \hat{\Phi}(t)$ will be zero when $\tan \Phi(t)$ equals 0 or $\pm\infty$, i.e., for $t = k/4h - \phi/2\pi h$, with $k = 0, 1, \ldots$, and will change its sign between these values, which means that it will oscillate at twice the tuning frequency h.

If $s(t)$ has a more complex structure (i.e., if it is a sum of sinusoids with different frequencies, amplitudes, and phases), this distortion cannot be characterized in an easy way, but it will have a significant effect on the measured phase.

This problem may be avoided if one uses filters that are forced to have zero gain for negative frequencies. In particular, one may use a bank of sinusoidal quadrature filters (SQF's) (Guerrero et al., 2005) which have the following frequency response:

$$G_{\omega_k,h}(\omega) = \begin{cases} \frac{1}{2}\left[1 + \sin\left(\frac{(h_k + 2(\omega-\omega_k))\pi}{2h_k}\right)\right], & \text{if } \omega \in [\omega_k - h_k, \omega_k], \\ \frac{1}{2}\left[1 + \sin\left(\frac{(h + 2(\omega-\omega_k))\pi}{2h}\right)\right], & \text{if } \omega \in [\omega_k, \omega_k + h_k], \\ 0 & \text{otherwise,} \end{cases} \quad (2)$$

where ω_k is the center frequency for the kth filter, h is the bandwidth, and $h_k = \min\{h, \omega_k\}$. The convolution kernel $g_{\omega_k,h}$ of the SQF's is found as the inverse Fourier transform of $G_{\omega_k,h}$. These filters have a response that is almost identical to Gabor filters at tuning frequencies higher than 6 Hz; however at lower tuning frequencies, the asymmetrical response of the sinusoidal quadrature filters yields a correct phase, as shown in Fig. 1a.

To analyze the effect of this distortion on the estimated synchrony between two signals, we make the following considerations: the filtered signals $F_{j,\omega,e}$, from which one can extract the instantaneous amplitude $A_{j,\omega,e}(t)$ and the instantaneous argument $\Phi_{j,\omega,e}(t)$, are obtained by convolution with a filter kernel $k_{\omega,h}$:

$$F_{j,\omega,e}(t) = (k_{\omega,h} \times V_{j,e})(t) = A_{j,\omega,e}(t)\exp[i\Phi_{j,\omega,e}(t)]. \quad (3)$$

If the actual argument Φ of the component with frequency ω is $\Phi(t) = \omega t + \phi_{j,\omega,e}(t)$, then the estimated argument $\hat{\Phi}$ may be expressed as a function ρ of the actual argument, where ρ is given by Eq. (1).

As one can see in Fig. 1a, for SQF's ρ is linear, while for Gabor filters it is clearly not. Since most phase-synchrony measures depend on the phase difference $\Delta\hat{\Phi}(t) = \hat{\Phi}_1(t) - \hat{\Phi}_2(t) = \rho(\omega t + \phi_1(t)) - \rho(\omega t + \phi_2(t))$, it is clear that a non-linear ρ will not cancel the terms involving ωt, and will instead introduce an oscillation in $\Delta\hat{\Phi}$, even if the true phase difference $\phi_1 - \phi_2$ is held constant.

We have performed a series of tests in order to demonstrate the improvement of SQF's over Gabor filters for synchrony estimation. For these tests we applied the average magnitude of the phase difference (MPD) as synchrony measure and the Bayesian analysis described below. Using Gabor filters, the sensitivity of the synchrony measure shows a cyclic dependence on the time t, which corresponds to the distortions in the phase observed in Fig. 1a.

The simulated data used for the tests is obtained from a very simple model which consists of a 2 Hz sinusoidal plus noise. The signals are given by:

$$V_{j,e} = \cos(2\pi f_0 t + \phi_{j,e}) + R_{j,e}(r,t), \quad \phi_{j,e} \sim \mathcal{N}(0,\sigma), \quad (4)$$

where j is the trial number, e the electrode index, $f_0 = 2$ Hz is the frequency of the sinusoidal, and σ is the standard deviation of the distribution of the phases, which controls the degree of synchrony between the signals (lower values of σ imply higher synchrony). The noise function $R_{j,e}(r,t)$ depends on the "noise level" r. For our tests, we used two electrodes ($e = 1, 2$), $\sigma_{\text{pre}} = \pi/10$ (pre-stimulus σ), and $\sigma_{\text{post}} = \pi/20$ (post-stimulus σ). Since $\sigma_{\text{pre}} > \sigma_{\text{post}}$, we are thus modeling an increase of synchrony in the full post-stimulus segment. We have generated 20 datasets with 50 trials each. For each dataset we perform the procedure described below in order to obtain a class label field $c_{\omega,e_1,e_2}(t)$ which indicates if synchrony between e_1 and e_2 at a frequency ω is significantly higher ($c = 1$), lower ($c = -1$), or equal ($c = 0$) with respect to the pre-stimulus average. The expected class is $c(t) = 1$ for all t in the post-stimulus segment.

For the first test we used Gaussian noise given by

$$R_{j,e}(r,t) \sim \mathcal{N}(0,r). \quad (5)$$

Please cite this article in press as: Alba A, et al., Exploration of event-induced EEG phase synchronization patterns in cognitive tasks using a time–frequency-topography visualization system, J Neurosci Methods (2006), doi:10.1016/j.jneumeth.2006.10.018

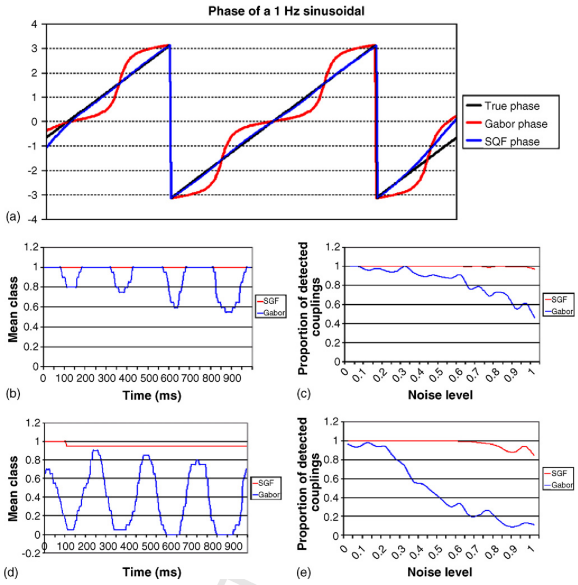

Fig. 1. Comparison between Gabor filters and SQF's. "(a) True phase and estimated phase (using Gabor and sinusoidal quadrature filters) for a 1 Hz sinusoidal input signal." (b–e) Comparison using simulated data with Gaussian noise for (b and c), and with interference of sinusoidals for (d and e). Graphs (b and d) show the average class $\bar{c}(t)$ computed across 20 datasets, whereas (c and e) show the proportion of detected couplings with respect to the noise level.

With a noise level $r = 0.5$, the average class $\bar{c}(t)$ across all datasets is shown in Fig. 1b. The blue line represents the results obtained using Gabor filters, whereas the red line corresponds to sinusoidal quadrature filters. The oscillating distortion is clearly present with the Gabor filters, and it corresponds to a frequency of 4 Hz (twice the tuning frequency, as shown above). Fig. 1c shows the proportion of detected couplings (i.e., with $c(t) = 1$) in the post-stimulus segment with respect to the noise level r (averaged across the 20 datasets). The proportion should remain close to 1; however, Gabor filters clearly start to fail with $r > 0.3$.

The second test uses a sum of interfering sine waves as noise function:

$$R_{j,e}(r,t) = \sum_{f \neq f_0} \frac{a_f}{f} \cos(2\pi f t + \phi_f),$$
$$a_f \sim \mathcal{U}(0,r), \quad \phi_f \sim \mathcal{U}(0,2\pi). \tag{6}$$

The sum is taken across frequencies from 1 to 50 Hz, except the frequency of interest f_0, and the components are attenuated according to their frequency. As in the previous test, we calculated the average class $\bar{c}(t)$ and the proportion of detected couplings with respect to the noise level. The results, presented in Fig. 1d and e, show the same differences as in the previous example.

It is worth mentioning that using real EEG datasets (such as the Figures experiment signals), there are clear differences between the results obtained with SQF's and those obtained from Gabor filters in the first 6 Hz. The tests with simulated data indicate that the results with Gabor filters may not be reliable in the delta and theta bands.

2.3. Synchrony measures

In this section, we discuss the most commonly used synchrony measures in the literature (e.g. coherence and circular variance of the phase difference), and propose two phase-based measures that focus on in-phase (phase difference equal to zero) or anti-phase (phase difference equal to π) synchrony. Later, we will perform a statistical comparison of all the measures presented here, and highlight some of their strengths and weaknesses.

Please cite this article in press as: Alba A, et al., Exploration of event-induced EEG phase synchronization patterns in cognitive tasks using a time–frequency-topography visualization system, J Neurosci Methods (2006), doi:10.1016/j.jneumeth.2006.10.018

2.4. Magnitude of phase difference (MPD)

According to David and Friston's neural mass model, the EEG/MEG signals from two distant cortical areas will show a phase difference of 0 or π when there is a bidirectional coupling between the two areas (David and Friston, 2003). This is supported by other works such as Friston et al. (1997) and Rodriguez et al. (1999), where the distribution of the phase differences concentrates around zero during episodes of high synchrony. Moreover, according to David and Friston (2003), and Varela et al. (2001), the proportion of reciprocal connections in the brain is very high. Therefore, it makes sense to consider as synchrony criterion the following: two signals with instantaneous phases $\phi_1(t)$ and $\phi_2(t)$ are in synchrony when $\phi_1(t) \approx \phi_2(t)$ for all t in a given time interval. A straightforward instantaneous measure would be the magnitude of the phase difference $|\phi_1(t) - \phi_2(t)|$ which can be wrapped between $-\pi$ and π. This makes it easy to obtain a normalized measure based on the phase difference:

$$\mu_{j,\omega,e_1,e_2}(t) = 1 - \frac{1}{\pi}|\text{wrap}(\phi_{j,\omega,e_1}(t) - \phi_{j,\omega,e_2}(t))|, \tag{7}$$

where wrap(ϕ) returns the angle ϕ wrapped to the interval $[-\pi, \pi)$.

2.5. Cumulative probability of phase difference (CPPD)

An alternative to the MPD measure consists on estimating the probability of the phase difference being smaller (in absolute value) than some $\epsilon > 0$. This probability can be estimated across all trials for each t, ω, e_1, and e_2 as follows:

$$\mu_{\omega,e_1,e_2}(t) = \frac{1}{N_r}\sum_{j=1}^{N_r} I(|\text{wrap}(\phi_{j,\omega,e_1}(t) - \phi_{j,\omega,e_2}(t))| < \epsilon). \tag{8}$$

where $I(P)$ equals 1 if P is true, and zero otherwise.

This measure allows a quantification of the degree of synchrony (by means of ϵ), regardless of any further transformation applied to the measure (such as the significance analysis we perform). We have used $\epsilon = \pi/5$ rad for our tests (equivalent to 10 ms at 10 Hz).

One can modify this measure to detect anti-phase synchrony (couplings which show a phase difference of π). A simple example is given by:

$$\mu_{\omega,e_1,e_2}(t) = \frac{1}{N_r}\sum_{j=1}^{N_r} I(|\text{wrap}(\phi_{j,\omega,e_1}(t) - \phi_{j,\omega,e_2}(t) - \pi)| < \epsilon). \tag{9}$$

However, one must be careful not to confuse a decrease in synchrony with anti-phase couplings. This can be done either by using small values for ϵ, or by comparing both phase and anti-phase measures. Our tests show that only a very small number of detected couplings correspond to anti-phase synchrony.

2.6. Phase-locking statistic (PLS)

Lachaux et al. proposed as synchrony measure one minus the circular variance (see Fisher, 1995) of phase differences across trials at instant t and called it *phase-locking statistic* (PLS) (Lachaux et al., 1999):

$$\mu_{\omega,e_1,e_2}(t) = \left|\frac{1}{N_r}\sum_{j=1}^{N_r} \exp[\text{i}(\phi_{j,\omega,e_1}(t) - \phi_{j,\omega,e_2}(t))]\right|, \tag{10}$$

where N_r is the number of trials in the EEG experiment.

2.7. Single-trial phase-locking statistic (STPLS)

In order to obtain a phase-locking measure for single trials, Lachaux et al. (2000) proposed a new measure based on the variance of the phase difference across a time window centered at time t, for each trial j:

$$\mu_{j,\omega,e_1,e_2}(t) = \left|\frac{1}{2w+1}\sum_{t'=t-w}^{t+w} \exp[\text{i}(\phi_{j,\omega,e_1}(t') - \phi_{j,\omega,e_2}(t'))]\right|, \tag{11}$$

This measure will be maximal when $\phi_1(t) - \phi_2(t)$ is approximately constant for all t in a given time window. According to Varela et al. (2001), most cognitive events have a typical duration of a few hundreds of milliseconds; therefore, in all our tests we have used $w = 10$ which is equivalent to a window size of 105 ms (the window size is $2w + 1$ samples).

2.8. Coherence

Statistical coherence is a measure of how closely two time series are related by a linear transformation (Gardner, 1992) and it is widely used as a measure of EEG synchrony (Bressler et al., 1993; Bressler, 1995; Nunez, 1995; Nunez et al., 1997; Gross et al., 2001). In order to estimate a coherence measure for a set of filtered EEG signals $F_{j,\omega,e}$ we first subtract their mean across the whole time segment:

$$F'_{j,\omega,e}(t) = F_{j,\omega,e}(t) - \sum_{t'=1}^{N_t} F_{j,\omega,e}(t'). \tag{12}$$

Then for each trial j we take the zero-lag coherence on a time window around time t which is given by

$$\mu_{j,\omega,e_1,e_2}(t) = \frac{|R_{j,\omega,e_1,e_2}(t)|}{|R_{j,\omega,e_1,e_1}(t)R_{j,\omega,e_2,e_2}(t)|^{1/2}} \tag{13}$$

where

$$R_{j,\omega,e_1,e_2}(t) = \frac{1}{2w+1}\sum_{t'=t-w}^{t+w} F'_{j,\omega,e_1}(t')(F'_{j,\omega,e_2}(t'))^*, \tag{14}$$

for each time t and electrode pair (e_1, e_2). A window size of 105 ms was also used for coherence measures.

Please cite this article in press as: Alba A, et al., Exploration of event-induced EEG phase synchronization patterns in cognitive tasks using a time–frequency-topography visualization system, J Neurosci Methods (2006), doi:10.1016/j.jneumeth.2006.10.018

2.9. Bayesian estimation of significant synchrony

Since we are interested in event-related activity, we must determine how significant are the changes of synchrony with respect to the pre-stimulus segment. To do this, we subtract the average synchrony in the pre-stimulus segment in order to obtain the relative synchrony X_{j,ω,e_1,e_2}:

$$X_{j,\omega,e_1,e_2}(t) = \mu_{j,\omega,e_1,e_2}(t) - \frac{1}{T_s}\sum_{t'=1}^{T_s} \mu_{j,\omega,e_1,e_2}(t'), \tag{15}$$

where T_s is the length of the pre-stimulus segment. Finally, we take the mean relative synchrony Y_{ω,e_1,e_2} across all trials:

$$Y_{\omega,e_1,e_2}(t) = \frac{1}{N_r}\sum_{j=1}^{N_r} X_{j,\omega,e_1,e_2}(t). \tag{16}$$

In order to estimate the significance of the Y-values, it is common to compute the p-value of each Y with respect to a null distribution and apply a threshold to them. In our case, the null distribution comes from the pre-stimulus segment (for each frequency and electrode pair), which by construction is centered at zero. Y-values which are "too positive" with respect to the null distribution correspond to significant synchrony increases, and similarly, "too negative" Y-values correspond to significant synchrony decreases.

To simplify interpretation and visualization, we would like to classify each Y-value in one of three classes: significantly higher (class $c = 1$), significantly lower (class $c = -1$), or equal ($c = 0$) to the pre-stimulus average. One possibility would be to simply apply a threshold to the p-values as mentioned above; however, we have chosen instead to use a more sophisticated classification method that permits one to impose additional constraints to control the granularity of the results. In particular, one would like that only those synchronous episodes with a duration greater than a minimum (physiologically motivated) value should be considered significant. According to studies related, for example, with the formation of short term memory (Jensen et al., 1996; Burle and Bonnet, 2000), this minimum value is in the order of one gamma oscillation, that is, around 20–50 ms.

It is worth noting that our final implementation of the classification method is relatively simple and efficient, as will be shown later.

A common technique for classification problems consists of Bayesian estimation with a prior Markov random field (MRF) model (Marroquin et al., 1987, 2001, 2004). With this method, one can model the class field $c_{\omega,e_1,e_2,t}$ as a random field with a prior Gibbs distribution of the form

$$P_{\mathrm{MRF}}(c) = \frac{1}{Z}\exp\left[-\lambda\sum_{C} V_C(c)\right], \tag{17}$$

where Z is a normalizing constant and V_C is a potential function that depends only on the values of the sites belonging to the clique C (a clique is either a single site, or any group of sites all of which are mutual neighbors, see Marroquin et al., 1987, 2001 for more details). For a classification problem, a popular model is the Ising model which enforces c to be piece-wise constant. If we consider a first-order neighborhood system, whose cliques are single sites and nearest neighbor pairs, the Ising potentials are given by:

$$V_{t,t'}(c) = \begin{cases} -1, & \text{if } c_{\omega,e_1,e_2,t} = c_{\omega,e_1,e_2,t'} \\ 1, & \text{if } c_{\omega,e_1,e_2,t} \neq c_{\omega,e_1,e_2,t'} \end{cases}, \tag{18}$$

where t and t' are adjacent sites in the time dimension. At this point, we are only interested in modeling persistence in time, and thus one can estimate the time-series $c_t = c_{\omega,e_1,e_2,t}$ in a decoupled manner for each frequency ω and electrode pair $\langle e_1, e_2\rangle$. However, it is also possible (although computationally expensive) to add constraints to model the consistency of c across different frequencies and/or across the spatial dimensions, in order, for example, to perform an automated segmentation of the TFT space.

Given prior probabilities $\alpha_k = P(c_t = k)$, the posterior distribution of c given Y can be calculated as

$$P(c|Y) = \frac{1}{Z'}\exp\left[\sum_t \log\, h_t(c_t) - \lambda\sum_{\langle t,t'\rangle} V_{t,t'}(c)\right], \tag{19}$$

where Z' is a normalization constant and $h_t(k) = P(Y_t \mid c_t = k)\alpha_k$.

The optimal estimator $\hat{c}$ can be found by maximizing the posterior marginal distribution $\pi_t(\hat{c}_t) = \sum_{c:c_t=\hat{c}_t} P(c \mid Y)$ for each t. This Maximizer of Posterior Marginals (MPM) estimator is usually approximated using stochastic Markov-chain methods such as Metropolis or the Gibbs sampler. These algorithms, however, are computationally expensive and require an unknown number of iterations, which makes them less than adequate for our multidimensional data set. A better solution consists on approximating the posterior marginal distributions with the *empirical marginals* $p_t(k)$ (Marroquin et al., 2001) which also form a MRF with the same neighborhood system as c and can be found by minimizing the energy function $U(p)$ given by:

$$U(p) = \sum_t |p_t - \hat{p}_t|^2 + \lambda'\sum_{\langle t,t'\rangle} |p_t - p_{t'}|^2, \tag{20}$$

with $\hat{p}_t(k) = h_t(k)/\sum_{k'} h_t(k')$.

Since each $p_t(k)$ is continuous, $U(p)$ can be minimized by solving the linear system obtained from equating the partial derivatives of U with respect to $p_t(k)$ to zero. Noting, however, that the optimal time-series $p(k)$ is a smoothed version of $\hat{p}(k)$, one can achieve a similar result by simply low-pass filtering each $\hat{p}(k)$ with a Gaussian kernel (for more details see Marroquin and Figueroa, 1997). The width of the Gaussian kernel will replace the model parameter λ' and will control the granularity of the results. In our case, we set this parameter so that blocks with constant c-values of length less than 25 ms occur less than 5% of the time (see Alba et al., 2006 for details).

Once we have p we can obtain the approximated MPM estimator as

$$c_t = \mathrm{argmax}_k\{p_t(k)\}. \tag{21}$$

Please cite this article in press as: Alba A, et al., Exploration of event-induced EEG phase synchronization patterns in cognitive tasks using a time–frequency-topography visualization system, J Neurosci Methods (2006), doi:10.1016/j.jneumeth.2006.10.018

2.10. Estimation of prior distributions and likelihoods

In order to calculate $h_t(k)$ (and thus $p_t(k)$) we need the prior probabilities α_k and likelihoods $P(Y_t \mid c = k)$. These can be estimated from the data if we consider that the complete distribution $P_Y(Y_t)$ can be expressed as:

$$P_Y(Y_t) = \sum_{k=-1}^{1} \alpha_k P(Y_t \mid c = k), \tag{22}$$

and also consider the following assumptions:

- $P(Y_t \mid c = 0)$ may be estimated empirically from the pre-stimulus data.
- $P(Y_t \mid c = 1) = 0$ for $Y \leq 0$.
- $P(Y_t \mid c = -1) = 0$ for $Y \geq 0$.

With these assumptions, we can obtain $P(c = 0)$ from Eq. (22) as follows:

$$\alpha_0 = \frac{P_Y(0)}{P(0 \mid c = 0)} \tag{23}$$

and also

$$h_t(0) = \alpha_0 P(Y_t \mid c = 0) \tag{24}$$

$$h_t(1) = \begin{cases} P_Y(Y_t) - h_t(0), & Y_t > 0 \\ 0, & Y_t \leq 0 \end{cases} \tag{25}$$

$$h_t(-1) = \begin{cases} P_Y(Y_t) - h_t(0), & Y_t < 0 \\ 0, & Y_t \geq 0 \end{cases} \tag{26}$$

$P_Y(Y_t)$ and $P(Y_t \mid c = 0)$ can be estimated from the data Y using non-parametric kernel estimation: the distribution p_Y is estimated from the sample $\{Y_t\}$ as the sum of superimposed kernel functions k_σ centered at each Y_t. In other words,

$$p_Y(y) = \frac{1}{Z} \sum_{i=1}^{N_t} k_h(y - Y_t), \tag{27}$$

where Z is a normalization constant chosen so that p_Y integrates to 1. The parameter h specifies the width of the kernel and determines the smoothness of p_Y. Adequate choice of h depends on the sample data; however, for automated applications, a rule of thumb for a Gaussian kernel (which we use) is provided by (Silverman, 1986):

$$h_{\text{opt}} = 1.06\sigma n^{-1/5},$$

where σ is the standard deviation of X (estimated from the sample). Note that $P_Y(Y_t)$ is estimated using the full time segment, whereas $P(Y_t \mid c = 0)$ is estimated by considering only the pre-stimulus segment.

The actual classification procedure for significative synchrony changes is performed (for each frequency ω and electrode pair $\langle e_1, e_2 \rangle$) as follows:

1. Estimate the pre-stimulus distribution $P_0(Y)$ and the full distribution $P_Y(Y)$ using kernel density estimation with bandwidth given by Silverman's rule of thumb.
2. Estimate $\alpha_0 = P(c = 0) = P_0(0)/P_Y(0)$.
3. For each t, calculate $h_t(k)$ for $k = -1, 0, 1$ as given by Eqs. (24)–(26).
4. Normalize h_t to obtain $\hat{p}_t$ for all t.
5. Obtain $p(k)$ by convolving $\hat{p}(k)$ with a Gaussian kernel g. The width σ of the filter controls the granularity of the c field.
6. Approximate the MPM estimator by $c_t = \text{argmax}_k\, p_t(k)$ for all t.

This procedure yields results that are roughly similar to those obtained by directly thresholding the p-values (with a threshold between 0.01 and 0.1); however, the value of the threshold (critical p-value) that yields the desired granularity (e.g. synchronous episodes which last at least 25 ms) varies for different data sets, and has to be set in an empirical way for each particular case.

It should also be noted that the parameter σ, which controls the granularity in the Bayesian method is not critical: one obtains very similar classifications for a wide range of values of this parameter, whereas classification based on z-scores or p-values is in general more sensitive to the precise value of the threshold.

2.11. Visualization

For a fixed time t and frequency ω it is possible to show the distribution of the synchrony pattern (SP) given by the class values $c_{\omega,e_1,e_2,t}$ in a multitoposcopic display, in which for each electrode e_1 one displays a head diagram (also called "toposcope") – within a bigger head – that shows the distribution of c across all sites e_2 (an example of this display can be seen in Fig. 2a).

A problem arises when one deals with high electrode density recordings since only so many toposcopes can be displayed within the bigger head. One can use interpolation techniques to display high-density data in a single toposcope (in particular, we use a Voronoi partition Aurenhammer, 1991, obtained by assigning each pixel in the toposcope the class corresponding to the nearest electrode), but the number of toposcopes may have to be reduced. One possibility consists in grouping the electrodes in N_g cortical areas $\{G_1, \ldots, G_{N_g}\}$, using again a Voronoi partition whose centers are, for example, the sites Fp1, Fp2, F3, F4, C3, C4, P3, P4, O1, O2, F7, F8, T3, T4, T5, T6, Fz, Cz, and Pz of the 10/20 system. One can then plot a toposcope for each group G_k computing, for each high-resolution electrode, the "most representative" synchrony class between this electrode and the electrodes in G_k. This most representative class may be computed in several ways; for example, the average class $\bar{c}$ of electrode e to group G_k which is computed as:

$$\bar{c}_{\omega,k,e,t} = \frac{1}{|G_k|} \sum_{e' \in G_k} c_{\omega,e',e,t} \tag{28}$$

or the class mode $\hat{c}$, which is computed as:

$$\hat{c}_{\omega,k,e,t} = \text{argmax}_{q \in \{-1,0,1\}} \left\{ \sum_{e' \in G_k} \delta(c_{\omega,e,e',t} - q) \right\}, \tag{29}$$

Please cite this article in press as: Alba A, et al., Exploration of event-induced EEG phase synchronization patterns in cognitive tasks using a time–frequency-topography visualization system, J Neurosci Methods (2006), doi:10.1016/j.jneumeth.2006.10.018

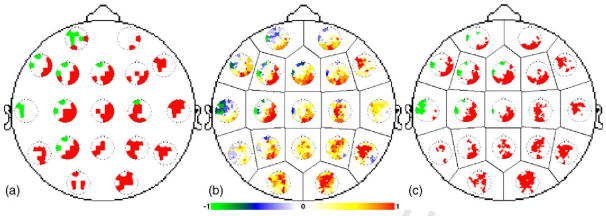

Fig. 2. Multitoposcopic displays for a 120-channel dataset using the MPD measure: (a) uses only channels Fp1, Fp2, F3, F4, C3, C4, P3, P4, O1, O2, F7, F8, T3, T4, T5, T6, Fz, Cz, and Pz from the 10/20 system: red regions represent electrode pairs that show a significant increase in synchrony ($c = 1$), while green regions correspond to significant synchrony decreases ($c = -1$). Graphs (b and c) use the 120 channels grouped in 19 cortical areas corresponding to the Voronoi partition whose centers are the electrodes used in (a). For each area, one can plot a toposcope representing a statistic of the synchrony classes between each of the 120 electrodes and the electrodes within the area: (b) uses the average class $\bar{c}$ (which may be between −1 and 1), whereas (c) uses the class mode $\hat{c}$ (see text for details). The three multitoposcopes represent the SP obtained at $t = 515$ ms and $f = 11$ Hz during a Go/NoGo experiment (see Harmony et al., submitted for publication, for details); the rest of the examples presented in this paper correspond to the Figures experiment described in the text.

where δ is the Kronecker delta function. An example of multitoposcopes corresponding to $\bar{c}$ and $\hat{c}$ are shown in Fig. 2b and c. More sophisticated methods could involve electrode clustering or TFT regularization; however, they are beyond the scope of this paper.

Multitoposcopic displays are useful to show a detailed connectivity pattern for a fixed time and frequency; however, it is important to visualize larger regions of the time–frequency plane in order to localize zones of interest where the synchrony pattern remains almost constant and might be related to specific cognitive processes. For this purpose, we can use a time–frequency-topography (TFT, Marroquin et al., 2004) display to present the data by reducing only one spatial dimension. We do this by counting, for each site e, the number of sites whose synchrony with e has significantly increased (or decreased). In other words, we can build a *synchrony increase histogram* (SIH) given by

$$H^{+}_{\omega,e}(t) = \sum_{e'=1}^{N_e} I(c_{\omega,e,e',t} = 1), \tag{30}$$

where $I(P) = 1$ only if P is true. $H^{+}_{\omega,e}(t)$ is the number of significantly stronger couplings (with respect to the pre-stimulus segment) for site e at time t and frequency ω. Similarly, we can define a *synchrony decrease histogram* (SDH) as

$$H^{-}_{\omega,e}(t) = \sum_{e'=1}^{N_e} I(c_{\omega,e,e',t} = -1). \tag{31}$$

These histograms can be presented in a TFT display as shown in Figs. 3 and 4.

Another option is to divide the TF plane in regions, and display a representative SP for each region (for example, the average SP, or the SP that corresponds to the center of the region). An example of this type of display is presented in Fig. 5, where the TF plane has been partitioned by frequency bands and at regular 300 ms intervals.

2.12. Comparison between synchrony measures

Fig. 6 show the SIH's for the MPD, CPPD, PLS, STPLS, and coherence measures. It is clear that CPPD and PLS give very similar results to the MPD measure. On the other hand, STPLS and coherence yield similar results themselves but different from MPD. The estimated correlation between each pair of measures (Fig. 7, left) confirms what we see. It is worth noting that similar correlation results were also obtained with five different experiments besides the Figures experiment presented here (see Alba et al., 2006 for details).

Seemingly, we have two groups of synchrony measures; thus it is important to understand what kind of similarities between signals are being quantified by each group, and how measures from the same group are related to each other. One thing to note is that STPLS and coherence are defined across a time window, while the other measures are "instantaneous". Because of this, STPLS and coherence may be less sensitive to trial-to-trial latency jitter, which characterizes induced responses (i.e., those that are not phase-locked to the stimulus). Typically, induced activity is revealed by performing a time–frequency decomposition of each trial, and averaging a positive definite function of the filters' output (e.g., the power) across all trials, whereas evoked activity is obtained by first averaging the raw signals across trials, and then applying a positive definite function (power analysis) to the average signals (David et al., 2006). The difference is that in the former case (induced responses) there will be no cancellations during averaging, whereas in the latter (evoked) case, there may be cancellations due to differences in sign across trials. It is clear then, that the methodology presented in the previous sections is basically an induced response analysis, where the positive definite function is the synchrony measure (we may call it "induced synchrony"), instead of the power; this function is averaged across trials and then the baseline is subtracted. This suggests that our procedure, with any of the synchrony measures presented here, should be at least as sensitive to induced responses as the typical average-power analysis. Of course, because of additional averaging across time, STPLS

Please cite this article in press as: Alba A, et al., Exploration of event-induced EEG phase synchronization patterns in cognitive tasks using a time–frequency-topography visualization system, J Neurosci Methods (2006), doi:10.1016/j.jneumeth.2006.10.018

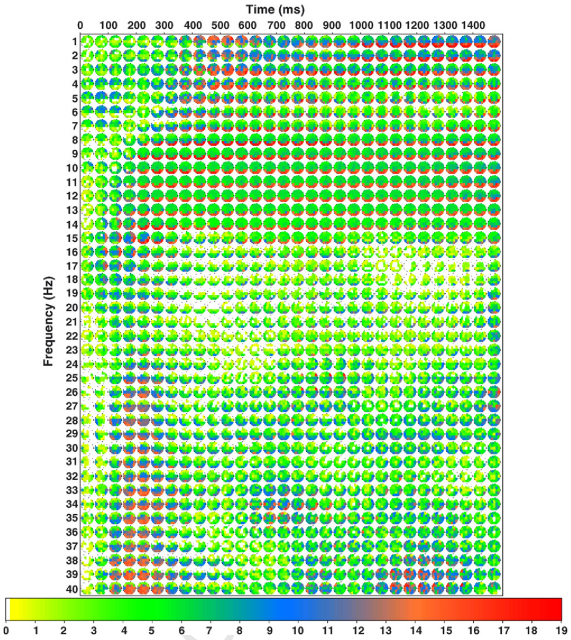

Fig. 3. Synchrony increase histogram for the Figures experiment. The color scale represents, for each recording site e, the number of sites that show a significant increment in synchrony (class $c = 1$) with e. There are 20 recording sites in the Figures experiment, thus each site may increase its synchrony with at most 19 other sites.

and coherence may be more robust to larger amounts of latency jitter.

A problem with the coherence and STPLS measures is that they may decrease their value (i.e., they may signal a spurious decoupling) if the local phase dispersion of either one of the two electrodes under consideration increases and vice versa. In particular, if the phase of one electrode in the STPLS measure (Eq. (11)) remains relatively constant across the time window, then this measure will be related to the dispersion of the other phase. To see how much this variance influences the STPLS, we estimated a local phase constancy (LPC) measure for each electrode, which equals one minus the local phase dispersion across a time window:

$$\mathrm{LPC}_{j,\omega,e}(t) = \frac{1}{2w+1}\left|\sum_{t'=t-w}^{t+w} \exp[\mathrm{i}\phi_{j,\omega,e}(t')]\right|. \quad (32)$$

Fig. 6 (bottom-right graph) shows the TFT map of significant LPC changes: red and green spots indicate significant increases and decreases, respectively, in the phase constancy across time. Note that red regions in the LPC map correspond to increases in STPLS and coherence. The green region in the alpha band in the LPC map also corresponds to a decrease in synchrony observed in the STPLS and coherence SDH's (not shown).

We estimated the correlation between the LPC changes and the average synchrony changes at each electrode for all the measures (Fig. 7, right). Effectively, both STPLS and coherence show high correlation with LPC, as well as a slightly higher correlation with amplitude changes (Marroquin et al., 2004) (which makes sense for coherence, since it uses both the magnitude and phase of the signals). This suggests that measures such as MPD and CPPD may be more specific for the detection of in-phase synchronous episodes, since they are less influenced by the temporal phase dispersion that may occur on one of the electrodes of the pair under study.

By looking at Eq. (10) one can see that PLS actually measures the consistency of the phase difference across all trials. We have also shown that the MPD and PLS measures are highly corre-

Please cite this article in press as: Alba A, et al., Exploration of event-induced EEG phase synchronization patterns in cognitive tasks using a time–frequency-topography visualization system, J Neurosci Methods (2006), doi:10.1016/j.jneumeth.2006.10.018

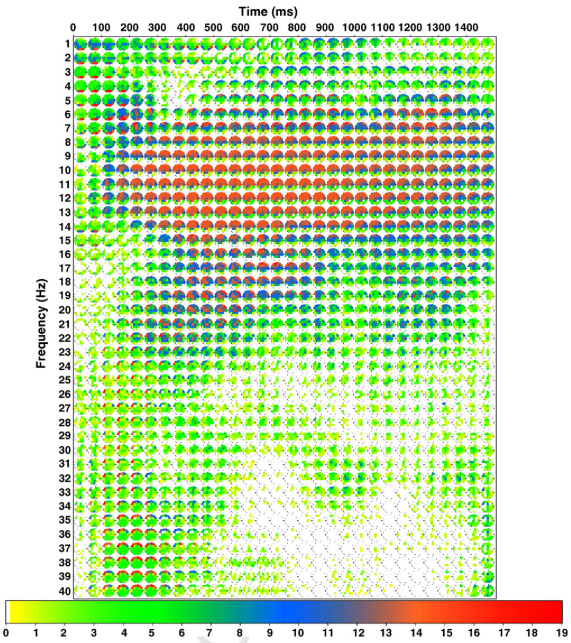

Fig. 4. Synchrony decrease histogram for the Figures experiment. The color scale represents, for each recording site e, the number of sites that show a significant decrease in synchrony (class $c = -1$) with e.

lated. This suggests that the processes that result in high synchronization (as measured by MPD) are fairly consistent across trials and subjects, and thus may be related to the task.

Furthermore, the CPPD measure is also highly correlated to the MPD, suggesting that synchronization effectively happens with near-zero phase difference. This is in accordance with the neural mass model proposed by David and Friston (2003) and other works (Friston et al., 1997; Rodriguez et al., 1999) which have also found zero-centered phase difference distributions during synchronous episodes between two electrodes.

Another important issue which directly affects the detection of EEG synchrony is the volume conduction (Nunez, 1995): the conductive properties of the cortex, skull, and scalp produce a smearing of the potentials across the surface, which may result in spurious correlations between EEG signals, especially between neighboring sites.

Nunez (1995, 2000), Nunez et al. (1997) have developed an extensive work on the effect of volume conduction in EEG coherence. Using simulated data from a three concentric spheres model, they estimated correlation coefficients for pairs of uncorrelated cortical sources using different EEG references (Cz, neck, linked ears, and average reference), cortical imaging, and Surface Laplacians (SL, (Perrin et al., 1989, 1990; Law et al., 1993). In all cases, except SL, spurious high correlations were observed for short inter-electrode distances (4–8 cm) (Nunez et al., 1997). However, since the potentials are relatively smooth across the surface (partly because of volume conductor effects), the SL, which is the second spatial derivative of the potentials, may have a relatively small magnitude, and thus may be more vulnerable to noise than the scalp potentials (Junghöfer et al., 1999). It is also worth stressing that accurate SL estimation requires high spatial sampling density (64–128 channels) (Law et al., 1993; Nunez, 1995; Junghöfer et al., 1999).

Since the SL acts as a bandpass filter on the raw potentials, true coherence with low spatial frequency (i.e., relatively smooth across the surface) may be underestimated. Because of this, Nunez suggests to use the SL to complement, rather than replace, the raw EEG potentials: correlations may be observed at different spatial scales (Nunez et al., 1997; Nunez, 2000) (just as correlations between customs of people from two different

Please cite this article in press as: Alba A, et al., Exploration of event-induced EEG phase synchronization patterns in cognitive tasks using a time–frequency-topography visualization system, J Neurosci Methods (2006), doi:10.1016/j.jneumeth.2006.10.018

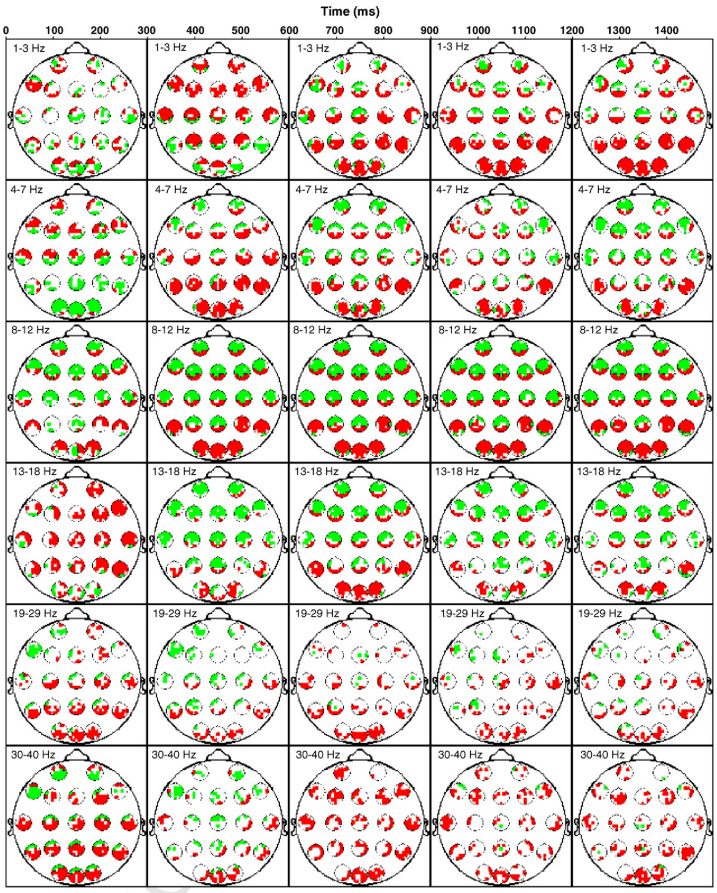

Fig. 5. Subdivided synchrony map for the Figures experiment. The TF plane is partitioned by frequency bands and at each 300 ms. The displayed SP in each region corresponds to the center point of the region.

cities may differ from correlations between two families, one from each city). Therefore, raw potential, Surface Laplacian, and cortical image coherency may, in general, represent correlations at different spatial scales of cortical dynamics.

Although these studies by Nunez focus only on coherence, it is reasonable to think that the volume conductor also has a significative influence on other synchrony measures. One may think that a synchronization measure that favors phase differences equal to zero (e.g. MPD or CPPD) might be more sensitive to volume conduction. However, this is not necessarily true, since if several sources influence two different sites via volume conduction, their net influence on the resulting electrode signals

Please cite this article in press as: Alba A, et al., Exploration of event-induced EEG phase synchronization patterns in cognitive tasks using a time–frequency-topography visualization system, J Neurosci Methods (2006), doi:10.1016/j.jneumeth.2006.10.018

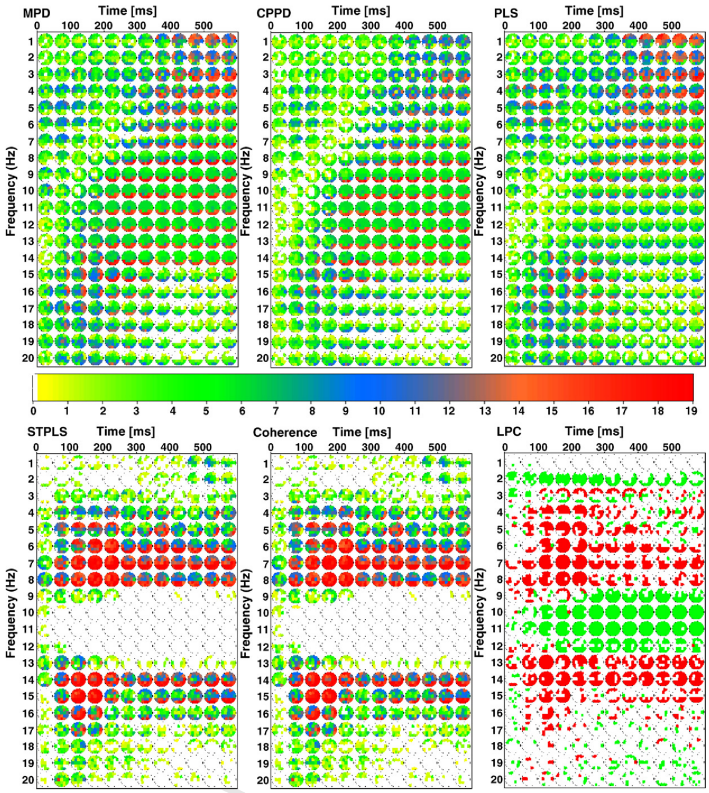

Fig. 6. Synchrony increase histograms for the Figures experiment using the five synchrony measures: MPD, CPPD, PLS, STPLS, and coherence. The bottom-right graph corresponds to the TFT map of significant changes in the LPC measure (red represents significant increases, whereas green corresponds to significant decreases), see text for details.

	MPD	CPPD	PLS	STPLS	Coherence
MPD	1.000	0.835	0.853	0.477	0.508
CPPD	0.835	1.000	0.755	0.500	0.525
PLS	0.853	0.755	1.000	0.503	0.536
STPLS	0.477	5.000	0.503	1.000	0.872
Coherence	0.508	0.525	0.536	0.872	1.000

	LPC	AMP
MPD	0.102	-0.019
CPPD	0.067	-0.114
PLS	0.131	0.067
STPLS	0.698	0.266
Coherence	0.673	0.273

Fig. 7. Correlation between pairs of synchronization measures (left), and between synchronization measures and local phase constancy or amplitude (power) changes (right). There are clearly two groups of measures: those similar to the MPD, and those similar to the STPLS. The latter group is characterized by a high correlation with LPC and a slightly higher correlation with power changes.

Please cite this article in press as: Alba A, et al., Exploration of event-induced EEG phase synchronization patterns in cognitive tasks using a time–frequency-topography visualization system, J Neurosci Methods (2006), doi:10.1016/j.jneumeth.2006.10.018

will correspond to different linear combinations of these source signals (with coefficients given by the corresponding attenuations), thus producing different phases (Lachaux et al., 1999; see also the discussion below on apparent phase). Furthermore, the MPD and CPPD measures are highly correlated to Lachaux's PLS measure, which measures synchrony with a constant phase lag (not necessarily zero), suggesting that at least these three measures are similarly affected by volume conduction. Lachaux also suggests that one may be able to identify conduction synchrony by looking at the neighboring sites of the two electrodes under analysis: if conduction synchrony is observed between two electrodes, then one should also observe high synchrony between their neighbors. To test this, we have estimated a cross-neighbor synchrony measure Z^+ given by:

$$Z^+_{\omega,e_1,e_2,t} = \frac{\sum_{k\in N_1, j\in N_2} I(c_{\omega,e_k,e_j,t} = 1)}{|N_1||N_2|} \cdot I(c_{\omega,e_1,e_2,t} = 1) \tag{33}$$

where $I(P)$ equals 1 if P is true and zero otherwise, and N_i is the set of neighboring sites for e_i (we have chosen a neighborhood radius such that each e_i has at least one neighbor). In other words, $Z^+_{\omega,e_1,e_2,t}$ represents the proportion of neighbor-pairs which show a significant increase of synchrony when e_1 and e_2 increase their synchrony. The c-values used to estimate Z^+ were obtained from thresholded p-values ($\alpha = 0.01$) to avoid any bias that may be introduced by the regularization constraints of the Bayesian method. One can then estimate the average Z^+ across all electrode pairs which show a significant increase of synchrony. Interestingly, STPLS and coherence produced the highest average values (around 0.16), while CPPD and PLS corresponded to the lowest (between 0.06 and 0.1). According to these tests, one therefore cannot conclude that a MPD or CPPD are more sensitive to conduction synchrony than the other measures.

All these findings lead us to believe that MPD and CPPD are suitable measures for long-range synchronization.

3. Discussion

A full analysis of the Figures experiment using the MPD measure is presented here as an example of the methodology. The full segmented MPD map is presented in Fig. 5 along with the corresponding SIH and SDH maps (Figs. 3 and 4, respectively). The TFT map of significant changes in amplitude is also shown in Fig. 8.

Recall that we are measuring the changes in synchrony during a particular state in relation to a previous condition that we may consider as neutral. It is possible to observe changes in phase-lock at all frequencies. Synchrony increases in the delta band in the anterior regions between 450 and 600 ms. After this time, the synchrony increased mainly in the posterior regions (Fig. 3). In the first 150 ms in the delta and theta bands there was a decrease in synchrony in occipital regions (Fig. 4). This may be due to the activation of the visual areas produced by the stimuli. In the theta range (4–7 Hz), the most generalized change in synchronization in the EEG after 300 ms is the phase-lock increase between posterior and anterior regions, which can be observed in the partitioned map (Fig. 5). This pattern may be related to activation of working memory (WM), which is the process of actively maintaining a representation of information for a brief period of time so that it is available for use. Attention, decoding, perception and maintenance in memory are processes that involve the activation of WM. Visual working memory involves the concerted activity of a distributed neural system, including posterior areas in visual cortex and anterior areas in prefrontal cortex (Ungerleider et al., 1998).

The increase in theta power in frontal regions has been related to activation of WM (Gevins et al., 1997; Rhom et al., 2001). Anterior regions are also involved in encoding (Klimesch et al., 2004) and maintaining the information in memory (Barde and Thompson-Schill, 2002). An increase in coherence in the theta range was found by Sarnthein et al. (1998) between prefrontal and posterior electrodes during retention of a string of characters.

In the alpha range, simultaneously with the increase in synchrony in the occipital regions, there was a decrease in synchrony between all regions except the occipital leads and the frontal regions on which synchrony increases. This increase may be indicating the projection loops between attentional control system in prefrontal cortex and activated meaning representations in semantic memory in posterior regions. The decrease in synchrony in the alpha band between 100 and 1500 ms coincides with the phenomena described in the 1930s by Adrian and Mathews of amplitude decrease or "desynchronization" and it has been related to attention (Gevins et al., 1997; Rhom et al., 2001; Klimesch, 1999).

Other change that was observed is the increase of synchrony in occipital regions in the beta band. In humans, in intracranial recordings that limited regions of extrastriate visual areas, separated by several centimeters, EEG activity in the beta range (15–25 Hz) became synchronized in an oscillatory mode during the rehearsal of an object in visual short-term memory. According to Tallon-Baudry et al. (2001) these findings confirm experimentally the hypothesis of a functional role of synchronized oscillatory activity in the coordination of distributed neural activity in humans, and support Hebb's (1949)popular concept of short-term memory maintenance by reentrant activity within the activated network.

In the gamma band an increase of synchrony in the interval 200–300 ms was observed. This increase in synchrony in the gamma band has been related to visual search and perception (Tallon-Baudry et al., 1997). The increase in synchronization during the interval of 600–800 ms in the gamma band might be related to preparation of the motor response.

From the analysis of these and other experimental data (see Alba et al., 2006 for details), one observes certain phenomena that may appear counter-intuitive; for example:

1. Synchronous episodes occur with near-zero phase lag, regardless of the distance between leads.
2. It is possible to have two (or more) electrodes increasing their synchrony with a third one (which acts as a nodal point), and at the same time, observe a decrease of synchronization between the non-nodal leads (see, for example, the SP associ-

Please cite this article in press as: Alba A, et al., Exploration of event-induced EEG phase synchronization patterns in cognitive tasks using a time–frequency-topography visualization system, J Neurosci Methods (2006), doi:10.1016/j.jneumeth.2006.10.018

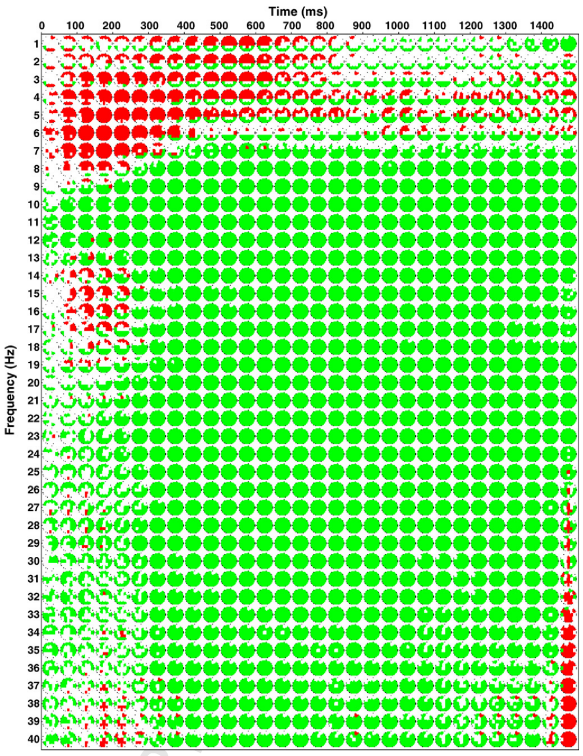

Fig. 8. Map of significant amplitude changes for the Figures experiment: sites whose amplitude is significantly higher than the pre-stimulus average are shown in red while those with significantly lower amplitude are shown in green. (For interpretation of the references to color in this figure legend, the reader is referred to the web version of the article.)

ated to the alpha band in Fig. 5, where occipital leads increase their synchrony with most of the other leads, while fronto-parietal leads show a decrease of synchrony among them). This phenomenon can also been observed in other studies, such as Rodriguez et al. (1999) and David et al. (2003).

3. When a single electrode e increases its synchrony with many sites, there is a high probability of a power decrease at e.

These phenomena may be explained by the following considerations: a scalp electrode provides estimates of synaptic action averaged over tissue masses containing between 10^7 and 10^9 neurons (Nunez, 1995). Moreover, there is evidence (obtained, for example, using retrogradely transported fluorescent dyes Morecraft et al., 1993, and single-cell recordings Quintana and Fuster, 1999) of extensively intermingled populations of neurons connected with different areas (e.g., frontal eye fields and posterior parietal cortex). Moreover, when performing a computational task, neurons may quickly associate into a functional group while disassociating from concurrently activated groups (Haalman and Vaadia, 1998).

All these facts suggest that the signal recorded by a scalp electrode may in fact result from a sum of macroscopic oscillations produced by functionally different neural populations (which may be histologically intermingled). Since each one of these sub-populations must be synchronized so that a macroscopic oscillation develops, a reasonable model for a complex

Please cite this article in press as: Alba A, et al., Exploration of event-induced EEG phase synchronization patterns in cognitive tasks using a time–frequency-topography visualization system, J Neurosci Methods (2006), doi:10.1016/j.jneumeth.2006.10.018

band-pass EEG signal (i.e., the output of a narrow band-pass quadrature filter tuned at frequency ω) is:

$$S(t,\omega) = \sum_k \alpha_k e^{i(\omega t+\phi_k)}, \tag{34}$$

where the positive coefficients α_k depend on the amplitude and relative proportion of subpopulation k and ϕ_k is the corresponding phase.

The apparent amplitude $A(t,\omega)$ and phase angle $\phi(t,\omega)$ (obtained by subtracting ωt from the argument of the complex signal S) will be given by the resultant of the sum (on the complex plane) of the vectors $\alpha_k e^{i\phi_k}$:

$$A(t,\omega)\exp[i\phi(t,\omega)] = \sum_k \alpha_k(t)\exp[i\phi_k]. \tag{35}$$

This explains why the apparent phase difference between two synchronized distant regions is zero, in spite of the fact that there may be a significant transmission delay: with two sub-populations one can model a unidirectional coupling between two distant cortical areas, in the sense that a sub-population in one area drives a sub-population in the other area with a certain phase lag δ. For a bidirectional coupling we just add a reciprocal connection, with the same phase lag. Fig. 9 shows a schematic of two populations in bidirectional coupling. It can be shown that if all sub-populations have approximately the same size (i.e. $\alpha_k = 0.5$, $k = 1, 2$), then the apparent amplitude and phase for each electrode would be given by

$$A_1^* \exp[i\phi_1^*] = 2\cos\left(\frac{\phi^1-\phi^2}{2}\right)\exp\left[i\frac{\phi^1+\phi^2}{2}\right], \tag{36}$$

$$A_2^* \exp[i\phi_2^*] = 2\cos\left(\frac{\phi^1-\phi^2-2\delta}{2}\right)\exp\left[i\frac{\phi^1+\phi^2}{2}\right]. \tag{37}$$

So that $\phi_1^* - \phi_2^* \approx 0$, except in the case where

$$\frac{\phi^1-\phi^2+3\pi}{2} < \delta < \frac{\phi^1-\phi^2+\pi}{2},$$

in which case $\phi_1^* - \phi_2^* \approx \pi$, which is in accordance with (David and Friston, 2003).

This model for the apparent phase also explains the fact, which we have observed in all the experiments we have analyzed, that when a given site is synchronized with several other sites, in most cases there is also an amplitude decrease with respect to the baseline. These sites act as characteristic nodes of a particular network, hence we call them *nodal points*. To study this in detail, we define a site e as k-nodal at time t and frequency ω if it shows significant increase in synchronization with at least k different sites. Let N_k be the number of k-nodal points in the TFT space and A_k^- the number of k-nodal points that also show a power decrease; then the conditional probability of significant power decrease given that a site is k-nodal can be estimated by $P_k^- = A_k^-/N_k$. One may similarly estimate the conditional probability of power increment P_k^+. These probabilities are shown in Fig. 10 for the Figures experiment, where it is clear that P_k^- increases with the number of couplings k. The same behavior can be observed with three other experiments, all of which are presented in (Alba et al., 2006).

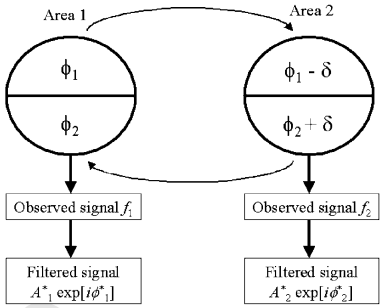

Fig. 9. Bidirectional coupling between two areas with two sub-populations each. If the sub-populations are approximately the same size, the apparent phase difference $\phi_1^* - \phi_2^*$ will be approximately 0 or π.

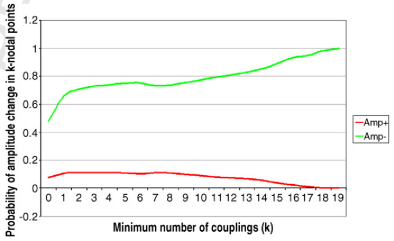

Fig. 10. Conditional probabilities of amplitude increment (red) and decrease (green) in k-nodal points for the Figures experiment.

This behavior may be also be explained from Eq. (35): suppose the population covered by the nodal electrode is divided into various sub-populations, each one of which increases its synchrony (with respect to the baseline) with a different site. The relative dispersion of the non-nodal phases may not be different from that of the baseline, so that these sites may not exhibit any significant synchrony change among themselves; the apparent phase of the nodal point, however, will show increased synchrony with all these sites, and due to the non-nodal phase dispersion, the nodal point will show a significant apparent amplitude decrease as well. A more detailed analysis of this situation, including some simulations, is presented in (Alba et al., 2006).

4. Conclusion

Brain electroencephalographic activity changes as a function of state. During the performance of different tasks, several neuronal assemblies become active simultaneously. These neuronal networks are not necessarily contiguous and may occupy different cortical areas producing complex spatiotemporal patterns

Please cite this article in press as: Alba A, et al., Exploration of event-induced EEG phase synchronization patterns in cognitive tasks using a time–frequency-topography visualization system, J Neurosci Methods (2006), doi:10.1016/j.jneumeth.2006.10.018

of synchronization or desynchronization in relation to a previous state. Zero phase measurements between leads indicate that the EEG recorded in such leads became highly synchronized and may be integrating a network related to a particular psychophysiological process. Thus, phase relationships between regions may give important information about the dynamics of different cell assemblies.

The detection of these phase relationships must be performed with care. First, the time–frequency decomposition method should not introduce artifacts in the phase estimations. In this sense, sinusoidal quadrature filters have proven to be reliable. Second, there are two important aspects of synchrony estimation: the significance of the phase-lock measure, and its consistency across time. We believe that separating these two aspects provides better results, and we do this by means of an instantaneous phase-lock measure, and the inclusion of granularity constraints in the estimation of significance. On the other hand, phase-lock measures that are estimated across a time window may be contaminated by the effect of local phase dispersion. Volume conduction seems to have a similar effect on all the measures presented here; therefore, a more accurate assessment of synchrony may be obtained by complementing the analysis of raw potentials with Surface Laplacian estimates from high-density recordings, as suggested by Nunez (1995, 2000), Nunez et al. (1997). Unfortunately, most of our test datasets contain only 19 or 20 channels, which are not enough to compute an accurate SL. However, the methodological contributions presented in this paper remain valid for synchrony estimation if SL, current sources, or MEG signals are used instead of the raw scalp potentials. Finally, TFT visualization techniques have proven to be very useful for the analysis of cognitive tasks as they allow for a quick and interactive exploration of the TF plane while still providing spatial detail. The new insights in the Figures experiment and the nodal sites are examples of the usefulness of these tools.

Uncited reference

Pascual-Marqui et al. (1988).

Acknowledgements

We would like to thank Dr. Thalia Fernandez for data acquisition for the Figures experiment. J.L. Marroquin was supported by Conacyt grant no. 46270. A. Alba was supported by PROMEP, Mexico.

References

Alba A, Marroquin JL, Peña J, Harmony T. Analysis and visualization of EEG event-induced dynamic synchronization patterns in cognitive tasks. Technical communication no. I-06-05/08-03-2006 (CC/CIMAT). http://www.cimat.mx/reportes/enlinea/I-06-05.zip(zipped PDF), 2006.

Aurenhammer F. Voronoi diagrams—a survey of a fundamental geometric data structure. ACM Comput Surv 1991;23(3):345–405.

Barde LH, Thompson-Schill SL. Models of functional organization of the lateral prefrontal cortex in verbal working memory: evidence in favor of the process model. J Cogn Neurosci 2002;14:1054–63.

Bastiaansen M, Hagoort P. Event-induced theta responses as a window of the dynamics of memory. Cortex 2003;39:967–92.

Bressler SL, Coppola R, Nakamura R. Episodic multiregional cortical coherence at multiple frequencies during visual task performance. Nature 1993;366:153–6.

BresslerSL. Large-scale cortical networks and cognition. Brain Res Rev 1995;20:288–304.

Burle B, Bonnet M. High-speed memory scanning: a behavioral argument for a serial oscillatory model. Cogn Brain Res 2000;9:327–37.

David O, Friston KJ. A neural mass model for MEG/EEG coupling and neuronal dynamics. NeuroImage 2003;20:1743–55.

David O, Cosmelli D, Lachaux JP, Baillet S, Garnero L, Martinerie J. A theoretical and experimental introduction to the non-invasive study of large-scale neural phase synchronization in human beings (invited paper). Int J Comput Cogn 2003;1(4):53–77.

David O, Cosmelli D, Friston KJ. Evaluation of different measures of functional connectivity using a neural mass model. NeuroImage 2004;21:659–73.

David O, Kilner JM, Friston KJ. Mechanisms of evoked and induced responses in MEG/EEG. NeuroImage 2006;31:1580–91.

Fisher NI. Statistical analysis of circular data. Cambridge University Press; 1995.

Friston KJ, Stephan KM, Frackowiak RSJ. Transient phase-locking and dynamic correlations: are they the same thing? Hum Brain Mapp 1997;5:48–57.

Gabor D. Theory of communication. Proc Inst Electr Eng 1946;93:429–41.

Gardner WA. A unifying view of coherence in signal processing. Signal Process 1992;29:113–40 (Elsevier).

Gevins A, Smith M, McEvoy L, Yu D. High-resolution EEG mapping of cortical activation related to working memory: effects of task difficulty, type of processing, and practice. Cereb Cortex 1997;7:374–85.

Gross J, Kujala J, Hämäläinen M, Timmermann L, Schnitzler A, Salmelin R. Dynamic imaging of coherent sources: Studying neural interactions in the human brain. PNAS 2001;98(2):694–9.

Guerrero JA, Marroquin JL, Rivera M, Quiroga JA. Adaptive monogenic filtering and normalization of ESPI fringe patterns. Opt Lett 2005;30(22):3018–20.

Haalman I, Vaadia E. Dynamics of neuronal interactions: relation to behavior, firing rates, and distance between neurons. Hum Brain Mapp 1998;5(4):249–53.

Harmony T, Fernandez T, Fernandez-Bouzas A, Silva-Pereyra J, Bosch J, Diaz-Comas L, et al. EEG changes during word and figure categorization. Clin Neurophys 2001;112:1486–98.

Harmony T, Fernandez T, Gersenowies J, Galan L, Fernandez-Bouzas A, Aubert E, et al. Specific EEG frequencies signal general common cognitive processes as well as specific task processes in man. Int J Psychophysiol 2004;53:207–16.

Harmony T, Alba A, Marroquin JL, Peña, J, Gonzalez-Frankenberger B. Time–frequency-topographic analysis of induced power and synchrony of the EEG signals during a GO/NO-GO task, submitted for publication.

Hebb DO. The organization of behaviour. New York: Wiley; 1949.

Jensen O, Idiart MA, Lisman JE. Physiologically realistic formation of autoassociative memory in networks with theta/gamma oscillations: role of fast NMDA channels. Learn Mem 1996;3:243–56.

Junghöfer M, Elbert T, Tucker DM, Braun C. The polar average reference effect: a bias in estimating the head surface integral in EEG recording. Clin Neurophysiol 1999;10(6):1149–55.

Kirschfeld K. The physical basis of alpha waves in the electroencephalogram and the origin of the "Berger effect". Biol Cybern 2005;92:177–85.

Klimesch W. EEG alpha and theta oscillations reflect cognitive and memory performance: a review and analysis. Brain Res Rev 1999;29:169–95.

Klimesch W, Schack B, Schabus M, Doppelmayr M, Gruber W, Sauseng P. Phase-locked alpha and theta oscillations generate the P1-N1 complex and are related to memory performance. Cogn Brain Res 2004;19:302–16.

Lachaux JP, Rodriguez E, Martinerie J, Varela FJ. Measuring phase synchrony in brain signals. Hum Brain Mapp 1999;8:194–208.

Lachaux JP, Rodriguez E, Le Van Quyen M, Martinerie J, Varela FJ. Studying single-trials of phase-synchronous activity in the brain. Int J Bifur Chaos 2000;10:2429–39.

Law SK, Nunez PL, Wijesinghe RS. High-resolution EEG using spline generated surface Laplacians on spherical and ellipsoidal surfaces. IEEE Trans Biomed Eng 1993;40(2):145–53.

Please cite this article in press as: Alba A, et al., Exploration of event-induced EEG phase synchronization patterns in cognitive tasks using a time–frequency-topography visualization system, J Neurosci Methods (2006), doi:10.1016/j.jneumeth.2006.10.018

969 Lopes da Silva FH. Neural mechanisms underlying brain waves: from
970 neural membranes to networks. Electroencephalogr Clin Neurophysiol
971 1991;79:81–93.
972 Marroquin JL, Mitter S, Poggio T. Probabilistic solution of ill-posed problems
973 in computational vision. J Am Stat Assoc 1987;82:76–89.
974 Marroquin JL, Figueroa JE. Robust quadrature filters. J Opt Soc Am
975 1997;14(4):779–91.
976 Marroquin JL, Velasco FA, Rivera M, Nakamura M. Gauss-Markov mea-
977 sure field models for low-level vision. IEEE Trans Pattern Anal Mach Int
978 2001;23(4):337–48.
979 Marroquin JL, Harmony T, Rodriguez V, Valdes P. Exploratory EEG data anal-
980 ysis for psychophysiological experiments. NeuroImage 2004;21:991–9.
981 Mizuhara H, Wang L, Kobayashi K, Yamaguchi Y. Long-range EEG phase syn-
982 chronization during an arithmetic task indexes a coherent cortical network
983 simultaneously measured by fMRI. NeuroImage 2005;27(3):553–63.
984 Morecraft RJ, Geula C, Mesulam MM. Architecture of connectivity within a
985 cingulo-fronto-parietal neurocognitive network for directed attention. Arch
986 Neurol 1993;50(3):279–84.
987 Nunez PL. Neocortical dynamics and human EEG rhythms. Oxford University
988 Press; 1995.
989 Nunez PL, Srinivasan R, Westdorp AF, Wijesinghe RS, Tucker DM, Silberstein
990 RB, et al. EEG coherency I: statistics, reference electrode, volume con-
991 duction, Laplacians, cortical imaging, and interpretation at multiple scales.
992 Electroencephalogr Clin Neurophysiol 1997;103:499–515.
993 Nunez PL. Toward a quantitative description of large-scale neocortical dynamic
994 function and EEG. Behav Brain Sci 2000;23:371–437.
995 Pascual-Marqui RD, Gonzalez-Andino SL, Valdes-Sosa PA, Biscay-Lirio R.
996 Current source density estimation and interpolation based on the spherical
997 harmonic Fourier expansion. Int J Neurosci 1988;43(3–4):237–49.
998 Perrin F, Pernier J, Bertrand O, Echallier JF. Spherical splines for scalp po-
999 tential and current density mapping. Electroencephalogr Clin Neurophysiol
1000 1989;72:184–7.
1001 Perrin F, Pernier J, Bertrand O, Echallier JF. Corrigenda: EEG 02274. Electroen-
1002 cephalogr Clin Neurophysiol 1990;76:565.
1003 Pfurtscheller G. Graphical display and statistical evaluation of event-
1004 related desynchronization (ERD). Electroencephalogr Clin Neurophysiol
1977;43:757–60.
Pfurtscheller G. Event-related synchronization: an electrophysiological correlate of cortical areas at rest. Electroencephalogr Clin Neurophysiol 1992;83:62–9.
Pfurtscheller G, Lopes da Silva FH. Event-related EEG/MEG synchronization and desynchronization: basic principles. Clin Neurophysiol 1999;110:1842–57.
Quian Quiroga R, Kraskov A, Kreuz T, Grassberger P. Performance of different synchronization measures in real data: a case study on electroencephalographic signals. Phys Rev E 2002;65:041903.
Quintana J, Fuster JM. From perception to action: temporal integrative functions of prefrontal and parietal neurons. Cereb Cortex 1999;9:213–21.
Rhom D, Klimesch W, Haider H, Doppelmayr M. The role of theta and alpha oscillations for language comprehension in the human electroencephalogram. Neurosci Lett 2001;310:137–40.
Rodriguez E, George N, Lachaux JP, Martinerie J, Renault B, Varela FJ. Perception's shadow: long-distance synchronization of human brain activity. Nature 1999;397:430–3.
Sarnthein J, Petsche H, Rappelsberger P, Shaw GL, Von Stein A. Synchronization between prefrontal and posterior association cortex during human working memory. Proc Natl Acad Sci USA 1998;95:7092–96.
Silverman BW. Density estimation for statistics and data analysis. London: Chapman and Hall; 1986.
Singer W. Synchronization of cortical activity and its putative role in information processing and learning. Ann Rev Physiol 1993;55:349–74.
Tallon-Baudry C, Bertrand O, Delpuech C, Pernier J. Oscillatory g-band (30–70 Hz) activity induced by a visual task in humans. J Neuroscience 1997;15:722–34.
Tallon-Baudry C, Bertrand O, Fisher C. Oscillatory synchrony between human extrastriate areas during visual short-term memory maintenance. J Neurosci 2001;15:RC177.
Ungerleider LG, Courtney SM, Haxby JV. A neural system for human visual working memory. Proc Natl Acad Sci USA 1998;95:883–90.
Varela FJ, Lachaux JP, Rodriguez E, Martinerie J. The brainweb: phase synchronization and large-scale integration. Nat Rev Neurosci 2001;2:229–39.

Please cite this article in press as: Alba A, et al., Exploration of event-induced EEG phase synchronization patterns in cognitive tasks using a time–frequency-topography visualization system, J Neurosci Methods (2006), doi:10.1016/j.jneumeth.2006.10.018

Appendix C

Software user manual

C.1 Introduction

C.1.1 What the Electro program does

Electro is a Windows application which preprocesses and analyzes data from an EEG experiment to detect changes in induced power and inter-electrode synchronization with respect to a neutral condition. The results are displayed as detailed Time-Frequency-Topography maps, which show the dynamics and spatial distribution of power and synchrony changes.

C.1.2 Installing Electro

Electro runs under Windows 95/98/ME/2000/XP. Because of the large datasets involved with EEG experiments, it is strongly suggested to use a fast processor (e.g., Intel Pentium 4 or AMD Athlon), large amounts of RAM (at least 512 Mb), and a large hard disk (80+ Gb). After preprocessing, some datasets may occupy several gigabytes of hard disk space.

To install *Electro* simply run the installer program (`electro_setup.exe`). A new item in the Start menu will be created and an icon will be placed in the desktop; *Electro* can be executed from any of these access points.

C.1.3 Types of files used by Electro

The program takes various input files, preprocesses them, and outputs several data files. Additional files may be created when computing alternate synchrony measures, or when analyzing evoked potentials. Here we present a list of the file types used by *Electro*.

Input files:

- Raw EEG samples (*.PLG): contains a series of EEG recordings for all channels. Typically, there is one PLG file per subject.
- Description of time windows (*.WIN): contains a description of the time segments that correspond to each trial in the experiment. There is one WIN file for each PLG file.
- Parameter file (*.dat): this is a text file which contains information about the experiment, including: location of PLG and WIN files, sample rate, number of channels, etc.

Output files:

- Amplitude of filtered signals (*.AMP): contains the amplitude of the output of the filter bank used for the time-frequency decomposition of the signals. There is one of these files for each frequency value.
- Phase of filtered signals (*.FAS): the phase component of the output of the filters. These, combined with the amplitud files, give the full time-frequency decomposition of the raw signals. There is one of these files for each frequency value.
- Time-Frequency-Topography (TFT) maps (*.dat): These files contain measures estimated across all frequencies, time samples, and electrodes (e.g., power changes, local phase constancy, etc.)
- Synchrony measures (*.dat): These files contain measures estimated across all frequencies, time samples, and electrode pairs (e.g., coherence, MPD, etc.)

C.2 EEG data files specification

Raw EEG data must be given in the form of PLG and WIN files. Typically, an EEG experiment consists of a series of voltage recordings $V_{j,e}(t)$, where j represents the trial number and e represents the recording channel. In most cases, all trials are recorded sequentially, without interrupting the recording process. Then, a series of markers (one per trial) are written as part of the data set. Each marker specifies the first and last sample which define the time window corresponding to each trial.

Moreover, it is possible that during the experiment, different trials correspond to different experimental conditions (EC's), but they are all recorded sequentially in a long time segment. In this case, it is necessary to specify, for each trial, the EC to which the trial belongs.

With this motivation, we proceed to describe the PLG and WIN file specification.

C.2.1 PLG files

PLG files contain the EEG recordings, for one subject, of all channels in the experiment as one long time series in which each sample is an array of N_e values (N_e being the number of channels). These values are stored as 16-bit signed integers (e.g. type short). Thus, PLG files are basically a two-dimensional array of shorts of the form:

```
short V[N_T][N_e]
```

where N_t is the total of samples recorded for the corresponding subject.

C.2.2 WIN files

WIN files contain the description, for each trial, of the experimental condition to which the trial belongs, and the first and last sample indices of the time window. They are stored as an array of structures of the following type:

```
struct {
    char EC;
    int ti;
    int tf;
} TRIAL_STRUCT;
```

It is important to know that `ti` and `tf` are 1-based, not zero-based; that is, the index corresponding to the first time sample is 1.

These structures are written sequentially, one for each trial. However, when reading the WIN file, there is no way to know the number of trials beforehand; one must read until the end of file (EOF) is reached.

Typically, there should be one WIN file per each PLG file, both files sharing the same name but with different extensions.

C.2.3 Example routine

The following example code shows how to read the raw EEG signals from a single PLG/WIN file pair into a three-dimensional (trial, time, and electrode) array of shorts. The parameters are two strings containing the name of the PLG and WIN files, respectively, and the number of channels (which is not stored in the files). It is also assumed that all trials have the same length in samples.

```
// start of sample code

typedef struct {
    char EC;
    int ti;
    int tf;
```

```
} TRIAL_STRUCT;

short ***ReadEEGData(char *plg_file, char *win_file, int n_chan) {
    TRIAL_STRUCT ts;
    int n_trials, n_time;
    int j, flag;
    short ***V;
    FILE *plg, *win;

    // open PLG and WIN files
    plg = fopen(plg_file, "rb");
    if (!plg) return NULL;
    win = fopen(win_file, "rb");
    if (!win) {
        fclose(plg);
        return NULL;
    }

    // Determine number and length of trials
    // (assume all trials have the same time length)
    flag = 1;
    n_trials = 0;
    while (flag) {
        if (fread(&ts, sizeof(ts), 1, win)) n_trials++;
        else flag = 0;
    }
    fseek(win, 0, SEEK_SET);
    n_time = ts.tf - ts.ti + 1;

    // Create array V[n_trials][n_time][n_chan]
    // and read signals into it.

    V = Create3DShortArray(n_trials, n_time, n_chan);
    if (V != NULL) {
        for (j = 0; j < n_trials; j++) {
            fread(&ts, sizeof(ts), 1, win);
            fseek(plg, (ts.ti - 1) * n_chan * sizeof(short), SEEK_SET);
            fread(V[j], sizeof(short), n_time * n_chan, plg);
        }
    }

    fclose(plg);
    fclose(win);
    return V;
}
```

```
// end of sample code
```

C.3 Parameter files

The location of the data files that one wants to process and other important information, such as the sampling rate and the number of channels, must be specified in a *parameter file*. This is a text file with extension **.dat** and the following format:

```
win = c:\EEGdata\experiment1\data\subject01.win
plg = c:\EEGdata\experiment1\data\subject01.plg
out = c:\EEGdata\experiment1\output\output.dat
pos = 8
iarch = 1
narch = 7
nt = 512
nf = 50
samplerate = 200
tstim = 200
condition = -1
nchan = 19
nelec = 19
sigmat = 15
nk = 128
```

The fields in the parameter files must be written in separate lines, but in no particular order. Each field has a parameter identifier (e.g., "samplerate", "out", "nchan", etc.), and a value. Some parameters have default values and may not be specified, while others are required. Tables C.1 and C.2 describe all parameters, the type of values each may take, and the default value for non-required fields.

medskip

Without special considerations, the program can handle up to 20 electrodes corresponding to sites Fp1, Fp2, F3, F4, C3, C4, P3, P4, O1, O2, F7, F8, T3, T4, T5, T6, Fz, Cz, Pz, and Oz of the 10/20 system (in that order). However, it is possible to handle other configurations (even high-resolution EEG with 120 or more electrodes) by writing a special file and adding an extra field in the parameter file. This procedure is explained with more detail in the section C.10.

C.3.1 Indexing of raw data files

It is possible to load more than one pair of PLG/WIN files. This is important, for example, when an experiment is performed by various subjects, each of which

Parameter	Type	Default	Description
`win`	alphanumeric	**required**	Full path to the WIN file corresponding to the first subject.
`plg`	alphanumeric	**required**	Full path to the PLG file corresponding to the first subject.
`out`	alphanumeric	**required**	Full path to the output files.
`pos`	integer	6	Specifies the character position corresponding to the index in the PLG and WIN files (see below for details).
`iarch`	integer	0	First index of the PLG and WIN files (see below for details)
`narch`	integer	0	Last index of the PLG and WIN files (see below for details)
`nt`	integer	**required**	Number of time samples in each trial.
`nf`	integer	20	Analysis bandwidth in Hertz. The signals will be analyzed at frequencies $f = 1, 2, \ldots,$ `nf` Hz.
`samplerate`	integer	**required**	Sample rate in Hertz.
`tstim`	integer	**required**	Length of pre-stimulus segment in samples.
`condition`	integer	-1	ID of experimental condition. Only trials corresponding to the specified EC will be loaded (-1 means that all trials will be loaded, regardless of their corresponding EC).
`nchan`	integer	**required**	Number of channels recorded in the PLG files.

Table C.1: Description of fields in a parameter file (part 1).

Parameter	Type	Default	Description
`nelec`	integer	`nchan`	Number of electrode channels to process. Only the first `nelec` channels of the recording will be processed. If this field is not specified, the program will assume `nelec = nchan`.
`sigmat`	integer	0.075 * `samplerate`	Width of the quadrature filters in time samples. Corresponds to the standard deviation of the Gabor filters. The default value corresponds approximately to 1.06 Hz.
`nk`	integer	128	Size of the filter kernels in time samples. Should be increased for high sample rates ($>$ 256 Hz) and/or large analysis bandwidths ($>$ 50 Hz).

Table C.2: Description of fields in a parameter file (part 2).

is related to a single PLG/WIN file pair. However, this must be done within a few restrictions.

The name of the PLG and WIN files must be equal, with the exception of a two-digit index. Here are a few examples of accepted file names:

- `eeg00.plg, eeg01.plg, eeg05.plg, ...`
- `subject001_x.plg, subject002_x.plg, ...`
- `data00010000.plg, data00011000.plg, data00012000.plg, ...`

In the first example, the "base" file name is `eeg##.plg`, where `##` represents the two digit index. In the second and third examples, the base file names are `subject0##_x.plg` and `data000##000.plg`, respectively. This limits the number of PLG files one can load to 100 for a single experiment.

There must be one WIN file for each PLG file, both sharing the same base name (minus the extension, of course). If any file is missing, or does not follow the naming scheme, the data for the corresponding subject will not be loaded.

The `iarch` and `narch` fields in the parameter file specify the first and last indices of the files that will be read. Typically, `iarch` will be zero or one, and `narch` will be the number of subjects, assuming the files are numbered sequentially.

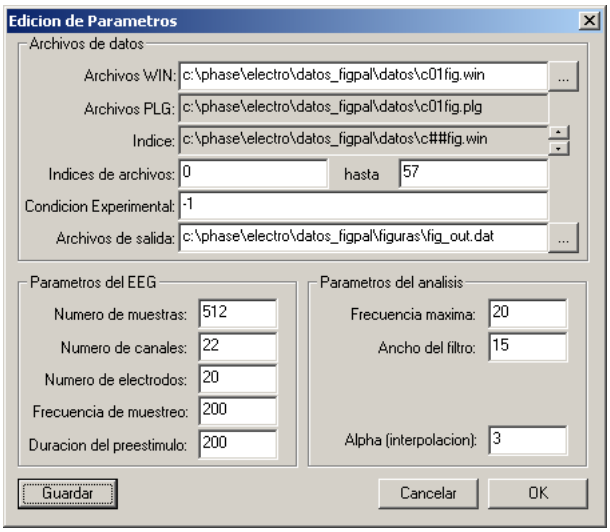

Figure C.1: Dialog box for editing a parameter file.

The `pos` parameter specifies the character position of the first digit of the index, starting from the end of the string. For example, if the base file name is `eeg##.plg` or `data0##.plg`, then `pos` should be equal to 6, whereas for `subject##_data.plg` the correct value for `pos` would be 11.

C.3.2 Creating a parameter file

To pre-process and analyze the data from an EEG experiment, it is necessary to create a parameter file with all the required information. This can be done in any text editor, using the format description shown in the previous sections; however, an easier interface is already provided by *Electro*. To create a parameter file this way, simply open the program and select the option **"Archivo"** — **"Editar archivo de parametros"** (i.e., click first on the **"Archivo"** menu and then select the option from the menu). This will open the dialog window shown in Figure C.1.

In this dialog box, one can simply press the upper-right button marked as "..." (see Figure C.2a) to search for any of the WIN files that belong to the experiment. Selecting a WIN file will also select the PLG file with the same name. The position of the file index is represented in the **"Indice"** field by the '`##`' symbols. One can use the up and down arrows (see Figure C.2b) to move these symbols, and thus change the index position. It is important to select the correct position so that the program will be able to load all the files from the experiment. The actual indices will cover the range indicated in the field **"Indices de archivos"**.

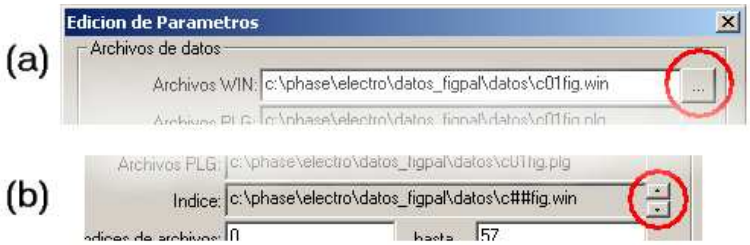

Figure C.2: **(a)** The button marked with the red circle opens a file dialog where one can search for any of the WIN files from the experiment. **(b)** The position of the WIN/PLG file index is represented by the ## symbols; to move the symbols, one can use the up and down arrows shown in the red circle.

Once the parameters have been edited, it is important to save the changes in the parameter file. To do this, click the button marked as **"Guardar"**.

C.3.3 Loading a parameter file

Once a parameter file has been created and saved, it is necessary to load it in order to read the raw EEG data files and pre-process them. To do this, simply select the option **"Archivo"** — **"Abrir archivo de parametros"** and select the parameter file. The program will ask if you want to load the raw EEG signals. If the data set has not been pre-processed already (e.g., if this is the first time you load the data set), you should answer "Yes". Loading the raw data is required for pre-processing and computing new measures. It is not required for displaying and navigating measure maps that have already been computed.

C.4 Loading and preprocessing the data

In order to compute most of the measures, it is necessary to perform a time-frequency decomposition of the raw signals by running them through a bank of bandpass filters. Since this is a computationally intensive task, it is better to perform it only once and save the filtered signals. Once the signals have been filtered, it is possible to compute TFT maps of induced changes in power and synchrony. *Electro* combines all these tasks into a single one called "pre-processing", and it is usually performed when loading the data for the first time.

In summary, what pre-processing does is

1. Run the raw EEG signals through a bank of bandpass filters with bandwidth specified by the field `sigmat` in the parameter file.

2. Compute the TFT map of amplitude (power) changes with respect to the pre-stimulus.

3. Compute the changes of synchronization (for all pairs of electrodes) with respect to the pre-stimulus using the MPD (mean phase difference) measure.

To pre-process the data one must load first the corresponding parameter file and let the program load the raw signals (answer "Yes" when asked to load the raw data). Then one must select the option **"Archivo"** — **"Preprocesar datos"**. Pre-processing is a relatively slow process which may take up to several hours (and several gigabytes of disk space), depending on the size of the data set. Once the process has finished, a dialog box will appear indicating that the data has been pre-processed. After the data has been pre-processed, one can display and navigate the amplitude and MPD maps, or compute other measures.

Always make sure you have plenty of disk space before preprocessing a data set. The data resulting from the time-frequency decomposition of the raw signals will take $8N_fN_rN_eN_t$ bytes, where N_f is the frequency limit of the analysis, N_r is the number of trials, N_e the number of electrodes, and N_t the length of each trial. This means that if one pre-processes an experiment with 20 electrodes, 512 samples per trial, 1000 trials, the time-frequency decomposition from 1 to 20 Hz ($N_f = 20$) will require around 1.5 Gb of disk space. Besides this, each synchrony map requires $4N_fN_e^2N_t$ (e.g., 15.6 Mb for the previous example).

C.5 Time-Frequency-Topography maps

In this section we describe the types of maps that can be generated after the data from a specific experiment has been pre-processed.

C.5.1 Amplitude map (induced power)

The amplitude map displays significative changes in induced power with respect to the pre-stimulus segment. The time scale is divided in windows of small length (e.g., 10 samples) and a head diagram is plotted for each time window and each frequency band. Each head diagram shows the distribution of power changes for the corresponding time-frequency window. Electrodes which show significant changes are represented with green or red dots, corresponding to power decreases or increases, respectively. An example is shown in Figure C.3a.

To show the amplitude TFT map select the option **"Mapa"** — **"Mapa TFT de amplitudes"**. A dialog box will appear with the following parameters:

- **Tiempo inicial:** Initial value of the time line (in samples). The default value is the pre-stimulus length, so that the map shows only the post-stimulus.

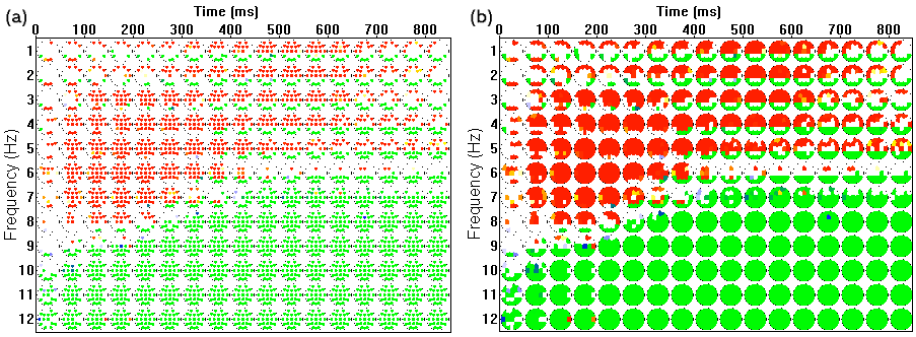

Figure C.3: **(a)** TFT map of induced power changes (see text for details). **(b)** Interpolated version of the same map.

- **Tiempo final:** Last value of the time line (in samples). The default value is the number of samples in the experiment (N_t) truncated to a multiple of 10 (e.g., if $N_t = 512$, the map will display up to $t = 510$).
- **Intervalo:** Length of the time window corresponding to each head diagram. The default value is 10 samples.
- **Escala:** Scale of the map. Larger values will result in larger maps. A map with scale smaller than 16 may not be legible. The default value is 24.
- **Umbral significancia:** Significance threshold. The color scale will be rescaled to show only significance values higher than this threshold. The default value is 0.99.

It is also possible to display whole regions within the head diagram as green or red instead of just using dots. This is done by generating a Voronoi partition of the head diagram given by the electrode positions (each point in the head diagram is assigned the value of the nearest electrode). The resulting display may give a better idea of the topographical distribution of the power changes, although it takes longer to compute than the "dotted" version. To turn this interpolation on or off, select the option **"Mapa"** — **"Interpolar topografia en mapa TFT"**. Figure C.3b shows an example of an interpolated map.

C.5.2 Synchrony histograms

Synchrony histograms represent, for each electrode, how many sites increase (or decrease) their synchronization with the electrode, with respect to the prestimulus average. In other words, they are a representation of the degree of involvement of each electrode in synchronous processes. A synchrony increase

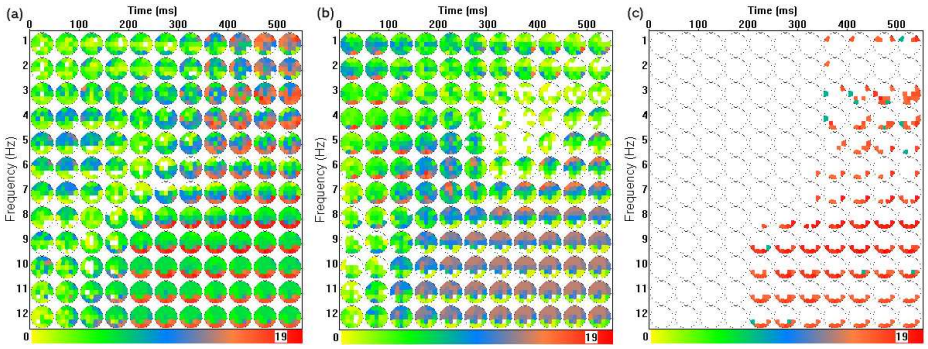

Figure C.4: **(a)** Synchrony increase histogram. The color scale represents the number of sites which show a significant increase in synchrony with each region within the head diagrams. **(b)** Synchrony decrease histogram for the same experiment as (a). **(c)** Synchrony increase histogram (same as (a)) showing only values greater or equal than 15 electrodes (nodal points).

histogram (SIH) shows the number of sites with which each electrode increases its synchrony (see Figure C.4a). Similarly, one can obtain a synchrony decrease histogram (SDH), which shows, for each electrode, how many sites decrease their synchrony with it (Figure C.4b).

To obtain a synchrony histogram select the option **"Mapa"** — **"Histograma TFT de aumento de sincronia"** (for an SIH), or **"Mapa"** — **"Histograma TFT de disminucion de sincronia"** (for an SDH). A dialog box will appear with the same options as the amplitude map. Note that the significance threshold determines which couplings are considered significant; therefore, even if the histogram shows low values (e.g., yellow and green), those already represent significant (although few) couplings. Besides these parameters, one can also specify the following:

- **Umbral histograma:** Histogram threshold. Only histogram values greater or equal than this threshold will be shown. This parameter is useful, for example, to show those electrodes which shown many significant couplings (nodal points).

Depending on the state of the **"Interpolar topografia en mapa TFT"** option, synchrony histograms will be shown either with dots or filled regions within each head diagram.

C.5.3 Multitoposcopic display

It is possible to show a detailed display of the synchrony pattern (SP - e.g., significant changes in synchrony for all electrode pairs) for a particular time and frequency in the form of a multitoposcopic display (Figure C.5a). This

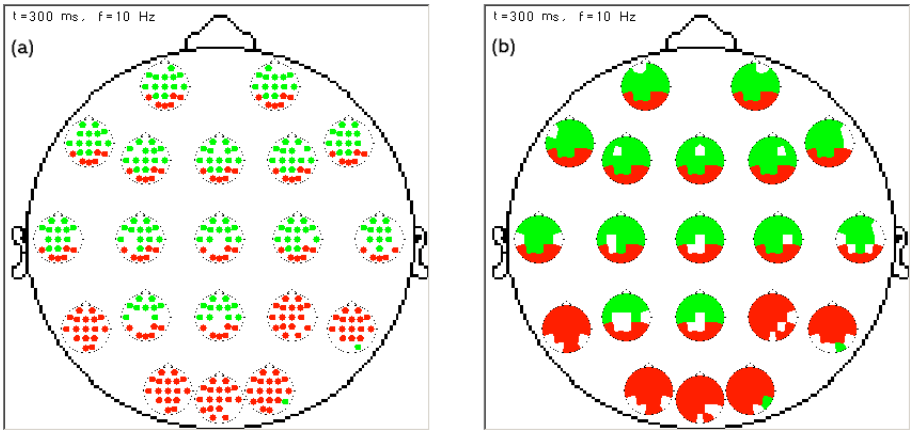

Figure C.5: **(a)** Multitoposcopic display of a synchrony pattern (SP). **(b)** Same SP as (a) but with interpolation turned on.

display shows a head diagram for each electrode e; this head diagram shows the distribution of synchrony changes between e and every other site: green regions represent synchrony decreases, whereas red regions correspond to increases in synchrony.

A multitoposcopic display can be opened by clicking on the amplitude map or synchrony histogram. Clicking on the point corresponding to time t and frequency f will bring the SP corresponding to that time-frequency point. While the multitoposcopic display is active, one can use the arrow keys to navigate through the time-frequency space: the left and right arrows change the display time, whereas the up and down arrows change the frequency.

It is also possible to present the SP display in interpolated form (Figure C.5b). To do this, go to the option **"Mapa"** — **"Interpolar topografia en mapa de sincronia"** to turn multitoposcope interpolation on or off.

C.5.4 Local phase constancy maps

Besides the amplitude and synchrony TFT maps, one can also display a TFT map of significant changes in the local phase constancy observed at each electrode. These maps, however, must be computed the first time they are displayed, as they are not computed during pre-processing.

There are two types of phase constancy maps: (1) phase constancy across time (**"Mapa"** — **"Consistencia de fases (en tiempo - LPC)"**), and (2) phase constancy across trials (**"Mapa"** — **"Consistencia de fases (en repeticiones - LPCT)"**). According to our population model for the apparent

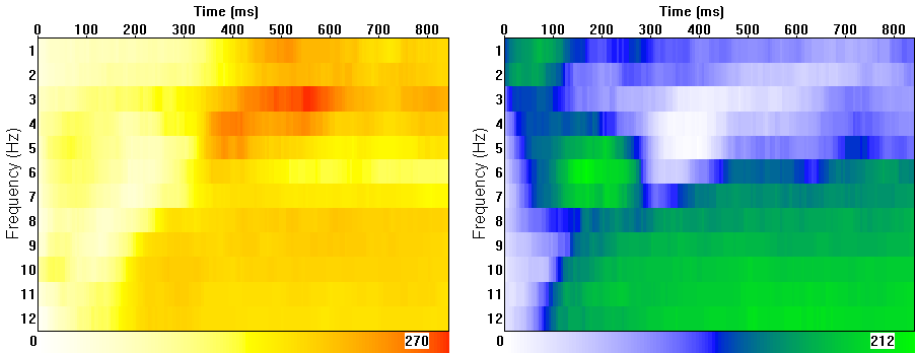

Figure C.6: TF histograms of increases (left) and decreases (right) of synchronization for a real EEG experiment. Note that the maximum number of electrode pairs which increase their synchrony at any time-frequency point is 270, whereas the maximum number of desynchronizations is 212.

phase [1], the first type of phase constancy may be related with the coupling of networks in the reception area of each electrode (local synchrony), while the latter is related to one of the mechanisms that may generate evoked activity (see Section C.9.2).

C.6 TF maps

There are two more types of display which may be useful or interesting. These are presented in the form of a time-frequency (TF) map and provide no information about the topographical distribution of synchronous activity.

C.6.1 TF synchrony histograms

Electro computes a TF synchrony increase (or decrease) histogram by simply counting, for each time-frequency point, the number of electrode pairs that show an increase (or decrease) of synchronization. To display these histograms, select the option **"Mapa"** — **"Mapas TF"** — **"Aumento de sincronia"** or **"Mapa"** — **"Mapas TF"** — **"Disminucion de sincronia"**. The options dialog box will appear with the same options as for the TFT histograms plus the following option:

- **Rango histograma:** Histogram range (maximum number significant couplings). The histogram will be normalized so that the color scale covers

[1] See Alba et al., 2006. Exploration of event-induced EEG phase synchronization patterns in cognitive tasks using a timefrequency-topography visualization system, J Neurosci Methods (in press).

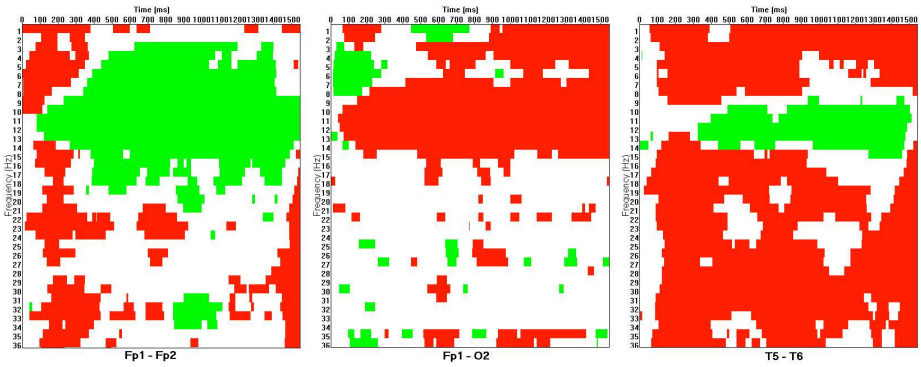

Figure C.7: TF maps of synchrony between pairs of electrodes. Red and green regions represent significant increases and decreases, respectively, of synchronization with respect to the baseline.

exactly this range of values. If this parameter is less or equal than zero, the range of the histogram will be equal to the maximum number of significant couplings (which will also be displayed in the color scale). This is done to take advantage of the full color scale, however it may not be adequate when comparing two different histograms (e.g., for two experimental conditions).

Figure C.6 shows the TF increase and decrease histograms for an experiment.

C.6.2 Synchrony between two electrodes

If one is interested in a particular pair of electrodes, a TF map of synchrony changes between those electrodes may be more intuitive than the full TFT display. An example is shown in Figure C.7.

To obtain a TF synchrony map between two electrodes, select the option **"Mapa"** — **"Mapas TF"** — **"Sincronia entre dos electrodos"**. A dialog box will appear to select the two electrodes[2]; one must select one electrode from each group (denoted as "Grupo 1" and "Grupo 2").

C.7 Partitioned synchrony maps

One can also obtain a detailed description of synchrony changes by dividing the time-frequency plane in various regions, and displaying a representative synchrony pattern (in the form of a multitoposcope) for each region. The representative pattern may be obtained in various forms, for example, it may be

[2]At this point, this feature is not complete. In the future, the dialog box will show the selected electrodes within the head diagram.

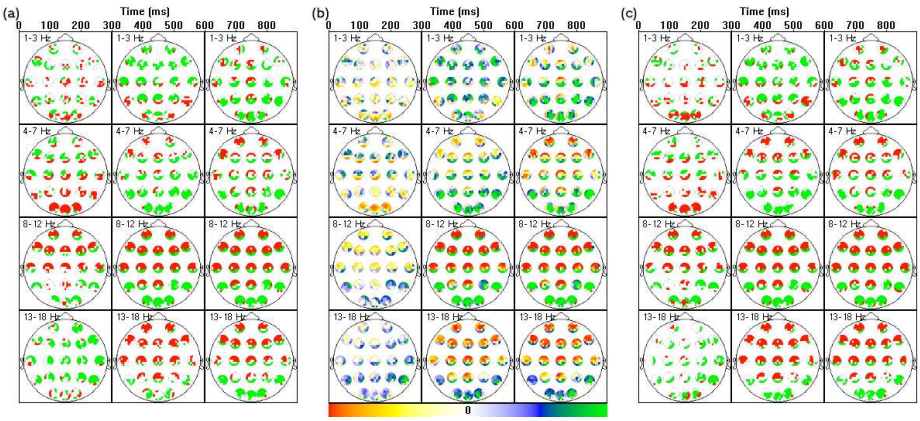

Figure C.8: Partitioned synchrony maps using a regular partition each 300 ms and by frequency bands (delta, theta, alpha, low beta). Each map is computed using a different statistic: **(a)** shows the SP corresponding to the center of each TF window, **(b)** shows the average class across the TF window for each electrode pair, and **(c)** shows the class mode.

the SP corresponding to a TF point within the region, or it may be obtained as an statistic (e.g., the average) of all the SP's in the region.

C.7.1 Generating a regular partition map

The first (and easiest) way to obtain a partitioned map consists on dividing the TF plane in regular windows of the same time length (e.g., 300 ms) and by frequency bands (delta, theta, alpha, etc.). An example is shown in Figure C.8 using as representative (a) the SP corresponding to the center of the region, (b) the average class for each electrode pair, and (c) the class mode for each electrode pair. One can choose which statistic will be used as representative in the menu **"Partición"** — **"Representante de área"**. The class mode is selected by default.

To obtain a regularly partitioned synchrony map, go to the option **"Particion"** — **"Mapa particionado definido por el usuario"**. An options dialog box will appear. In this dialog box one can select the time range and frequency bands that will be shown, and the time length of each window. There are two lists of frequency bands: the one on the left side contains a few preset bands including delta (1-3 Hz), theta (4-7 Hz), alpha (8-12 Hz), low beta (13-18 Hz), high beta (19-29 Hz), etc. The list on the right side contains the frequency bands that will be included in the partitioned synchrony map and is initially empty. One can select any number of preset bands (by clicking on them) and add them to the right side list by clicking on the **"Agregar"** button. One can also add any arbitrary frequency band (e.g., 10-11 Hz, or 1-30 Hz) by typing

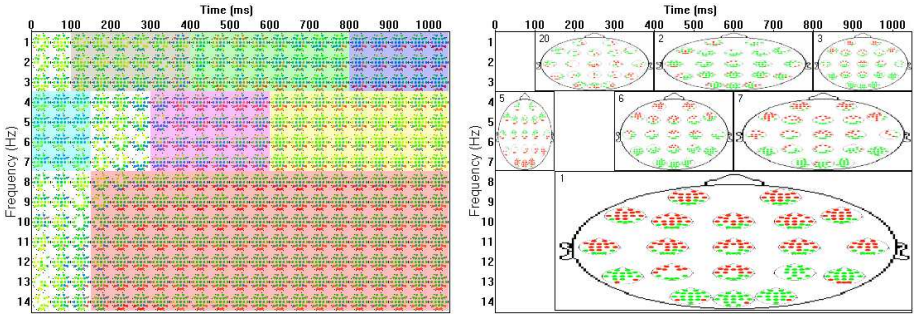

Figure C.9: Manual partition of a TFT synchrony histogram (left graph), and the corresponding TFT synchrony map (right graph).

the frequencies in the text fields labeled as **"Banda arbitraria"** and clicking on the **"Agregar"** button. To eliminate a frequency band from the right side list, select it and click on the **"Eliminar"** button.

Other options in the dialog box include the time interval (fields **"Inicio"** and **"Final"**), and the length of the windows in which time interval will be subdivided (field **Subdivisión**). Note that these parameters are given in milliseconds, not in samples, and that 0 ms indicates the stimulus onset. By default, the time interval goes from 0 ms to the length of the pre-stimulus segment, and the subdivision time is 300 ms. Finally, one can also specify the scale of the map (field **Escala**), which has the same meaning as in the other TFT maps.

C.7.2 Manual partitions

Ideally, one would like to partition the TF space in regions where the synchrony pattern is relatively constant. This may be done by manually selecting the regions in one of the TFT synchrony histograms. As an example, Figure C.9 shows a TFT synchrony increase histogram (left graph) where regions with constant SP (defined by hand) are shown as colored rectangles, and the synchrony map (right graph) obtained from the same partition.

To generate these kind of maps, one must first display a TFT synchrony histogram, and select one or more time-frequency regions within the histogram. Only rectangular regions may be selected. To add a new region, press SHIFT and right-click on any point in the TF space. A small square will appear on the clicked site. One can expand this square into a larger region by pressing the SHIFT key, and dragging the square with the right mouse button[3]. To move the region, simply drag it (without pressing SHIFT) using the right button.

The following table lists all of the region operations that can be performed. Note that all of these operations make use of the right mouse button, instead of the left one.

[3]Regions can only be expanded rightwards and/or downwards.

Operation	Mouse action	Keyboard action
Select region	Right-click	
Create new region	SHIFT + Right-click	
Delete region	CTRL + Right-click	
Move selected region	Right-button drag	Arrow keys
Expand selected region	SHIFT + Right-button drag	SHIFT + Arrow keys

Once the regions have been selected, one must select the option **"Partición"** — **"Generar Mapa Particionado"** in order to display the partitioned map. This may take a few minutes, depending on the number and size of regions.

There are other useful options within the **"Partición"** menu:

- **"Guardar Partición"** (Save Partition) - Allows one to save the selected regions in a file, so they can be recovered at any time.
- **"Cargar Partición"** (Load Partition) - Reads a partition file from disk and displays the corresponding regions in the active TFT map.
- **"Borrar Partición"** (Delete Partition) - Clears all area selections.
- **"Partición predefinida"** (Preset partition) - Generates a partition by frequency bands and regular time intervals.

The Load/Save options are particularly useful if one wants to create a manual partition, for example, from the synchrony increase histogram, and then apply it to the synchrony decrease histogram to adjust some regions or add new ones.

C.8 Other synchrony measures

By default, *Electro* computes changes in synchronization using the Mean Phase Difference (MPD) measure. This particular measure responds when the electrode signals under study are nearly in phase. Besides this measure, *Electro* implements various other synchrony measures that may give different results, depending on the data set. Table C.3 shows all the synchrony measures that are currently implemented[4]. Note that most of them require a parameter, which may have to be adjusted for each particular data set.

[4]The Anti-phase CPPD and Modulo-π CPPD measures are experimental anti-phase measures which have been implemented only for testing purposes. At this point, we do not suggest using them for the analysis of cognitive experiments.

Measure	Parameter	Parameter default
Mean Phase Difference (MPD)	N/A	N/A
Cumulative Probability of Phase Dif. (CPPD-ms)	Threshold (ms)	10 ms
Cumulative Probability of Phase Dif. (CPPD-rad)	Threshold (rad)	0.05 rad
Lachaux's Phase Locking Statistic (PLS)	N/A	N/A
Single-Trial Phase Locking Statistic (STPLS)	Window size (ms)	100 ms
Coherence	Window size (ms)	100 ms
Anti-phase CPPD (AP-CPPD-rad)	Threshold (rad)	0.05 rad
Modulo-π CPPD (MP-CPPD-rad)	Threshold (rad)	0.05 rad

Table C.3: Synchrony measures implemented in *Electro*.

C.8.1 Computing other measures

To compute a different measure (than MPD) one must first load the raw EEG signals: when loading the parameter file, answer "Yes" when asked to load the raw data. Then select the option **"Mapa"** — **"Seleccionar medida de sincronía"**. A dialog box will appear where one can select any of the measures described above, and adjust their parameter (if necessary). If the selected measure has been previously computed, then it will be used for any subsequent TFT map that is displayed. Otherwise, a dialog box will appear asking if one wants to compute the measure.

Keep in mind that computing a new measure (or even a previously computed measure but with a different parameter value) is computationally expensive and may take some time (up to a few hours), depending on the measure, size of the dataset, and computer speed. It will also require some disk space (more specifically, $4N_f N_e^2 N_t$ bytes, as previously stated).

C.8.2 Computing and comparing multiple measures

It is also possible to instruct the program to compute various measures, so that one can leave the system unattended while it is working. To do this, make sure you have loaded the raw EEG signals, and then go to the option **"Mapa"** — **"Calcular múltiples medidas"**. Select the first measure you want to compute (and its parameter) and press the OK button. Then select the second measure, and press OK again. Repeat this procedure until you have entered all the measures you would like to compute, and then press the **"Calcular"**

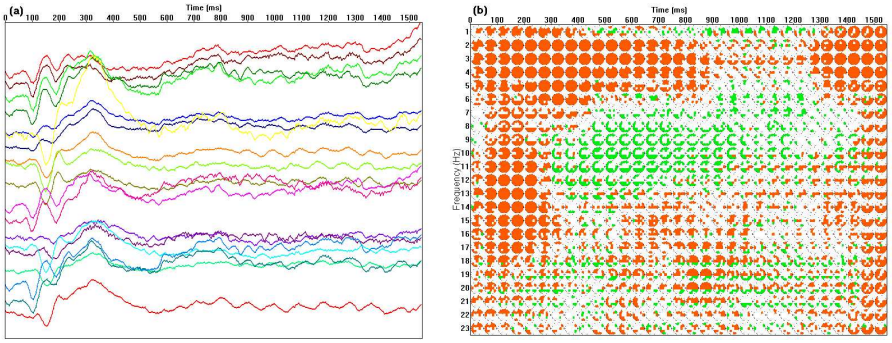

Figure C.10: **(a)** Evoked signals obtained from an EEG experiment. **(b)** TFT map of relative changes in evoked power for the same experiment.

button. **Electro** will start computing the measures and will display a message when finished.

Once various measures have been computed, it is possible to compare them by estimating the correlation between each pair of measures. To do this, select the option **"Mapa"** — **"Comparar Medidas"**. A dialog box will appear where one can specify up to 8 different measures (with their respective parameters). After the correlations have been estimated for each pair of the given measures, the program will ask the user to enter a file name, where the results will be saved as a table in text format. This table provides an estimate of the degree of similarity between different measures, which may be used to avoid exploring redundant information.

C.9 Evoked activity maps

Electro can also perform various analyses involving evoked activity. The evoked signals (also called event-related potentials, or ERP's) are obtained as the average of the raw potentials across trials. Since the raw signals are required for estimating evoked activity, the user must tell *Electro* to load the raw data after loading the parameter file (see Section C.3.3).

All the evoked activity analyses are located under the **"PEV"** menu. However, be aware that these options are still under development and may be modified in the future.

C.9.1 Evoked signals and evoked power

One can display the evoked signals (i.e., the inter-trial average potentials) by choosing the option **"PEV"** — **"Graficar potenciales evocados"**. The evoked signals are plotted against time using a different color for each electrode

(see, for example, Figure C.10a); one can see which electrode corresponds to each of the displayed signals by moving the mouse pointer over the signal: the electrode name will appear in the status bar (in the bottom part of the main window). Note that this is only a very rough display in which the amplitude scale is unknown; therefore, it is not adequate for serious studies.

It is also possible to estimate the relative changes in evoked power with respect to the pre-stimulus average. This analysis is similar to the one presented in Section C.5.1, but applied to the set of evoked signals. The resulting TFT map (Figure C.10b) shows, for each time and frequency, for which electrodes the evoked power increases (red) or decreases (green) significatively, with respect to the pre-stimulus.

C.9.2 Evoked power, induced power, and phase constancy

There are two plausible theories which have been proposed to explain the generation of evoked potentials: the first one suggests that the populations of neurons which respond to a determined stimulus generate a waveform that is added to the background EEG, which is unrelated to the stimulus. The second theory proposes that the presentation of a stimulus forces the phases of ongoing oscillations to shift to a determined value, which translates into constructive interference when averaging across trials, resulting in an event-related potential[5].

One may be able to determine if one of these mechanisms is related to a specific event-related potential by detecting correlations between (1) the relative changes in evoked power, (2) the relative changes in induced power (Section C.5.1), and (3) changes in local phase constancy across trials. The first of these correlations (i.e., evoked power vs induced power) can be displayed in form of a TFT map with the option **"PEV" — "TFT de potencia evocada vs potencia inducida"**. In this map, electrodes are shown as red, green, or blue circles (or areas) according to the following possibilities:

- **Red.-** Simultaneous increase in both evoked and induced power at the electrode.
- **Green.-** Significant increase in evoked power, but not in induced power.
- **Blue.-** Significant increase in induced power, but not in evoked power.

Coincidences between evoked power and phase constancy across trials may also be interesting. One can display a TFT map of these correlations with the option **"PEV" — "TFT de potencia evocada vs LPCT"**. In this map, each electrode is displayed in red, green, or blue, according to the following possibilities:

[5]Reference: Mazaheri, A., Picton, T.W., 2005. EEG spectral dynamics during discrimination of auditory and visual targets. Cognitive Brain Research. 24: 81-96.

- **Red.-** Simultaneous increase in both evoked and phase constancy (across trials).
- **Green.-** Significant increase in evoked power, but not in phase constancy.
- **Blue.-** Significant increase in phase constancy, but not in evoked power.

Finally, the option **"PEV" — "Potencia evocada vs potencia inducida vs LPCR"** displays a TFT map in which each point is classified in one of the following cases:

- **Red.-** Simultaneous increase in evoked power, induced power, and phase constancy.
- **Green.-** Simultaneous increase in evoked power and phase constance, but not in induced power.
- **Blue.-** Simultaneous increase in evoked power and induced power, but not in phase constancy.
- **Yellow.-** Significative increase in evoked power, but not in induced power nor in phase constancy (i.e., evoked responses which cannot be explained by any of the two mechanisms).

These maps may help to distinguish which mechanisms are involved in the generation of a specific evoked response.

C.9.3 Evoked power vs induced synchrony

The option **"PEV" — "Mapa de potencia evocada vs sincronía inducida"** computes and shows a partitioned map of correlations between evoked power changes and induced synchrony changes. Each electrode pair is displayed in red, green, or blue, according to the following possibilities:

- **Red.-** Simultaneous increase in evoked power at both electrodes, and an increase in induced synchronization between the electrodes.
- **Green.-** Increase in evoked power at both electrodes, but not in synchrony between them.
- **Blue.-** Increase in induced synchrony between the electrodes, but not in evoked power at both of them.

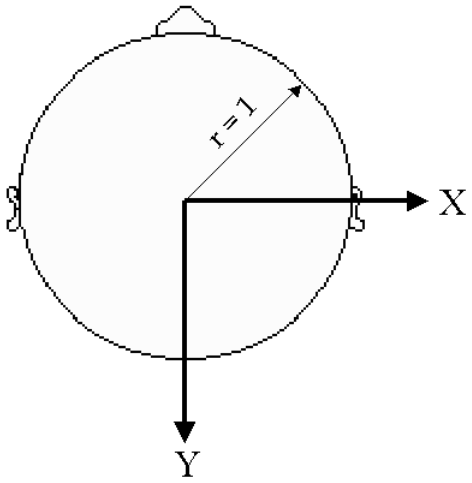

Figure C.11: Coordinate system of the head diagram in which the electrodes are located: the X-axis goes from left to right, the Y-axis goes from top to bottom, and the head has radius 1.

C.10 Alternate electrode configurations

Although the program has been designed to work with electrode configurations in the 10-20 system, it is possible to use alternate configurations by providing a special text file which specifies the electrode positions within a circle of radius 1, which corresponds to a head diagram with the nose pointing upwards and electrode Cz at the center ($X = 0, Y = 0$); the X (horizontal) axis goes from left to right, and the Y (vertical) axis goes from top to bottom (see Figure C.11).

The text file should one line for each electrode in the configuration, and in each line, one must specify the following fields separated by tabulations:

- Electrode label
- X-coordinate of the electrode within the head diagram
- Y-coordinate of the electrode within the head diagram
- The zenith angle (from the positive z-axis) of the electrode within a sphere of radius 1, given as a fraction of the full circle. This field is currently not used and can be set to zero).
- The azimuth angle (from the positive x-axis) of the electrode within a sphere of radius 1, given as a fraction of the full circle. This field is currently not used and can be set to zero).

As an example, we show here the electrode position file corresponding to the 10-20 system:

```
Fp1     -0.333      -0.947      0.25    0.05
Fp2     0.350       -0.947      0.25    0.95
F3      -0.456      -0.491      0.1875  0.1
F4      0.456       -0.491      0.1875  0.9
C3      -0.491      0.000       0.125   0.25
C4      0.491       0.000       0.125   0.75
P3      -0.456      0.491       0.1875  0.4
P4      0.456       0.491       0.1875  0.6
O1      -0.315      0.947       0.25    0.45
O2      0.315       0.947       0.25    0.55
F7      -0.807      -0.596      0.25    0.15
F8      0.807       -0.596      0.25    0.85
T3      -1.000      0.000       0.25    0.25
T4      1.000       0.000       0.25    0.75
T5      -0.824      0.561       0.25    0.35
T6      0.824       0.561       0.25    0.65
Fz      0.000       -0.491      0.125   0
Cz      0.000       0.000       0       0
Pz      0.000       0.491       0.125   0.5
```

After writing the electrode position file, one must edit the parameter file (using a text editor) to include a line which indicates the location of the electrode position file. This is done by adding the following line to the parameter file:

```
elecposfile = <electrode position file path>
```

After this modification, one must re-load the parameter file so the electrode positions are updated. One should be aware that if there are more than 20 electrodes, *Electro* will group them in cortical areas when displaying synchrony patterns in multitoposcopic form.

Bibliography

[1] Aurenhammer, F., 1991. Voronoi Diagrams - A Survey of a Fundamental Geometric Data Structure. ACM Computing Surveys. 23(3): 345-405.

[2] Baddeley, A., 1999. Human memory. Allyn and Bacon, Boston, MA.

[3] Barde, L.H., Thompson-Schill S.L., 2002. Models of functional organization of the lateral prefrontal cortex in verbal working memory: Evidence in favor of the process model. J Cogn Neurosci. 14: 1054-1063.

[4] Basar-Eroglu, C., Basar, E., Demiralp, T., Schurmann, M., 1992. P-300 response: posible psychophysiological correlates in delta and theta frequency channels. A review. Int J Psychophysiol. 13: 161-179.

[5] Basar-Eroglu, C., Demiralp, T., 2001. Event-related theta oscillations: an integrative and comparative approach in the human and animal brain. Int J Psychophysiol. 39: 167-196.

[6] Bastiaansen, M., Hagoort, P., 2003. Event-induced theta responses as a window of the dynamics of memory. Cortex. 39: 967-992.

[7] Berger, H., 1929. Uber das Elektrenkephalogramm des Menchen. Archives fur Psychiatrie. 87:527-70.

[8] Bressler, S.L., Coppola, R., Nakamura, R., 1993. Episodic multiregional cortical coherence at multiple frequencies during visual task performance. Nature. 366: 153-156.

[9] Bressler, S.L., 1995. Large-scale cortical networks and cognition. Brain Research Reviews. 20: 288-304.

[10] Burgess, A.P., Gruzelier, J.H., 1997. Short duration synchronization of human theta rhythm during recognition memory. Neuroreport. 8: 1039-1042.

[11] Burle, B., Bonnet, M., 2000. High-speed memory scanning: a behavioral argument for a serial oscillatory model. Cognitive Brain Research. 9: 327-337.

[12] Croxson, P.L., Johansen-Berg, H., Behrens, T.E., Robson, M.D., Pinsk, M.A., Gross, C.G., Richter, W., Richter, M.C., Kastner, S., Rushworth, M.F., 2005. Quantitative investigation of connections of the prefrontal cortex in the human and macaque using probabilistic diffusion tractography. J Neurosci. 25: 8854-8866.

[13] David, O., Garnero, L., Varela, F.J., 2001. A New Approach to the MEG/EEG Inverse Problem for the Recovery of Cortical Phase-Synchrony. Lecture Notes In Computer Science. Vol. 2082: 272-285.

[14] David, O., Cosmelli, D., Lachaux, J.P., Baillet, S., Garnero, L., Martinerie, J., 2003a. A theoretical and experimental introduction to the non-invasive study of large-scale neural phase synchronization in human beings. International Journal of Computational Cognition. Vol. 1, No. 4: 53-77.

[15] David, O., Friston, K.J., 2003b. A neural mass model for MEG/EEG coupling and neuronal dynamics. NeuroImage. 20: 1743-1755.

[16] David, O., Cosmelli, D., Friston, K.J., 2004. Evaluation of different measures of functional connectivity using a neural mass model. NeuroImage. 21: 659-673.

[17] David, O., Kilner, J.M., Friston, K.J., 2006. Mechanisms of evoked and induced responses in MEG/EEG. Neuroimage. 31: 1580-1591.

[18] Fell, J., Dietl, T., Grunwald, T., Kurthen, M., Klaver, P., Trautner, P., Schaller, C., Elger, C.E., Fernandez, G., 2004. Neural bases of cognitive ERPs: more than phase reset. J Cogn Neurosci. Vol 16. No 9: 1595-1604.

[19] Fisher, N.I., 1995. Statistical Analysis of Circular Data. Cambridge University Press.

[20] Foxe, J.J., McCourt, M.E., Javitt, D.C., 2003. Right hemisphere control of visuospatial attention: line-bisection judgements evaluated with high-density electrical mapping and source analysis. Neuroimage. 19: 710-726.

[21] Freeman, W.J., Schneider, W., 1982. Changes in spatial patterns of rabbit olfactory EEG with conditioning to odors. Phsychophysiology. Vol 19. No 1: 44-56.

.

[22] Friston, K.J., Stephan, K.M.,Frackowiak, R.S.J., 1997. Transient Phase-Locking and Dynamic Correlations: Are They the Same Thing?. Human Brain Mapping. 5: 48-57.

[23] Gabor, D., 1946. Theory of communication. Proc. Inst. Electr. Eng. 93: 429-441.

[24] Gardner, W.A., 1992. A unifying view of coherence in signal processing. Signal Processing. 29: 113-140. Elsevier.

[25] Gevins, A., Smith, M., McEvoy, L., Yu, D., 1997. High-resolution EEG mapping of cortical activation related to working memory: effects of task difficulty, type of processing, and practice. Cereb Cortex. 7: 374-385.

[26] Gevins, A., Smith, M.E., Leong, H., McEvoy, L., Whitfield, S., Du, R., Rush, G., 1998. Monitoring working memory load during computer-based tasks with EEG pattern recognition methods. Hum Factors. 40: 79-91.

[27] Gross, J., Kujala, J., Hamalainen, M., Timmermann, L., Schnitzler, A., Salmelin, R., 2001. Dynamic imaging of coherent sources: Studying neural interactions in the human brain. PNAS. Vol. 98, No. 2: 694-699.

[28] Guerrero, J.A., Marroquin, J.L., Rivera, M., Quiroga, J.A., 2005. Adaptive monogenic filtering and normalization of ESPI fringe patterns. Opt Lett. 30, 22: 3018-3020.

[29] Hagemann, D., Naumann, E., Thayer, J.F., 2001. The quest for the EEG reference revisited: A glance from brain asmmetry researh. Psychophysiology. 38: 847-857. Cambridge University Press.

[30] Haalman, I., Vaadia, E., 1998. Dynamics of neuronal interactions: Relation to behavior, firing rates, and distance between neurons. Human Brain Mapping. Vol. 5, No. 4: 249-253.

[31] Harmony, T., Fernández, T., Silva, J., Bernal, J., Díaz-Comas, L., Reyes, A., Marosi, E., Rodríguez, M., 1996. EEG delta activity: An indicator of attention to internal processing during performance of mental tasks. Int J Psychophysiol. 24: 161-171.

[32] Harmony, T., Fernandez, T., Fernandez-Bouzas, A., Silva-Pereyra, J., Bosch, J., Diaz-Comas, L., Galan, L., 2001. EEG changes during word and figure categorization. Clin. Neurophys. 112: 1486-1498.

[33] Harmony, T., Fernandez, T., Gersenowies, J., Galan, L., Fernandez-Bouzas, A., Aubert, E., Diaz-Comas, L., 2004. Specific EEG frequencies signal general common cognitive processes as well as specific task processes in man. International Journal of Psychophysiology. 53: 207-216.

[34] Hebb, D.O., 1949. The organization of behaviour. Wiley, New York.

[35] Hjorth B., 1975. An On-Line Transformation of EEG Scalp Potentials Into Orthogonal Source Derivations. Electroencephalography and Clinical Neurophysiology. 39: 526-530. Elsevier.

[36] Hoechstetter K., Bornfleth H., Weckesser D., Ille N., Berg P., Scherg M., 2004. BESA Source Coherence: A New Method to Study Cortical Oscillatory Coupling. Brain Topogr. 16(4): 233-238.

[37] Jansen, B.H., Rit, V.G., 1995. Electroencephalogram and visual evoked potential generation in a mathematical model of coupled cortical columns. Biol. Cybern. 73: 357-366.

[38] Jensen, O., Idiart, M.A., Lisman, J.E., 1996. Physiologically realistic formation of autoassociative memory in networks with theta/gamma oscillations: role of fast NMDA channels. Learn Mem. 3: 243-256.

[39] Junghöfer, M., Elbert, T., Tucker, D. M., Braun, C., 1999. The polar average reference effect: a bias in estimating the head surface integral in EEG recording. Clinical Neurophysiology, Volume 110, Issue 6: 1149-1155.

[40] Karakas, S., Basar-Eroglu, C., Ozesmi, C., Kafadar, H., Erzengin, O.U., 2001. Gamma response of the brain: a multifunctional oscillation that represents bottom-up with top-down processing. Int J Psychophysiol. 39: 137-150.

[41] Kirschfeld K., 2005. The physical basis of alpha waves in the electroencephalogram and the origin of the "Berger effect". Biol Cybern. 92: 177-185.

[42] Klimesch, W., 1999. EEG alpha and theta oscillations reflect cognitive and memory performance: a review and analysis. Brain Res Rev. 29: 169-195.

[43] Klimesch, W., Schack, B., Schabus, M., Doppelmayr, M., Gruber, W., Sauseng, P., 2004. Phase-locked alpha and theta oscillations generate the P1-N1 complex and are related to memory performance. Cogn Brain Res, 19: 302-316.

[44] Kolev, V., Yordanova, J., Schurmann, M., Basar, E., 2001. Increased frontal phase-locking of event-related alpha oscillations during task processing. Int J Psychophysiol. 39: 159-166.

[45] Lachaux, J.P., Rodriguez, E., Martinerie, J., Varela, F.J., 1999. Measuring Phase Synchrony in Brain Signals. Human Brain Mapping. 8: 194-208.

[46] Lachaux, J.P., Rodriguez, E., Martinerie, J., Adam, C., Hasboun, D., Varela, F.J., 2000a. A quantitative study of gamma-band activity in human intracranial recordings triggered by visual stimuli. European Journal of Neuroscience. 12: 2608-2622.

[47] Lachaux, J.P., Rodriguez, E., Le Van Quyen, M., Martinerie, J., Varela, F.J., 2000b. Studying single-trials of phase-synchronous activity in the brain. Int J Bifur Chaos. 10: 2429-2439.

[48] Law, S.K., Nunez, P.L., Wijesinghe, R.S., 1993. High-Resolution EEG Using Spline Generated Surface Laplacians on Spherical and Ellipsoidal Surfaces. IEEE Transactions on Biomedical Engineering. Vol. 40, No. 2: 145-153.

[49] Makeig, S., Westerfield, M., Jung, T.P., Enghoff, S., Townsend, J., Courchesne, E., Sejnowski, T.J., 2002. Dynamic Brain Sources of Visual Evoked Responses. Science. 295: 690-694.

[50] Malmvuo, J., Plonsey, R., 1995. Bioelectromagnetism: Principles and applications of bioelectric and biomagnetic fields. Oxford University Press, New York.

[51] Marroquin, J.L., Mitter, S., Poggio, T., 1987. Probabilistic Solution of Ill-Posed Problems in Computational Vision. J. Am. Stat. Assoc. 82: 76-89.

[52] Marroquin, J.L., Figueroa, J.E., 1997. Robust quadrature filters. J. Opt. Soc. Am. Vol. 14, No. 4, 779-791.

[53] Marroquin, J.L., Velasco, F.A., Rivera, M., Nakamura, M., 2001. Gauss-Markov Measure Field Models for Low-Level Vision. IEEE Transactions on Pattern Analysis and Machine Intelligence. Vol. 23. No. 4: 337-348.

[54] Marroquin, J.L., Harmony, T., Rodriguez, V., Valdes, P., 2004. Exploratory EEG data analysis for psychophysiological experiments. NeuroImage. 21: 991-999.

[55] Mazaheri, A., Picton T.W., 2005. EEG spectral dynamics during discrimination of auditory and visual targets. Cognitive Brain Research. 24:81-96.

[56] Mizuhara, H., Wang, L., Kobayashi, K., Yamaguchi, Y., 2005. Long-range EEG phase synchronization during an arithmetic task indexes a coherent cortical network simultaneously measured by fMRI. NeuroImage. Vol. 27, No. 3: 553-563.

[57] Morecraft, R.J., Geula, C., Mesulam, M.M., 1993. Architecture of connectivity within a cingulo-fronto-parietal neurocognitive network for directed attention. Arch Neurol. Vol. 50, No. 3: 279-284.

[58] Niedermeyer, E., Lopes da Silva, F.H., 2004. Electroencephalography: Basic Principles, Clinical Applications, and Related Fields. Lippincott Williams & Wilkins.

[59] Nunez, P.L., 1995. Neocortical Dynamics and Human EEG Rhythms. Oxford University Press.

[60] Nunez, P.L., Srinivasan, R., Westdorp, A.F., Wijesinghe, R.S., Tucker, D.M., Silberstein, R.B., Cadusch, P.J., 1997. EEG coherency I: statistics, reference electrode, volume conduction, Laplacians, cortical imaging, and interpretation at multiple scales. Electroencephalography and clinical Neurophysiology. 103: 499-515.

[61] Nunez, P.L., Silberstein, R.B., Shi, Z., Carpenter, M.R., Srinivasan, R., Tucker, D.M., Doran, S.M., Cadusch, P.J., Wijesinghe, R.S., 1999. EEG coherency II: experimental comparisons of multiple measures. Clinical Neurophysiology. 110: 469-486.

[62] Nunez, P.L., 2000. Toward a quantitative description of large-scale neocortical dynamic function and EEG. Behavioral and Brain Sciences. 23: 371-437.

[63] Osaka, N., Osaka, M., Kondo, H., Morishita, M., Fukuyama, H., Shibasaki, H., 2004. The neural basis of executive function in working memory: an fMRI study based on individual differences. Neuroimage. 21:623-631.

[64] Pascual-Marqui, R.D., Gonzalez-Andino, S.L., Valdes-Sosa, P.A., Biscay-Lirio, R., 1988. Current Source Density Estimation and Interpolation Based on the Spherical Harmonic Fourier Expansion. Int J Neurosci. 43(3-4): 237-249.

[65] Pascual-Marqui, R.D., 1999. Review of Methods for Solving the EEG Inverse Problem. International Journal of Bioelectromagnetism. Vol. 1. No. 1: 75-86.

[66] Penny, W.D., Kiebel, S.J., Kilner, J.M., Rugg, M.D., 2002. Event-related brain dynamics. Trends Neurosci. Vol 25. No 8: 387-389.

[67] Perrin, F., Pernier, J., Bertrand, O., Echallier, J.F., 1989. Spherical splines for scalp potential and current density mapping. Electroencephalography and clinical Neurophysiology. 72: 184-187. Elsevier Scientific Publishers, Ltd.

[68] Perrin, F., Pernier, J., Bertrand, O., Echallier, J.F., 1990. Corrigenda: EEG 02274. Electroencephalography and clinical Neurophysiology. 76: 565. Elsevier Scientific Publishers, Ltd.

[69] Pfurtscheller, G., 1977. Graphical display and statistical evaluation of event-related desynchronization (ERD). Electroenceph clin Neurophysiol. 43: 757-760.

[70] Pfurtscheller, G., 1992. Event-related synchronization: an electrophysiological correlate of cortical areas at rest. Electroenceph clin Neurophysiol. 83: 62-69.

[71] Pfurtscheller, G., Lopes da Silva F.H., 1999. Event-related EEG/MEG synchronization and desynchronization: basic principles. Clinical Neurophysiology. 110: 1842-1857.

[72] Press, W.H., Vetterling, W.T., Teukolsky, S.A., Flannery, B.P., 1992. Numerical Recipes in C: the art of scientific computing. Cambridge University Press, Second Edition.

[73] Quian Quiroga, R., Kraskov, A., Kreuz, T., Grassberger, P., 2002. Performance of different synchronization measures in real data: A case study on electroencephalographic signals. Physical Review E. 65, 041903.

[74] Quintana, J., Fuster, J.M., 1999. From Perception to Action: Temporal Integrative Functions of Prefrontal and Parietal Neurons. Cerebral Cortex. 9: 213-221.

[75] Rhom, D., Klimesch, W., Haider, H., Doppelmayr, M., 2001. The role of theta and alpha oscillations for language comprehension in the human electroencephalogram. Neurosci Lett. 310: 137.140.

[76] Rodriguez, E., George, N., Lachaux, J.P., Martinerie, J., Renault, B., Varela, F.J., 1999. Perception's shadow: long-distance synchronization of human brain activity. Nature. 397: 430-433.

[77] Salenius, S., Ramelin, R., Neuper, C., Pfurtscheller, G., Hari, R., 1996. Human cortical 40 Hz is closely related to EMG rhthmicity, Neuroscience Letters. 213: 75-78.

[78] Sarnthein, J., Petsche, H., Rappelsberger, P., Shaw, G.L., Von Stein, A., 1998. Synchronization between prefrontal and posterior association cortex during human working memory. Proc Natl Acad Sci USA. 95: 7092-7096.

[79] Sauseng, P., Klimesch, W., Schabus, M., Doppelmayer, M., 2005. Fronto-parietal EEG coherence in theta and upper alpha reflect central executive functions of working memory. Int J Psychophysiol. 57: 97-104.

[80] Schack, B., Klimesch, W., Sauseng, P. 2005. Phase synchronization between theta and upper alpha oscillations in a working memory task. International Journal of Psychophysiology. 57: 105-114.

[81] Shibata, T., Shimoyama, I., Ito, T., Abla, D., Iwasa, H., Koseki, K., Yamanouchi, N., Sato, T., Nakajima, Y., 1999. Event-related dynamics of the gamma band oscillation in the human brain: information processing during a GO/NO GO hand movement task. Neuroscience Research. 33: 215-222.

[82] Silverman, B.W., 1986. Density Estimation for Statistics and Data Analysis. Chapman and Hall, London.

[83] Singer, W., 1993. Synchronization of cortical activity and its putative role in information processing and learning. Ann Rev Physiol. 55: 349-374.

[84] Stephenson W.A., Gibbs F.A., 1951. A balanced non-cephalic reference electrode. Electroencephalogr Clin Neurophysiol. 3: 237240.

[85] Tallon-Baudry, C., Bertrand, O., Delpuech, C., Pernier, J., 1997. Oscillatory g-Band (30-70 Hz) activity induced by a visual task in humans. J Neuroscience. 15: 722-734.

[86] Tallon-Baudry, C., Bertrand, O., Fisher, C., 2001. Oscillatory synchrony between human extrastriate areas during visual short-term memory maintenance. J Neurosci. 15, RC177.

[87] Ungerleider, L.G., Courtney, S.M., Haxby, J.V., 1998. A neural system for human visual working memory. Proc Natl Acad Sci USA. 95: 883-890.

[88] Varela, F.J., Lachaux, J.P., Rodriguez, E., Martinerie, J., 2001. The Brainweb: Phase Synchronization and Large-Scale Integration. Nature Reviews, Neuroscience. 2: 229-239.

[89] Vogel, C.R., 2002. Computational methods for inverse problems. Frontiers in applied mathematics. SIAM, Philadelphia.

[90] Von Stein, A., Sarnthein, J., 2000. Different frequencies for different scales of cortical integration: from local gamma to long range alpha/theta synchronization. Int J Psychophysiol. 38: 301-313.

[91] Zhang, Z., 1995. A fast method to compute surface potentials generated by dipoles within multilayer anisotropic spheres. Physics in Medicine and Biology. 40: 335-349.